Fabrication of Optoelectronic Integrated Circuits Using Quantum Well Intermixing

A thesis for the degree of

Doctor of Philosophy,

submitted to the Faculty of Engineering,

University of Glasgow

by

Ooi Boon Siew

November 1994

ProQuest LLC.
789 East Eisenhower Parkway
P.O. Box 1346
Ann Arbor, MI 48106 – 1346

Acknowledgement

I would like to acknowledge the help of the following personnel, whose contributions have proved invaluable during the course of my project.

Firstly I would like to thank *John Marsh*, my academic supervisor, for the flexibility he gave me during the project, patiently guiding and encouraging me throughout the course. His concern and help over the last two years is gratefully acknowledged.

Catrina Bryce, my second supervisor, for working with me and providing supervision whenever required.

John Roberts of Sheffield University for growing the excellent MOVPE materials that were used in the course of this project, the Electrical Department of Surrey University for doing the ion implantation and *Alastair Chew* of Loughborough University of Technology for the SIMS analysis.

Lois Hobbs and the rest of the cleanroom staff, *Douglas McIntyre* and the team in the Ultrasmall Structure lab for being so helpful, and *Peter McKenna* for processing all the TEM pictures in this thesis.

In the Optoelectronics Research Group:
Karen McIlvaney, for being a constant source of encouragement.
Steve Ayling, for showing me techniques of laser characterisation and some helpful discussion on SISA process.
Jacques Beauvais (now with Sherbrooke University, Canada), who kept me busy for the first three months of my research.
Jim Gray, our group technician, for all the help.

In Physics and Astronomy Department:
John Chapman, the head of Solid State Research Group, for making the TEM available for this project.
Jeremy Martin, for supporting me on the TEM work during the early stage of the project and for teaching me the operation of the TEM before he left the Department.
Colin Scott, for showing me the technique of specimen preparation.

In dry-etching: *Ray Darkin*, *David Clifton*, and *Gillian Hopkins* for their technical assistance in the dry etching facilities, and *Simon Hicks*, for the work on laser reflectometry measurements.

In my office: *Andrew Brown*, *Colin Lamond*, *Andrew McLaughlin* and *Daniel Ortega*, for filling the office with joy.

I would especially like to thank *Peter Laybourn* and BNR (Europe) Ltd. for their financial support during my project.

Special thanks to my girl friend *Keat Boey* for her understanding, love and invaluable moral support. Last but not least, my family headed by my parents, *Ooi Cheng Ho* and *Chan Suan Heoh*, for their unconditional financial support and relentless encouragement.

To my father

Abstract

The effects of C_2F_6 overetching on subsequent $SiCl_4$ etching of GaAs/AlGaAs structures are investigated. This study is important for the fabrication of photonic devices in the later part of this project. A new reactive ion etching (RIE) damage detection technique, using a quantum well intermixing (QWI) probe, was developed and was used to investigate the RIE processes used in device fabrication. Using this damage detection technique, both the depth of RIE damage and propagation depth of the point defects generated by RIE can be probed and profiled.

A new QWI process, called plasma induced layer intermixing, has been developed. Bandgap tuned oxide stripe lasers have been fabricated. The quality of the material was found to be maintained after intermixing using this technique. Oxide stripe extended cavity lasers have also been demonstrated. Losses as low as 18.1 dB cm^{-1} have been measured in lasers with 500 μm long extended cavity sections intermixed using this new QWI process.

The diffusion and the intermixing mechanisms of fluorine and boron impurity induced disordering (IID) are investigated. Diffusion models and intermixing mechanisms for these species are proposed. A transmission electron microscope (TEM) was used to study the residual damage induced by these species in GaAs/AlGaAs structures. Comparing these two species, fluorine was found to be a better candidate to be used in neutral IID since it results in less residual damage, lower loss, and larger degree of intermixing. Low loss rib waveguides have been fabricated using fluorine IID and the propagation loss was found to be reduced to as low as 20 dB cm^{-1} at the lasing wavelength.

A new technique, called selective intermixing in selected area (SISA), has been developed to control the degree of intermixing in selected areas. Five distinguishable wavelengths (861 nm, 855 nm, 848 nm, 844 nm and 840 nm) have been observed from bandgap tuned lasers fabricated on a single chip intermixed using this technique.

Contents

Chapter 1 Introduction

1.1 Quantum well intermixing (QWI)

The light sources of interest in optical communications can be divided into two main groups: (i) GaAs/$Al_xGa_{1-x}As$ devices for the 0.65–0.9 μm wavelength region, and (ii) long wavelength devices, mostly $In_xGa_{1-x}As$ or $In_xGa_{1-x}P_yAs_{1-y}$, for the 1.1–1.7 μm wavelength region. Wavelengths from 0.8–1.55 μm are of interest since silica based optical fibre has low-loss and low-signal-dispersion in these regions. In addition, red wavelengths have gradually became important for polymer fibre.

Indium based ternary or quaternary devices are attractive for long-haul optical communication, such as trans-ocean submarine cable, since the lowest-signal-dispersion and lowest-loss windows of optical fibre lie at 1.3 and 1.55 μm. GaAs/AlGaAs devices, however, are well developed for the short-haul optical data links and have been widely used for CD players, CD-ROM and local area networks. GaAs/AlGaAs devices are likely to be components for application in high speed supercomputers and bidirectional communications in near future. Moreover, in the 0.8-0.9 μm region, inexpensive and high-quality Si-photodetectors are readily available on a commercial basis. It was, therefore, chosen to study GaAs/AlGaAs material in this project for the advantages of its wider range of applications and lower system cost than the indium based devices. In addition, it is also believed that much of the technology which applies to GaAs/AlGaAs compounds may also be transferred to In-based material for long wavelength devices.

The monolithic integration of several optoelectronic devices in photonic integrated circuits (PICs) and optoelectronic integrated circuits (OEICs) was first proposed by Miller[1]. Until recently, the integration of optoelectronic devices usually required many steps of etching and the regrowth on a bulk material. This approach always suffers from a mismatch in the optical propagation coefficient or dimensions of a waveguide at regrown interface. In addition, this process is time consuming, and of low yield, and therefore adds cost to the final product.

Optical waveguides in photonic integrated circuits play a similar function to the interconnection wires in an electrical circuit. However, laser action usually occurs just above the semiconductor band edge, which means that the passive waveguide section is highly absorbing at lasing wavelength. One of the solutions to this problem was developed by using the quantum well intermixing (QWI)[2] technique. In this process the bandgap of QW structures is modified in selected regions by intermixing the wells with the barriers to form an alloy semiconductor. A larger bandgap energy will be obtained after intermixing compared to the as-grown quantum well (QW) structure, thus providing a route to form low-loss optical waveguides. Bandgap-shifted QCSE modulators, lasers and detectors can also be fabricated monolithically using only one epitaxial step.

---

[1] S.E. Miller, Bell Syst. Tech. J. **48**, 2059 (1969).

[2] D.G. Deppe and N. Holonyak, Jr., 'Atom diffusion and impurity-induced layer disordering in quantum well III-V semiconductor heterostructures', J. Appl. Phys. **64**, R93 (1988).

Two commonly used QWI techniques for the GaAs/AlGaAs system are impurity-induced disordering (IID) and impurity free vacancy disordering (IFVD)[3]. To avoid increased free carrier absorption, which may result in high loss, neutral IID using fluorine and boron was introduced and has been intensively studied in the Department[4,5]. Each of these intermixing techniques has their own advantages. For example, a highly vertical intermixing profile can be obtained by IID, and IFVD is free from free carrier absorption and therefore lower loss can be obtained. There are, however, shortcomings such as residual damage for the IID process and low spatial resolution for IFVD. All of the advantages and shortcomings of these techniques have to be considered in order to fabricate a reliable device.

QWI techniques using IID and IFVD are studied in this thesis. The study of residual damage after intermixing and the intermixing conditions was carried out with neutral IID species. Low loss waveguides are fabricated and characterised using fluorine implanted and intermixed material. The mechanisms of the neutral intermixing processes are developed from experimental results obtained. In the case of IFVD, the study is concerned with the spatial control of the bandgap values using a one–step process. These fundamental studies are essential for the future work on fabrication of photonic integrated circuits (PICs) and optoelectronic integrated circuits (OEICs) using QWI techniques.

1.2 Reactive ion etching (RIE)

The fabrication of modern semiconductor devices often involves the spatial definition of ultra small pieces of material and features on nanometric scale. Conventional wet etching techniques can hardly be used reliably below 3 μm because of undercutting and poor uniformity. Using reactive ion etching (RIE) techniques, however, is possible to etch small geometries with minimal undercutting, and maintain accurate pattern transfer. In addition, the etching of material by reaction with chemically active radicals in a glow discharge is dry and clean, increases the reproducibility, and offers process simplification and better dimensional control compared to the existing wet-etching processes. The applications of plasma etching, however, have been held back because of its two main shortcomings, — RIE damage and surface contamination.

The exposure of the semiconductor to the impinging ions of plasma may cause damage up to a depth of a few tens of nm. The creation of non-radiative recombination centres or electronic traps through this damage will limit the use of RIE in the fabrication of nanoscale optical and electronic devices. Take integrated optical devices for example: low damage etching is important in producing

---

[3] see for example, J.H. Marsh, 'Quantum well intermixing', Semicond. Sci. Technol.. **8**, 1136 (1993).

[4] J.H. Marsh, S.R. Andrew, S.G. Ayling, J. Beauvais, S.A. Bradshaw, A.C. Bryce, S.I. Hansen, R.M. De La Rue and R.W. Glew, 'Neutral impurity disordering of III-V quantum well structures for optoelectronic integration', Mat. Res. Soc. Symp. Proc. **240**, 679 (1992).

[5] J.H. Marsh, S.I. Hansen, A.C. Bryce, R.M. De La Rue, 'Applications of neutral impurity disordering in fabricating low-loss optical waveguides and integrated waveguide devices', Optical and Quantum Electronics **23**, S941 (1991).

low scattering loss[6] waveguides. Quantum well (QW) devices such as QW lasers, heterojunction field effect transistors (HFET) *etc*, are sensitive to the presence of point defects. A possible problem for these devices after an annealing step is quantum well intermixing, which may change the bandgap energy and make the control of the required bandgap difficult.

The major source of contamination is from the reaction of etchant gases with the semiconductor surface to form nonvolatile products, for example the exposure of AlGaAs to a fluorocarbon[7,8] plasma will result in the formation of nonvolatile compounds such as AlF_3, GaF_3, AlF and fluorocarbon polymer. These contaminants may deposit on the semiconductor surface and act as micromasks during the etching of the semiconductor. These micromasks could inhibit the subsequent etching of the semiconductor and cause the etched surface to be rough. Multi etching steps are usually involved in the fabrication of modern semiconductor devices. For example, two etching steps are required for a device fabricated using silica as an etch mask, i.e. first etching of silica to define patterns followed by etching of the semiconductor. The contamination of a surface subjected to oxide overetch has to be considered after the first stage, in order to achieve a highly smooth etched surface and controllable etch rate during the subsequent etch.

None of the RIE process reported to date are free from ion bombardment damage and surface contamination. From an engineering point of view, understanding the effects of RIE damage and contamination for commonly used processes is crucial in order to make fabrication of highly efficient devices possible. Therefore, these two main problems are looked at in the first part of this thesis.

1.3 Thesis outline

This thesis is organised in two parts. Part one, from Chapter 2 to 5, is concerned with the studies of RIE damage, surface contamination, and the potential use of RIE damage to achieve QWI for photonic device applications. Part two documents the studies of QWI techniques using impurity induced disordering (IID) and impurity free vacancy disordering (IFVD).

Chapter 2, the starting chapter of part one, introduces some background of RIE, which includes the etching mechanisms, *in-situ* measurement techniques and the measurement techniques for both RIE damage detection and semiconductor characterisation. Chapter 3 presents the experimental results of contamination on a surface subjected to C_2F_6 overetch and the etch rate selectivity between SiO_2 and GaAs, and between GaAs and AlGaAs under different rf powers in the C_2F_6 process. Chapter 4 is concerned with the development of a QWI probe for RIE damage detection, and Chapter 5 documents the development of a novel RIE damage induced layer intermixing process, and

---

[6] M.W. Austine, 'GaAs/GaAlAs curved rib waveguides', J. of Quantum Electronics QE**18**, 795 (1982).

[7] S.J. Pearton, M.J. Vasile, K.S. Jones, K.T. Short, E. Lane, T.R. Fullowan, A.E. Von Neida, N.M. Haegel, 'Reaction ion etching of GaAs with CCl_2F_2:O_2: Etch rates, surface chemistry, and residual damage ', J. Appl. Phys. **65**, 1281 (1989).

[8] K.L. Seaward, N.J. Moll, D.J. Coulma, and W.F. Stickle, 'An analytical study of etch and etch-stop reactions for GaAs on AlGaAs in CCl_2F_2 plasma', J. Appl. Phys. **61**, 2358 (1987).

experimental results of bandgap tuned oxide stripe lasers and extended cavity lasers fabricated using this intermixing technique.

Part two of this thesis starts in Chapter 6. A brief introduction to QWI and the possible intermixing mechanisms of neutral IID using fluorine and boron are presented in this Chapter. Chapter 7 documents the experimental results of residual damage resulting from neutral IID using transmission electron microscopy. The results and discussion of loss measurements in fluorine IID rib waveguide are documented in Chapter 8. Chapter 9 reports the use of IFVD method to control selective intermixing in selected areas (SISA) and Chapter 10 suggests future work and summarises the findings of this project.

Chapter 2 Background of RIE and semiconductor characterisation techniques

2.1 Introduction

The technology of reactive ion etching (RIE) is briefly discussed in this Chapter. *In-situ* measurements of RIE systems such as laser interferometry and optical emission spectroscopy are documented. Etching mechanisms of $SiCl_4$ and C_2F_6 on GaAs/AlGaAs and SiO_2 are proposed. These two plasmas are studied, since they are widely used world-wide for device fabrication. The final part of this Chapter introduces the measurement techniques used to assess the properties of semiconductors. Among these techniques, photoluminescence (PL) spectroscopy and secondary ion mass spectrometry (SIMS) profiling techniques are discussed in some detail since they are going to be used in the studies of quantum well intermixing (QWI) reported in the later part of this thesis.

2.2 Reactive ion etching (RIE)

2.2.1 Plasma properties

Plasma is responsible for the etching process during the RIE, and therefore, the concept of plasma is important for the later understanding of the etching mechanisms of RIE. Basically, plasma can be considered as a partially ionised gas consisting of equal numbers of positive and negative charges, and a different number of un-ionised neutral molecules[1]. Consider a neutral gas which is placed within a tube to which is applied a dc potential across two conducting electrodes (Figure 1). The released electrons are then accelerated toward the positive electrode, or anode, and along the way undergo a series of elastic and inelastic collisions and the plasma is, therefore, formed or grown.

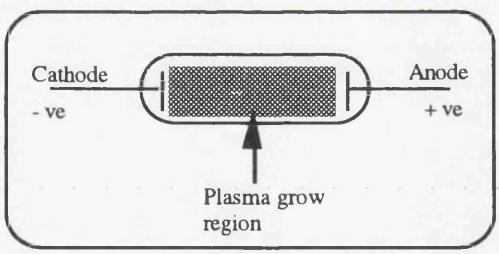

Figure 2.1: The schematic diagram representation of a dc glow discharge.

Kinetic energy is conserved in elastic collisions. Since an electron has a very much smaller mass than an atom, the energy transfer is negligible and the electron will simply change direction. All other types of electron collision are inelastic and will result in ionised species or excited neutral species in the plasma. Four important mechanisms in the plasma are excitation, relaxation, ionisation and recombination.

In the ionisation process, a bound electron in an atom is ejected from the atom. Electron impact ionisation, which is a type of inelastic collision, is important for sustaining the plasma. In this

[1] B. Chapman, 'Glow discharge process', (Wiley, New York, 1980).

process the primary electron removes an electron from the atom, producing a positive ion and two electrons, e.g. $2e + Cl_2 \rightarrow 2(2e + Cl^+)$. The two electrons produced in the ionising collision can then be accelerated by an electric field until they, too, can produce ionisation. Besides electron impact, ionisation resulting from photoionisation is also significant in the RIE system. Recombination is the inverse process of ionisation, i.e. an electron coalesces with a positive ion to form a neutral atom.

Excitation is a process in which a less dramatic transfer of energy to the bound electron occurs and which enables the electron to jump to a higher energy level within the atom with a corresponding quantum absorption of energy. This process can result from both electron impact excitation or photoexcitation. The excitation potential is always lower than the ionisation potential since ionisation removes the electron from the atom but excitation only raises an electron to a higher shell in an atom.

The relaxation process is just the inverse process of excitation. The excited states are rather unstable and the electron configuration soon returns to the ground state in one or several transitions, with lifetimes varying enormously from nanoseconds to seconds. Each transition is accompanied by the emission of a photon of very specific energy $h\nu$. Due to the relaxation process in the plasma, the technique of optical emission spectroscopy (OES) is useful for detecting and determining the presence of various atoms in the plasma.

Besides the four inelastic collisions discussed above, two other processes — dissociation and electron attachment — are also important in the plasma. The process of dissociation is the breaking apart of a molecule. A result of dissociation is an enhancement of chemical activity, since the products are usually more reactive than the parent molecule, for example

$e + C_2F_6 \rightarrow e + 2CF_3$ (Dissociation)

$e + C_2F_6 \rightarrow 3e + 2CF_3^+$ (Dissociation ionisation).

There is a possibility that an electron colliding with an atom may join onto the atom to form a negative ion. This process is known as electron attachment. Take the $SiCl_4$ plasma, for example, $e + SiCl_4 \rightarrow SiCl_3^- + Cl$.

2.2.2 *Basic theory of RIE*

Figure 2.2 shows a conventional parallel plate ac RIE system. The etching chamber consists of two parallel electrode plates. The top electrode is grounded and the bottom electrode is driven by an 13.56 MHz rf generator, connected through a capacitor and an impedance matching circuit. The sample is placed on the bottom electrode. An etch gas is fed into the etch chamber which is kept under a pumped evacuated environment. Free electrons in the chamber gain energy by following the oscillation of the applied rf power which leads to the formation of plasma as discussed in Section 2.2.1.

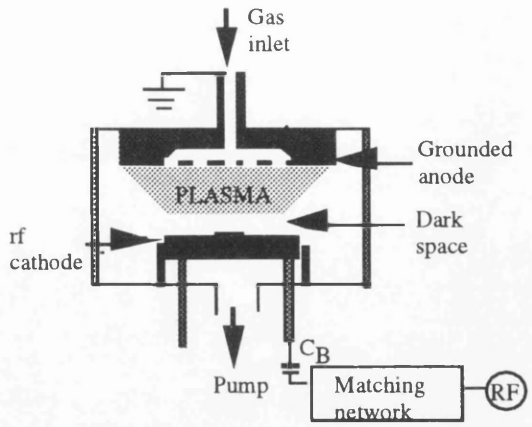

Figure 2.2 : The schematics diagram of a parallel plates rf RIE system.

The rf driven electrode of the RIE system is dc isolated from the power supply by a capacitor C_B. The function of this capacitor is to block the electrode from discharging through the power supply. The response of the plasma to the positive and negative cycles is different. When the electrode is positive, many highly mobile electrons are accelerated towards the electrode causing a significant accumulation of negative charge. When the electrode (the cathode) is negative, heavy, immobile ions are accelerated towards it. However, only relatively few of these ions strike the electrode compared to the number of electrons on the previous cycle. Therefore, a high electric field region is formed around the cathode. This region is known as the plasma sheath, or the dark space, where ion acceleration takes place before bombarding the electrode.

The plasma potential is determined by the expression[2] $V_c = V_a\left(\frac{A_c}{A_a}\right)^4$, where V_c is the potential difference between the powered electrode (cathode) and the plasma, V_a is the potential difference between the ground electrode (anode) and the plasma and A_c / A_a is the ratio of the respective electrode areas. The accelerating field for the ions near the sample is, therefore, greatly enhanced since the bottom electrode is smaller in area than the top electrode. The resultant potential distribution is shown in Figure 2.3. If no collisions occur in the sheath regions, the average kinetic energy of singly ionised positive striking the cathode is $(V_p - V_c)$eV, where V_p is the plasma potential.

The typical etch pressure used in RIE system is relatively low (5–100 mTorr). Hence, the mean free path of the ions is increased so that they are not randomised in direction. The above features such as the driven electrode being placed at the bottom (where the sample is placed), electrode asymmetry and low pressure operation all lead to an enhancement in the energy and directionality of the ions bombarding the surface being etched, thus increasing the degree of anisotropy. Therefore RIE utilises both chemical and physical etch mechanisms.

---

[2]S.M. Sze, 'VLSI Technology', 2nd. edit., (Mcgraw–Hill, New York,1988).

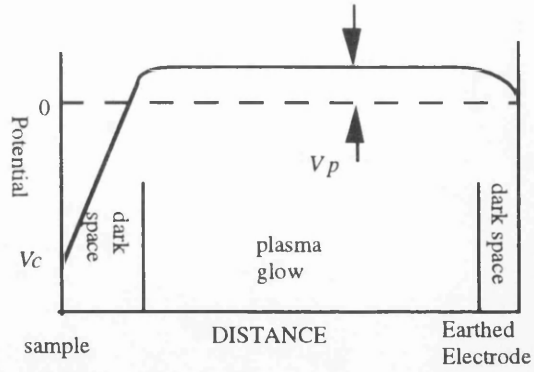

Figure 2.3: Plot of the average potential within the two electrodes. Vc is the cathode potential, Vp is the plasma potential.

2.2.3 RIE mechanisms

In general four steps are involved in reactive ion etching mechanisms: these are; (i) transport of the reactive species to the surface, (ii) adsorption of the reactive species onto the substrate surface, (iii) reaction with the substrate and the formation of volatile product, and (iv) transport of the volatile product away from the substrate.

The potential difference between anode and cathode makes the positive ions accelerate to the substrate. The gas-phase species chemisorb onto the surface of the substrate. In the case of molecular gases, this chemisorption will often involve dissociation of the molecule. However, even in cases where chemisorption is nondissociative, the radiation necessarily present in the glow discharge will usually cause the adsorbed molecule to fragment. The third step is the formation of the volatile reaction product and the final step is the desorption of the reaction product into the gas phase.

Take the $SiCl_4$ etch of GaAs/AlGaAs as an example. In the discharge chamber, $SiCl_4$ will first dissociate with the probable products of $SiCl_3^+$, $SiCl_2^+$, Si, Cl_2 *etc* with the probable dissociation mechanisms of $SiCl_4 \xrightarrow{e-dissociation} SiCl_x^a, Si^b, Cl_y^c$, where x and y are equal to 1, 2 or 3 and a, b and c, can be + or –. Since most of the etching of GaAs has been carried out by chlorine ions and radicals[3] and the formation of compounds between GaAs/AlGaAs and $SiCl_4$ is negligible, only chlorine molecules are to be considered as in the etching mechanisms below:

Chemisorption: $(Cl_2)_{gas} \rightarrow (Cl_2)_{ads} \rightarrow 2Cl_{ads}$,

Reaction: $Ga + xCl_{ads} \rightarrow (GaCl_x)_{ads}$,

$As + xCl_{ads} \rightarrow (AsCl_x)_{ads}$,

$Al + xCl_{ads} \rightarrow (AlCl_x)_{ads}$ and

Desorption:

$$(AsCl_x)_{ads} + (GaCl_x)_{ads} + (AlCl_x)_{ads} \rightarrow (AsCl_x)_{gas} + (GaCl_x)_{gas} + (AlCl_x)_{gas}.$$

[3]S.K. Muraad, PhD thesis, University of Glasgow, 1994.

Apart from $AsCl_3$ and $GaCl_3$ (with volatility at 25 °C of ≈40 and ≈0.08 Torr respectively)[4,5], other etch products given in the above equations are highly volatile.

In the case of RIE of SiO_2 in C_2F_6 plasma, the dissociation process may produce $C_2F_6 \xrightarrow{e-dissociation} C_xF_y{}^a, C^b, F_z^c$. Both carbon and fluorine can act as active etching species in this case, with carbon responsible for reaction with O_2 and fluorine with silicon. Although COF_2 is always detected during the etch of SiO_2 using fluorocarbon gases[6], when discussing the mechanisms carbon and fluorine are considered separately. The following etching mechanisms are proposed:

Chemisorption: $C_xF_y{}^a, C^b, F_z^c \rightarrow (C_xF_y)_{ads}, (C)_{ads}, (F_z)_{ads} [+electrons]$,

Reaction: $(C_xF_y)_{ads}, (C)_{ads}, (F_z)_{ads} + SiO_2 \rightarrow w(SiF_4)_{ads}, (CO_z)_{ads}$,

Desorption: $w(SiF_4)_{ads}, (CO_z)_{ads} \rightarrow w(SiF_4)_{gas}, (CO_z)_{gas}$.

Where *w*, *x*, *y* and *z* here is equal to 1 or 2.

2.2.4 *RIE damage*

High biases, of an order of ≥300 V, are usually employed in a RIE system in order to obtain anisotropic etching of a semiconductor. This high bias, and hence high ion bombardment energy, can cause considerable degradation to the electrical and optical properties of devices, which is known as dry etch damage. It is known from the ion implantation model that the depth penetration of an implanted species is directly proportion to the energy and inversely proportion to the mass. Therefore, the degree of RIE damage is highly dependent on the accelerating potential and the mass of the ion species. The principal source of surface damage may result directly from the ion flux. For material near to patterned edges, however, the rebound ions, sputtered material and chemical reactants from the sidewall may also cause damage to the surface (Figure 2.7). Similar to surface damage, sidewalls suffer damage from the direct bombardment by directional ions and reactive radicals, effects from nondirectional ions, reactive radicals, possibly deposition and ricocheting particles from the bottom surface (Figure 2.7).

---

[4] CRC Handbook of Chemistry and Physics (Chemical Rubber, Cleveland, Ohio, 1970).

[5] S.C. McNevin, 'Chemical etching of GaAs and InP by chorine: The thermodynamic predicted dependence on Cl_2 pressure and temperature', J.Vac.Sci. Technol. B 4,1216 (1986).

[6] H.F. Winters, J.W. Coburn, and E. Kay, 'Plasma etching – A pseado-black box approach', J. Appl. Phys. **48**, 4973 (1977).

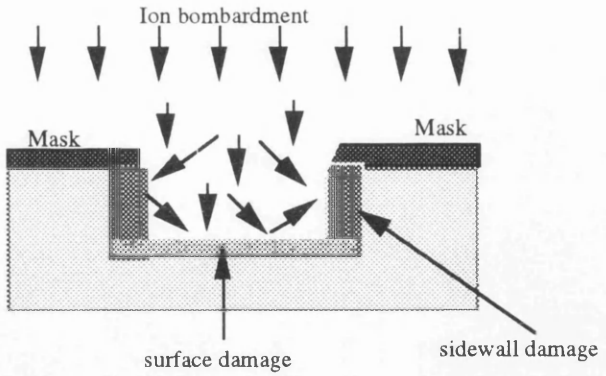

Figure 2.4: The model of RIE damage.

RIE damage has been observed to reduce the transconductance of MESFETs where gate recess etching has been carried out using RIE[7], to degrade the Schottky barrier after the surface has been exposed to plasma in the RIE[8,9], and to degrade the PL intensity by generating nonradiative centres[10].

Damage depths induced by RIE are always found to be in the range 200—2000 Å from the surface, which is considerably deeper than the projected range of ions crossing the plasma sheath. This is ascribed to channelling of these relatively low-energy particles, and recombination-enhanced motion of defects[11,15]. The degree of damage has also been found to be inversely proportional to the ion mass, and directly proportional to the ion energy[12,28].

Sidewall damage on a sample subjected to RIE is more difficult to measure than surface damage, since the fabrication of devices on the sidewalls is not practical. However, this damage can be assessed using the conductance measurement technique[13,14], and Schottky diodes characteristics made on the sidewalls[15]. In the case of the conductance measurement technique, wires with different widths are fabricated and the conductances of the wires are measured. The sidewall damage can then be determined from the cut off width (from the plot of conductance as a function of width) and by solving

---

[7]see for example, S. Salimian, C.Yuen, C. Shih, C. Smith and C.B. Cooper, 'Damage studies of dry etched GaAs recessed gates for field effect transitors', J.Vac. Sci. Technol. B **9**, 114 (1991).

[8] T. Hara, H. Suzuki, and A. Suga, 'Radiation damage of GaAs induced by reactive ion etching', J. Appl. Phys. **62**, 4109 (1987).

[9] R.Cheung, Y.H. Lee, K.Y. Lee, T.P. Smith, and D.P. Kern, S.P. Beaumont and C.D.W. Wilkinson, 'Comparison of damage in the dry etching of GaAs by conventional reactive ion etching and by reactive ion etching with an electron cyclotron resonance generated plasma', J. Vac. Sci. Technol. B **7**, 1462 (1989).

[10] K. Gamo, H. Miyake, Y. Yuba, and S. Nambe, 'Defect study in GaAs bombarded by low-energy focused ion beams', J. Vac. Sci. Technol. B **6**, 2124 (1988).

[11]H.F. Wong, D.L. Green, T.Y. Liu, D.G. Lishan, M. Bellis, E.L. Hu, M. Petroff, P.O. Holtz, and J.L. Merz, 'Investigation of reactive ion etching induced damage in GaAs/AlGaAs quantum well structures', J. Vac. Sci. Technol. B **6**, 19 (1988).

[12]S.W. Pang, G.A. Lincoln, P.W. McClelland, P.D. DeGraff, M. Geiss, and W.J. Piacontini, 'Effects of dry etching on GaAs', J. Vac. Sci. Technol. B **1**, 1334 (1983).

[13]S. Thoms, S.P. Beaumont, C.D.W. Wilkinson, J. Frost, and C.R. Stanley, in Microcircuit Engineering (1986), edited by H. W. Lehman and Ch. Bleicker (North Holland, Amsterdam, 1986), p.249.

[14] S.K. Murad, C.D.W. Wilkinson, P.D. Wang, W. Parkes, C.M. Sotomayar-Torres, and N. Cameron, 'Very low damage etching of GaAs', J. VAc. Sci. Technol. B **11**, 2237 (1993).

[15]R. Cheung, S. Thoms, M. Watt, M.A. Ford, C.M. Sotomayor-Torres, C.D.W. Wilkinson, U.J. Cox, R.A. Cowley, C. Dunscombe, and R.H. Williams, 'Reactive ion etching induced damage in GaAs and $Al_{0.3}Ga_{0.7}As$ using $SiCl_4$', Semicon. Sci. Technol. **7**, 1189 (1992).

the equation of surface depletion depth due to the air-GaAs interface, $x_o = (2\varepsilon f_s / \varepsilon n)^{1/2}$, where $\varepsilon = \varepsilon_o \varepsilon_r$ is the permittivity, f_s is the Fermi level near the midgap, and n is the carrier concentration. Sidewall damage during dry etching can be more significant than the surface damage, since the sidewall is exposed to the plasma for longer than the etched surface. Sidewall damage has been found to be directly proportional to the etch time[16]. The observation of quantum effects in fabricated structures of reduced dimentionality such as quantum wires has been found to be inhibited by sidewall damage[17].

Annealing, using a rapid thermal processor or furnace, of samples at temperatures in the range of 200 to 450 °C for a few seconds to a few minutes, depending on the degree of RIE damage, has been reported to lead to at least partial removal of surface damage. Temperatures higher than 500 °C are usually required to restore the initial carrier concentration when hydrogen is involved in the discharge. The drop in carrier concentration is due to the combined effects of hydrogen passivation and serious damage from the light H^+ ions[23]. In most cases, annealing at temperatures of about 400 °C is proven to be effective at reactivating the quality of the material[21]. Subsequent wet etching[18] to remove the damaged layer is also reported. However, these methods are inefficient and difficult to control since wet etching is involved. To the best of our knowledge, however, there is no systematic study yet reported on recovery techniques for sidewall damage.

2.3 In-situ measurements of RIE

2.3.1 Introduction

In-situ monitoring techniques commonly used in RIE are optical emission spectroscopy (OES), mass spectroscopy (MS)[19,20], laser reflectometry[21] , and ellipsometry[22]. These techniques are commonly used to determine the *in-situ* etch rate, end point detection at an interface and, within the bulk, gas phase chemistry and materials chemistry. From a device engineering perspective, end point detection is the most important.

---

16 M. Rahman, N.P. Johnson, M.A. Ford, A.R. Long, M.C. Holland and C.D.W. Wilkinson, 'Model for conductance in dry-etching damaged n-GaAs structures', Appl. Phys. Lett. **61**, 2335 (1992).

17 S.W. Pang, W.D. Goodhue, T.M. Lyszczarz, D.J. Ehrlich, R.B. Goodman, and G.D. Johnson, 'Dry etching induced damage on vertical sidewalls of GaAs channels', J. Vac. Sci. Technol. B **6**, 1916 (1988).

18 A.C. Papadopoulo, C. Dubon-Chevallier, J.F. Bresse, A.M. Duchenois, and F.Heliot, 'Etching procedures of GaAs : Cathodoluminescence study of the induced damages and of the recovering techniques', J. Vac. Sci. Technol. B **8**, 407 (1990).

19 see for example, P. Collot, T. Diallo and J. Canteloup, 'Dry-etch monitoring of III-V heterostructures using laser reflectometry and optical emmision spectroscopy ', J. Vac. Sci. Technol. B **9**, 2497 (1991).

20 see for example, S.E. Hicks, W. Parkes, J.A.H. Wilkinson and C.D.W. Wilkinson, 'Reflectance modelling for In-situ dry etch monitoring of bulk SiO_2 and III-V miltilayer structures', to be appeared in Nov. 1994 issue of J. Vac. Sci. Technol. B.

21 see for example, T.R. Hayers, P.A. Heimann, V.M. Donnelly, and K.E. Strege, 'Maskless laser interferometric monitoring of InP/InGaAsP heterostructure reactive ion etching', Appl. Phys. Lett. **57**, 2817 (1990).

22 see for example, R. Muller, '*In-situ* etching depth monitoring for reactive ion etching of InGaAs(P)/InP heterostructure by ellipsometry', Appl. Phys. Lett. **57**, 1020 (1990).

The usual practice for predicting the etch depth of an RIE process is to calibrate the process and simply time the etch run. However, from experience, precise control of the etch rate is difficult and can only be accurate to about 10 % from run to run. More accurate etch depth control can be achieved by etching the sample for 1/2 of the predicted etch time, measuring the etch depth and then predicting the time required to finish the etch. This method will still usually lead to an inaccurate etch depth, especially if the material consists of an AlGaAs layer, since an AlGaAs layer will be oxidised rapidly when exposed to the air, resulting in a longer induction time for the subsequent etch[23]. This method is also time consuming, sometimes material wasting and, therefore, high cost.

A simple and frequently applicable technique is to monitor the dc bias potential while holding the rf power constant. Since the voltage/power dependence is related to plasma chemistry, a change in this relationship often occurs when the plasma contribution from the etched layer is no longer present. However, this technique is limited to structures with an etch stop layer.

The OES and laser reflectometry measurement techniques are to be briefly described in this Section since there are widely used in the Department. In addition, the laser reflectometry measurement is going to be used for the study of the variation of the real time etch rate after oxide overetch. The results of this study are to be reported in the next Chapter.

2.3.2 Optical emission spectroscopy (OES) and laser reflectometry

A typical optical emission spectroscopy (OES) system is represented in Figure 2.5. This system uses a monochromator which consists of a spectrometer equipped with a 1200 grooves mm^{-1} grating (focal length = 20 cm, slit width = 125 μm) which provides a spectral range from 200 to 800 nm. This range of wavelengths is sufficient since most of the fluorocarbon, Al, As, Ga and the compounds of Ga fluoresce in the wavelength range of 200 to 450 nm. The usual case is to use the signals from the Ga = 417.2 nm line[6] and the 261.4 nm line from AlCl for the application the of *in-situ* etch rate measurement, since these lines are stronger in emission intensity. The spectrometer is connected using a silica optical fibre to a viewport of the RIE chamber equipped with a focusing lens. This system is dedicated to plasma analysis, monitoring and diagnostics.

---

[23] B.S. Ooi, S.E. Hicks, A.C. Bryce, C.D.W. Wilkinson, and J.H. Marsh, 'Study of C_2F_6 overetch induced damage and the effects of overetch on subsequent $SiCl_4$ etch of GaAs/AlGaAs', accepted by J. Appl. Phys.

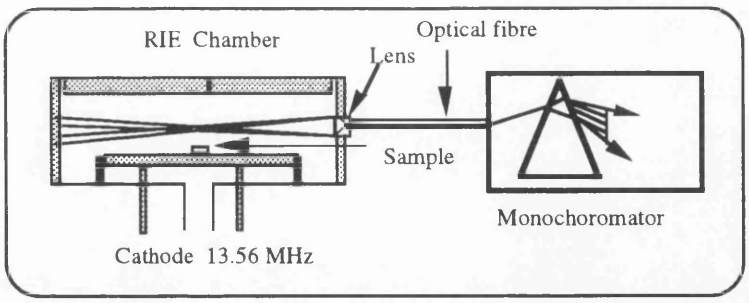

Figure 2.5: The schematic diagram of OES measurement set-up.

OES and MS can only be used to detect the variation in intensity of certain etch products as the etch process proceeds through layers of differing composition. They cannot therefore be used to determine the etch depth within a particular layer. The laser reflectometry measurement, however, overcomes this problem by permitting a real time measurement of etched thickness, etch rate, and interface determination.

The experiment set-up for the laser reflectance measurement is shows in Figure 2.5. The laser reflectometry unit used in the Department is commercially available from Sofia Instruments. This unit consists of a solid state diode laser (wavelength 679.0 nm ± 0.5 nm) with a beam spot size of about 40 μm. A beamsplitter directs the reflected signal along an optical fibre to a 10 nm bandpass filter. The filtered signal is then detected using a Hamamatsu R928 photomultiplier and the output collected and analysed using a computer.

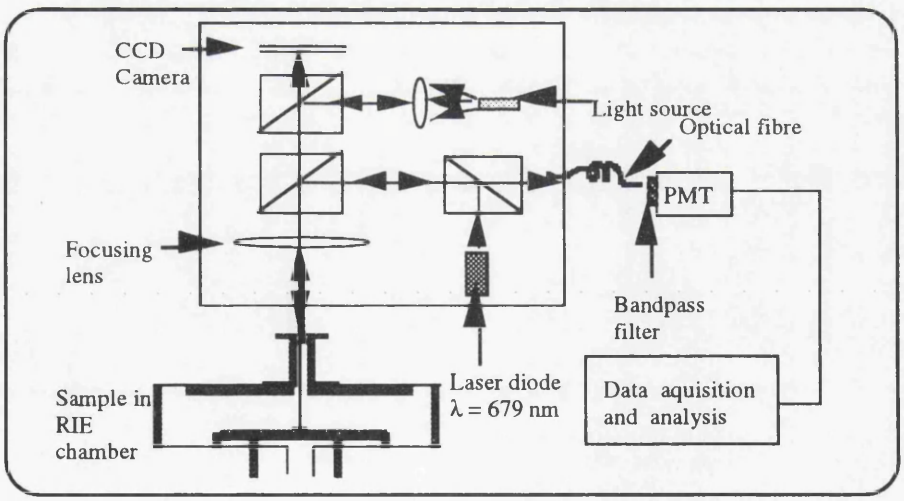

Figure 2.6: Experimental set-up used to measure in-situ laser reflectance as a function of time whilst etching.

The amplitude of the reflected signal is dependent upon the reflection coefficient between the top surface and air, and upon the reflection coefficients at the interfaces of any subsequent layers, with due allowance for the phase of the light reflected from these layers.

During etching, the intensity of laser light reflected off a substrate surface oscillates. This oscillation occurs because of the phase interference between the light reflected from the outer and inner

interfaces of the etched layer. The period of the oscillation is related to the change in film thickness by $\Delta d = \lambda / 2(n^2 - \sin^2 \theta_i)^{1/2}$, where Δd is the change in film thickness for one period of reflected light. λ is the wavelength of laser light, n is the refractive index of the etching layer and θ_i is the angle of incidence with respect to the normal. In the case of normal incidence, the equation can be simplified as $\Delta d = \lambda / 2n$.

The refractive indexes for GaAs = 3.86 and 40 % AlGaAs = 3.57 at the wavelength of 679 nm[24]. The peak to peak period of the reflectance signal is equivalent to 95 nm for 40 % AlGaAs and 88 nm for GaAs respectively. Taking a DQW material structure as an example, the reflectance signals corresponding to the particular layers are simulated and given in Figure 2.6. These reflectance and the derivative signals are obtained using a theoretical simulation created by Hicks *et al.*

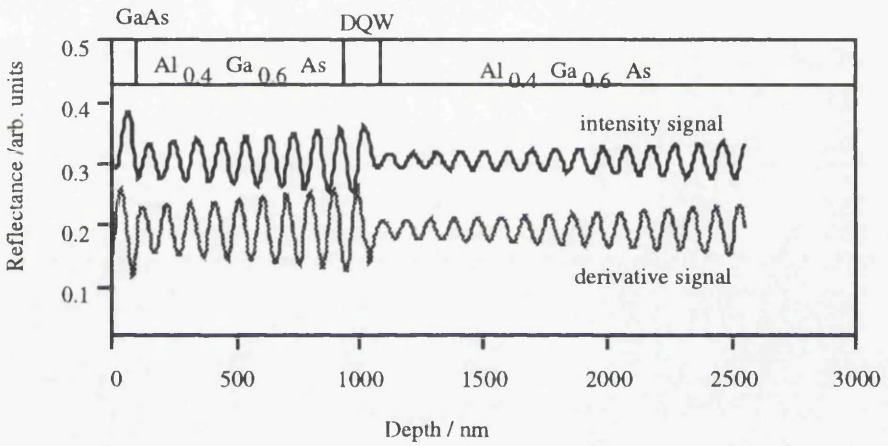

Figure 2.7: The reflectance signal and the derivative signal from a double QW GaAs/AlGaAs structure.

2.4 Measurement techniques for evaluating the material properties

2.4.1 Introduction

This Section documents the electrical and optical measurement techniques used to study both the optical and the electrical properties of a semiconductor. These measurement techniques are concerned with both RIE damage and semiconductor characterisation. Profiling techniques using secondary ion mass spectrometry (SIMS) and photoluminescence (PL) measurement are discussed in some detail in this Section since these techniques are to be used frequently in the study of QWI in this project.

2.4.2 Electrical measurement techniques

The RIE damage and the quality of a semiconductor can be evaluated by studying the electrical characteristics of Schottky diodes or electrical characteristics derived from ohmic contacts patterned and

---

[24]S. Adachi, 'GaAs, AlAs, and $Al_xGa_{1-x}As$: material parameters for use in research and device applications', J. Appl. Phys. **58**, R1 (1985).

analysed using the Transmission Line Model (TLM) and from Van der Pauw measurements. These electrical measurement techniques are commonly used to measure the surface damage. In the TLM method, a line of ohmic contacts with an increasing separation is needed. After measurement, the resistance between adjacent contacts is plotted against the separation distance. The slope of the resulting straight line gives the sheet resistance of the semiconductor layer and the intercept at zero separation gives the contact resistance of the ohmic contacts.

The Hall mobility, sheet carrier concentration, and sheet resistivity, all of which can be determined using Van der Pauw Hall measurements, are commonly used since these measurements correspond directly to electronic device properties. This measurement technique can be carried out readily at either room or liquid nitrogen temperature (77 K). Damage to the lattice will degrade the mobility of carriers due to scattering, therefore information about the quality of a semiconductor can be obtained from the carrier mobility of a sample.

I-V characteristics can be measured from Schottky diodes. The Schottky contact, usually a TiPtAu contact, is defined and the ideality factor, the Schottky barrier height, and the diode characteristics (reverse breakdown voltage and reverse leakage current) can be determined from the *I-V* measurement. The damage induced by RIE is then deduced from the decrease of barrier height and increase of the ideality factor

The main drawback of the electrical measurements, however, is that they do not provide information about the damage profile and the nature or the physical extent of damage. In addition, the sample preparation for electrical measurements is complex and destructive since metal contacts are involved, and the semiconductor material used in these measurement has to be relatively heavily doped.

2.4.3 Profiling technique using secondary ion mass spectrometry (SIMS)

One of the commonly used and highly sensitivity depth profiling technique is secondary ion mass spectrometry (SIMS). In SIMS, the sample is bombarded in a vacuum chamber by an energetic beam of primary ions with energy in the range 1 to 20 keV. The interaction of primary ions with the target atoms of the semiconductor gives rise to both removal and ionisation of the sample atoms. As a result, particles from the semiconductor are sputtered, some of which are in the form of secondary ions. For example, O_2^+ is used as a primary ion to bombard the semiconductor and the emission of positive secondary ions is detected for tracing boron in the semiconductor, and Cs^+ is used as primary ion to study the emission of negative secondary ions from fluorine atoms. The positive or negative secondary ions are then extracted into a mass spectrometer and separated according to their mass to charge ratio. By monitoring the intensity of one or more mass peaks as a function of bombardment time, a depth concentration profile is obtained. To obtain a quantitative depth profile, the data of mass intensity versus time is then converted into concentration versus depth. A simplified version of an SIMS system is shown schematically in Figure 2.8.

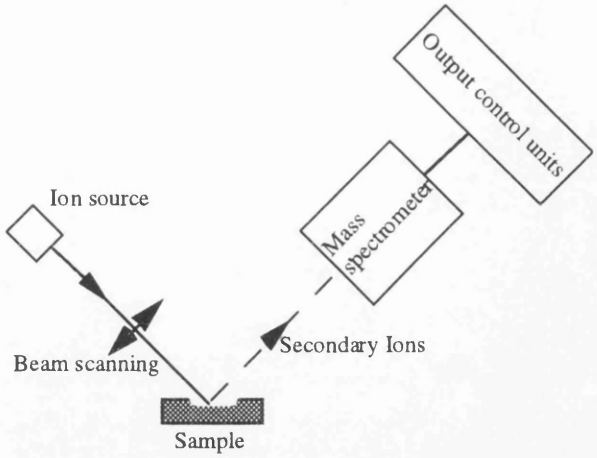

Figure 2.8: The schematic diagram of a SIMS system.

SIMS is usually used to study ion implantation profiles, depth profiles of epitaxial grown layers, and the intermixing of QWs[25]. In the case of RIE, it can be used to profile the change of doping concentration[26] and analyse semiconductor passivation with hydrogen after RIE[27].

2.4.4 Surface and cross sectional observation using transmission electron microscopy (TEM)

Transmission electron microscopy (TEM) has been widely used to analyse residual damage[28], QW intermixing[29], strain and interfaces[30], dislocations[31], surface morphology of a semiconductor, *etc*. It is also used to determine the Al composition within the AlGaAs ternary[32], since dark field (002) electron microscopy of GaAs/AlGaAs cross sectional images are sensitive to the composition of the Al composition of superlattice layers. The existence of impurities or defects in a semiconductor lattice can also be determined from the diffraction patterns of the material[26]. In the case of RIE, TEM was used to study the sidewall damage of wires[33], and the dislocation loops formed after dry-etching of GaAs/GaAlAs[34] using Cl_2/Ar. High resolution transmission electronic microscopy (HRTEM) is usually required for a detailed analysis of RIE damage, since the primary damage induced by dry etching

---

[25] see for example, J.H. Marsh, 'Quantum well intermixing', Semicond. Sci. Technol. 8, 1136 (1993).

[26] J.C. Mikkelsen, Jr. and I-W. Wu, 'Severe loss of dopant activity due to CHF_3+CO_2 reactive ion etch damage', Appl. Phys. Lett. **49**, 103 (1986).

[27] S.J. Pearton, U.K. Chakrabarti, and W.S. Hobson, 'Reactive ion etching induced damage in GaAS and AlGaAs using $C2H_6$/H_2/Ar or CCl_2F_2/O_2 gas mixtures', J. Appl. Phys. **66**, 2061 (1989).

[28] see for example, B.S. Ooi, A.C. Bryce, J.H.Marsh, and J.Martin, 'Transmission electron microscope study of fluorine and boron implanted and annealed GaAs/AlGaAs', Appl. Phys. Lett. **65**, 85 (1994).

[29] see for example, S. Chen, S.T. Lee, G. Rajeswaran and P. Fellinger, 'Correlation between defetc characteristics and layer intermixing in Si implanted GaAs/AlGaAs superlattices', Mat. Res. Soc. Symp. Proc. **147**, 279 (1989).

[30] see for example, P.M. Petroff, 'Role of electron microscopy in semiconductor electronic defects analysis', Mat. Res. Soc. Symp. Proc. **46**, 433 (1985).

[31] see for example, H.L. Tsai, Y.C. Kao, 'Generation and propagation of threading dislocation in GaAs grown on Si', J. Appl. Phys. **67**, 2862 (1990).

[32] P.M. Petroff., ' Transmission electron microscopy of interfaces in III–V compound semiconductors', J. Vac. Sci. Technol. **14**, 973 (1977).

[33] M.A. Ford, Ph D thesis, University of Glasgow, (1992).

[34] S.Pang, paper presented at EPIB, to be appeared in J. Vac. Sci. Technol. B , Nov. 1994.

is near surface point defects and impurity passivation. The use of TEM in the study of residual damage will be discussed in more detail in Chapter 7.

2.4.5 *Optical measurement technique using photoluminescence (PL) spectroscopy*

The main optical measurement techniques used in characterising semiconductors are Raman scattering, photoluminescence (PL) and cathodoluminescence (CL). However, only the PL measurement technique is to be described in this Section since this luminescence technique is to be used frequently in this project. PL measurement is a sensitive tool for QW characterisation and for investigating quantum well intermixing[35]. It has advantages over other techniques since the PL measurement technique does not required any particular sample preparation, is a non-destructive process, and allows the study of a complete wafer prior to device fabrication. PL from a QW structure is always closely related to the exciton effects. Therefore, an understanding of the exciton is important prior to the discussion of PL spectroscopy.

A free electron and free hole are created whenever a photon of energy greater that the energy gap is absorbed in a crystal. This electron and hole can then be bound together, by an attractive coulomb interaction force, to create an electron–hole pair which is known as exciton. Excitons are unstable with respect to radiative recombination in which the electron drops into the hole in the valence band, accompanied by the emission of a photon. The threshold energy for creating an excitation is $\hbar\omega > E_g$ in a direct bandgap semiconductor. The energy required for an indirect bandgap semiconductor is higher, such as silicon, since the recombination process is assisted by phonons. At low temperature, excitons usually have energies just below the bandgap energy. At room temperature, however, the linewidth of excitons is broadened by the large concentration of phonons and the exciton levels merge into the continuum absorption spectrum. As a result, the absorption spectrum from excitons can hardly be separated from the continuum absorption spectrum.

In the case of QW structures, when the QW thickness is smaller than Bohr radius, the exciton binding energy will be $R_{2D} = 4R_{3D}$, where R_{2D} and R_{3D} are the Rydberg values, or the exciton binding energies, in two and three dimensional structures respectively. The value of R_{3D} is 4.2 meV for bulk GaAs[36]. The binding energy in the 2D limit is given by [37]

$$R_{n,2D} = R_{3D}\left[\frac{1}{(n-\frac{1}{2})^2}\right],$$

where n is the quantum level. The increase of the exciton binding energy in a 2D system means QW structure have their optical properties dominated by exciton effects even at room temperature. Exciton recombination in a QW structures always occur at the $n = 1$ electron-heavy hole (E_{1h}) transition since

---

[35] Y. Hirayama, Y. Suzuki, and H. Okamoto, 'Ion-species dependedce of interdiffusion in ion-implanted GaAs–AlAs superlattices', Jpn. J. Appl. Phys. **24**, 1498 (1985).

[36] C. Kittel, 'Introduction to solid state physics', 6th. edit., (Wiley, New York, 1991).

[37] F. Stern and W.E. Howard, Phys. Rev. **163**, 816 (1967).

this level has the highest exciton binding energy. Exciton effects in absorption spectra of 3D and 2D systems are illustrated in Figure 2.9.

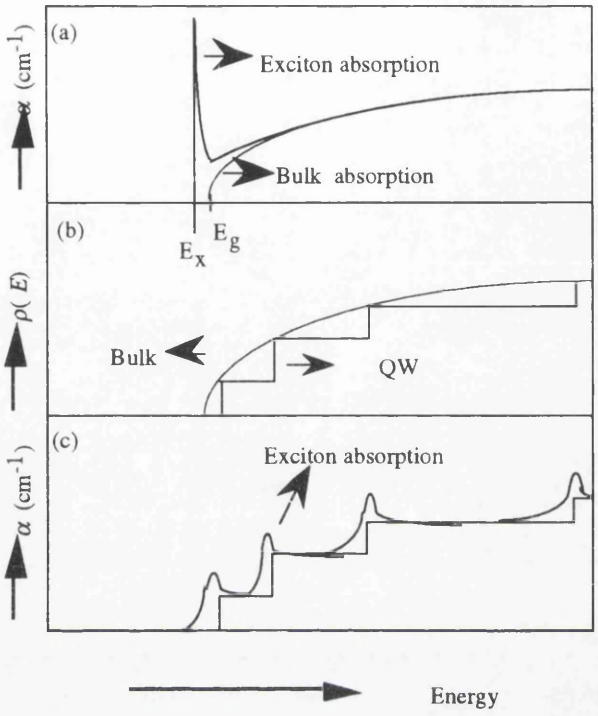

Figure 2.9: (a) The absorption edge spectrum of GaAs including exciton effects and the bulk (3D) density of states. (b) The two dimensional energy band in an QW has a step function density of states. (c) The absorption edge spectrum predicted for a GaAs QW with a step function density of states is compared with that for bulk GaAs, including the contribution from exciton creation.

The experimental set–up of the PL system used in this project to assess RIE damage assessment and bandgap shift due to intermixing is given in Figure 2.10. In brief, the 514.5 nm line of an argon laser is focused onto the sample surface to excite the exciton luminescence from the QWs. The laser beam is modulated by an optical chopper and luminescence is detected using a lock in amplifier. For low temperature (77 K) PL measurements, the sample is cooled by immersion in liquid nitrogen. The reflected and excited light are guided to a monochromator, whilst the luminescence is detected by a liquid nitrogen cooled Ge–detector. The spectral data is then analysed using a computer.

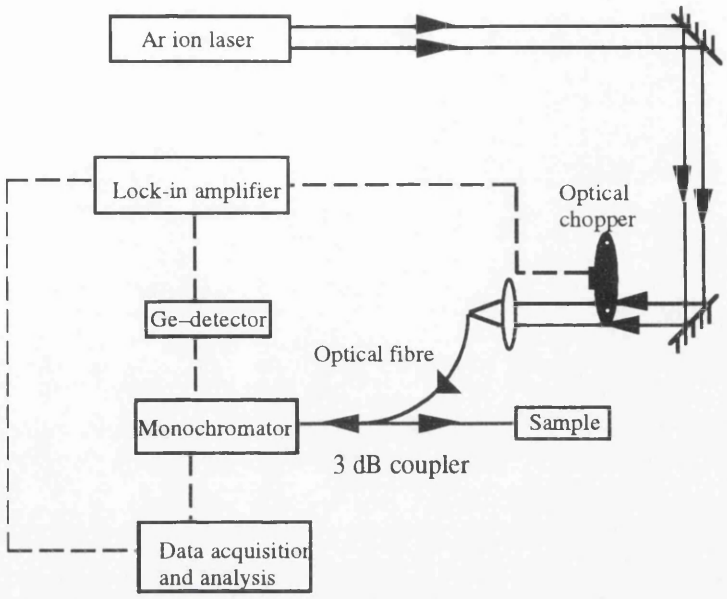

Figure 2.10: The experimental set–up for PL measurement.

2.5 Summary

The concept of plasma and the conventional parallel plate RIE system have been briefly described in this Chapter. The etching mechanisms of GaAs/AlGaAs using $SiCl_4$ and SiO_2 using C_2F_6 have been proposed and the origins of RIE damage were briefly discussed. A description of *in-situ* measurement techniques was given, in particular optical emission spectroscopy and laser reflectometry. The electrical measurement techniques, using TLM, Van der Pauw and Schottky diodes, were briefly introduced. The SIMS and TEM techniques were briefly discussed and depth profiling and direct observation techniques were taken as examples. The background to the optical measurement technique using PL spectroscopy and its experimental realisation were also described in this Chapter.

Chapter 3 RIE of SiO_2 and GaAs/AlGaAs in C_2F_6 and $SiCl_4$ plasmas

3.1 Outline

This Chapter documents the experimental results of SiO_2 and GaAs/AlGaAs dry-etching using C_2F_6 and $SiCl_4$ reactive ion etching (RIE). Factors such as the etch rate, damage to underlying semiconductor, etch profile, selectivity of etching of oxide on semiconductor and the ability to subsequently etch the semiconductor after completion of oxide etch are examined. Surface contamination after over-exposure of the samples to C_2F_6 plasma is investigated using *in-situ* laser reflectometry measurements.

3.2 Introduction

Silica is commonly used as the masking material in the fabrication of optoelectronic integrated circuits and photonic integrated circuits — a suitable dry-etch for SiO_2 is C_2F_6. C_2F_6 is chosen for the advantages of providing a high etch rate and producing relatively vertical etch profiles. To ensure complete etching of SiO_2 , it is common practice to overetch the sample for a few seconds. This overetch stage is necessary to compensate for any etch rate non–uniformity, layer thickness non–uniformity, or underlying topography. The problems which may be encountered in the case of overetch will be surface contamination, selectivity of the etch of the oxide over the semiconductor and surface damage.

Surface smoothness and controllable etch rate are important in most device processing applications. RIE can introduce both ion-bombardment damage and surface chemical contamination. The major source of contamination is from the reaction of etchant gases with the semiconductor surface to form nonvolatile products. For example, the exposure of AlGaAs to a C_2F_6 [1,2] plasma will result in the formation of nonvolatile compounds such as AlF_3, GaF_3, AlF and fluorocarbon deposits. These contaminants may deposit on the semiconductor surface and act as micromasks during the etching of the semiconductor. These micromasks could inhibit the subsequent etching of the semiconductor and also cause the etched surface to be rough.

In this Chapter, first we study the etch rates of SiO_2 and GaAs/AlGaAs in C_2F_6 RIE under various rf powers. The etch profile of SiO_2, and etch rate of masking materials are also investigated. The induction time and the etch rate of GaAs and AlGaAs layers were investigated using *in-situ* laser reflectometry measurements during the subsequent etch using $SiCl_4$. The damage to the underlying material due to oxide overetch will be discussed in Chapter 4.

---

1. S.J. Pearton, M.J. Vasile, K.S. Jones, K.T. Short, E. Lane, T.R. Fullowan, A.E. Von Neida, N.M. Haegel, 'Reactive ion etching of GaAs with CCl_2F_2:O_2: Etch rates, surface chemistry, and residual damage', J. Appl. Phys. **65**, 1281 (1989).
2. K.L. Seaward, N.J. Moll, D.J. Coulma, and W.F. Stickle, 'An analytical study of etch and etch-stop reactions for GaAs on AlGaAs in CCl2F2 plasma', J. Appl. Phys. **61**, 2358 (1987).

3.3 Dry-etching of SiO_2 and GaAs/AlGaAs in C_2F_6 plasma

3.3.1 Experiment and measurement methods

A conventional 13.56 MHz parallel-plate RIE system (Plasma Technology RIE80) was used for the C_2F_6 RIE studies. The etching process was carried out at 20 °C and the gas flow rate was kept at 20 sccm with an etch pressure of 15 mTorr. RF etching powers in the range of 10 to 100 W, with corresponding dc self biases of -150 to -450 V, were investigated here. The cathode plate of the RIE80 has a diameter of 17.7 cm, therefore the power density varied between 0.041 W cm^{-2} and 0.406 W cm^{-2} for the rf power range between 10 and 100 W. These etching conditions were chosen since there are commonly used in the C_2F_6 RIE process in the Department.

The material used in this study was grown by metalorganic vapour phase epitaxy (MOVPE) at Sheffield University. The sample had the structure of a separate confinement heterostructure (SCH) double quantum well (DQW) laser. The GaAs quantum wells were 100 Å wide, separated by a 100 Å $Al_{0.2}Ga_{0.8}As$ barrier. The top and bottom $Al_{0.2}Ga_{0.8}As$ QW barriers were 0.1 μm thick. The DQW and the barriers were undoped. The upper cladding layer was $Al_{0.2}Ga_{0.8}As$ doped with carbon (p-type, 5×10^{17} cm^{-3}) and the lower cladding layer was silicon doped $Al_{0.2}Ga_{0.8}As$ (n-type, 5×10^{17} cm^{-3}). The uppermost epilayer consisted of 0.1 μm of GaAs doped with 5×10^{18} cm^{-3} of zinc. This wafer was designed to be an optical waveguide and is to be used in the fabrication of devices in the later part of this project. A summary of the structure is given in Appendix A1.

The samples used in the study of SiO_2 etch rate, etch profile, and GaAs/AlGaAs etch rate under various etching rf powers were first cleaved into 5 x 5 mm^2 followed by deposition of 5000 Å of silica, using Plasma Enhanced Chemical Vapour Deposition (PECVD). Patterns with stripe widths between 2 and 5 μm were defined using photolithography. The photoresist used in this experiment was of type S1400–31, giving a thickness of ≈1.8 μm after spinning at 4000 rpm for 30 s. After developing the patterns, the samples were baked at 120 °C for 15 min to make the resist stick harder on the SiO_2 surface before being subjected to the ion bombardment of RIE. Samples were subsequently cleaved into 2.5 x 2.5 mm^2 and exposed to C_2F_6 plasma for 20 min under various etching powers. An SEM (Hitachi S800), was used to measure the SiO_2 etch profile and a Talystep was used to determine the etch rate of SiO_2 and GaAs/AlGaAs.

3.3.2 Results and discussion

Both chemical and physical reactions are involved in the etching mechanisms of an RIE process. The probable chemical reactions between C_2F_6 plasma and SiO_2 have been discussed in Chapter 2. The physical etch mechanism is merely a sputtering process which results from energetic ion bombardment. Therefore, the etch rate and the etch profile of a semiconductor are greatly influenced by two parameters — the rf power, and hence dc bias, and the gas flow rate. The gas flow rate is

responsible for the chemical reaction and the supplied dc bias, where the ions gain their energy, is responsible for the physical etch mechanism. In general, the isotropic or anisotropic etch of a material is highly dependent on the rf power of the RIE process. At low power, the ions and reactive radicals accelerated across the plasma sheath may suffer collisions with each other, and their momentum will be randomised. This will result in an isotropic etch due to the non–directionality of the low energy ions bombarding the etch surface, but will be highly selective because of the chemical nature of the reactive radicals. At high power, however, the ion flux directed on the material will be perpendicular to the etch surface, and therefore, an anisotropic etch can be obtained. In this Section the etch rates and etch profiles of SiO_2 in C_2F_6 RIE under various rf power and a constant flow rate are studied.

The self dc bias induced by an rf power in the range between 10 and 100 W C_2F_6 RIE is represented in Figure 3.1. It is noticed that the dc bias varied by about –20 V from run to run. The self dc bias provides information about the ion acceleration and energy gained from ion bombardment of the material. Therefore the etch rate is expected to vary with the varying dc bias. The higher the self dc bias, the higher the sputtering rate due to ion bombardment. The relationship of $a = Ee / m$ (acceleration a of a particle of mass m and charge e due to an electrical field E), implies that, for a higher applied potential, an ion will gain a higher energy and, when bombardment occurs, the energy will be transferred and result in sputtering. The transport rates, both the reactive ions to the substrate and the volatile layer away from the substrate, will also be influenced by the applied potential. The transport rates will be higher in a high potential condition. As a result, a higher etch rate will be obtained.

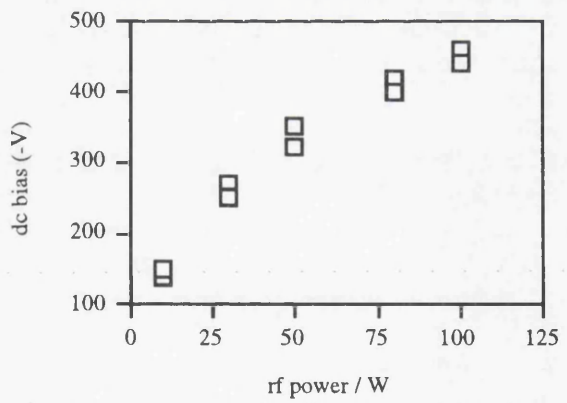

Figure 3.1 : Self dc bias versus rf power for C_2F_6 RIE using a Plasma Technology RIE80. The small variations in dc bias from run to run may due to residual gases and chamber conditions.

The etch rate of SiO_2 varied from 120 Å/min to 500 Å/min as the power was varied from 10 W to 100 W (Figure 3.2). Figure 3.3 shows that C_2F_6 etching results in a relatively low selectivity between SiO_2 and GaAs, and also that the selectivity was strongly dependent on the rf power. The formation of nonvolatile GaF_3 on GaAs layers is difficult using fluorocarbon gas RIE[3], since the GaAs surface is depleted of fluorine by reaction with arsenic and subsequent desorption of

[3] S. Salimian and C.B. Cooper, III, 'Selective dry etching of GaAs over AlGaAs in $SF_6/SiCl_4$ mixtures' J. Vac. Sci. Technol. B **6**, 1641 (1988).

arsenic fluorides such as AsF_3 and AsF_5, which are very volatile, occurs. Besides the formation of highly volatile arsenic fluorides gases, the reaction between C_2F_6 plasma and GaAs may result in the formation of other products such as C_3As_4, $Ga(CF_4)$ and $As(CF_4)$ so giving rise to the high etch rates of GaAs. Highly selective etching of SiO_2 over GaAs could only be obtained using low power C_2F_6 RIE.

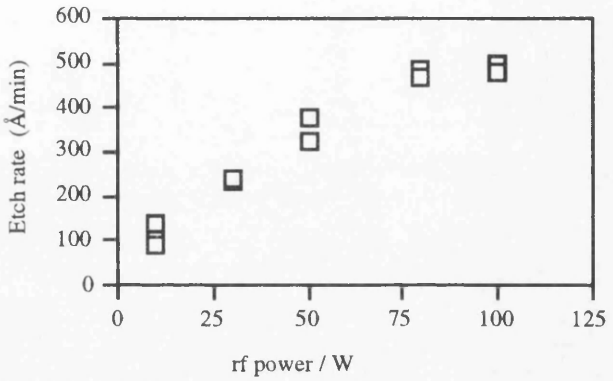

Figure 3.2: The SiO_2 etch rates as a function of rf power for C_2F_6 RIE.

C_2F_6 was expected not to etch AlGaAs, since it is well known that fluorocarbons form nonvolatile AlF_3 and AlF to inhibit the etching of AlGaAs. However, the etch depth measurements showed that C_2F_6 etched both GaAs and $Al_{0.4}Ga_{0.6}As$ at rf powers of 30 W and above, with the selectivity factors given in Figure 3.3. It was not possible to calculate the etch rate selectivity for an rf power of 10 W since the AlGaAs layer was not etched under this condition. The selectivity factor is defined here as the ratio of the GaAs (or SiO_2) etch rate to that of AlGaAs (or GaAs). Relatively low selectivity values were obtained at high rf powers and these were found to increase rapidly at low powers. Under high-energy ion bombardment conditions, the nonvolatile layers such as AlF_3 are expected to be sputtered away effectively, so providing a free surface with which the C_2F_6 plasma can react. Increasing the concentration of C_2F_6 or the fluorine to carbon ratio is expected to increase the selectivity factor between GaAs and AlGaAs layers. This can be attributed to the formation of a greater thickness of nonvolatile AlF_3 on the AlGaAs layer. However, the formation of this nonvolatile layer will make the subsequent etch of GaAs/AlGaAs difficult, and a rough surface will be obtained.

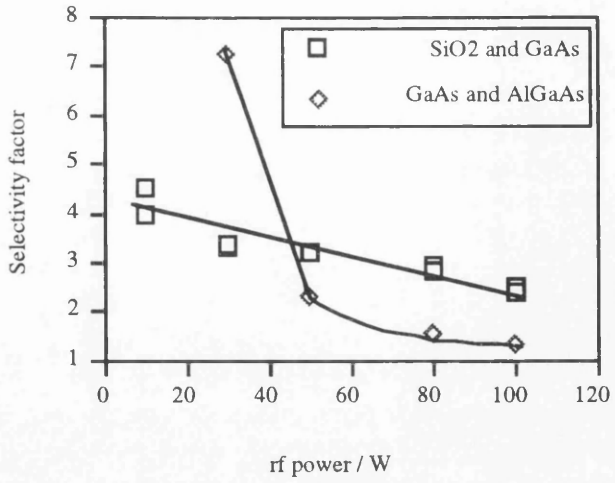

Figure 3.3: The selectivity of C_2F_6 between SiO_2 and GaAs, and between GaAs and AlGaAs as a function of rf power.

The SiO_2 profiles etched under different powers are given in Figure 3.4. Although the etch power of 100 W provided a highly vertical etch profile, the other etch powers studied in this experiment gave overcutting. The definition of the undercut angle is shown inset. At low power, the absorbed reactant species on the sidewall did not gain enough energy from bombarding ions to be transported and therefore overcutting resulted. At high powers, however, the energised ions provided energy to the adsorbed species so enabling the reaction between the reactant species and SiO_2 to take place and, hence, anisotropic etching was achieved.

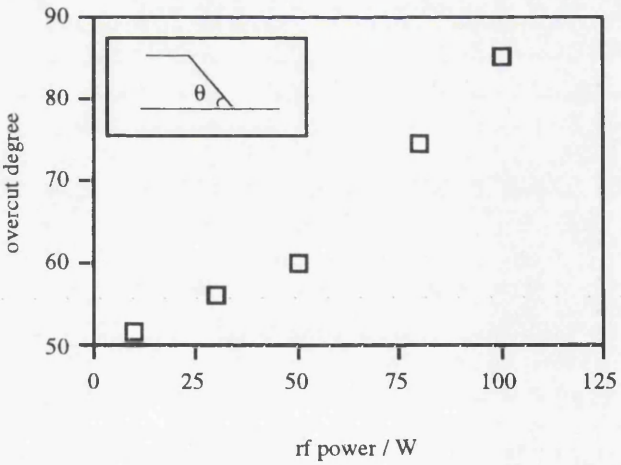

Figure 3.4.: Overcutting degree verses rf power. The overcutting degree is defined in the inset.

Most types of resist are either etched or sputtered during the C_2F_6 process. The three types of masking material studied here were phototresist (type S1400-17 and S1400-31), e-beam resist {(PMMA) 8% BDH + 4% ELV and 12% BDH + 4% ELV}, and 500 Å of NiCr. The precise etch rate was not measured, but only the maximum time for which the resists survived in C_2F_6 plasma at one particular etch power of 100 W (Table 3.1).

Masking material	Thickness	Preparation conditions	Max. survival time
S1400-31	1.8 μm	4000 rpm, 30 s	20 min
S1400-17	0.7 μm	4000 rpm, 30 s	7 min
8% BDH+4% ELV	≈ 0.3 μm	5000 rpm, 1 min	3 min
12% BDH+4% ELV	≈ 0.5 μm	5000 rpm, 1 min	5 min
NiCr	500 Å	evaporation	30 min.

Table 3.1: The maximum time for which certain types of photoresist, e-beam resist and NiCr survived in C_2F_6 RIE using a power of 100 W.

Results from Table 3.1 suggest that e-beam resists are not useful for masking C_2F_6 plasma etching since they can be sputtered away with a relatively fast rate. Both photoresists and e-beam resists are make of organic substances. Therefore they can either be sputtered or react with C_2F_6 plasma easily, forming organic gases. Metals such as NiCr are more likely to be sputtered away rather than be etched, however, NiCr is a useful mask for etching a thick layer of SiO_2 in the case of C_2F_6 RIE.

3.4 Surface contamination

3.4.1 Experiment

The same material was used to study the influence of surface contamination, due to exposure to the C_2F_6 plasma, on the subsequent etching of the GaAs/AlGaAs structure using $SiCl_4$. In this study, samples were cleaved to 2 x 2 mm^2 and were exposed to C_2F_6 plasma for 5 min, the rf powers of the plasmas being again varied between 10 and 100 W (0.041 and 0.406 W cm^{-2}). The subsequent etch using $SiCl_4$ was performed in another Plasma Technology RIE80 machine. The etching conditions were set to 30 W (-150 V), 9 sccm, and 8 mtorr. $SiCl_4$ was chosen because it produces good surface morphologies after RIE, if a clean surface is etched, and provides similar etch rates for both GaAs and AlGaAs.

In-situ laser reflectometry measurements were carried out directly on the etched surface, during the subsequent $SiCl_4$ etch, to measure the real–time etch rate of the layers and the induction time. The detail of the experimental set-up and technique for this measurement is documented in Chapter 2. For comparison, laser reflectometry measurements were also carried out on samples after the GaAs cap was removed using a selective wet etch of NH_3:H_2O_2 (1:20) for 15 s. A Hitachi S800 scanning electron microscope (SEM) was again used to examine the surface of the samples after exposure to the C_2F_6 plasma and subsequent etch in $SiCl_4$.

A sample implanted with fluorine was used to study the influence of fluorine on the real-time etch rate during the $SiCl_4$ RIE. This sample had a similar grown structure and doping densities as the

other samples used in this study, but with only 0.9 μm of upper cladding layer. The implantations were performed at Surrey University and the implantation energies and doses were 1.53 x 10^{13} cm^{-2} at 80 keV, 3.3 x 10^{13} cm^{-2} at 260 keV and 5.1 x 10^{13} cm^{-2} at 700 keV. These implantation conditions will give a constant fluorine impurity concentration of 5 x 10^{17} cm^{-3} throughout a range of ≈ 1.5 μm deep. This implantation profile, obtained from SIMS, under the above implantation conditions will be described more detail in Chapter 6.

3.4.2 Effect of C_2F_6 overetch on GaAs and AlGaAs layers

To investigate the effect of C_2F_6 overetch on subsequent $SiCl_4$ etch, samples with a 0.1 μm GaAs cap and 1.3 μm $Al_{0.4}Ga_{0.6}As$ were exposed to the C_2F_6 plasma for 5 min at different powers and subsequently etched using $SiCl_4$ at a dc bias of around –150 V. Laser reflectometry was used to measure the real–time etch rate of the layers and the induction time. No other sample preparation was required for these measurements.

In the case of normal incidence, the period of the oscillation of the laser reflectometry is related to the change in film thickness by $\Delta d = \lambda / 2n$, where Δd is the change in film thickness for one period of reflected light, λ is the wavelength of laser light and n is the refractive index. Taking the refractive indexes for GaAs as 3.86 and 40% AlGaAs as 3.57 at wavelength of 679 nm, the peak to peak periods of the reflectance signals are equivalent to 95 nm for 40% AlGaAs and 88 nm for GaAs respectively. The first, large peak, oscillating from 74 to 114 s of the etch time of the as-grown sample corresponds to the GaAs layer, whilst the subsequent oscillations correspond to the etch of the AlGaAs (Fig.3.5). The induction time was measured by noting the time duration of the slowly changing reflectance signal before the oscillations started.

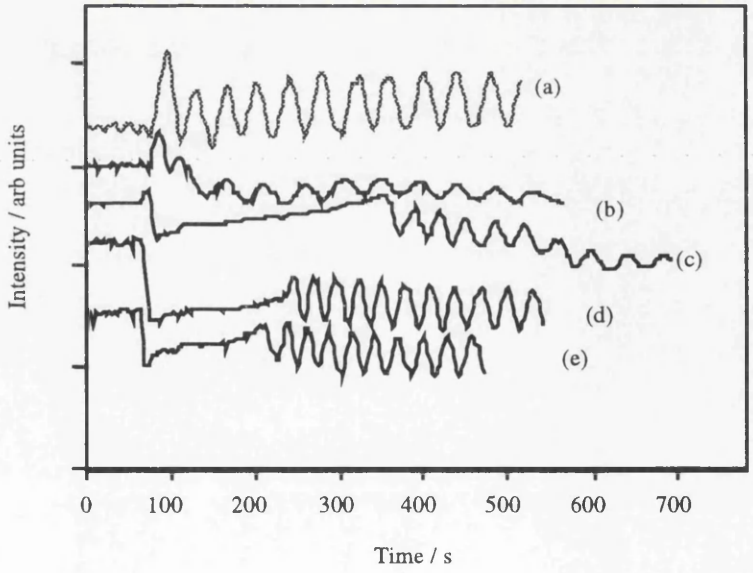

Figure 3.5: The reflectance signals obtained from the (a) as-grown sample, and samples exposed to C_2F_6 using rf powers of (b) 10 W, (c) 30 W, (d) 50 W and (e) 80 W.

After 5 min of C_2F_6 exposure, only the sample exposed to 100 W C_2F_6 had the 0.1 μm GaAs cap completely removed. The as–grown sample had the same GaAs induction time (16 s) and etch rate as the 10 W and the fluorine implanted samples (Fig.3.5 and Fig.3.8). The induction time measured from as-grown and fluorine implanted samples may be attributed to the time taken to sputter away the native oxide, consisting mainly of Ga_2O_3 and As_2O_3 having a thickness of ≈ 20 Å [4]. The GaAs cap was not etched by the 10 W C_2F_6 RIE, therefore either the oxide was not removed or the oxide was removed and replaced by a C–F contaminated layer. The GaAs induction time would be expected to be the same as for the as-grown sample if the oxide were not removed. If the oxide was removed and replaced by a fluorocarbon layer deposited on the surface, the time then taken to sputter away the fluorocarbon layer would have to be, by coincidence, the same as the time to remove the oxide.

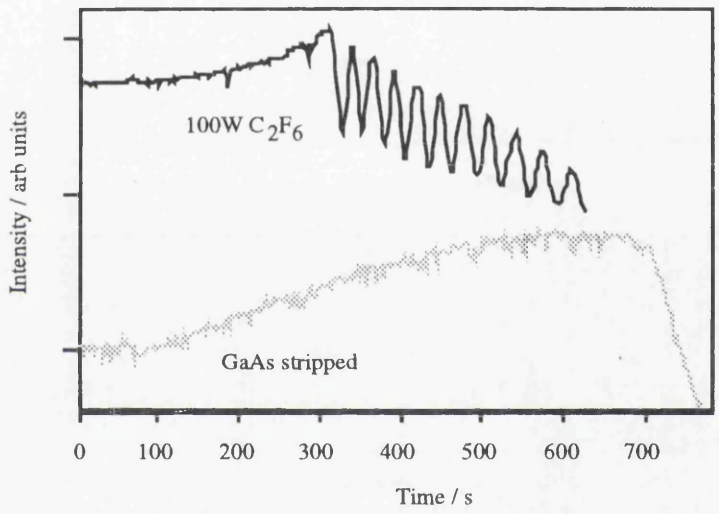

Figure 3.6: The reflectance signals obtained from the 100 W C_2F_6 treated and the GaAs stripped (using wet etching) samples.

For the 30 to 80 W C_2F_6 treated samples, the GaAs induction time is much less (2 to 10 s). The GaAs caps of these samples were etched by the C_2F_6 and therefore the oxide was removed. The induction times observed for these samples during the $SiCl_4$ etch may be caused by either a new oxide, since samples were exposed to the air for about 2 hours before subsequent etch, or the fluorocarbon[5] polymer which protected the surface from subsequent oxidation. The formation of both Ga_2O_3 and As_2O_3 on a GaAs surface is negligible for these time scales[4]. If fluorocarbon contamination is responsible, then the contamination on the GaAs is relatively volatile in $SiCl_4$ as it only takes a short time to be removed.

---

[4] W.F. Stickle and K.D. Bomben, Thin Solid Film **154**, 301 (1987).

[5] S.J. Pearton, U.K. Chakrebarti, W.S. Hobson, and A.P. Kinsella, 'Reactive ion etching of GaAs, AlGaAs, and GaSb in Cl_2 and $SiCl_4$', J. Vac. Sci. Technol. B **8**, 607 (1990).

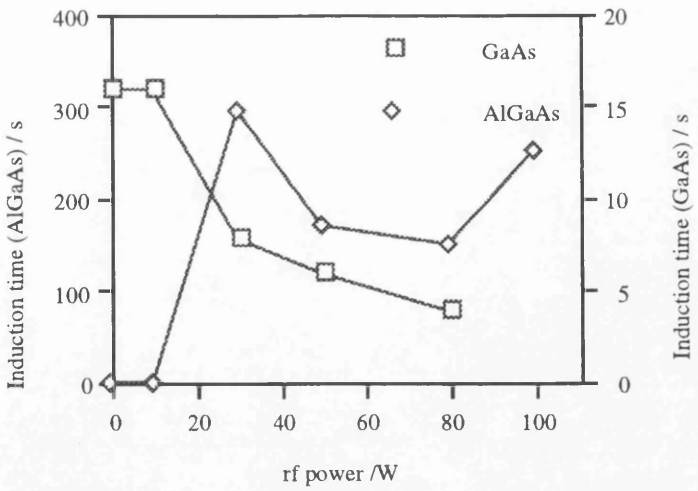

Figure 3.7: The induction times of GaAs and AlGaAs measured during the $SiCl_4$ RIE after the samples being exposed to C_2F_6 at different powers for 5 min.

The formation of the fluorocarbon deposits arises from the dissociative chemisorption of radicals such as CF_3 on the surface of the semiconductors [6]. The degree of contamination is expected to increase with decreasing C_2F_6 etch power due to the combined effects of a lower contamination sputter rate and lower GaAs etch rate. Energetic ions may deposit fluorine deep into the structure when etching using a high bias[3]. The mechanism by which this happens is the same principle as ion-implantation and, therefore, the penetration depth is expected to be directly proportional to ion energy and indirectly proportional to the mass of ions. However, the energy induced by the C_2F_6 RIE in this study is relatively low (< 500 eV), and therefore it is believed that the major contamination after C_2F_6 RIE was the formation of a fluorocarbon contamination layer rather than fluorine ions being implanted to a significant depth. The induction times for GaAs layers were found to be longer during the $SiCl_4$ subsequent etch for samples previously treated at low power (Fig.3.7). This observation is consistent with the above suggestion, i.e. a thicker contamination layer would be formed on samples exposed to the low power plasma.

The 100 W C_2F_6 plasma completely removed the GaAs cap. The AlGaAs surface was therefore either exposed to the air and therefore heavily oxidised, or it was protected by C-F deposits. The induction time was relatively long (≈ 250 s) (Figure 3.6). The wet etched (GaAs stripped) sample was exposed to the air for about 20 min, so no contamination other than the formation of oxide (mainly aluminium oxide) was expected. The induction time for this sample was far longer (600 to 1000 s), the sample was extremely rough, and the reflectance measurements indicated no etching was taking place. These results suggest that the 100 W sample was protected from oxidation by C-F contamination. The induction time of 250 s suggests that this polymer is much more involatile on the AlGaAs than on GaAs. The formation of involatile AlF_3 and AlF is expected on the surface of

[6] J.W. Coburn and H.F. Winters, 'Plasma etching — A discussion of mechanisms', J. Vac. Sci. Technol. **16**, 391 (1979).

AlGaAs in the case of the 100 W treated sample, whilst only C–F polymer layer will be formed on the GaAs layer for other cases.

As the rf power was decreased, an increase in induction time (from 150 s to 300 s) for etching the AlGaAs layer was observed for samples treated with 30 W to 80 W C_2F_6 plasmas (Figure 3.7). The precise mechanisms responsible for these induction times are not known. However, possible explanations are (i) an implantation effect building up fluorine at the AlGaAs surface inhibiting the etch of the AlGaAs for a while or (ii) redeposition of the surface contaminants onto the AlGaAs surface. The first suggestion is unlikely, as the longest AlGaAs induction time corresponds to the sample with greater than 40 nm of GaAs cap remaining. In addition, the damage depth found under these etching conditions (documented in Chapter 4) and from TRIM simulations suggests the impossibility of fluorine reaching such a depth. Moreover the induction time decreases with increasing bias; if it were due to fluorine implantation then it would be expected to increase with increasing F contamination, that is with increasing bias.

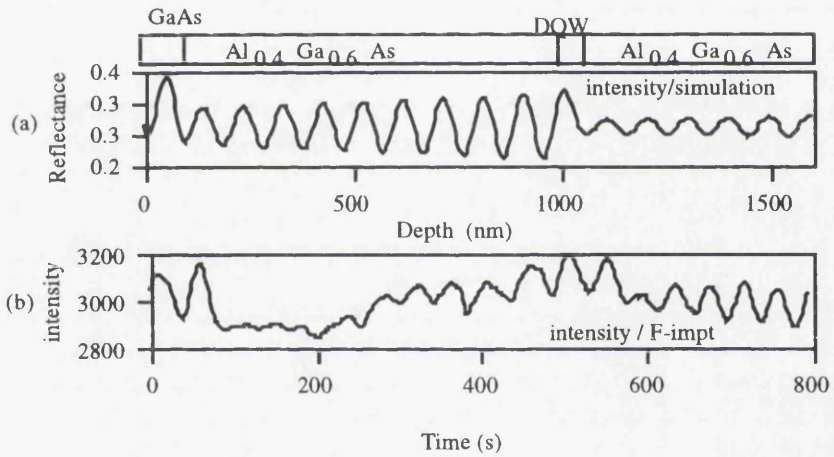

Figure 3.8: The derivative of the reflectance signals from (a) theoretical simulation and (b) from fluorine implanted sample.

A fluorine implanted sample was used to investigate the effect of fluorine in the AlGaAs layer on the etching of that layer, as it is possible that the presence of fluorine could result in these long AlGaAs induction times. The reflectance signal from this sample was initially weak and noisy (Figure 3.8b). This is due to the large degree of damage induced by the implantation process resulting in an increased absorption coefficient at the laser wavelength of 679 nm. A total of 10 oscillation peaks are expected during the etching of 0.9 μm of AlGaAs before reaching the DQW region. The transition from the etch of AlGaAs to the DQW can be clearly seen from the reflectance signal. Comparing the observed reflectance signal with the simulation result (Figure 3.8a) we conclude that the implantation of fluorine resulted in a negligible change in induction time on the AlGaAs layer. The plot of etch rate versus etching time (Figure 3.9) was also found to be about the same as for the as-grown material, which indicates the existence of fluorine in the lattice, at a concentration of 5×10^{17} cm^{-3}, and the large amount of damage in this sample, did not effect the $SiCl_4$ etch.

These results lead us to the conclusion that redeposition of the surface contaminants does occur. As the C_2F_6 power (and hence bias) is increased, the degree of surface contamination decreases due to an increased GaAs etch rate combined with an increased contamination sputter rate. Hence increasing the C_2F_6 power leads to less surface contamination and smaller AlGaAs induction times. To confirm the presence of C–F deposits on the GaAs surface, which result in a long induction time on AlGaAs layer, samples treated with 30 W C_2F_6 were Ar-cleaned before the subsequent etch in $SiCl_4$. The Ar cleaning was performed in an RIE chamber with the conditions of 100 sccm, 100 mTorr, 100 W, –230 V for 3 min. Any surface contamination due to C_2F_6 overetch is expected to be sputtered away under these conditions. A sample which had not been cleaned using the Ar plasma, but had been treated with the same C_2F_6 conditions, was again observed to have a significant induction time on the AlGaAs, which is consistent with the previous observations. However, the AlGaAs induction time was negligibly short for the Ar-cleaned samples. The etch rate of the Ar-cleaned samples was significantly reduced compared to the samples which had not been Ar-cleaned, a possible mechanism for this is discussed below.

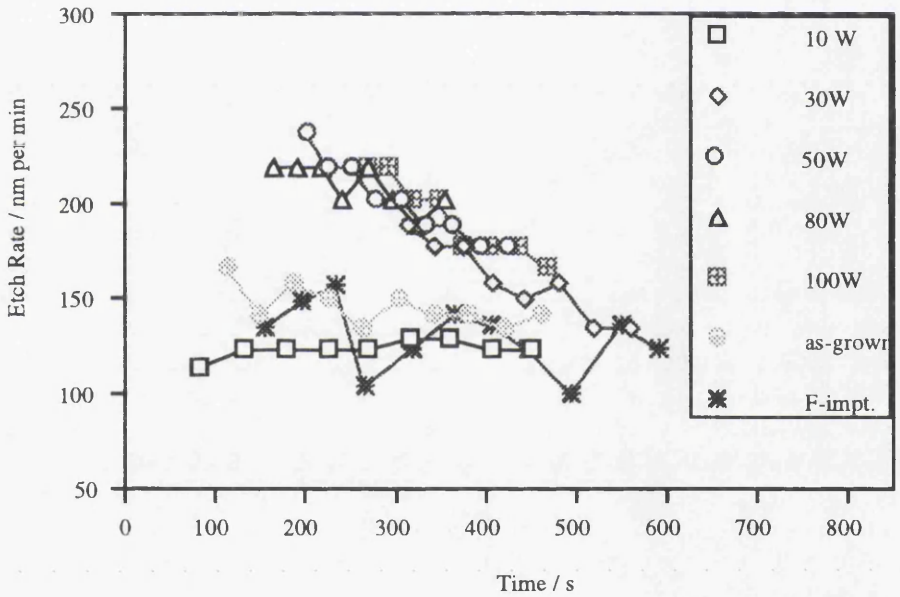

Figure 3.9: The variation of etch rates under a period of etching time. These etch rates were deducted from the reflectance signals.

Figure 3.9 shows that the time dependence of the etch rates falls into two categories. The as-grown, F^+ implanted and the 10 W C_2F_6 samples have an almost constant etch rate of $\approx$ 130 nm min^{-1}. In contrast, the 30 – 100 W C_2F_6 samples start with far higher etch rates ($\approx$ 230 nm min^{-1}) which fall steadily as the etch proceeds. These effects are interpreted in terms of the interaction between the residual O_2 in the chamber with the fluorocarbon contaminants and the AlGaAs surface. For any vacuum system, there exists an inevitable small leak from the surrounding atmosphere. We have measured this leak rate to be equivalent to a pressure rise of $\approx$ 0.5 mtorr min^{-1}. This indicates that, during the $SiCl_4$ etch, there exists a constant supply of background O_2 which is known to reduce the etch rate of AlGaAs. We propose that the C–F surface contaminants on the 30 -

100 W samples interact with the O_2 in the chamber resulting in a lower partial pressure of O_2 and, hence, the elevated AlGaAs etch rate. As the contaminants are gradually removed from the chamber, the O_2 partial pressure increases leading to the observed fall in the AlGaAs etch rate. The as-grown, F^+ implanted and the 10 W samples have a low and constant etch rate as a consequence of the relatively high and constant O_2 background partial pressure.

3.4.3 Results from SEM observations

An SEM was used at this stage to study the etched surface of the sample both before and after being subjected to the $SiCl_4$ RIE. The samples with rectangular patterns studied here were etched using C_2F_6 under various rf powers for 15 min and subsequently etched using 30 W $SiCl_4$ RIE for 5 min.

A relatively smooth sputtered surface, but a rough and non-vertical side wall, were observed in the SEM after the sample was exposed to the 100 W C_2F_6 plasma for 15 min (Figure3.10). There were no visible indications of the surface contamination believed to be present. The surface contamination in this case was believed to be in the form of AlF_3 and AlF, only a few monolayers thick, and the observation of these layers using an SEM is impossible. However, the observation of side wall roughness implies that the etching mechanism of this process at 100 W is mainly sputtering.

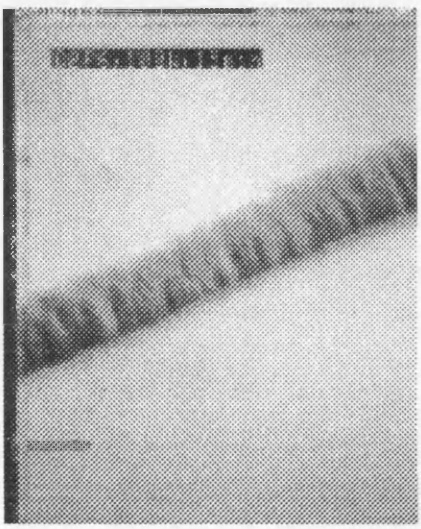

Figure 3.10: A relatively smooth etched surface but a rough and non-vertical side wall was observed from the sample etched using 100 W C_2F_6 RIE for 15 min.

Surface roughness was observed on the samples exposed to C_2F_6 at rf powers of 30 W or greater, followed by a subsequent etch using $SiCl_4$ (Figure 3.11a). Also, two distinct regions on the etched wall were observed: an upper region etched by C_2F_6 which was rough, and a lower region, etched by $SiCl_4$ which was smooth. The surface roughness was probably caused by micromasking due to contamination introduced by the C_2F_6 plasma. In contrast, reasonably clean and smooth $SiCl_4$ etched surfaces have been observed from samples exposed to 10 W C_2F_6 and 5 min overetch (Figure 3.11b). A relatively thick GaAs layer was still left on the surface during the $SiCl_4$ and therefore no

redeposition occurred on this sample. As a result, a smooth surface was obtained from sample treated by 10 W C_2F_6 .

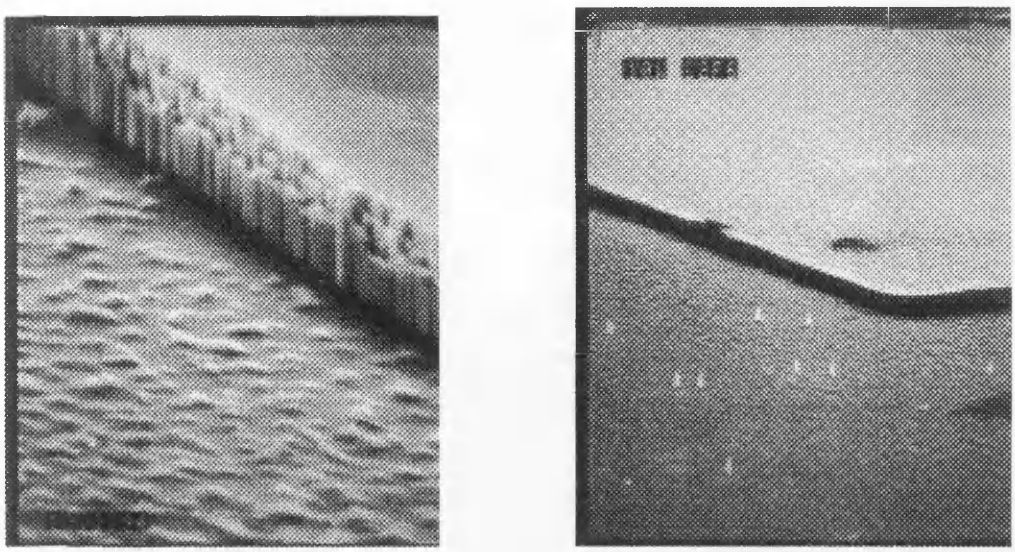

(a) (b)

Figure 3.11: SEM pictures: (a) A rough surface can be clearly observed from the C_2F_6 (100 W) contaminated samples after subsequent etching using $SiCl_4$, and (b) a reasonably clean surface has been obtained from the sample exposed to 10 W C_2F_6 followed by subsequent etching using $SiCl_4$.

3.5 Summary

Both etch rate and the verticality of the side wall reduce with the reducing of the etch power. A relatively vertical etched side wall of SiO_2 can only be obtained using a high power C_2F_6 RIE process. The maximum survival time for different types of masking materials have been investigated using 100 W C_2F_6 RIE.

The C_2F_6 plasma was found to etch both GaAs and AlGaAs at rf powers of 30 W and above. It is believed that the mechanism causing the etching of the AlGaAs is physical sputtering rather than RIE. Etching of the AlGaAs layer, however, did not occur at lower rf powers, which is believed to be due to the formation of involatile compounds such as AlF and AlF_3.

Results from laser reflectometry imply that, during a C_2F_6 etch, C–F contaminants are deposited on the GaAs surface to an extent which is dependant on the rf power used. These deposits protect the surface from subsequent oxidation and result in a reduction of the GaAs induction time during subsequent $SiCl_4$ etching. However, the presence of these deposits also results in a significant induction time for the underlying AlGaAs, a non-constant etch rate, and etched surface roughening during $SiCl_4$ etching.

Chapter 4 RIE damage and damage detection using a quantum well intermixing probe

4.1 Outline

In this Chapter the development of a quantum well intermixing (QWI) probe technique for RIE damage detection is documented. A short review of optical measurement techniques using a multiple quantum well as probe for RIE damage detection is given in the first Section of this Chapter. RIE processes, using C_2F_6 and $SiCl_4$ plasmas, and selective etch processes using $SiCl_4$ and $SiCl_4$:SiF_4 were studied using QWI probe technique and the experimental results are discussed here. A model of RIE damage was developed to explain behaviour of both high and low etch rates processes based on the results and the observations obtained.

4.2 Introduction

Most of the techniques used for semiconductor characterisation can also be applied to the study of RIE damage. Among these techniques, electrical and optical measurement techniques are the most commonly used. A short account of these measurement techniques is given in Chapter 2. In this Section, damage detection using luminescence techniques on GaAs/AlGaAs QW structures are introduced.

Luminescence techniques using photoluminescence (PL) and cathodoluminescence (CL) spectroscopy have been established for a long time for investigating both intrinsic electronic transitions, and electronic transitions at impurities and defects in a semiconductor. These techniques are simple, non-destructive, and measurements can be performed directly on samples. PL measurements performed on bulk material, however, cannot be used to determine the damage profile and depth induced by RIE. PL performed on processed material can only be compared qualitatively with the control material in the case of using a bulk semiconductor.

An RIE damage detection technique using multiple quantum wells as probes was first introduced by Wong *et al.*[1]. In this technique, QWs were placed at different depths as probes to study the effects of exposing the sample to plasma. The wafer structure consisted of three QWs placed within the top 1000 Å region to serve as probes to detect RIE induced damage. A well was placed at 4500 Å from the surface to act as reference. CL measurements were then performed on etched and protected areas of the sample and the luminescence signals were normalised to study the damage propagation depth induced by RIE. This technique is based on the phenomenon that luminescence from the unprocessed sample is dominated by radiative recombination whereas dry etching–induced damage in the QW layers will give rise to nonradiative recombination. Therefore, a decrease of

[1]H.F. Wong, D.L. Green, T.Y. Liu, D.G. Lishan, M. Bellis, E.L. Hu, P.M. Petroff, P.O. Holtz, and J.L. Merz, 'Investigation of reactive ion etching induced damage in GaAs–AlGaAs quantum well structures', J. Vac. Sci. Technol. B **6**, 1906 (1988).

luminescence intensity will be obtained from the plasma exposed region. By exposing selected regions of the material to the RIE, a depth profile of damage distribution can then be estimated by comparing the luminescence spectra from the exposed and protected areas.

Two assumptions have been made using this technique. First, the changes observed in the luminescence spectrum are only attributed to ion damage associated with the dry etching process and second, the damage profile measured is related only to the etch process parameters and not to the composition of the MQW itself. Degradation of the intensity and unexpected features in the PL spectrum have been observed for QWs placed less than 200 Å below the surface[2], a result conformed by Green *et al.*[3]. These workers postulated that the changes were a result of the interaction between quantum well states and surface states. Therefore, this technique can only be sensitive to a relatively high damage RIE process and the etch rate of the process has to be slow and well-controlled. In addition, the grown MQW structures have to be highly homogeneous in the QW thickness, as well as having no alloy composition fluctuation in the material. Following Wong *et al.*[1] this technique has been widely used either using PL or CL to study the damage depth induced by RIE[4,5,6] and ion beam etching[7] on a variety of material structures.

The multiple quantum well probe technique has been further modified in this study, by using the principle of point defect induced intermixing in the quantum wells. A similar MQW structure to that of Wong *et al*[1] has been used, but the sensitivity of the technique was proven to be increased by subsequently annealing the samples with an SrF_2/SiO_2 cap. Blue shifts in the PL from the QWs are induced by the diffusion of RIE point defects so providing a sensitive method of detecting the presence of RIE damage. The development of this technique is documented in this Chapter.

4.3 Experiment

4.3.1 Experiment design considerations

RIE damage primarily consists of point defects due to ion-bombardment[8]. An increase in the density of point defects in a sample will increase the density of non-radiative recombination centres

---

[2]J.M. Moison, K. Elcess, F. Houzay, J.Y. Marzin, J.M. Gerard, F. Bathe, and M. Bensoussan, 'Near-surface GaAs/$Ga_{0.7}Al_{0.3}As$ quantum wells: Interaction with the surface states', Phys. Rev. B **41**, 12945 (1990).

[3]D.L. Green, J.A. Skidmore, D.G. Lishan, E.L. Hu, and P.M. Petroff, 'Calibration of the multiple quantum well probe technique for dry-etching-induced damage analysis', Appl. Phys. Lett. **62**, 1253 (1993).

[4] R. Germann, A. Forchel, and M. Bresch, and H.P. Meier, 'Energy dependence and depth distribution of dry etching-induced damage in III-V semiconductor heterostructures', J. Vac. Sci. Technol. B **7**, 1475 (1989).

[5] M. Joseph, F.E.G. Guimaraes, J. Kraus, and F.J. Tegude, 'Characterisation of reactive ion etched AlGaAs/GaAs heterostructures by photoluminescence and low temperature Hall measurements', J. Vac. Sci. Technol. B **9**, 1456 (1991).

[6]E.M. Clausen,Jr., J.G. Craighead, J.P. Harbision, A.Scherer, L.M. Schiavone, B. Van der Gaag, and L.T. Florez, J. Vac. Sci. Technol. B **7**, 2011 (1989).

[7] Y. Idle, N. Takado, and K. Asakawa, 'Optical characterisation of reactive ion beam etching induced damage using GaAs/AlGaAs quantum well structures', Inst. Phys. Conf. Ser. No 106: Chapter 7, paper presented at Int. Symp. GaAs and Related Counpound, Japan, 495 (1989).

[8]D. Lootens, P. Van Daele, P. Demeester and P. Clauws, J. Appl. Phys. **70**, 221 (1991).

and therefore degrade and broaden the full wave at half maximum (FWHM) of the quantum well luminescence signal. The intermixing effect is widely accepted to be due to the diffusion of charged point defects[9]. Because most of the point defects introduced by ion-bombardment are charged, their equilibrium concentration is determined by temperature and by the position of the Fermi level. When the sample is subjected to a high temperature (usually in the range between 800 °C and 950 °C) anneal, the charged point defects diffuse and hence intermix the QW.

The development of this RIE damage detection technique is, therefore, based on the above two phenomena, i.e. (i) non-radiative recombination centres induced by RIE damage degrade the luminescence intensity of a QW, and (ii) the diffusion of charged point defects during the annealing stage intermixes the QW, i.e. changes the bandgap of the QW.

RIE damage always occurs deeper than predicted by the theoretical model of ion implantation[10]. Ion bombardment energies of a few hundred eV are usually used in RIE process and cause damage to a depth of about 3000 Å . In theory, the projected range of incoming ions is only a few atomic monolayers, at most, using an energy of a few hundred eV. This is generally insufficient to cause any obvious damage which can be detected either using electrical or optical techniques. Damage observed, however, is related to mechanisms such as channelling effects, vacancy migration, and enhanced diffusion of vacancies induced by ion bombardment[11].

The following layer structure, which contains a stack of QWs placed at different depths, was designed after considering the possible damage depth induced by RIE. QWs are placed within the top 3000 Å region to detect damage, and a QW is placed well below the damage depth to provide a reference signal. This structure was grown by metal organic vapour phase epitaxy (MOVPE) on a semi-insulating GaAs substrate. First a 0.2 μm GaAs buffer layer was grown, this was followed by 200 Å of $Al_{0.4}Ga_{0.6}As$, a 95 Å GaAs quantum well and then 0.3 μm of $Al_{0.4}Ga_{0.6}As$. On top of this were 5 quantum wells of widths 70 Å, 60 Å, 43 Å, 36 Å and 25 Å in that order, each of the wells being separated by 200 Å of $Al_{0.4}Ga_{0.6}As$. Above the top well 250 Å of $Al_{0.4}Ga_{0.6}S$ and a 50 Å GaAs cap were grown. The top five wells were placed close to the surface in order to determine the damage distribution range and magnitude after RIE. The 95 Å well was placed 0.43 μm below the surface to provide a reference signal, this depth is believed to be well below any damage induced by the dry-etching. The schematic diagram of the material structure is given in Figure 4.1 and a summary of this layer structure is also documented in Appendix A2.

---

[9]D.G.Deppe and N.Holonyak, Jr., 'Atom diffusion and impurity-induced layer disordering in quantum well III-V semiconductor heterostructures', J. Appl. Phys. **64**, R93 (1988).

[10]J. Chevallier, W.C. Dautremont-Smith, C.W. Tau, and S..J. Pearton, Appl. Phys. Lett. **47**, 108 (1985).

[11]M. Rahman, M.A. Foad, S. Hicks, M.C. Holland and C.D.W. Wilkinson, 'Defects penetration during the plasma etching of semiconductors', Mat. Res. Soc. Proc. **279**, 775 (1993) (and references within)

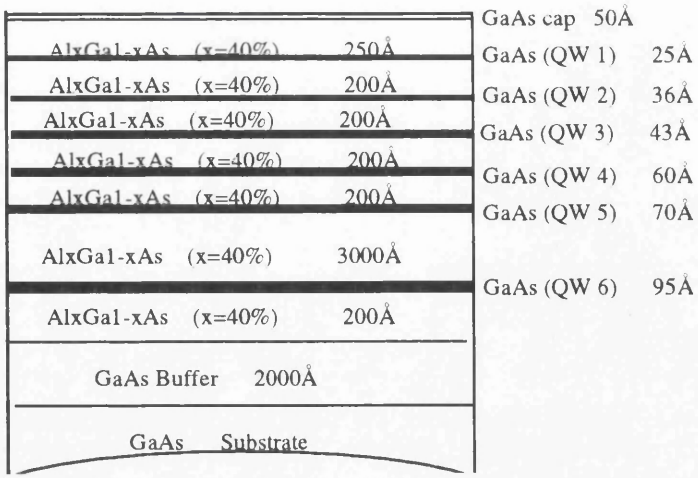

Figure 4.1 : The multiple QW probe structure used in RIE damage detection.

4.3.2 RIE conditions

Four different RIE processes were investigated using the quantum well intermixing damage detection technique, namely RIE using C_2F_6 and $SiCl_4$ processes, and two selective etch RIE processes using $SiCl_4$ and $SiCl_4/SiF_4$. These processes will be labelled as P1, P2, P3, and P4 respectively in the rest of this Chapter. As a damage free comparison, wet-etching using a H_2SO_4:H_2O_2:H_2O solution was also studied.

A Plasma Technology RIE80 system was used for the C_2F_6 RIE with the same etching conditions mentioned in Chapter 3 (Section 3.2.2).

Dry-etching using $SiCl_4$ was performed in a conventional 13.56 MHz parallel-plate RIE system (Plasma Technology RIE80). This etching was carried out at dc self bias of – 350 V with a $SiCl_4$ flow rate of 9 sccm and an rf power of 100 W. The etch pressure was maintained around 10.5 mTorr and the table temperature was fixed at 38 °C. From experience, it is known that GaAs and AlGaAs have similar etch rates (to within 5%), the average etch rate for the GaAs/AlGaAs sample was 1400 Å min^{-1} under the above conditions.

The GaAs/AlGaAs selective etch processes were carried out in an Oxford Plasma Technology RIE80. Process P3, using pure $SiCl_4$, was developed by Murad *et al*[12] and was reported to give a selectivity >10000:1 for etching GaAs/$Al_{0.3}Ga_{0.7}As$. An etch stop layer of about 4 monolayers thick (11 Å) was used and a highly anisotropic etch has been obtained. The etch stop was achieved by the formation of an involatile layer of Al_2O_3 or AlN from the residual oxygen, air or moisture in the

[12]S.K. Murad, C.D.W. Wilkinson and S.P. Beaumont, 'Selective and Nonselective RIE of GaAs and $Al_xGa_{1-x}As$ in $SiCl_4$ plasma', Microelectronic Eng. **23**, 357 (1994).

chamber. The rf power used in this process was around 10 W. A gas flow rate of 5 sccm, dc bias of around 50 V, and a pressure of around 9 mtorr were used.

Process P4, using $SiCl_4$:SiF_4, was also an selective RIE process. A mixture of $SiCl_4$ and SiF_4 gases were used and the etch stop was achieved by the formation of an involatile layer of AlF_3. This process was again performed in a low power environment. Powers of around 13 W were used with the dc bias as low as about 5 V. The flow rate of $SiCl_4$:SiF_4 was 2.5:9 sccm. The etch profile, etch rates, and selectivity obtained from P4 were about the same as process P3.

The conditions specified above were chosen as they are commonly used in the RIE processes in this Department. A summary of the etching conditions is tabulated in Table 4.1.

Process	Gas	Flow rate (sccm)	rf power (W)	dc bias (V)	Etch pressure (mTorr)
P1	C_2F_6	20	10-100	–450	15
P2	$SiCl_4$	9	100	–350	10.5
P3	$SiCl_4$	5	≈ 10	≈–50	9
P4	$SiCl_4$: SiF_4	2.5 : 9	≈ 10	≈ –5	9

Table 4.1 : The RIE conditions used in the damage study using the QWI probe technique.

4.3.3 Experiment

The wafer was cleaved into samples of area 3 x 6 mm^2. Half the area of each sample was covered with photoresist, type S1400–31, to serve as a control area and to provide an etch depth reference. A Talystep was used to determine the etch depth. In order to assess the relative number of point defects produced close to the sample surface by these dry-etches, QWI was used. After etching, the photoresist was removed, and layers of SrF_2 (2000 Å) followed by SiO_2 (2000 Å) were deposited on the samples. The SrF_2 layer deposition was performed using an evaporator and the SiO_2 was deposited using plasma enhanced chemical vapour deposition (PECVD) technique. The SrF_2 layer has the function of suppressing intermixing of the QWs[13] and the SiO_2 cap is to protect the SrF_2 when annealing.

The annealing process was performed by rapid thermal annealing (RTA) at 900 °C for 30 s, with a rise time of 15 s. During RTA, samples were placed face-down on a piece of GaAs and a second piece of GaAs was placed over the back of the sample to provide proximity capping to the sample and prevent the desorption of arsenic. During the RTA stage, QWI takes place as the point defects diffuse into the QWs and change the QW bandgap, this provides a sensitive technique for detecting the presence of point defects.

---

[13] J. Beauvais, J.H. Marsh, A.H. Kean, A.C. Bryce, and C. Button, 'Suppression of bandgap shifts in GaAs/AlGaAs quantum wells using strontium fluoride caps', Electron. Lett. **28**, 1670 (1992).

PL at 77 K was measured before and after annealing. The reference signal from well 6 was used to normalise the PL spectra in order to compare the intensities of the PL signal from the other five wells before and after processing the samples. This technique is simple since no complicated sample preparation process is involved. Besides allowing the damage depth to be determined, this technique also offers information about the point defect diffusion depth.

4.4 Results and discussion

4.4.1 100 W C_2F_6 RIE (Process P1)

Figure 4.2 shows, from top to bottom, the PL spectrum from as–grown material, the spectra from samples etched for 9 s, 18 s and 36 s using 100 W C_2F_6 RIE and a spectrum from a sample which has been etched for 36 s and annealed. It can be seen that the spectrum from the fourth well was not clearly resolved at 77 K. However, this does not affect the experiment since only the normalised PL signals from the first three wells (widths 25 Å, 36 Å, and 43 Å) were used. The wells which have been damaged by the RIE process exhibit reduced PL intensities. The signal from the first well (25 Å) after 18 s of exposure to the plasma is not discernible due to the non-radiative recombination resulting from the damage caused by the ion bombardment.

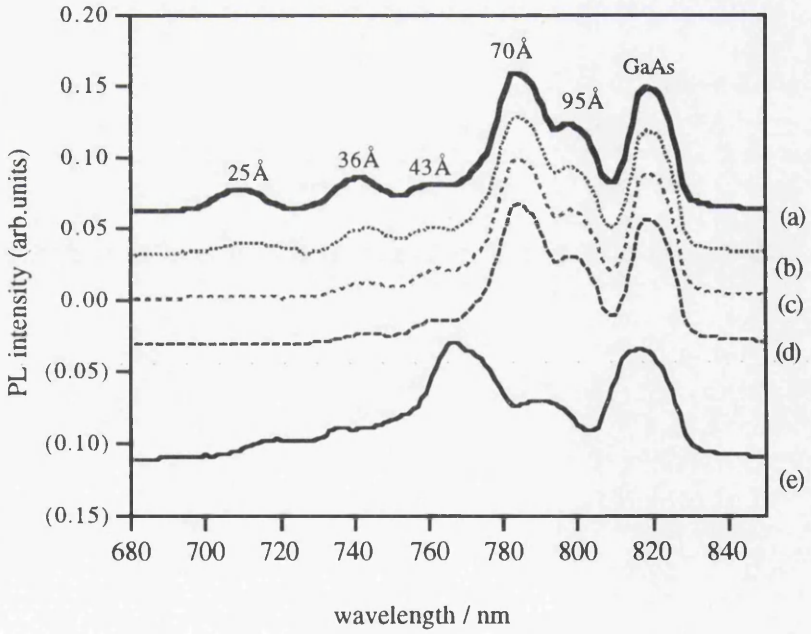

Figure 4.2: 77 K PL spectra from (a) protected region, samples etched for (b) 9 s (c) 18 s and (d) 36 s using 100 W C_2F_6 RIE , and (e) sample etched for 36 s after RTA at 900 °C for 30 s. Spectrum (e) is not normalised.

Figure 4.3 shows the normalised PL intensity against C_2F_6 etch time. Damage was observed for times as short as 9 s of etching, and it can be seen that the PL signals from well 1 and well 2 decreased significantly at this time. An increase in etch time from 9 to 12 s contributes to an increase in the amount of damage, a further drop in PL intensity from the top two wells being observed. The

intensity of the PL signal from well 3, however, was unaffected indicating that the depth of the damage had not increased. The normalised PL intensity of well 3 showed a decrease after 15 s of etching, this etch time also resulting in an etch depth of around 20 Å. The magnitude of the damage completely destroyed the optical quality of the first well after 25 s of etching. At etch times of less than 9 s, the depth of the damage was found to increase proportionally with the exposure time and become saturated after 9 s (not shown in Fig 4.3). It is concluded that the depth of the damage, caused by etching for 9 s or longer using C_2F_6 , is about 650 Å .

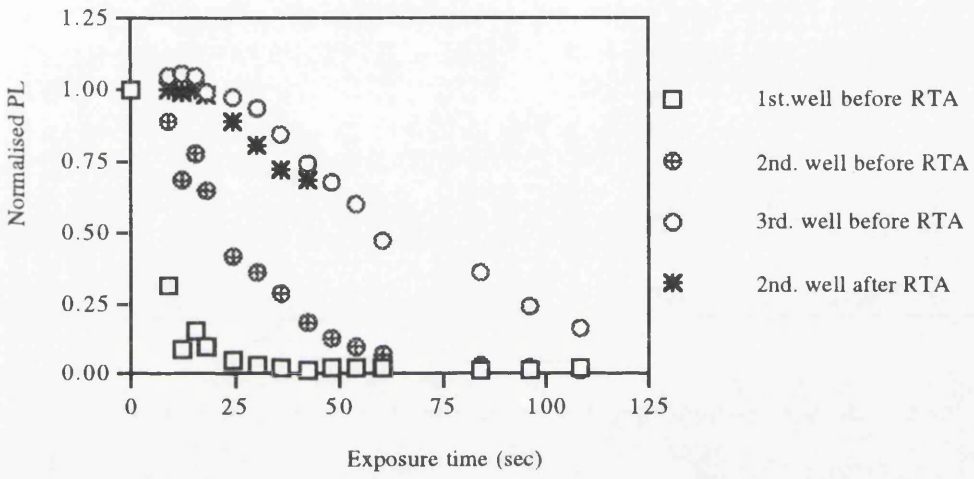

Figure 4.3: Variation of the normalised PL intensity as a function of exposure time to 100 W C_2F_6 plasma for the first three wells before RTA and 2nd well after RTA at 900 ^{O}C for 30 s.

After RTA at 900 °C for 30 s with SrF_2/SiO_2 caps, the PL signal from the first well vanished in all cases. This is likely to be due to the interaction of SrF_2 with the GaAs/AlGaAs layer during the RTA stage, and the interaction depth is estimated to be between 300 and 500 Å. The loss of the PL signal may be caused by non-radiative recombination in the well due to defects such as dislocations which could be formed during the annealing. Another possibility is that the well has totally intermixed with the AlGaAs and no longer exists.

Comparing the normalised PL intensities from the remaining wells before and after annealing (Figure 4.3), it can be seen that the annealing promoted partial or total recovery of the material quality, depending on the magnitude of the damage.

4.4.2 10—100 W C_2F_6 RIE

This experiment has been carried out using the same RIE conditions with various rf powers. The damage depths for powers in the range 10 – 100 W are summarised as in Table 4.2.

Etch power (W)	100	80	50	30	10
Damage depth (Å)	650	700	550	350	200

Table 4.2 : Damage distribution depth after exposed to different C_2F_6 etching power.

Blue shifts were observed from both the protected and etched areas after annealing. In the etched areas this shift was almost independent of the exposure time. Figure 4.4 shows the average energy shift from well 2, 3, 5 and 6 from both the etched and protected areas as a function of etching time. The larger shift in the etched areas can be explained by defect propagation during annealing which would induce intermixing in the QWs. The energy shifts in the protected areas are induced by the high temperature RTA and, although larger than expected for this annealing temperature with SrF_2 caps, are reproducible in the different samples studied from this wafer. The energy shift of the 6th well is almost identical for both regions, which indicates that the point defects induced by RIE do not diffuse any deeper than about 4000 Å at this annealing temperature. In addition, the energy shift of about 10 meV from the 6th well can be considered as relatively small, confirming that SrF_2 is a good candidate for suppressing intermixing in a deep well. A major drawback of SrF_2 is its interaction with the surface of the epitaxial layer where it creates damage which causes intermixing in wells close to the surface and makes it unsuitable for use with shallow QW devices such as quantum wire devices using the above RTA conditions.

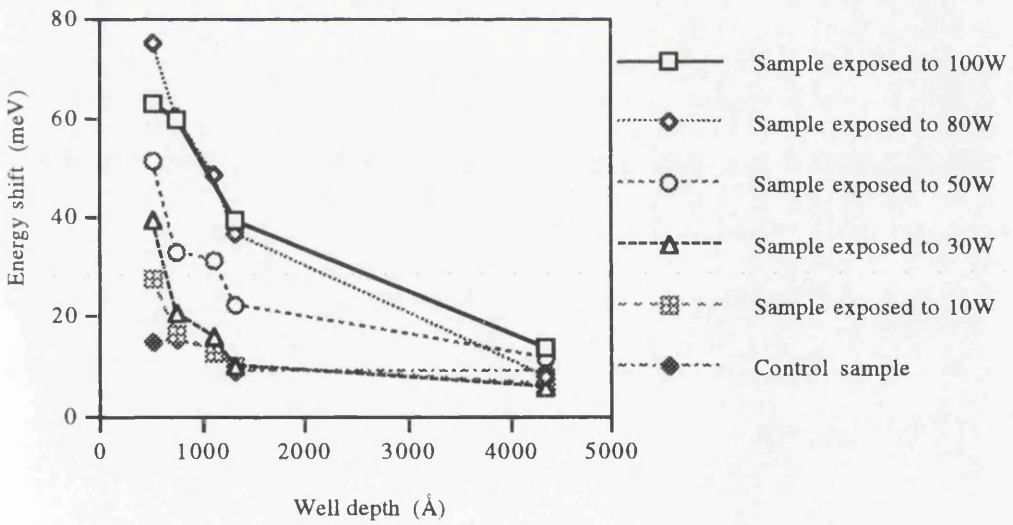

Figure 4.4: The dependence of energy shift with well depth after annealing for C_2F_6 samples exposed to different rf power after RTA.

In the case of different rf powers, the damage distribution depth increased with increasing power density up to about 80 W. For higher powers than this there appeared to be no further increase in damage depth. The damage depth measured for the rf power density of 10 W may be an overestimate of the damage induced by RIE, since a decrease in normalised PL intensity can also be

attributed to a shallow QWs placed around 200 Å below surface[2]. No red shift has been observed from samples etched to a depth for which the QW was less than 200 Å from the surface. This observation is in agreement with Green *et al*[3] but is in contrast to the results of Moison *et al*[2].

Compared to ion-implantation, these damage depths are far beyond the range predicted by TRIM[14]— a Monte Carlo simulation programme used to predict ion implantation depths. Using an implantation energy of 0.5 keV (corresponding to the bias of -500 V) the maximum vacancy depths generated by F^+ and C^+ in GaAs were found to be about 90 Å and 100 Å respectively. Channelling effects, vacancy migration, and enhanced diffusion induced by ion bombardment may be occurring during the RIE [15,16] resulting in a deeper damage depth.

The energy shifts of the PL from the quantum wells in samples which had been exposed to the C_2F_6 plasma for 30 s are shown in Figure 4.4. It can be seen that, as the rf power increased up to about 80 W, the degree of intermixing of the wells increased, indicating that the amount of damage to the material increased with increasing rf power. When the power was further increased, the blue shift saturated indicating that the number of point defects generated by the plasma saturated at an rf power of about 80 W, corresponding to the saturation of the damage depth. For the lowest rf powers, only the uppermost wells exhibited significant intermixing, implying that the amount of damage generated at these powers was very low. The blue shift in the deepest well showed little dependence on rf power indicating that the point defects generated by the plasma did not diffuse in significant densities to the depth of 4000 Å.

4.4.3 100 W $SiCl_4$ RIE (Process P2)

By using the same method of analysis as for C_2F_6, we estimated a damage distribution range of 100 Å for $SiCl_4$ (Figure 4.5). The first well is 300 Å below the surface and so the PL signal from this well disappears after removing 300 Å of material. The damage range is smaller than that for C_2F_6, which is partly due to the lower dc self bias and lower flow rate but, in addition, C_2F_6 has a lighter ion mass than $SiCl_4$ and it is known that a lighter ion will induce more damage than a heavier ion[17].

---

[14] J.F. Ziegler, J.P. Biersack, and U. Littmark, *The Stopping and Range of Ions in Solids,* (Pergamon, New York, 1985).

[15] S.W. Pang, G.A. Lincoln, R.W. McClelland, P.D. DeGraff, M.W. Geis, and W.J. Piacentini, 'Effects of dry etching on GaAs', J. Vac. .Sci. Technol. B **4**, 1334 (1983).

[16] M.E. Harper, J.J. Cuomo, and H.R. Kaufman, 'Technology and applications of broad-beam ion sources used in sputtering. Part II. Applications', J. Vac. Sci. Technol. **21**, 737 (1982).

[17] J.C. Bean, G.E. Becker, P.M. Petroff, and T.E. Seider, J. Appl. Phys. **48**, 907 (1977).

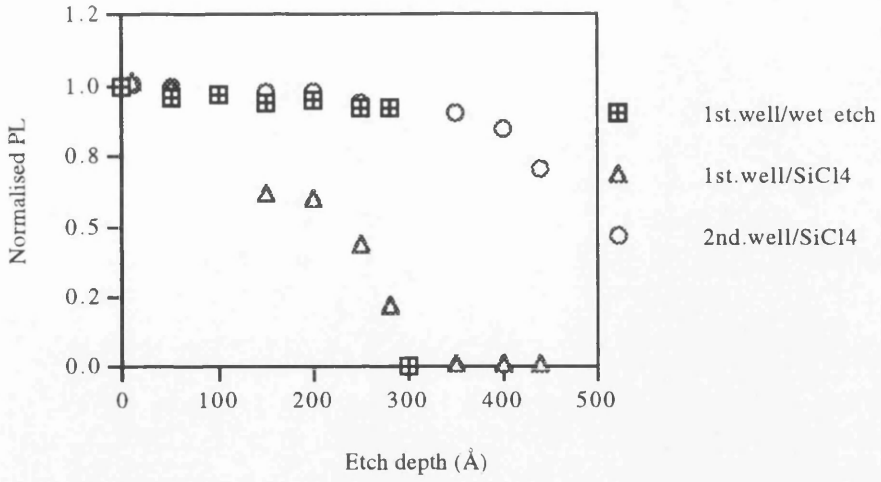

Figure 4.5: Variation of the normalised PL intensity for the first two wells as a function of $SiCl_4$ etch depth and for the first well using wet-etching.

The results after annealing show complete recovery of the PL intensity from the 2nd well. (PL was not observed from the first well as discussed above.) However the QWI results (Figure 4.6) do reveal that point defects were induced by the RIE process with average energy shifts of about 30 meV for the 2nd well of the etched region being observed. These shifts contrast with shifts of only 15 meV from the protected region. They are also substantially smaller than the shifts observed in the C_2F_6 samples indicating that $SiCl_4$ etching generates considerably fewer point defects. The energy shift from well 6 was similar to that in the samples etched using C_2F_6. Therefore, again, we conclude that energy shift in the damaged region is greater than in the protected area, indicating that $SiCl_4$ creates point defects close to the surface, and that QWI using SrF_2 caps is a sensitive method of revealing point defects arising from RIE.

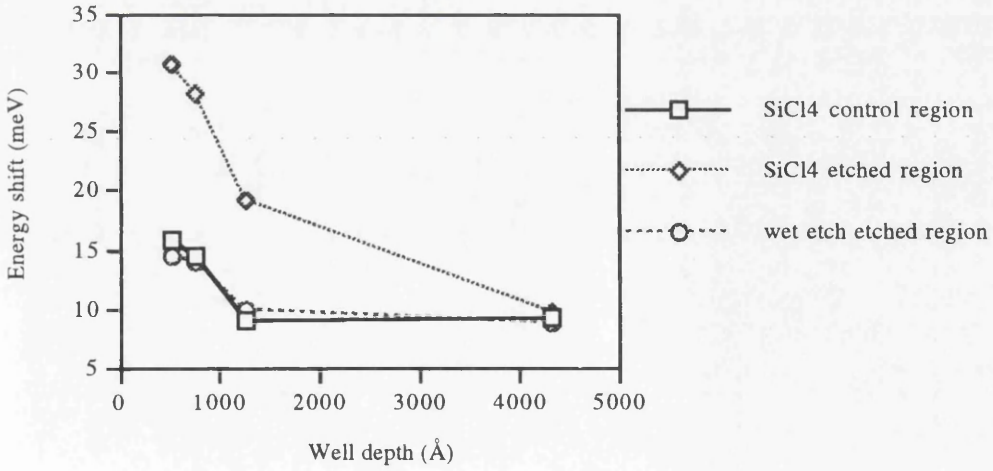

Figure 4.6: The dependence of energy shift with well depth after annealing fro $SiCl_4$ and wet-etched samples.

4.4.4 Selective etching using $SiCl_4$ and $SiCl_4$:SiF_4 (Processes P3 and P4)

In this study, the 50 Å GaAs cap layer was etched and the etching was stopped on the AlGaAs layer whilst ions continued to bombard the AlGaAs surface. The GaAs etch rates of process P3 (using pure $SiCl_4$) and P4 (using $SiCl_4$:SiF_4) were both about 50 nm min^{-1}, therefore the removal of a 50 Å GaAs layer only takes a few seconds.

The PL spectra obtained after 7 minutes of etching using both processes are shown in Figure 4.7. It is noticed that signals from all the wells are well resolved without significantly declining in magnitude or becoming noisy compared to the PL spectrum from the control region. These observations suggested a damage range of less than 250 Å. The small energy shifts (about 15 meV for the 2nd well and less than 10 meV from the 3rd and 4th wells) after RTA are not significant enough to conclude that a sufficiently high concentration of point defects is generated on the surface to intermix the wells during RTA. These small shifts may be attributed to the thermal effect or outdiffusion of As during RTA. Owing to the fact that it was not possible to resolve the PL signal from the first well, whether or not the first well was shifted to a higher energy is not known.

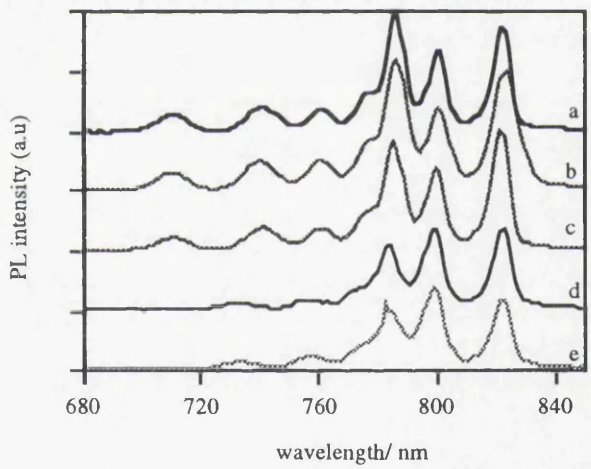

Figure 4.7: Spectrum (a) is taken from the protected region, (b) and (c) are the spectra taken after 7 minutes etch using pure $SiCl_4$ and $SiCl_4$+SiF_4 plasmas respectively, and (d) and (e) are the spectra taken after 7 min etch followed by RTA using dielectric caps for RIE using pure $SiCl_4$ and $SiCl_4$+SiF_4 plasmas respectively.

The density of point defects generated by these processes may be too low to activate the energy shift during RTA. Compared to RIE using $SiCl_4$ at rf power of 100 W (Section 4.3.2), it can be deduced that these two processes produce a very much lower density of point defects and a damage depth of less than 100 Å.

In short, no obvious damage effects can be seen in the normalised PL from the MQW system used in this study. This may be because the damage propagation depth is too shallow to be detected by this experiment. The densities of point defects generated by these processes, if any, are not high enough to activate the well intermixing during the annealing step. From the negligible degree of

energy shift after RTA, these RIE processes are concluded to be of very low damage and the damage depths must be «100 Å. No distinction can be made between these two processes since very similar results were obtained.

4.4.5 Wet etching

Wet-etching using H_2SO_4:H_2O_2:H_2O (1:8:600) is expected to be a damage-free process. Our results confirm this as the normalised PL intensities from all the wells are unaffected by wet-etching (Figure 4.5). Only a slight decline in the PL signal has been observed even when the first QW was less than 200 Å below the surface, which is in contradiction to the observation made by Moison *et al* [2]. It is possible that our observation may due to an inaccurate estimation of etch depth, since the etch depths were estimated by assuming that the etch rate was constant. In addition the etched surface may not be even. As a result, not all of the etched surface would then have same amount of the material removed, therefore the PL signal would not degraded much as the PL would be dominated by the regions where the QW was deeper.

Wet-etching gives rather poor uniformity and undercutting for a shallow etch using the above composition of wet etching solution. Good wet-etching can be obtained using a more concentrated solution, for instance 1:8:40. However, this solution results in an extremely fast and uncontrollable etch rate, and is only useful for etch depths of about a few microns. Although wet-etching is one of the techniques capable of removing the damaged layer after dry-etching[18], it is not, in general, practical for small QW devices because of its non-controllable etch rate.

After RTA, the energy shift profile of the wet-etched region was almost the identical to that of the protected region (Figure 4.5 and Figure 4.6), this result confirming that wet-etching does not form point defects on the sample surface.

4.5 RIE damage model

The qualitative damage model proposed here is based on the experimental results obtained above, which can be summarised as follows. (i) The magnitude of the damage increases with the etch time but the damage depth remains constant. (ii) The magnitude of the damage is higher in the low etch rate process than in higher etch rate process. (iii) The amount of damage is expected to saturate after a long time of exposure to the plasma. Assuming that a single type of material (GaAs or AlGaAs) is used, the induced ion damage per unit time is constant for a fixed ion energy and, with a constant etch rate throughout the layer, the damage is of the shape profile illustrated as Figure 4.8.

The triangle in Figure 4.8 represents the damage profile induced by a unit time of etching. As the etching proceeds, a certain amount of the material is removed thereby removing the damaged layer

[18] A.C. Papadopoulo, C. Dubon-Chevallier, J.F. Bresse, A.M. Duchenois, and F. Heliot, 'Etching procedures of GaAs: Cathodoluminescence study of the induced damages and of the recovering techniques', J. Vac. Sci. Technol. B8, 407 (1990).

near the surface. At the same time, new damage is introduced at a constant rate, and is accumulated in the material. The accumulated damage is represented by this triangle-like polygon. It is noted that in both cases of illustration, the damage depth is constant but the total damage increases with time. This simple model also predicts that the magnitude of damage is higher for the low etch rate process. The model also indicates that damage induced by a fast etch rate process will reach saturation point faster than the low etch rate process, which corresponds closely to the experiment results obtained.

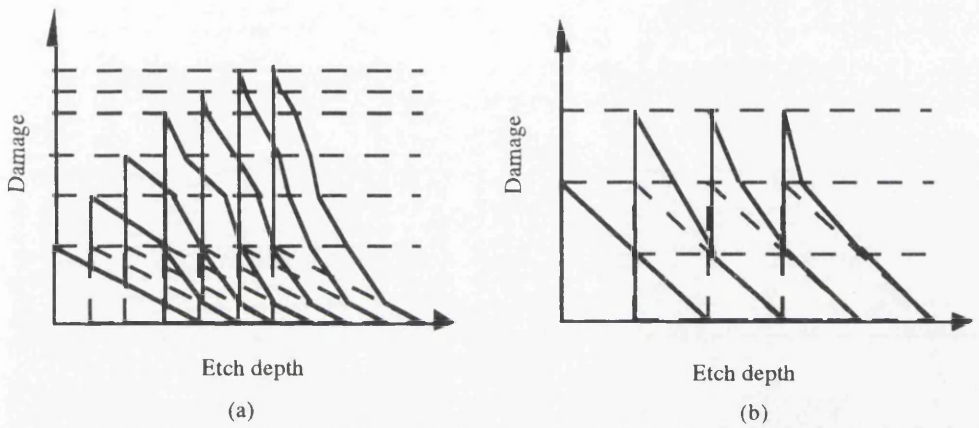

Figure 4.8: Schematic diagram illustrating the damage profile from (a): a low etch rate and (b): a high etch rate. The x axis represents the concentration of damage–induced defects and the y axis represents the depth from the surface.

4.6 Conclusion

Using a GaAs/AlGaAs QW probing system we have demonstrated that C_2F_6 RIE has an induced damage distribution range of 650 Å . The magnitude of the damage increases with etch time, for a time of 9 s or longer, but the depth remains constant. Propagation of damage induced by RIE after annealing has been observed and blue-shifts as large as 64 meV have been measured. $SiCl_4$ RIE shows similar damage characteristics, but with a much smaller damage range estimated to be 100 Å. The material quality recovers for both RIE techniques after RTA at 900 °C for 30 s. From measurements of the bandgap change arising from QWI, it was found that the RIE induced damage propagated to a depth of about 4000 Å during the annealing process. SrF_2 was confirmed to be a good candidate for suppressing QWI in deep wells, however, a damage distribution range of about 300 Å has been found after annealing and this may limit the application of SrF_2 in processing shallow QW devices. No significant damage can be detected using the selective etch processes. These processes were proven to induce a relatively low amount of damage and a low density of point defects. Based on the results obtained, a qualitative RIE damage model was developed to explain the results of etching at both low and high etch rates.

Chapter 5 The development and the fabrication of photonic devices using plasma damage induced layer intermixing

5.1 Introduction

Chapter 4 identified the observation of bandgap shift from samples subjected to RIE damage and annealed. In this Chapter the possible use of this intermixing technique in the fabrication of integrated photonic devices is studied. A high damage RIE process, using H_2 plasma, has been investigated. Significant bandgap shifts have been observed from a DQW material after 5 to 6 cycles of plasma exposure followed by annealing. Oxide stripe bandgap shifted lasers have been fabricated and the results have shown that the material is still high in quality after intermixing. To demonstrate the use of this intermixing technique in a photonic integrated circuit application, oxide stripe extended cavity lasers, which contain an integrated passive optical waveguide, have been fabricated and studied. Losses as low as 18.1 dB cm^{-1} were measured in the passive waveguide section of this device.

5.2 H_2 plasma damage induced layer intermixing

5.2.1 Introduction

RIE damage primarily comprises point defects[1] which can, in turn, induce QW intermixing when the sample subject to annealing. Damage induced by C_2F_6 RIE was found to induce QW intermixing (Chapter 4). It was also learned from the same study that the point defect diffusion depth was not larger than 400 nm for that particular process. C_2F_6 etches GaAs/AlGaAs at a relatively high etch rate when a high power. is used. Further more, the choice of the masking material to define a selective area might be difficult since this plasma etches both SiO_2 and Si_3N_4. In order to obtain good optical confinement and to avoid radiation leakage of light in the GaAs cap region, the upper cladding layer of a QW lasers structure is usually in the range of 1 μm thick. The active region is therefore considerably deeper than the point defects induced by C_2F_6 can reach. Therefore, C_2F_6 plasma is not a suitable candidate for use as a one-step intermixing process in the fabrication of photonic devices.

Two important requirements have to be fulfilled before a particular RIE damage induced intermixing process can be applied in photonic device fabrication. The process has to (i) induce relatively high damage, and (ii) have a low GaAs/AlGaAs etch rate. H_2 plasma was considered to be suitable since the H^+ ion has the lowest atomic mass and a high concentration of point defects is expected using a high power process. Serious damage has been observed from RIE process using H_2 plasma, which has been attributed to the damage effect of light H^+ ions in the discharge[2,3]. A low

---

[1] D. Lootens, P. Van Daele, P. Demeester and P. Clauws, 'Study of electrical damage in GaAs induced by $SiCl_4$ reactive ion etching', J. Appl. Phys. **70**, 221 (1991).

[2] S.J. Pearton, U.K. Chakrabarti, and W.S. Hobson, 'Reactive ion etching induced damage in GaAs and AlGaAs using $C_2H_6/H_2/Ar$ or CCl_2F/O_2 gas mixtures', J. Appl. Phys. **66**, 2061 (1989).

[3] S.W. Pang, 'Surface damage induced on GaAs by reactive ion etching and sputter etching', J. Electrochem. Soc. **133**, 784 (1986).

GaAs/AlGaAs etch rate can be obtained by proper control of the gas flow rate and other parameters such as pressure and dc bias.

Mixtures of H_2 and methane (CH_4) have been reported to etch GaAs[4] and In-based compounds[5]. Besides being used to clean the RIE chamber from residual gases, H_2 plasma at low pressure has also been used to clean the surface of GaAs from residual As and As_2O_3 [6] with the probable reactions of $As + 3H \rightarrow (AsH_3)_{gas}$ and $As_2O_3 + 12H \rightarrow (3H_2O)_{gas} + (2AsH_3)_{gas}$. H_2 plasma was reported to etch the native oxides of GaAs with about 30 nm min^{-1} at 100 W[7]. Although H_2 plasma results in high damage when a high power process is used, it is however never found to induce damage deeper than the range of more than a few hundreds of nanometer. To diffuse this damage towards the QW, the possible use of a method called "drive–in diffusion" was developed here. This method is to carry out repeated cycles of plasma exposure, to create point defects in the material, followed by annealing to drive–in diffuse the point defects to the QW.

5.2.2 Process development and optimisation

The RIE machine used in this study was an Electrotech SRS Plasmafab 340 RIE machine (ET340), and the hydrogen used was 99.999% hydrogen from Air Products. This machine was chosen for the advantages of being able to supply a high energy (maximum bias of around 2 kV) to ions and because it could be operated at relatively low pressure (<5 mTorr). The process was carried out at rf power of 150 W with dc bias about –1 kV, gas flow rate of 5 sccm, table temperature of about 30 °C, and at a pressure of 5 mTorr. The ion energy was set to around 1 keV, but not any higher to avoid the formation of an amorphous layer on the surface of the semiconductor, which would require a higher annealing temperature to recrystalise the material.

A low pressure and a low H_2 flow rate were used in order to obtain a high ion acceleration energy combined with a low GaAs/AlGaAs etch rate. The GaAs/AlGaAs etch rate under the above process conditions was influenced by the condition of the chamber. It was found to vary from 50 Å min^{-1}, in a precleaned chamber, to more than 200 Å min^{-1} in a chamber without precleaning. This machine is frequently used for the etching of InP and its related compounds using a mixture of CH_4:H_2 gases. Therefore, residual CH_4 may result in the high etch rate of GaAs/AlGaAs. In this RIE system, H_2 plasma will not strike by itself but is helped to strike by gases such as O_2 or CH_4. The GaAs/AlGaAs etch rate was, therefore, also influenced by the gases used to strike the H_2 plasma. In order to obtain a minimum etch rate of GaAs, the RIE chamber was cleaned using O_2 (100 W, 10 sccm,

---

[4]see for example, R. Cheung, S. Thoms, S.P. Beaumont, G. Doughty, V. Law, C.D.W. Wilkinson, 'Reactive ion etching of GaAs using a mixture of methane and hydrogen', Electron. Lett. **23**, 857 (1987).

[5]see for example, J. Werking, J. Schramm, C. Nguyen, E.L. Hu, and H. Kroemer, 'Methane/hydrogen-based reactive ion etching of InAs, InP, GaAs, and GaSb', Appl. Phys. Lett. **58**, 2003 (1991).

[6]R.A. Gottscho, B.L. Preppernau, S.J. Pearton, A.B. Emerson, and K.P. Giapis, 'Real-time monitoring of low-temperature hydrogen plasma passivation of GaAs', J. Appl. Phys. **68**, 440 (1990) and references within.

[7]R.P.H. Chang, C.C. Chang, and S. Darack, 'Hydrogen plasma etching of semiconductors and their oxides', J. Vac. Sci. Technol.. **20**, 45 (1982).

≈ –500 V, 50 mTorr), followed by H_2 (under the same conditions specified above) for 30 min each before carrying out the plasma exposure process. O_2 was chosen to strike the H_2 plasma to avoid residual CH_4 gas which would result in a high etch rate of GaAs/AlGaAs.

Not all of the gas molecules is disassociated and ionised in the RIE chamber. In a usual case, only about 10% of the gas is ionised but the rest remains neutral. The ionised percentage of H_2 is, however, about 60% in an RIE system, which is considerably higher compared to other gases. H_2 plasma etches SiO_2 at a relatively fast etch rate, forming the etch products SiH_4, H_2O (gas) and other hydride compounds which are very volatile[6]. It was found to sputter off the 200 nm of SiO_2 layer in less than 1 min under the above process conditions. Therefore SiO_2 is not a suitable masking material for this process. However, it is fortunate that H_2 etched SrF_2 at only about 5 nm min^{-1}. Therefore a thick layer of SrF_2 can be used as both the exposure mask and the annealing mask to define a selected protected region in this process.

The maximum vacancy depth generated by H^+ in SrF_2 was calculated using 'TRIM' to be about 25 nm under an implantation energy of 1 keV (corresponding to about – kV dc bias)[8]. A 500 nm thick SrF_2 layer was chosen in this case to prevent the penetration of both H_2 ions and point defects generated in the semiconductor. H^+ ions and point defects diffusing inwards will be trapped at the non-lattice matched interface between the dielectric and the semiconductor and, therefore, only a very small amount of damage or ions is expected to penetrate and reach the material.

MQW probe samples, with the layer structure documented in Chapter 4 Section 4.3.1, have been used to study the damage distribution under the above RIE conditions. After exposure, the PL signals from the first three wells were not resolved and the 4th and 5th wells were degraded (Figure 5.1(a)). The PL signal from the 5th well has been broadened after the plasma exposure which may be due to interface roughness between the barrier and the well. From the normalised PL signal, it is predicted that a damage depth of more than 100 nm can be obtained using this process. Due to the heavy damage, only partial recovery of the PL signal was obtained after an annealing step of 500 °C for 60 s (Figure 5.1(b)). This annealing step was performed using RTA without any annealing cap since As out diffusion is not expected at this low temperature. No bandgap shift was observed after this annealing step since 500 °C is too low to activate intermixing. Although this annealing temperature is not high enough to recover the PL signal to 100%, signals from all the wells can be clearly identified. These results indicated that the first 3 wells of the as-exposed samples were not etched by the H_2 plasma.

---

[8] J.F. Ziegler, J.P. Biersack, and U. Littmark, *The stopping and Range of Ions in Solids*, (Pergamon, New York, 1985).

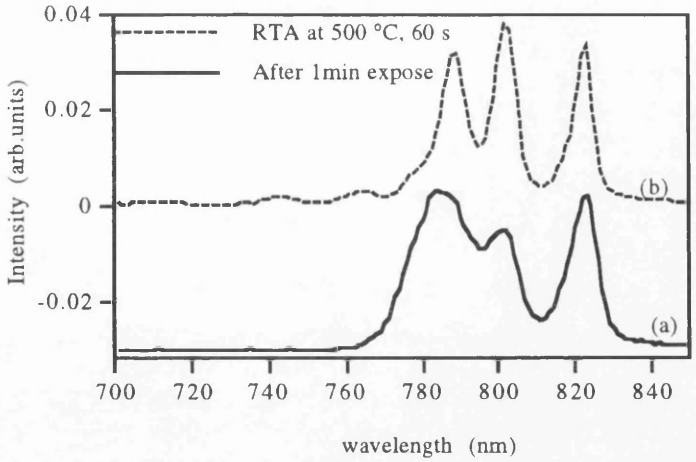

Figure 5.1: 77 K PL from (a) sample after exposed to the H_2 plasma for 1 min, and (b) PL signals after the sample was annealed using RTA at 500 °C for 60 s.

The PL signals from the second well down were observed after the sample was annealed using SrF_2/SiO_2 dielectric caps at 900 °C for 60 s. The first well may have been totally intermixed or damaged by the dielectric cap during annealing. Results from Figure 5.2 indicate that the damage to the material after exposure to H_2 plasma can be removed so that the PL intensity recovers to more than 80% for most of the wells after annealing at high temperature and, therefore, residual damage should not be a problem in this process. Bandgap shifts were observed from the first five wells after the annealing step, but no energy shift have been obtained from the last well indicating the point defect density is not high enough to induce a bandgap shift in this well.

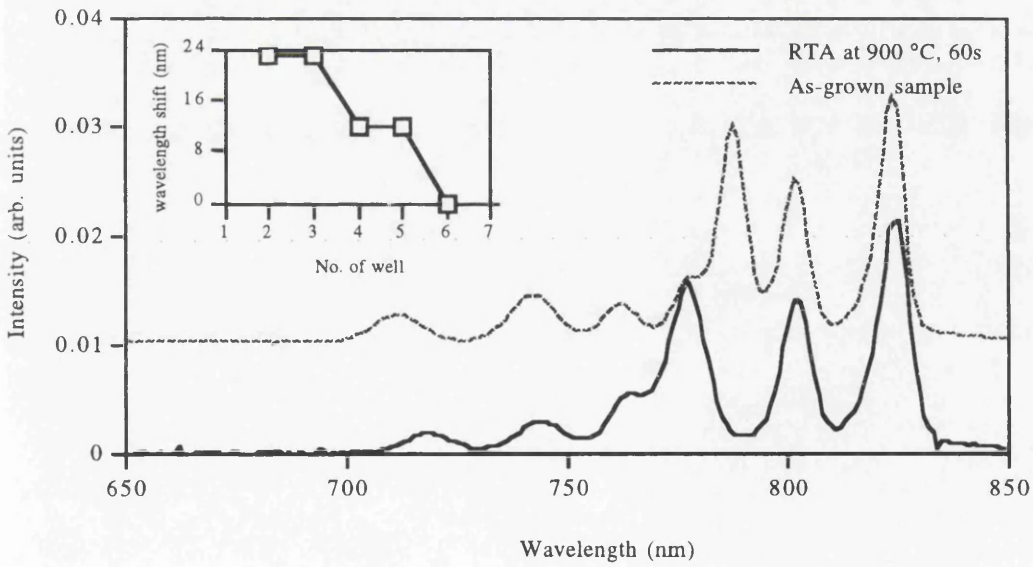

Figure 5.2: Blue shift have been observed from well 2 to 5 after RTA at 900 °C for 60 s with SrF_2 and SiO_2 dielectric caps. The plot of wavelength shift as a function of the number of well is given in the inset.

The number of point defects induced by RIE is expected to saturate after a period of exposure time according to the RIE damage model documented in Chapter 4. The MQW probe samples were again used in studying the saturation time and the saturation time was found to be less than 30 s.

Therefore the process time was set to 1.5 min to allow some time to initiate the growth of the plasma and to ensure complete saturation was achieved.

5.2.3 Drive–in diffusion intermixing process

As mentioned, the drive–in diffusion process used here consists of cycles of a plasma exposure step and an annealing step. First, a high point defect concentration is created, using H^+ bombardment, on the surface of semiconductor. We can consider the profile of the point defect concentration profile as a step-like function after this stage. During RTA, the point defects diffuse in random directions in the material. Defects which diffuse towards the topmost layer will relax and disappear at the surface but defects which diffuse inwards will cause group III interdiffusion. Therefore, the point defect concentration profile is expected to become an erfc function after RTA. The material is then exposed to the plasma again, to form another high concentration of point defects at the surface. Therefore, a quasi-constant surface–concentration condition is maintained during the annealing steps so driving the point defects deep into the material. This process is illustrated schematically in Figure 5.3.

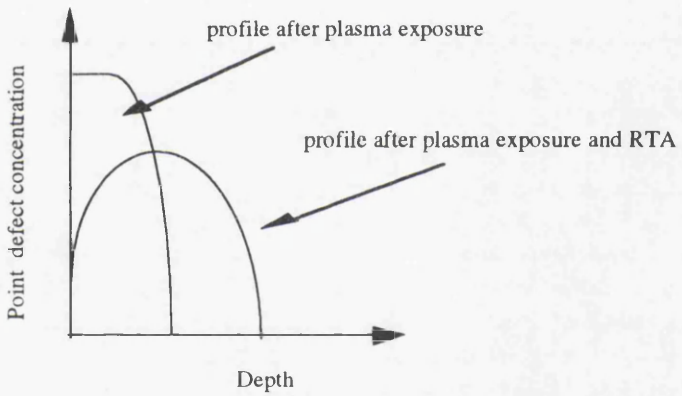

Figure 5.3: The probable point defect profiles after plasma exposure, and plasma exposure and RTA.

DQW material, with the layer structure as given in Appendix A1, was used to investigate intermixing induced by of the drive–in diffusion process. The intermixing process was achieved by repeated cycles of plasma exposure and annealing to 'drive' the point defects generated by H^+ bombardment into the QWs. The annealing cycle was kept at 850 °C for 30 s. A relatively low temperature (about 100 °C lower than the IFVD and IID processes) was used here to avoid a high degree of intermixing in the control region and to avoid damage to the dielectric cap on the GaAs surface. Samples with 500 nm of SrF_2 dielectric cap were also subjected to the same process cycle. Control samples which went through only the annealing step were studied to compare the degree of intermixing. PL measurements at 77 K were performed to assess the bandgap shift. The conditions used during the plasma exposure and the annealing stages are summarised in Table 5.1.

Pressure	rf power	Flow rate	dc bias	Exposure time	RTA conditions
5 mTorr	150 W	5 sccm	≈ – 1000 V	1.5 min	850 °C, 30 s

Table 5.1: The exposure and annealing conditions used in the plasma induced damage layer intermixing process.

PL measurements were performed after every cycle and the results are given in Figure 5.4. It is noted that the SrF_2 control sample exhibited a negligible shift of about 2 nm after 10 process cycles. The bandgap shift from the unexposed, uncapped annealed samples was about 6 nm, which is significantly higher, after 10 process cycles. The energy shift from the control samples (with only proximity cap) may be due to the out diffusion of as during the annealing step. Three samples which were exposed to the H_2 plasma and annealed were found to have induced bandgap shifts of up to 20 nm. The shift seems to saturate after the 7th process. The reason for this saturation is not clear and two probable causes are proposed. (i) A bad surface covered with a black substance was been observed on the GaAs after the 7th annealing cycle. This contaminant was believed to be composed of carbon from the graphite susceptor and arsenic. The formation of this contaminant layer may act as a barrier and reduce the density of point defects created in the semiconductor, and hence, inhibit the intermixing process. (ii) The intermixing process after the 7th cycles may be inhibited by the formation of dislocation loops resulting from the cumulative serious damage to the wafer[9]. Although the maximum bandgap shift is only about 38 meV (20 nm), it is, however, large enough for most photonic device applications.

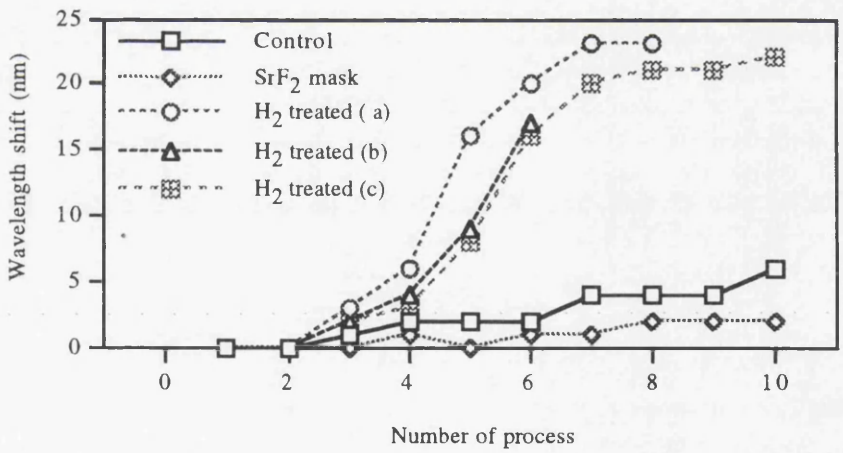

Figure 5.4: The energy shift observed from the DQW samples after treated by H_2 plasma, samples with annealing cycles only and samples protected by SrF_2 cap. The DQW material consists of a 1.3 μm upper cladding layer .

The number of cycles required to induce a significant bandgap shift was also found to be depth dependent on the well depth. The required number of cycles was found to be smaller when material with similar structure but with only a 0.9 μm upper cladding layer (Appendix A3) was used. On the other hand, a DQW placed 1.5 μm below the surface (Appendix A4) was found not to be intermixed even after 8 cycles (Figure 5.5). The small shift of the 1.5 μm deep DQW samples may

[9]T. Venkatesan, S.A. Schwarz, D.M. Hwang, R.Bhat, M. Koza, H.W. Yoon, P. Mei, Y. Arakawa, and A. Yariv, 'Dose-dependent mixing of AlAs-GaAs superlattices by Si ion implantation', Appl. Phys. Lett. **49**, 701 (1986).

either result from an extremely stable crystal quality or the wells are too far away from the surface for the diffusion of point defects to reach. These results, however, suggest that the diffusion of point defects induced by plasma require a longer time to reach a deeper depth

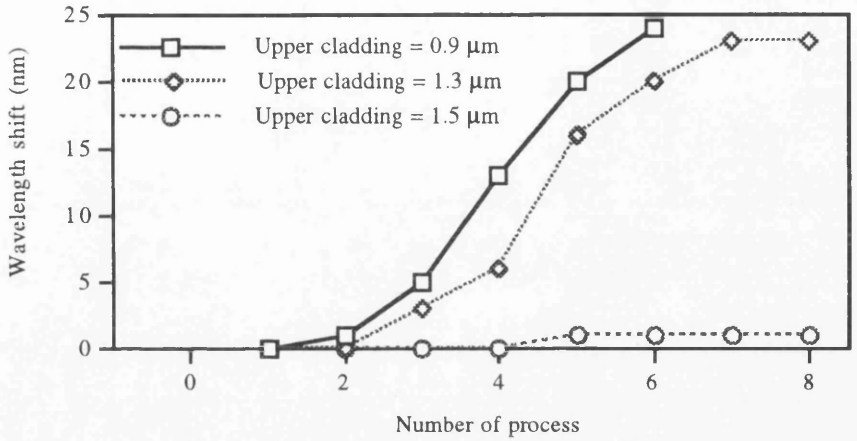

Figure 5.5: DQW placed at different depth was found to influent the process cycles using the plasma damage induced layer intermixing process.

5.3 Bandgap shifted oxide stripe lasers

In order to investigate the quality of the material and the lasing wavelength after intermixing, DQW material with an upper cladding layer thickness of 1.3 μm was used to fabricate bandgap shifted oxide stripe lasers (layer structure is documented in Appendix A1). Information such as threshold current density for infinite cavity length (J_o), transparency current (J_T), internal quantum efficiency (η_i) and internal propagation loss (α) can be obtained from *L–I* (Light output power versus Injected current) characteristics of these broad area oxide stripe lasers.

5.3.1 Laser characterisation

Laser oscillation occurs when the gain reaches the total of the absorption loss in the laser cavity. The required gain at threshold, g_{th}, of a QW semiconductor is given by:

$$g_{th} = \alpha + \frac{1}{L}\ln\left(\frac{1}{R}\right). \qquad (5.1)$$

where α is the loss coefficient, L is the cavity length, and R is the reflection coefficient of the end facets. Above threshold the laser action is initialised under a constant g_{th} and the extra injected carriers will recombine and emitted as light. The relationship between g_{th} and the quantum efficiency is given by :

$$\eta = \eta_i\left(1 - \frac{\alpha}{g_{th}}\right) \qquad (5.2)$$

where η_i is the internal quantum efficiency which is defined as the probability that an injected carrier recombine radiatively within the active region. η is the external quantum efficiency or slope efficiency above threshold, which can be measured from the slope of the *L–I* curve above threshold, and is defined as the rate of change of the photon output rate versus the rate of change of the carrier injected rate.

The gain up to threshold can be related to the current density in a QW laser by the following relationship:

$$g(J) = n\Gamma g_o \ln\left(\frac{\eta_i J}{nJ_t}\right) \tag{5.3}$$

where n is the number of quantum wells, Γ is the optical confinement per well and is defined as the ratio of the power within the well to the total power carried by the laser mode, g_o is the gain coefficient for one well and J_t is the transparency current density, which can be explained as the current needed in a well to overcome the resonant and make the well lossless or transparent. From Equation (5.1) and (5.2) we obtain:

$$\frac{1}{\eta} = \frac{1}{\eta_i} - L\left(\frac{\alpha}{\eta_i \ln R}\right). \tag{5.4}$$

Therefore the η_i can be obtained from the plot of η against L. From the gradient of the same plot (by assuming that the reflectivity R =30 % for a cleaved facet), the optical loss α can be determined.

From Equation (5.3), the gain coefficient at threshold will be:

$$g_{th} = n\Gamma g_o \ln\left(\frac{\eta_i J_{th}}{nJ_t}\right) \tag{5.5}$$

where J_{th} is the threshold current density. By substituting Equation (5.1) into Equation (5.5), and rearranging the equation, we obtain:

$$\ln(J_{th}) = \left[\frac{\alpha}{n\Gamma g_o} + \ln\left(\frac{nJ_t}{\eta_i}\right)\right] - \frac{1}{L}\left(\frac{\ln R}{n\Gamma g_o}\right). \tag{5.6}$$

Defining

$$\ln(J_o) = \left[\frac{\alpha}{n\Gamma g_o} + \ln\left(\frac{nJ_t}{\eta_i}\right)\right], \tag{5.7}$$

Equation (5.6) will be:

$$\ln(J_{th}) = \ln(J_o) - \frac{1}{L}\left(\frac{\ln R}{n\Gamma g_o}\right) \tag{5.8}$$

where J_o is the threshold current density for infinite length. Therefore, J_o and $n\Gamma g_o$ can be deduced from the intercept and the slope respectively of the plot of the $\ln(J_{th})$ versus $\frac{1}{L}$, following Equation (5.8). J_t can be calculated from J_o using α , η_i, and $n\Gamma g_o$ found previously.

5.3.2 Experiment, results and discussion

Five sets of such lasers were fabricated, i.e one set each from the as-grown material and from the control sample (without the SrF_2 cap) after 9 annealing processes, and three other samples intermixed to different degree (after 6, 8, and 10 process cycles respectively).

The samples were first coated with a layer of 200 nm of SiO_2. The 75 μm stripe windows were defined using photolithography and dry etching using C_2F_6 RIE to open the windows. To minimise the RIE damage from the C_2F_6 process, the dry etching process was carried out using 100 W C_2F_6 for 2.5 min and finished by etching the remaining 75 nm of SiO_2 using 30 W C_2F_6 for 4 min. These lasers are gain-guided since the injected current produced population inversion and a subtle waveguide effect only in the 75 μm stripe regions. Samples were then thinned to a thickness of around 180 nm and metal contacts (n- Au/Ge/Au/Ni/Au, 14nm/14nm/14nm/11nm/240nm, p-Ti/Pb/Ti/Au, 30nm/33nm/30nm/140nm) were evaporated using a computer controlled metal evaporator ('Plassys'). The samples were then annealed using RTA at 360 °C for 60 s and scribed into individual lasers with lengths of 300, 500, 700, and 900 μm. A diagram of a bandgap shifted oxide stripe laser is given in Figure 5.6.

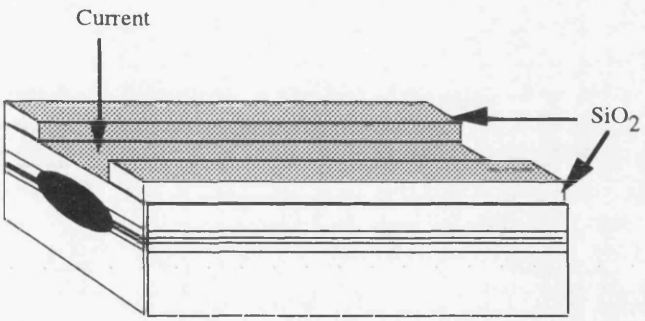

Figure 5.6: Schematic diagram of a 75 μm wide oxide stripe laser.

The lasers were operated in pulsed current mode at room temperature (≈20 °C). The current pulse width was 400 ns and the repetition rate was 1 kHz (duty cycle 1:2500). Measurements such as *L–I* characteristics, and lasing spectrum were performed. About 5 lasers were measured for each of 4 different cavity lengths from samples with different degrees of intermixing. Only the best data were selected for analysis. Table 5.2 gives a summary of the number of process steps, peak PL wavelength measured at 77 K and the lasing wavelength of the lasers. The lasing wavelengths were determined using an optical spectrum analyser ('Advantest') and were taken from the 500 μm length lasers operated just above threshold.

Sample	Process	No. of process	77 K PL wavelength (nm)	Lasing wavelength (nm)
S1	as-grown	-	810	864
S2	non plasma treated	9	804	860
S3	H_2 treated	6	795	848
S4	H_2 treated	8	788	839
S5	H_2 treated	10	787	not lasing

Table 5.2: A summary of the samples used for the fabrication of the broad area oxide stripe lasers and their lasing wavelength.

It is noted from Table 5.2 that no lasing was observed from S5, which was treated by the H_2 plasma and subject to 10 cycles of the process. The p-contact of this sample was inferior and a very high resistance was observed in the *I-V* characteristics. The fabrication processes of all these lasers, including the metal deposition, were carried out at the same time. Therefore the bad quality of the metal contact on sample S5 may not be due to the fabrication process. The p^{++}–GaAs layer of this sample may either be completely removed or the contamination layer mentioned above may not have been removed completely during the deoxidisation step using HCl before metalisation. Either of these explanation could account for the poor quality of the metal contact. The PL signal from this sample did not seem to exhibit any large broadening or be noisy, and therefore, a good QW quality is still expected in this sample. The lasing wavelengths were in close agreement with the PL wavelength for lasers fabricated from other samples.

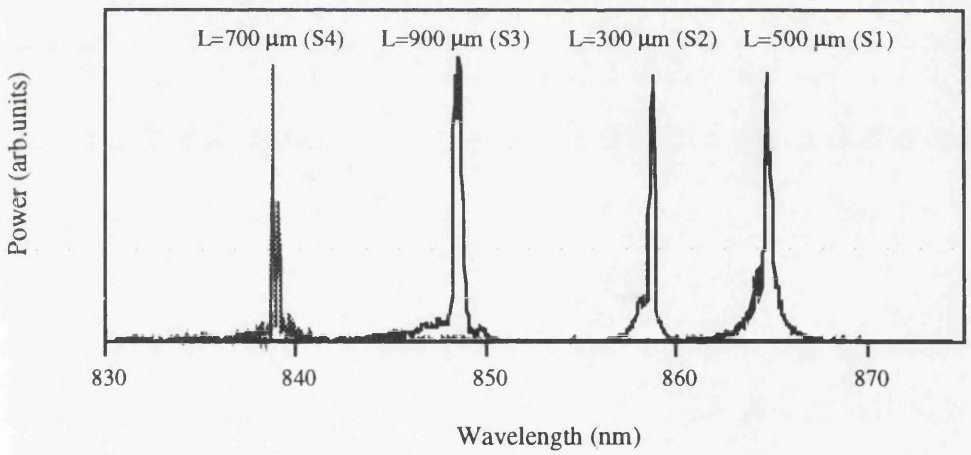

Figure 5.7: Emission spectra of bandgap shifted oxide stripe lasers showing blue shifts of up to 23 nm. L is the cavity length of the laser.

Figure 5.7 shows the spectra from the lasing devices. These spectra were obtained from lasers operated just above threshold. They lased multi–moded since these lasers are gain-guided with weak optical confinement and are simple Fabry-Perot devices. The largest wavelength shift to be obtained was 23 nm. The shift from the control sample S2 is quite large ($\approx$ 5 nm), an effect which is undesired, but it is expected that this could be reduced by using a lower temperature during the annealing step.

The *L-I* characteristics of these lasers were measured and the threshold current density for infinite length (J_o), transparency current density per QW (J_t), internal quantum efficiency (η_i) and the internal propagation loss (α) have been deduced from the threshold current densities and the slope efficiencies obtained from the *L–I* characteristics as explained above. A summary of these results is tabulated in Table 5.3.

Sample	J_o (A cm^{-2})	J_t (A cm^{-2})	η_i (%)	α (cm^{-1})
S1	264	71	73	9.4
S2	317	81	66	9.7
S3	285	74	63	9.5
S4	308	78	69	9.8

Table 5.3: Summary of the threshold current density for infinite length (J_o), transparency current density (J_t), internal quantum efficiency (η_i) and the internal propagation loss (α) from samples S1 to S4.

A relatively low internal quantum efficiency has been obtained from all of the laser. This may due to poor collection of the laser emission since the photo detector was placed relatively far away from the divergent beam during the measurements to avoid the saturation of the detector. Although the reduction in η_i causes a reduction in the transparency current, it does not affect the measured loss as the error cancels out by itself. Apart from the low η_i (include the as-grown lasers), there is no obvious increase in loss, threshold current density for infinite length and transparency current, or decrease in internal quantum efficiency after intermixing (Table 5.3). We therefore concluded that the samples were still of good quality after being intermixed using the above technique.

Surface contamination after long annealing times is dependent on the choice of the RTA susceptor. This problem has been seen to improve after using a silicon susceptor. Although the GaAs sputtering rate in the hydrogen plasma is quite high, the problem of the removal of the contact layer can be overcome by modifying the layer structure by using a thicker p^{++}–GaAs cap. However, the high sputtering rate is not a problem for the fabrication of certain devices, such as extended cavity lasers, for which the GaAs cap layer is to be removed in any case from the bandgap widened section in order to reduce absorption and current spreading. The saturation of the degree of intermixing is believed to be contamination related, and larger shifts can be obtained by using a higher Al concentration barriers and by reducing the thickness of the upper cladding layer. Lowering the annealing temperature is expected to reduce the bandgap shift seen in the control samples, although an increase the number process cycles may result. A negligible shift, however, has been obtained from the SrF_2 capped control samples and wavelength control in selected areas may not be a problem.

5.4 *Extended cavity lasers*

The integration of semiconductor lasers with passive optical waveguide sections, which are transparent at the laser wavelength, is of great importance for integrated photonic circuits. This integration is also essential for grating–coupled emission, and integrated extended cavity mode–locked lasers. The used of QWI techniques to carry out such integration promises excellent mode matching and virtually no optical reflection between the active and passive waveguides. In this Section, extended cavity lasers, which consist of active regions integrated with passive low-loss waveguides, have been fabricated and studied. The passive waveguide sections were bandgap widened using the intermixing technique developed above to reduce the propagation loss.

5.4.1 *Fabrication procedures*

Material used in the fabrication of the extended cavity lasers was the same as that used for the oxide stripe bandgap shifted lasers reported the last Section. The samples were intermixed under the same process conditions documented in Section 5.2.3. First, the lift-off process was used to define 500 nm thick region of SrF_2 over the laser active regions to act as both the annealing and the plasma exposure mask, leaving gaps of between 500 and 2000 μm for the extended cavities. 8 cycles of the process were carried out, with the last plasma exposure cycle being struck with 5 sccm of CH_4 plasma to etch away the remaining GaAs cap layer from the passive waveguide section. The removal of the highly doped GaAs cap minimises current spreading into the passive areas and the absorption of light in these regions. The SrF_2 cap was then cleaned off using concentrated HCl. A good surface morphologies was obtained after removal of the SrF_2 layer. A 200 nm thick layer of SiO_2 was then deposited and 75 μm stripe windows were then opened using the same method as described in Section 5.3. The p–contact was defined over the laser active sections using lift-off. The devices were then cleaved to give a 450 μm long active region with the passive region range from 500 to 2000 μm in length. Samples were also cleaved to give a 450 μm long active region only. For comparison, DQW active layer devices were fabricated as control samples, where the plasma exposure and annealing stages were omitted. Such samples had their GaAs cap region removed, from the passive waveguides, using the selective etch H_2O_2:NH_3 (20:1) for 30 s. These control samples will be refereed to as untreated samples throughout the rest of the text. The schematic diagram of an oxide stripe extended cavity laser is given in Figure 5.8.

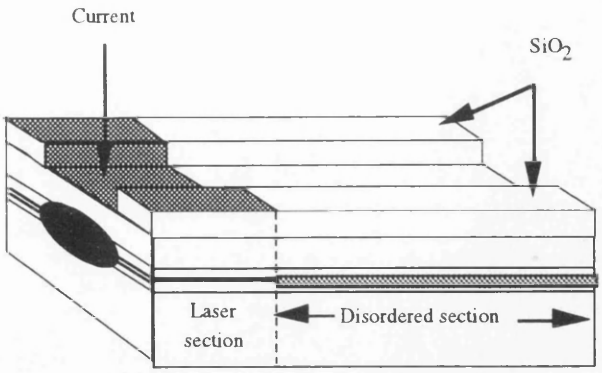

Figure 5.8: Diagram of an oxide stripe extended cavity laser.

Small pieces of control sample with and without the SrF_2 cap were also put through the same process cycles to study the degree of intermixing. From 77 K PL measurements, the extended cavity region was found to shift by 20 nm (≈ 38 meV) whilst there was only a small shift of about 1 nm in the SrF_2 protected section.

5.4.2 Results and discussion

Figure 5.9 shows the *L–I* curves from the extended cavity lasers for different passive cavity lengths from the plasma treated samples (Figure 5.9a) and the untreated sample (Figure 5.9b). These results were taken from the devices with the best threshold current operated pulsed using the same conditions as the bandgap shifted oxide stripe lasers.

The loss measurements were initially performed by measuring the spontaneous emission power output from both facets, well below the lasers' threshold[10]. This method assumes that the optical output from the extended cavity facets is always lower than the optical output from the laser facet due to the absorption and the scattering loss in the extended cavity. It was, however, found that the output power from the extended cavity facet was always greater than that from the laser facet. This effect might be due to the extended cavity having a slightly different mode shape which could be coupled better into the fibre, hence resulting in an apparently higher optical output from the facet of the passive waveguide. This technique was eventually abandoned and the loss measurements reported here were found by calculation using the formula:

$$\frac{I_{ex}}{I_{nor}} = \exp\left(\frac{\alpha_e L_e}{n\Gamma g_o L_a}\right) \qquad (5.9)$$

where I_{ex} and I_{nor} are the threshold current of extended and normal devices, α_e and L_e are the absorption coefficient and the length of the passive cavity region, and L_a is the length of the active region. A DQW laser material was used in this study, therefore n, the number of wells, is 2, and Γ = 2.75% and g_o = 840 cm^{-1} are the theoretical values for 10 nm wells in GaAs.

---

[10]I. Gontijo, T. Krauss, R.M. De La Rue, J.S. Roberts and J.H. Marsh, 'Very low loss extended cavity GaAs/AlGaAS lasers made by impurity-free vacancy diffusion', Electron. Lett. **30**, 145 (1994).

The slope efficiencies have also been calculated and the results are summarised in Table 5.4.

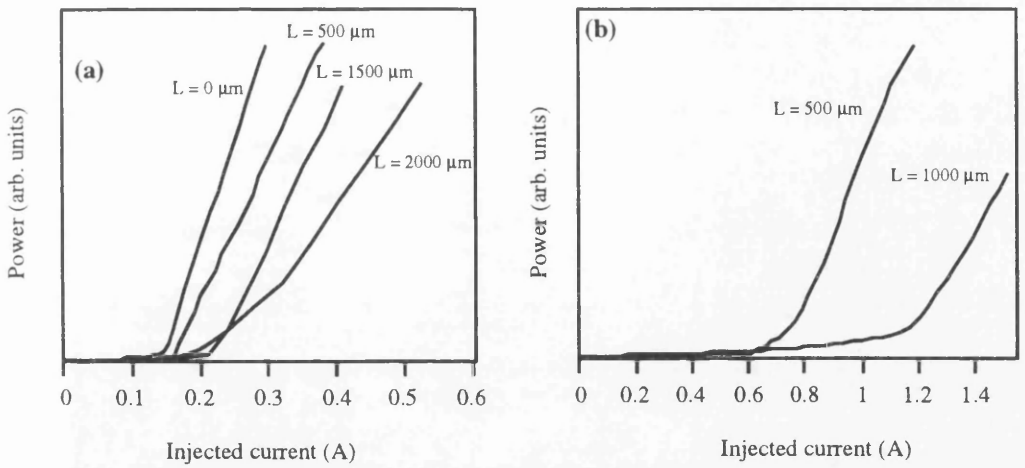

Figure 5.9: *L–I* curves from (a) four plasma treated lasers with different extended cavity lengths, and (b) lasers from the untreated sample. These measurements were taken from lasers with the best threshold.

Extended cavity length (µm)	Best I_{th} (mA)	Slope efficiency per–facet (W A^{-1})	Loss (cm^{-1})	Loss (dB cm^{-1})
0	145	0.27	—	—
500	160	0.22	4.3	18.1
1500	220	0.19	5.7	24.1
2000	242	0.18	5.4	22.7

Table 5.4: The results summary of the loss calculated from the threshold current and the slope efficiencies from the plasma treated extended cavity lasers.

It is noticeable that only a small increase in the threshold current was seen in the plasma treated samples with different passive cavity lengths (Table 5.4). This observation is an indication that the propagation losses in the passive regions are lower than in the untreated lasers. The passive regions of the untreated lasers were electrically unpumped and therefore will be highly absorbing at the laser emission wavelength. From these *L–I* curves, it is clear that selective quantum well intermixing helped to reduced the threshold current by around a factor of 5.

The lowest loss was measured in the laser with the 500 µm long extended cavity section being about 4.1 cm^{-1} or 18.1 dB cm^{-1} in the plasma treated lasers, which corresponds to about 9 dB cm^{-1} per well. This loss is still relatively high compared to the propagation loss obtained from the extended cavity lasers prepared using IFVD techniques [10] (3.6 dB cm^{-1}) and is about the same loss as the extended cavity lasers prepared using fluorine IID (19±8 dB cm^{-1})[11]. It is, however, relatively low

[11] S.R. Andrew, J.H. Marsh, M.C. Holland, and A.H. Kean, 'Quantum well laser with integrated passive waveguide fabricated by neutral impurity disordering', IEEE Photonics Technol. Lett. **4**, 426 (1990).

comparing to Si IID[12] lasers. In the case of silicon disordering, however, a propagation loss of around 10 cm^{-1} has been measured in a DQW structure. By using the same Equation (5.9) a loss of about 50 cm^{-1} (around 25 cm^{-1} per well) has been calculated in the untreated lasers with 500 μm long passive waveguide. This loss is relatively low if compared to the predicted value of 100 cm^{-1} [13], however it is quite well agreed with the calculated value of 60 cm^{-1} given by Tarucha *et al*[14].

In the case of the plasma treated lasers, the slope efficiencies were found to decrease with the increasing the cavity length. This indicates that the unpumped passive waveguides are still absorbing. However, the decrease of the slope efficiency becomes insignificant when compared to the untreated lasers, where the slope efficiencies of 0.12 W A^{-1} and 0.08 W A^{-1} were obtained from lasers with cavity lengths of 500 μm and 1000 μm respectively. The low slope efficiencies from the untreated lasers indicate a high loss which caused mainly by the band edge absorption.

5.5 Summary and conclusion

A new technique using energetic H_2 plasma to create damage was found to induce intermixing in a DQW GaAs/AlGaAs sample. Significant degrees of disordering have been obtained after drive–in diffusion of the point defects using 5 to 6 cycles of plasma exposure and annealing. A relatively low annealing temperature (850 °C) has been used in this process and the bandgap shift in selected regions can be inhibited using a thick SrF_2 cap. Although intermixing was found to saturate after the 7th process cycle, the bandgap shift is significant enough to be used in photonic integration applications. Bandgap shifted oxide stripe lasers have been fabricated and the material was found to remain of good quality after intermixing. Extended cavity lasers, containing an integrated passive optical waveguide, were successfully fabricated and propagation losses as low as 18.1 dB cm^{-1} have been measured in the passive waveguide section.

---

[12] J. Werner, T.P. Lee, E. Kapon, E. Colas, N.G. Stoffel, S.A. Schwarz, L.C. Schwartz, and N.C. Andreadakis, 'Single and double quantum well lasers with a monolithically integrated passive section', Appl. Phys. Lett. **57**, 810 (1990).

[13] R.L. Thornton, J.E. Epler, and T.L. Poili, 'Monolithic integration of a transparent dielectric waveguide into an active laser cavity by impurity–induced disordering', Appl. Phys. Lett. **51**, 1983 (1987).

[14] S. Tarucha and H. Okamoto, 'Monolithic integration of a laser diode and an optical waveguide modulator having a GaAs/AlGaAs quantum well double heterostructure', Appl. Phys. Lett. **48**, 1 (1986).

Chapter 6 Neutral impurity induced disordering using boron and fluorine

6.1 Outline

A brief introduction to impurity induced disordering (IID) of GaAs/AlGaAs QWs is documented in the first Section of this Chapter. The model of IID, proposed by Deppe and Holonyak[1], is discussed. SIMS analysis was used to study the diffusion of fluorine and boron in p- and n-type AlGaAs, and the experimental results are presented. The diffusion models for boron and fluorine in p- and n-type AlGaAs are proposed and the mechanisms of neutral IID are then discussed in the last Section of this Chapter.

6.2 Introduction

The impurity induced disordering (IID) effect was first observed in GaAs/AlAs superlattices by Laidig *et al*[2]. Since then, this technique has been viewed as a potential technique for the fabrication of optoelectronic integrated circuits (OEICs) and photonic integrated circuits (PICs), as it can be used to modify a chosen QW region by increasing the effective bandgap energy and lowering the refractive index. The fabrication of monolithic devices using QWI can, therefore, eliminate a series of etch and regrowth processes. Several potential applications of QWI techniques in integrated optoelectronics have been identified[3]: for example, bandgap-tuned modulators, bandgap-tuned lasers, low-loss waveguides for interconnecting components on an OEIC, integrated extended cavities for line-narrowed lasers, single-frequency distributed Bragg reflector (DBR) lasers, mode-locked lasers, non-absorbing mirrors and either gain or phase gratings for DFB (distributed feedback) lasers.

After Laidig *et al*[2], various methods have been reported to induce intermixing in QWs. Three of the widely used techniques are (i) impurity induced disordering (IID), (ii) impurity-free vacancy disordering (IFVD), and (iii) photoabsorption induced disordering (PAID)[4,5] and other laser related process[6,7]. This Chapter, however, is only concerned with the IID process in the GaAs/AlGaAs system. A more detail introduction to the IFVD process is given in Chapter 9.

---

[1]D.G.Deppe and N.Holonyak,Jr., 'Atom diffusion and impurity-induced layer disordering in quantum well III-V semiconductor heterostructures', J. Appl. Phys. **64** , R93 (1988).

[2]W.D. Laidig, N. Holonyak,Jr., M.D. Camras, K. Hess, J.J. Coleman, P.D. Dapkus, and J. Bardeen, 'Disorder of AlAs-GaAs superlattice by impurity diffusion', Appl. Phys. Lett. **38**, 776 (1981).

[3]J.H. Marsh, S.I. Hansen, A.C. Bryce, R.M. De La Rue, 'Applications of neutral impurity disordering in fabricating low-loss optical waveguides and integrated waveguide devices', Optical and Quantum Electronics **23** , S941 (1991).

[4]C.J. McLean, J.H. Marsh, R.M. De La Rue, A.C. Bryce, B. Garrett, R.W. Glew, 'Layer selective disordering by photoabsorption induced thermal diffusion in InGaAs/InP based multiple quantum well structures', Electron.Lett. **28**, 1117 (1992).

[5]C.J. McLean, A. McKee, J.H. Marsh, R.M. De La Rue, 'Lateral control of the bandgap in GaInAs/GaInAsP MQW structures using photoabsorption induced disordering', Electron.Lett. **29**, 1657 (1993).

[6]J. Ralston, A.L. Moretti, R.K. Jain, F.A. Chambers, 'Intermixing of $Al_xGa_{1-x}As$/Gaas superlattices by pulsed laser irradiation', Appl. Phys. Lett. **50**, 1817 (1987).

[7]J.E. Epler, R.D. Burnham, R.L. Thornton, T.L. Paoli, and M.C. Bashaw, 'Laser induced disordering of GaAs-AlGaAs superlattice and incorporation of Si impurity', Appl. Phys. Lett. **49**, 1447 (1986).

The IID process is achieved by introducing impurities to the QW structure using ion-implantation or diffusion followed by an appropriate annealing step usually at a temperature of higher than 800 °C. In the IID technique, donors such as Si, Ge, S, Sn, and Se, as well as the acceptors Zn, Be and Mg have been proven to be species that can be used to intermix the QW.

Three major problems have been identified for using IID process in integrating optoelectronic devices. (i) A typical impurity concentration of $>10^{18}$ cm^{-3} is usually used to enhance QW intermixing. Most of the charged impurities mentioned above are shallow impurities which ionise at room temperature and contribute to high free carrier absorption. Taking IID using Si for example, the lowest absorption coefficient ever reported was around 43 dB cm^{-1} (10 cm^{-1}), which is a consequence of free carrier absorption. (ii) The charged impurities are unlikely to enable electrical isolation resistances of 100 kΩ for interconnection waveguides in OEIC to be achieved. (iii) Residual damage from implantation which will degrade the quality of the material and directly influence the efficiency and lifetime of the devices. Problem (iii) can be minimised by optimising the implantation and annealing conditions. To overcome the first two problems, neutral impurities such as boron and fluorine have been introduced[8,9].

Being neutral impurities at room temperature, boron and fluorine have the advantages such as providing lower propagation loss and higher electrical resistivity over other impurities. An ion concentration of 5 x 10^{17} cm^{-3} and annealing time of 2-3 hours at 890 °C in a furnace or ≈ 30 s at 950 °C in an RTA are typically used for neutral IID to obtain a sufficient bandgap shift in the GaAs/AlGaAs system. In the GaAs/AlGaAs system, fluorine has been found to produce larger energy shifts (up to ≈ 100 meV) than boron for similar annealing conditions. By using fluorine as the IID species, losses as low as 4.6 dB cm^{-1} have also been measured in ridge waveguides from a MQW structure[10,11], and losses of 19 ± 8.4 dB cm^{-1} were estimated from a 600 μm passive section of a extended cavity laser fabricated using DQW material[12]. The intermixing technique using neutral IID is also found to induce disordering in the GaInAs/GaInAsP[13], and GaInAs/AlGaInAs [14]systems.

Neutral IID using fluorine and boron will be discussed in some detail in this Chapter. The physics of IID is discussed. The objectives of this Chapter are to investigate the diffusion and IID

---

[8]J.H. Marsh, S.R. Andrew, S.G. Ayling, J. Beauvais, S.A. Bradshaw, A.C. Bryce, S.I. Hansen, R.M. De La Rue and R.G. Glew, 'Neutral impurity disordering of III-V quantum well structure for optoelectronic integration', Mat. Res. Soc. Symp.Proc. **240**, 679 91992).

[9]J.H. Marsh, 'Quantum well intermixing', Semicond. Sci. Technol. **8**, 1136 (1993)

[10]M. O'Neil, J.H. Marsh, R.M. De La Rue, J.S. Roberts, C. Jeynes, 'Multiple quantum well optical waveguides with large absorption edge blue shift produced by boron and fluorine impurity-induced disordering', Appl. Phys. Lett. **55**, 1373 (1989).

[11]M. O'Neil, J.H. Marsh, R.M. De La Rue, J.R. Roberts, and R. Gwilliam, 'Reduction of the propagation losses n impurity disordered quantum well waveguides', Electron. Lett. **26**. 1613 (1990).

[12] S.R. Andrew, J.H. Marsh, M.C. Holland and A.H. Kean, 'Quantum well laser with integrated passive waveguide fabricated by neutral impurity disordering', Photonics Tech. Lett. **4**, 426 (1992).

[13]J.H. Marsh, S.A. Bradshaw, A.C. Bryce, R. Gwilliam and R.W. Glew, J. Electron Mater. **20**, 973 (1991).

[14]A.C. Bryce, J.H. Marsh, R. Gwilliam and R.W. Glew, 'Impurity induced disordering in InGaas/InGaAsP quantum wells using implanted fluorine and boron', IEE Proc. Pt. J: optoelectronics **138**, 87 (1991).

behaviour of fluorine and boron in p- and n-type GaAs/AlGaAs. Diffusion models of fluorine and boron are proposed, and the mechanisms of neutral IID in the GaAs/AlGaAs system are then discussed.

6.3 Physics of IID

The model of IID presented in Section is based on the IID model proposed by Deppe and Holonyak[1]. This model explains the effects of the crystal Fermi energy on the group III interdiffusion rate. The effects of the concentration of the charged point defects, particularly group III vacancies and interstitials, and the As partial pressure on the position of Fermi level of the crystal are then discussed.

6.3.1 Effect of the As partial pressure and doping densities on V_{III} and I_{III}

The majority of the point defects generated by ion-implantation are vacancy and interstitial defects. Out of six possible point defects, i.e. Ga and As vacancies (V_{Ga}, V_{As}), Ga and As antisites (Ga_{As}, As_{Ga}), and Ga and As interstitials (I_{Ga}, I_{As}), only V_{Ga}, Ga_{As} are expected to act like acceptors and the other four are expected to behave as donors. Among these defects, only group III vacancies and group III interstitials are expected to contribute to QWI since Al atoms will be taken over to the Ga sites of the GaAs layer during disordering. In the case of the GaAs/AlGaAs system, the intermixing rate will depend on the concentration of the total defect concentration of group III vacancies V_{III}, or of group III interstitials I_{III}. Therefore, only V_{III} and I_{III} will be considered in this analysis.

Firstly, consider the change of the entropy (ΔS) of an elemental system after point defects are introduced:

$$\Delta S = k_B \ln P \tag{6.1}$$

where k_B is Boltzman constant and P is the number of ways of arranging the system, i.e. the number of ways in which n vacancies can be arranged among N lattice sites. Therefore, the entropy of this system can be written as:

$$\Delta S = k_B \ln\left[\frac{N!}{(N-n)!n!}\right]. \tag{6.2}$$

Applying Stirling's approximation, $\ln x! \approx x(\ln x - 1)$, to Equation 6.2 gives:

$$\Delta S = k_B[(N \ln N - (N-n)\ln(N-n) - n \ln n] \tag{6.3}$$

Suppose ΔU is the energy required to create a vacancy. The internal energy of the system W is therefore increased by the creation of a vacancy. The energy increment for n vacancies is given by $\Delta W = n\Delta U$. Therefore the change of the free energy ΔF associated with the reaction will be:

$$\Delta F = n\Delta U - T\Delta S \tag{6.4}$$

where T is the temperature. By substituting Equation (6.3) into (6.4), the thermal equilibrium condition can be expressed by minimising ΔF with respect to n,

$$\frac{\partial(\Delta F)}{\partial n} = \Delta U - k_B T[\ln(N-n) - \ln n] = 0, \tag{6.5}$$

Hence

$$n = (N-n)\exp\left(-\frac{\Delta U}{k_B T}\right). \tag{6.6}$$

since $N >> n$, therefore,

$$n = N\exp\left(-\frac{\Delta U}{k_B T}\right) \tag{6.7}$$

We learned from Section 6.3.1 that vacancies in GaAs behave like acceptors with the possible reaction of:

$$V_{III} \Leftrightarrow V_{III}^{-} + h. \tag{6.8}$$

Applying the law of mass action, we obtain:

$$K_T = p\frac{[V_{III}^{-}]}{[V_{III}]} \tag{6.9}$$

where p is the hole concentration, K_T is a temperature dependent constant and $[X]$ represents concentration of X. Combining Equation (6.9) with the charge neutrality condition:

$$[V_{III}^{-}] + n = p \tag{6.10}$$

and the hole-electron equilibrium condition:

$$np = n_i^2, \tag{6.11}$$

we obtain:

$$[V_{III}^{-}] = \frac{K_T[V_{III}]n_i^2}{p}. \tag{6.12}$$

By analogy, the Ga interstitial concentration $[I_{III}^{+}]$, a donor like defect, can be written as:

$$[I_{III}^{+}] = \frac{K_T'[I_{III}]p}{n_i^2}. \tag{6.13}$$

$[V_{III}]$ and $[I_{III}]$ are highly dependent on the partial pressures of the components above the compound[15,16]. When GaAs is annealed under a high As vapour pressure, the crystal surface will act as a sink for group III interstitial defects, thus increasing the concentration of group III vacancies deeper in the crystal. Likewise, under As-poor annealing conditions, As will evaporate from the crystal, leaving a Ga-rich surface. The excess Ga atoms can then diffuse into the crystal increasing the concentration of group III interstitials.

Assuming the defects generated under an As vapour pressure are Frenkel's defects, i.e defects which consist of an interstitial and a vacancy, then $0 \Leftrightarrow I_{III} + V_{III}$ and

$$[I_{III}][V_{III}] = K_T^{''}. \tag{6.14}$$

Assume that the As vapour appears in the form of As_4. The reaction between Ga interstitials and As_4 vapour can then be written as:

$$0 \Leftrightarrow \tfrac{1}{4} As_4(vapour) + I_{III}. \tag{6.15}$$

Applying the law of mass action, Equation (6.15) becomes:

$$[I_{III}] = K_T^{'''} P_{As_4}^{-\frac{1}{4}}. \tag{6.16}$$

Combining Equation (6.14) and (6.15) we obtain:

$$[V_{III}] = K_T^{''''} P_{As_4}^{\frac{1}{4}}. \tag{6.17}$$

By taking the As vapour pressure into consideration, Equation (6.12) and (6.13) can be simplified as:

$$[V_{III}^{-}] \propto P_{As} n, \tag{6.18}$$

and

$$[I_{III}^{+}] \propto P_{As}^{-1} p. \tag{6.19}$$

Equation (6.18) and (6.19), therefore, explain that $[V_{III}^{-}]$ is lower in p-type material than in n-type material and that $[V_{III}^{-}]$ increases with increasing partial pressure of As. In the case of $[I_{III}^{+}]$, however, p-type material supports a higher $[I_{III}^{+}]$ than in n-type material, and the formation of $[I_{III}^{+}]$ is only favoured under As-poor conditions.

---

[15]L. Guido, N. Holonyak, Jr., K.C. Hsieh, R.W. Kaliski, W.E. Plano, R.D. Burnham, R.C. Thornton, J.E. Epler, and T.L. Paoli, 'Effects of dielectric encapsulation and As overpressure on Al-Ga interdiffusion in $Al_xGa_{1-x}As$-GaAs quantum well heterostructure', J. Appl. Phys. **61**, 1372 (1987).

[16]A. Furuya, O. Wada, A. Takamori, and H. Hashimoto, 'Arsenic pressure dependence of interdiffusion of AlGaAs/GaAs interface of quantum well', Jpn. Appl. Phys. **26**, L926 (1987).

6.3.2 *Effects of Al-Ga interdiffusion on the position of Fermi level*

The relationship between the equilibrium number of charged defects and the Fermi energy can be related by writing Equation (6.9) as:

$$p\frac{[V_{III}^-]}{[V_{III}]} = pF(E) = N_V \exp\left[\frac{(E_V - E_A)}{k_B T}\right] \tag{6.16}$$

where

$$p = N_V \exp\left[\frac{(E_V - E_F)}{k_B T}\right], \tag{6.17}$$

$F(E)$ is the Fermi distribution function, N_V is the density of states in the valence band, and E_V and E_A are the valence and the vacancy acceptor energy levels respectively. Therefore:

$$[V_{III}^-] = [V_{III}]\exp\left[\frac{(E_F - E_A)}{k_B T}\right]. \tag{6.18}$$

Similarly,

$$[I_{III}^+] = [I_{III}]\exp\left[\frac{(E_D - E_F)}{k_B T}\right] \tag{6.19}$$

where E_D is the interstitial donor energy level. Any change in the equilibrium number of the charged defects V_{III} and I_{III} will, therefore, result in a change of the position of the Fermi level.

Assuming that the interdiffusion of Al and Ga only proceeds through vacancies and interstitials, the interdiffusion rate will be dependent on the diffusion rate of these defects and the concentration of the defects. Therefore the total group III interdiffusion rate D_{III} is directly proportional to the group III vacancy diffusion rate $D_{V_{III}}$ and $[V_{III}]$, and the group III interstitial diffusion rate $D_{I_{III}}$ and $[I_{III}]$, i.e.

$$D_{III} \propto D_{V_{III}}[V_{III}] \text{ and } D_{I_{III}}[I_{III}]. \tag{6.20}$$

Combining the factors such as Fermi level and As partial pressure , we obtain:

$$D_{III} = f_1 P_{As_4}^{1/4}\left\{D_{V_{III}} + D_{V_{III}^-}\exp\left[\frac{(E_F - E_A)}{k_B T}\right]\right\} + f_2 P_{As_4}^{-1/4}\left\{D_{I_{III}} + D_{I_{III}^+}\exp\left[\frac{(E_D - E_F)}{k_B T}\right]\right\} \tag{6.21}$$

where f_1 and f_2 are functions which depend on the crystal structure, and $D_{V_{III}^-}$ and $D_{I_{III}^+}$ are the acceptor vacancy diffusion rate and donor interstitial diffusion rate respectively. In summary, at a constant temperature, $[V_{III}^-]$ and $[I_{III}^+]$ depend on the As partial pressure, the Fermi level, and the doping concentration of the material.

6.4 *Diffusion and IID of fluorine and boron in n- and p-type AlGaAs*

The diffusion of fluorine and boron in n- and p-type AlGaAs and their intermixing behaviour in these materials can now be studied. The SIMS depth profiling technique has been employed on fluorine and boron implanted samples, both before and after annealing, to determine the diffusion profiles of the impurities. PL measurements have been carried out to study the bandgap shifts after intermixing.

6.4.1 *Experiment*

Two wafers with different layer structures were grown by MOVPE at Sheffield University. These layers had a similar layer structure to the DQW laser material apart from the DQW region being replaced by a 200 Å SQW. The first wafer, QT592, consisted of a 1 μm GaAs buffer layer, followed by a 1.0 μm $Al_{0.37}Ga_{0.63}As$ lower cladding layer doped with carbon to a concentration of 1.4×10^{17} cm^{-3}. A 200 Å GaAs QW was grown to act as a marker for SIMS analysis and to provide a reference signal for PL measurements. The upper barrier consisted of two regions. The first region, grown directly on top of the GaAs QW, was 0.1 μm of $Al_{0.37}Ga_{0.63}As$ doped with a concentration of 1.4×10^{17} cm^{-3} and above was a layer consisting of 0.9 μm of $Al_{0.37}Ga_{0.63}As$ to a higher carbon concentration of 4.8×10^{17} cm^{-3}. A 0.01 μm GaAs cap was then grown on top of this layer to prevent oxidation the of AlGaAs.

The second wafer, QT595R, was of similar structure to QT592, apart from the upper barrier being doped with $5.6 \times 10^{17} cm^{-3}$ of Si in the 0.9 μm AlGaAs region and the 0.1 μm upper barrier region being left undoped. The undoped layer was placed here to prevent the diffusion of Si into the QW unintentionally disordering the well during annealing. The lower layers were also left undoped for similar reasons. The schematic diagrams of these two material structures are given in Figure 6.2. These structures are also documented in Appendix A5 and A6.

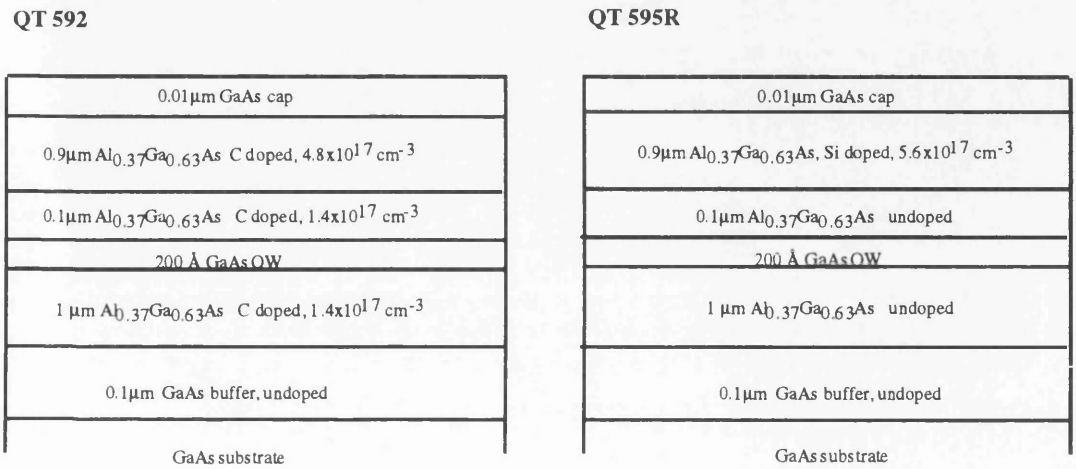

Figure 6.2: The upper AlGaAs of QT 592 was carbon doped and that of QT 595R was doped with Si. The reason for placing the 0.1 μm undoped AlGaAs layer is to stop the diffusion of impurity into the QW.

Implantations of fluorine and boron were then performed at Surrey University. The fluorine implantation energies and doses were 1.53 x 10^{13} cm^{-2} at 80 keV, 3.3 x 10^{13} cm^{-2} at 260 keV and 5.1 x 10^{13} cm^{-2} at 700 keV. These implantation conditions give a constant fluorine impurity concentration of about 5 x 10^{17} cm^{-3} throughout a range of ≈ 1.2 μm deep. The implantation energies and doses for boron were 1.8 x 10^{13} cm^{-2} at 50 keV, 3.3 x 10^{13} cm^{-2} at 170 keV, and 4.9 x 10^{13} cm^{-2} at 400 keV. The implantation profiles for fluorine and boron in QT592 are shown in Figure 6.3a and 6.3b respectively. Three peaks can clearly be identified in both the fluorine and the boron as-implanted profiles indicating that three energies and doses are implanted at different depths. The Al profile is included to show the position of the QW.

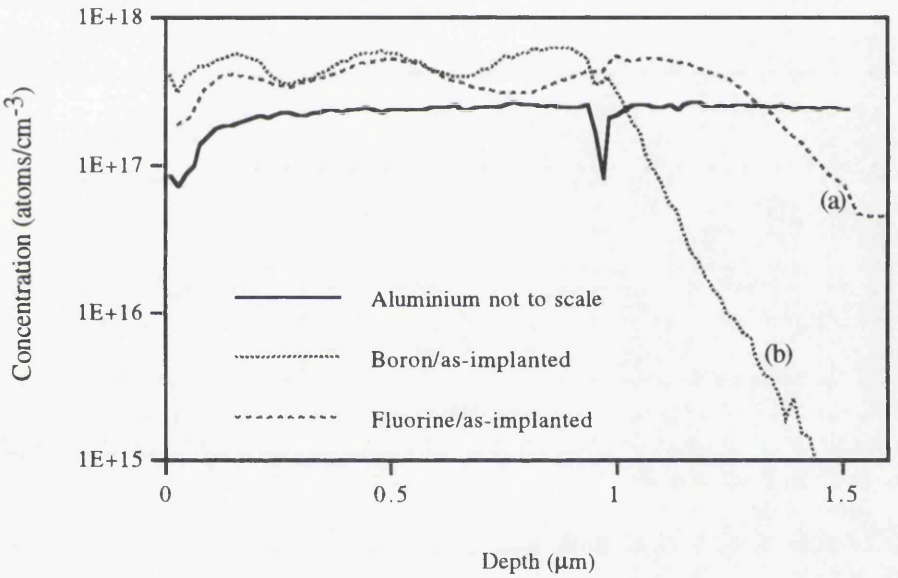

Figure 6.3: The as-implanted profiles for (a) fluorine and (b) boron in QT592R. The Al profile is given to show the position of the QW.

Annealing was performed using a conventional furnace. The annealing temperatures were about 880 ± 10 °C with the annealing time varied between 30 s and 4 hours. During annealing, a GaAs cap was placed on top of the surface to provide an As overpressure and the annealing cap used here was a layer of ≈ 120 nm SrF_2. The SrF_2 cap was removed using HCl before performing the SIMS analysis.

The SIMS analysis was performed at the Loughborough University of Technology. In this study, O_2^+ with an energy of 10 keV was used as a primary ion to bombard the samples for the emission of positive secondary ions from boron, and Cs^+ was used as primary ion to study the emission of negative secondary ions from fluorine atoms.

6.4.2 Diffusion and IID of boron in n- and p-type AlGaAs

In the case of carbon doped p-type samples (QT592), the boron profile has been clearly altered after 1.5 hours of annealing (Figure 6.4), indicating that diffusion of boron has taken place. The three implantation peaks become indistinguishable after 1.5 hours of annealing and the profile becomes completely flat after 3 hours of annealing. The peak concentration of boron was also reduced. Boron diffused both towards the surface and deep into the substrate with a diffusion depth of around 0.5 μm after 3 hours of annealing. The diffusion coefficient of carbon at 950 °C is less than 10^{-16} cm^{-2} s^{-1}.[17,18] Therefore, carbon is expected to show only negligible diffusion under the annealing conditions used in this study and the GaAs QW region is free from carbon after annealing. The QW region shape cannot be deduced from the Al profile, for assessing the degree of disordering, since the SIMS analyses performed here were of relatively low resolution.

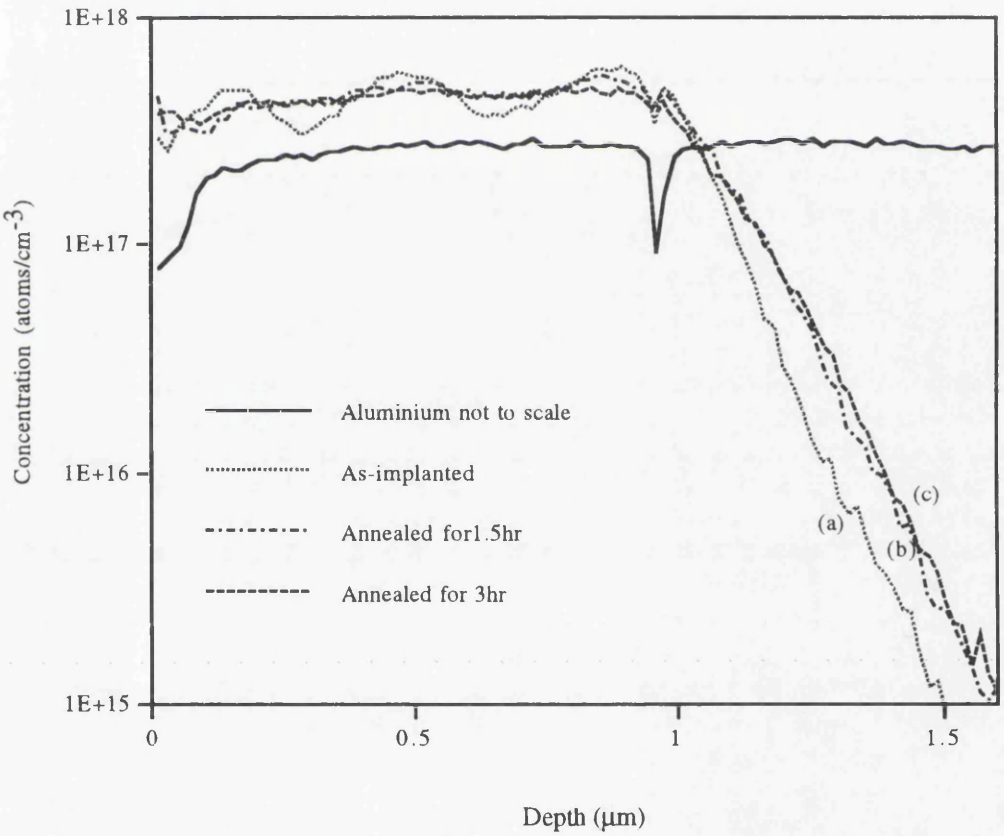

Figure 6.4: Boron profiles in p-type AlGaAs samples for (a) as-implanted, annealed for (b) 1.5 and (c) 3 hours.

In the case of Si doped n-type material (QT595R) however, the diffusion of boron is almost negligible even after 3 hours of annealing (Figure 6.5). The position of three implantation peaks can still be clearly recognised after this annealing time. This observation is consistent with previous results

[17]C.R. Abernathy, S.J. Pearton, R. Canuso, F. Ren, and J. Kovalchik, 'Ultrahigh doping of GaAs by carbon during metalorganic molecular beam epitaxy', Appl. Phys Lett. **55**, 1750 (1990).

[18]B.T. Cunningham, L.J. Guido, J.E. Baker, J.S. Major,Jr., N. Holonyak,Jr., and G.E. Stilman, 'Carbon diffusion in undoped, n-type, and p-type GaAs', Appl. Phys. Lett. **50**, 687 (1987).

obtained from undoped MQW material implanted with boron[8,9]. A similar observation has been made by many other workers[19,20] in boron implanted n-doped GaAs.

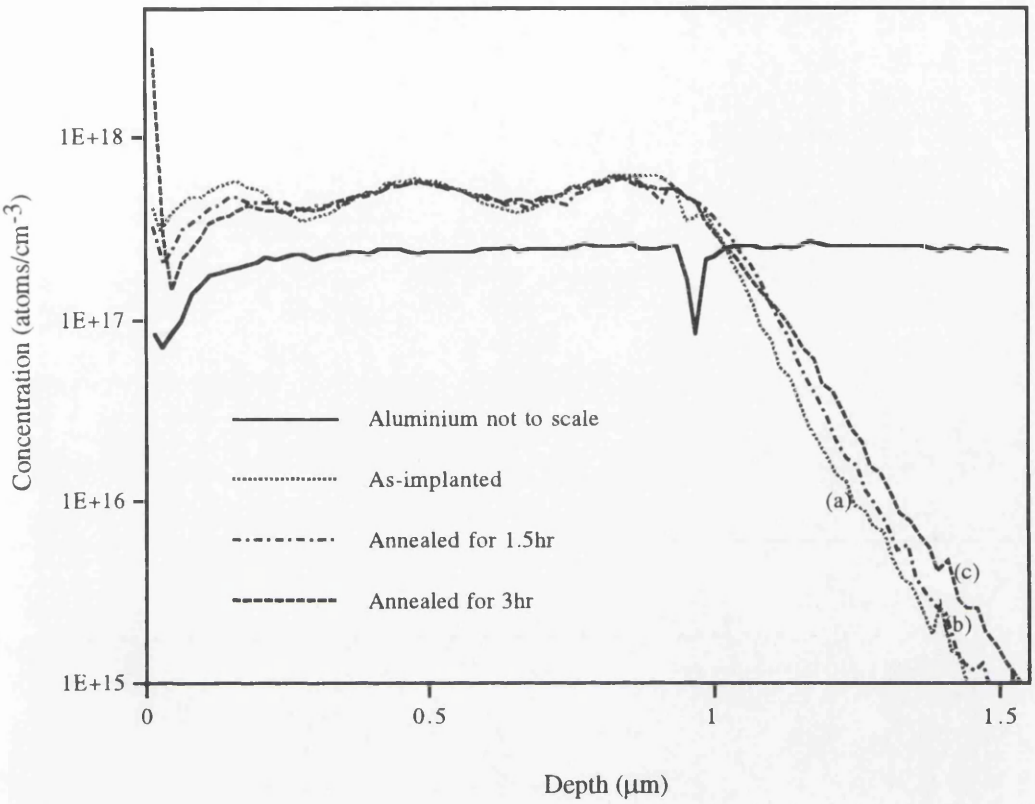

Figure 6.5: Boron profiles in n-type AlGaAs samples for (a) as-implanted, annealed for (b) 1.5 and (c) 3 hours.

The energy shifts of these samples after disordering were assessed using PL measurements at 77 K and the results are given in Figure 6.6. No significant bandgap shifts were obtained from the p-doped sample for up to 4 hours of annealing. The maximum bandgap shift obtained was only about 5 meV, which is completely negligible. In contrast, a maximum bandgap shift of around 50 meV was obtained from material with the upper barrier doped by silicon.

[19]T.J. Magee, K.S. Lee, R. Ormond, R.J. Blattner, and C.A. Evans,Jr., 'Annealing of damage and redistribution of Cr in boron-implanted Si_3N_4-capped GaAs', Appl. Phys. Lett. **37**, 447 (1980).

[20]C.G. Hopkins, V.R. Deline, R.J. Blatnner, C.A. Evans,Jr., and T.J. Magee, 'Incorporation of boron during the growth of GaAs single crystals', Appl. Phys. Lett. **36**, 989 (1980).

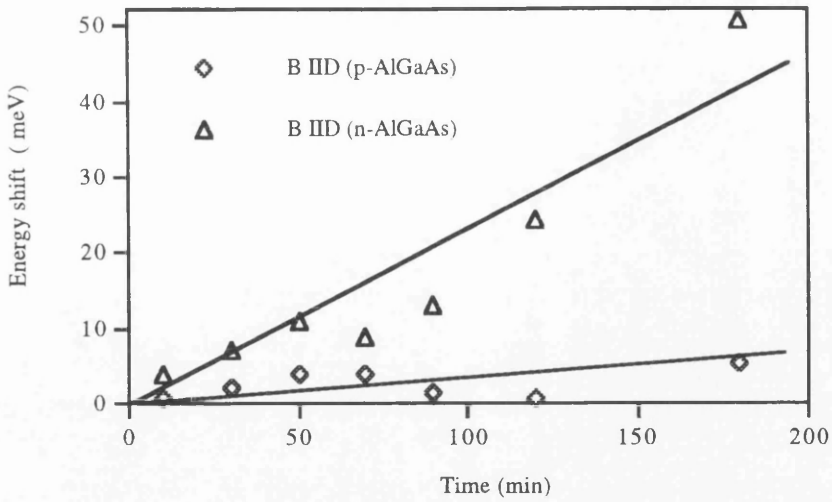

Figure 6.6: The bandgap shifts obtained from boron implanted n- and p-type AlGaAs material with different annealed time.

Boron impurities have been reported to sit both on Ga sites to form isoelectric B_{Ga}, and on As sites to form B_{As} in both n- and p-type GaAs[21,22]. The formation of the deep acceptor B_{As} was also proposed to be responsible for the compensation behaviour of boron in n-doped GaAs[23].

Boron in GaAs/AlGaAs may diffuse from interstitial sites to occupy either As or Ga sites so forming stable B_{As} or B_{Ga}, since a relatively low diffusion rate of boron has been observed. The majority of boron atoms are expected to sit interstitially in the lattice after ion implantation. When thermal energy is supplied during annealing, boron will diffuse and occupy As lattice sites to form B_{As}. Assuming that B_{As} has a singly charge state and requires an As vacancy to form a B_{As}^-, the reaction of this process will be:

$$B_i + V_{As} \Leftrightarrow B_{As}^- + h, \tag{6.22}$$

Expression 6.22 may possibly explain the compensation behaviour of boron in n-doped GaAs, since a hole is created after the formation of each B_{As}^-. Equation 6.22 also implies:

$$\left[B_{As}^-\right] \propto p^{-1}. \tag{6.23}$$

Equation 6.23 suggests that a higher $\left[B_{As}^-\right]$ (but, on the other hand, lower $\left[B_i\right]$) can be found from n-type to p-type material.

---

[21] J. Woodhead, R.C. Newman, I. Grant, D. Rumsby, and R.M. Ware, 'Boron impurity anti-site defects in p-type gallium-rich gallium arsenic', J. Phys. C. **16**, 5523 (1983).

[22] D.W. Fischer, P.W. Yu, 'Infrared absorption and photoluminescence of defect level in the 204 to 255 meV range in p-type GaAs', J. Appl. Phys. **59**, 1952 (1986).

[23] E.V.K. Rao, N. Duhamel, P.N. Favennec, and H. L'Haridon, 'Investigation of compensation in implanted n-GaAs', J. Appl. Phys. **49**, 3898 (1978).

In the study reported here, boron was found to show larger diffusion rate in p-type than in n-type material. This observation suggests that more boron interstitial (B_i) in p-type material than in n-type material, since B_i is a rapidly diffusing species, which is very well agreed with the implication from Equation 6.23. The presence of B_i in p-type material might suppress the concentration of Ga_i and hence give less blue shift, as observed from the p-type samples (Figure 6.6).

The formation of dislocation loops is favoured in boron implanted GaAs (Chapter 7)[24], which can in turn, trap point defects, especially vacancies and interstitials, and so suppress the intermixing[25]. Diffusion of boron in this material is, however, not found to be correlated with intermixing since boron was found to diffuse but the degree of disordering of this material was negligible.

6.4.3 Diffusion and IID of fluorine in n- and p-type AlGaAs material

An extremely fast diffusion rate has been observed in fluorine implanted and annealed QT592 and QT595R (Figure 6.7). This observation is, again, consistent with the previous experimental results obtained from MQW samples [8,9].

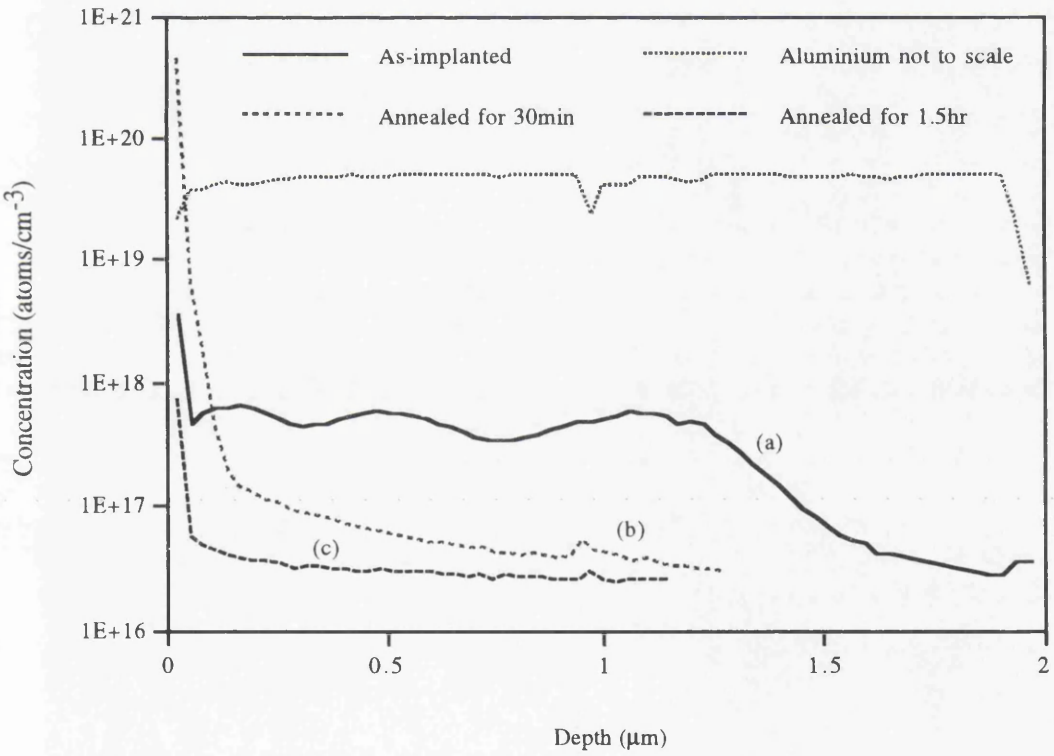

Figure 6.7: The fluorine profiles obtained from (a) as-implanted, annealed for (b) 30 min and (c) 1.5 hours in p-type AlGaAs samples. Similar diffusion profiles have been obtained from the n-type material.

---

[24]B.S. Ooi, A.C. Bryce, J.H. Marsh, J. Martin, 'Transmission electron microscopy study of fluorine and boron implanted and annealed GaAs/AlGaAs', Appl. Phys. Lett. **65**, 58 (1994).

[25]T. Venkatesan, S.A. Schwarz, D.M. Hwang, R. Bhat, M. Koza, H.W. Yoon, P. Mei, Y. Arakawa, and A. Yariv, 'Dose-dependent mixing of AlAs-GaAs superlattices by Si ion implantation', Appl. Phys. Lett. **49**, 701 (1986).

No correlation can be found between the doping type and the diffusion behaviour of fluorine since both p- and n-type AlGaAs materials show similar diffusion profiles after annealing. It is noticed from Figure 6.7 that fluorine diffuses against its concentration gradient towards the surface and although it is believed to occur, there is little sign of diffusion taking place deep into the substrate. A pile-up of fluorine atoms has been observed near the surface region after 30 min of annealing .

The rapid out-diffusion of fluorine is consistent with an interstitial diffusion mechanism as proposed by Gray *et al* for the diffusion of fluorine in GaAs[26]. In this model fluorine atoms diffuse from interstitial to interstitial without occupying lattice sites but sit interstitially in the lattice at equilibrium. However, it is postulated that the diffusion of fluorine could also be taking place in 'random jumps' and in hopping from vacancies to interstitials, since the majority of the fluorine atoms observed here diffuse toward the surface of the semiconductor against the concentration gradient.

The degrees of intermixing were assessed using 77 K PL measurements. The results are given in Figure 6.8.

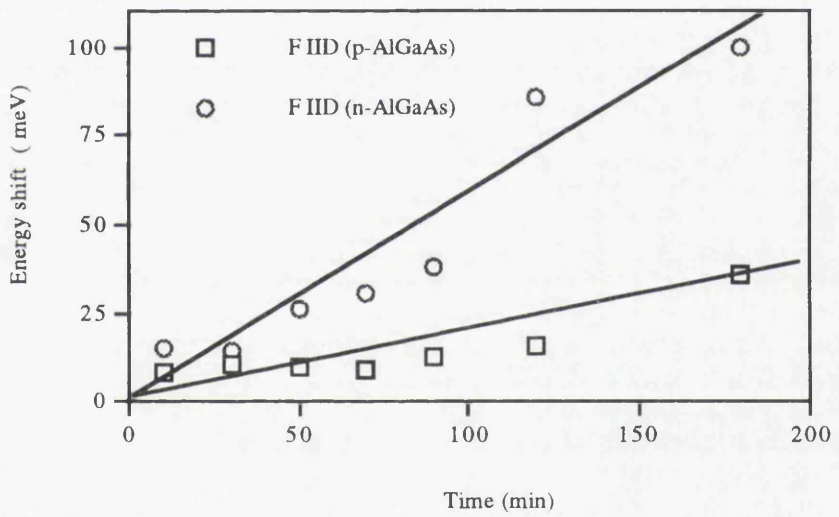

Figure 6.8: Bandgap shifts observed from fluorine implanted n- and p-type AlGaAs samples after annealed at different time.

Although fluorine is neutral at room temperature, it is thought to be ionised, becoming negatively charged at the annealing temperature, therefore promoting intermixing as described by Equation (6.21). The existence of ionised fluorine increases the total electron concentration, and hence supporting more Ga vacancy, in n-type material following $n_{doping} + n_{Fluorine}$., where n_{doping} and $n_{Fluorine}$ are the electron concentration of the dopant and fluorine respectively. In the case of p-type material, however, the total electron concentration in p-type material is very much lower than in n-type, and hence results in a lower intermixing rate.

---

[26]M.L. Gray, J.M. Parsey, Jr., R.E. Ahrens, S.J. Oearton, K.T. Short, L. Sargent, and J.S. Blakemore, 'Characterisation of n-type regions in GaAs formed by silicon fluodine molecular ion implantation', J. Appl. Phys. **66**, 4176 (1989).

6.5 *Summary and conclusion*

Model of IID based on the Fermi effects is discussed.

After annealing, boron is proposed to occupy both As and Ga sites to form the deep acceptor B_{As} and isoelectric B_{Ga} in both n- and p-type materials. Significant diffusion has been observed in the p-type sample and it is proposed that this is due to the diffusion of B_i.. The presence of B_i. is also proposed to suppress the concentration of Ga_i and hence give less blue shift in p-type material.

An extremely fast fluorine diffusion rate has been observed in both p- and n-type material during annealing. The diffusion mechanism of fluorine is proposed to be an interstitial related mechanism, in which fluorine does not occupy lattice sites but only sits interstitially in the lattice. Fluorine is postulated to be ionised and charged negative at the annealing temperature, and therefore promotes intermixing by increasing the total electron concentration (which in turn support more Ga vacancy) in the material. A greater intermixing rate has been observed from the n-type than p-type material since the total electron concentration will be very much higher in n-type than in p-type material following the ionisation of fluorine at the annealing temperature.

Chapter 7 Residual damage in fluorine and boron implanted and annealed GaAs/AlGaAs

7.1 Outline

This Chapter presents the experimental results of the study of fluorine and boron implanted and annealed GaAs/AlGaAs using transmission electron microscopy (TEM). The basic background on image formation using a TEM and the theory of (002) dark field imaging are described. The experimental results of the residual damage caused by boron and fluorine before and after RTA are presented in this Chapter.

7.2 Introduction

Ion implantation and thermal annealing are frequently involved in impurity induced disordering (IID) processes. The defects introduced by ion-implantation are non-equilibrium in nature. Although these defects can be largely removed after annealing, residual damage created during the implantation stage will degrade device efficiency, increase the scattering loss of waveguides and, especially, reduce device reliability.

A short introduction to the use of TEM in characterising III–V semiconductors have been given in Section 2.5.4 of Chapter 2. In the case of QWI, TEM has been widely used to study the intermixing profile and degree of intermixing of the IFVD process[1,2], and the residual damage of IID processes[3]. In this Chapter, a conventional TEM has been used to study the residual damage caused by both boron and fluorine before and after rapid thermal annealing (RTA). Cross sectional specimens from a multilayer GaAs/AlGaAs sample, implanted with fluorine and boron, were prepared and observed using transmission electron microscopy (TEM). A short introduction to the image formation of TEM and the (002) dark field image are also given in this Chapter.

7.3 TEM background

The layout of a TEM and the dark field image formation is discussed in this Section. The diffraction pattern in the (002) orientation is of great interested in analysing GaAs/AlGaAs material since in the (002) dark field orientation, AlGaAs layers appear relatively bright and GaAs appears to be dark. This is because of the large structure factor differences between AlGaAs and GaAs for this reflection angle and the theoretical explanation of this contrast are given in this Section

---

[1]L.J. Guido, N. Holonyak,Jr., K.C. Hsieh, R.W. Kaliski, and W.E. Plano, R.D. Burnham, R.L. Thornton, J.E. Epler, and T.L. Paoli, 'Effects of dielectric encapsulation and As overpressure on Al-Ga interdiffusion in $Al_xGa_{1-x}As$-GaAs quantum-well heterostructures', J. Appl. Phys. **61**, 1372 (1987).

[2]L.J. Guido, J.S. Major,Jr., J.E. Baker, W.E. Plano, N. Holonyak,Jr., K.C. Hsieh, R.D. Burnham, 'Column III vacancy- and impurity-induced layer disordering of $Al_xGa_{1-x}As$-GaAs heterostructures with SiO_2 or Si_3N_4 diffusion source', J. Appl. Phys. **67**, 6813 (1990).

[3]see for example, B.C. De Cooman, S.H. Chen, C.B. Carter, J. Ralston and G.D. Wicks, 'The structure of ion implanted $Al_xGa_{1-x}As$/GaAs seperlattices', Microsc. Semicon. Mater. **76**, 301 (1985).

7.3.1 Basic layout of an TEM

The illumination source of an electron microscope consists of a triode electron gun with a hairpin tungsten filament, a grid, and an anode which accelerates electrons to the required energy. The beam of an electron microscope is almost monochromatic with wavelength λ determined by;

$$\lambda = \frac{h}{(2m_0 eV_r)^{1/2}} \qquad (7.1)$$

where $V_r = V_o\left(1+\frac{eV_o}{2m_oc^2}\right)$ and V_o, m_0, e, h and c, are the electron acceleration voltage, electron mass, electron charge, Planck's constant, and velocity of light respectively. A wavelength as small as 0.037 Å can be obtained using a conventional 100 keV TEM. However, the resolution of a TEM is not comparable with the electron wavelength, but lies in the range 2 to 4 Å. In practice, lens aberrations, electrical and mechanical stabilities, and the thickness of the specimen limit the resolution to a value considerably worse than the electron wavelength.

In general, the electron intensity of a TEM is controlled by the two condenser lenses (Figure 7.1). The specimen is mounted in a special holder which fits into the bore of the objective lens and enables the specimen to be tilted through angles greater than 30 °. Electrons which pass through the thin specimen are brought to a focus in the back focal plane of the objective lens. The objective lens also acts as a converging lens and thus a diffraction pattern can be formed in this plane. An inverting image is formed in the first image plane and the three subsequent lenses in the column, namely the diffraction lens, the projector lenses 1 and 2 are used either to magnify this image or to magnify the diffraction pattern. Thus, if the diffraction lens is focused on the back focal plane of the objective lens a diffraction pattern is magnified and displayed, whereas if the first image plane is imaged by the diffraction lens then a magnified image of the specimen is produced. A schematic ray diagram for the imaging mode is shown in Figure 7.1.

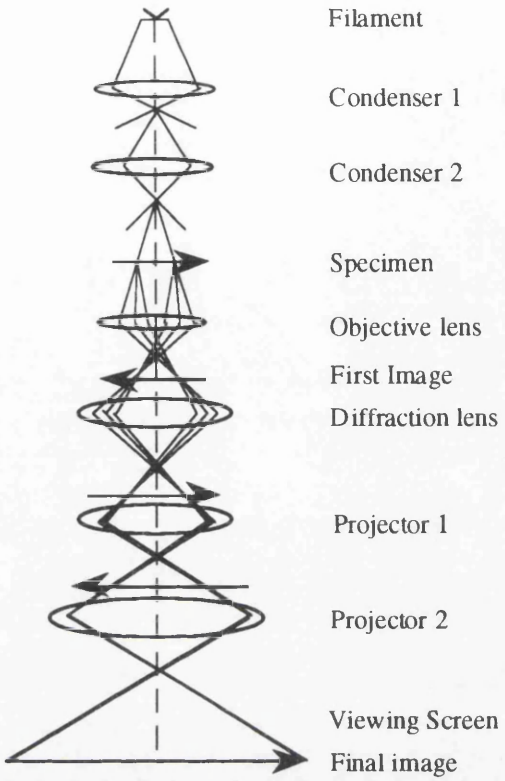

Figure 7.1: Ray diagram for a conventional TEM of the type used in this study.

7.3.2 *(002) Dark field image and contrast analysis*

A parallel beam of electrons incident on the specimen is diffracted through various different angles (θ_B), as shown schematically in Figure 7.2a. This angle (θ_B) is refer to as Bragg angle[4] which is defined as $2d_{hkl}\sin(\theta_B) = n\lambda$. Where d_{hkl} is the lattice spacing between successive (hkl) parallel planes, where h, k and l are the Miller indices and λ is the wavelength of the incident beam of electrons and n is an integral number.

The direct beam transmitted through the crystalline specimen is brought to a focus on the optic axis of the microscope and those which are diffracted through some angle θ_B, are brought to a focus at some position off of the optic axis as shown in Figure 7.2a. In general, only either direct beam or one diffracted beam enter the aperture of the objective lens, and other diffracted beams are blocked by the aperture of the objective lens. The image formed by the direct beam is called the *bright field* image, and image formed by one of the diffracted beams is refereed to as the *dark field* image. In normal practice, rather than placing the aperture off-axis, as would be the case for Figure 7.2a, the incident beam is tilted prior to the specimen in such a way that the required diffracted beam travels down the optical axis, as illustrated in Figure 7.2b.

[4]see for example, C. Kittel, *Introduction to Solid State Physics*, Wiley (1986).

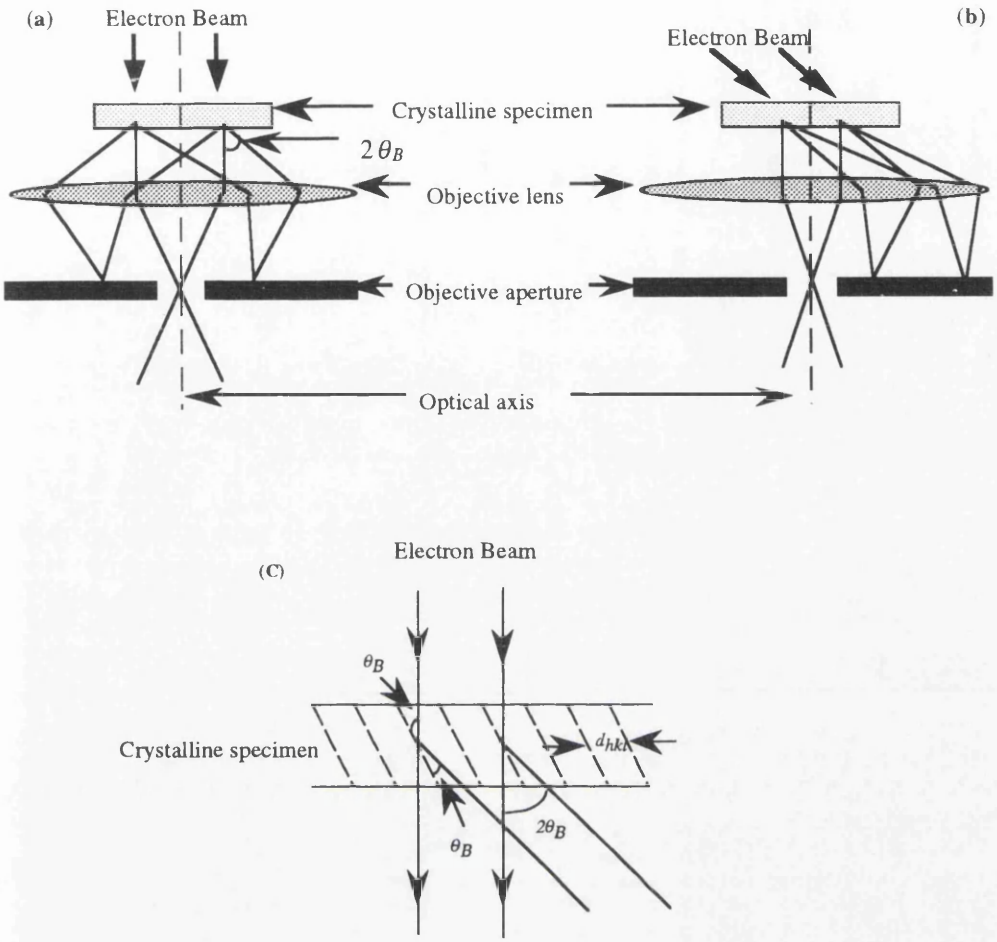

Figure 7.2: Schematic diagram showing the effect of the objective lens and the stop in bringing the diffracted beam to the focus, (a) off-axis and (b) on the optic axis. In both cases the beam is bought to a focus in the diffraction plane. Figure (c) shows the Bragg reflection angle from lattice planes.

GaAs/AlAs has a face centred cubic structure with a basis of two atoms (one Ga/Al and one As) at each lattice point. The diffraction patterns of a high purity GaAs sample grown by molecular beam epitaxy (MBE) is given in Figure 7.3a and each of the spots is indexed in Figure 7.3b. The (002) orientation is to be used as an example in analysing the contrast different between GaAs and AlGaAs since this orientation is widely used to determine the Al composition and to study defect study in the GaAs/AlGaAs system[5,6].

[5]P.M. Petroff, 'Transmission electron microscopy of interfaces in III-V compound semiconductors', J. Vac. Sci. Technol. **14**, 973 (1977).

[6]P.M. Petroff, 'Role of electron microscope in semiconductor electronic defects analysis', Mat. Rec. Soc. Symp. Proc. **46**, 433 (1985).

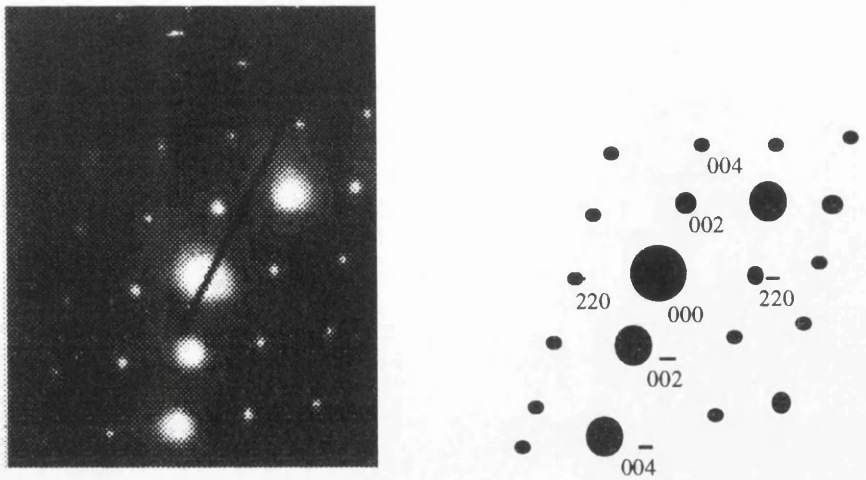

Figure 7.3: (a) The diffraction patterns produced by a high purity GaAs specimen and (b) the spots indexed corresponded to the diffraction patterns.

The intensity of a TEM image is related to the structure factor which is defined as an integer over a single cell. The structure factor $F_{002}(GaAs)$ of a face centred cubic structure with the GaAs unit cell is given by[5];

$$F_{002}(GaAs) = 4(S_{002/Ga} - S_{002/As}) \tag{7.2}$$

Where $S_{002/Ga}$ and $S_{002/As}$ are the scattering factors of Ga and As at the Bragg angle appropriate to (002) planes. Similarly for an AlAs film,

$$F_{002}(AlAs) = 4(S_{002/Al} - S_{002/As}). \tag{7.3}$$

The structure factor for $Al_xGa_{1-x}As$ alloy is obtained by assuming that the atoms occupying the Ga sites in the unit cell are either Ga or Al and have an atomic scattering amplitude $S(\theta) = (1-x)S_{\theta/Ga} + xS_{\theta/Al}$. The structure factor of $Al_xGa_{1-x}As$ at the (002) orientation is given by,

$$F_{002}(Al_xGa_{1-x}As) = 4\left[(1-x)S_{002/Ga} + xS_{002/Al} - S_{002/As}\right] \approx 4x(S_{002/Al} - S_{002/Ga}) \tag{7.4}$$

The diffracted intensity for the (002) dark-field image is directly proportional to the structure factor and is given by

$$I_{002} \propto F_{002}F^*_{002}. \tag{7.5}$$

Where F_{002} and F^*_{002} denote the (002) structure factor and complex conjugate of the (002) structure factor of GaAs respectively.

As the atomic numbers of Ga and As are similar, $S_{002/Ga}$ and $S_{002/As}$ are also similar, and hence $F_{002}(GaAs)$ is very small (Equation 7.2). Therefore a (002) dark field image from a perfect GaAs

crystal is very low in intensity. On the other hand, the intensity of $Al_xGa_{1-x}As$ increases with increasing aluminium composition as predicted by Equation 7.3 and 7.4.

7.4 Residual damage caused by neutral IID using fluorine and boron

7.4.1 Experiment

The material used in this study consisted of 7 layers of GaAs and AlGaAs each 0.1 μm thick, with the topmost layer of GaAs alternating with $Al_{0.26}Ga_{0.74}As$. A thick layer of AlGaAs was placed at a depth between 0.7 μm and 1.2 μm. The bright field TEM micrograph is given in Figure 7.4. The detail of the structures is also documented in Appendix A7. This material was grown by molecular beam epitaxy (MBE), was undoped and was designed so that the layers suffering the heaviest damage could be studied easily.

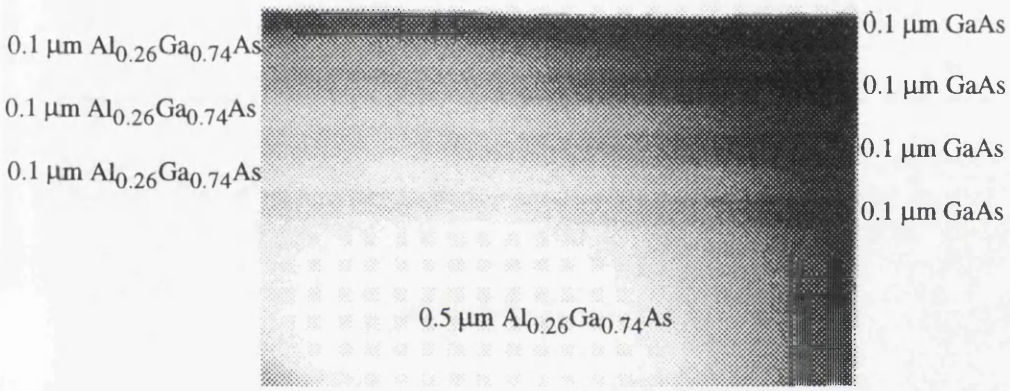

Figure 7.4: The bright field TEM micrograph shows the material structure used in this study.

This material was implanted with fluorine and boron with the implantation energies and doses specified in Chapter 3. This implantation conditions provided a constant impurity concentration of about 5×10^{17} cm^{-3} throughout the 7 layers.

Cross-section specimens from as-grown samples together with specimens from the as-implanted, and implanted and annealed samples were prepared for TEM analysis. Annealing was performed in rapid thermal annealer (RTA) at 925 °C for 30 s with proximity caps, i.e. the samples were placed face down on a piece of GaAs and another piece of GaAs was placed over the back when annealing.

TEM was carried out in a 120 keV JEOL 1200EX microscope. Cross-section specimens were prepared by mechanical polishing, dimple grinding and, finally, ion-milling to electron transparency. Argon was used as the ion species for ion thinning with the conditions of 5 kV, 5 mA and 14° incidence to the specimens. In order to reduce damage due to ion-bombardment induced artefacts, this process was carried out using a liquid nitrogen cooled specimen stage. A detail description of the specimen preparation is given in Appendix C.

The micrographs were recorded using both bright- and dark-field imaging techniques. In the dark-field (002) orientation, AlGaAs layers appear relatively bright and GaAs appears to be dark as described in Section 7.3. The alignment of the (002) dark field image is carried out with the assistance of the Kikuchi pattern[7]. This is done by tilting the specimen until the (002) Kikuchi band (Figure 7.5) is placed on top of the (002) diffraction spot. The intensity of the (002) Kikuchi band is maximised, again by tilting the specimen, after having placed this band on top of the (002) spot to ensure that the incident beam is at the Bragg angle appropriate to the (002) plane.

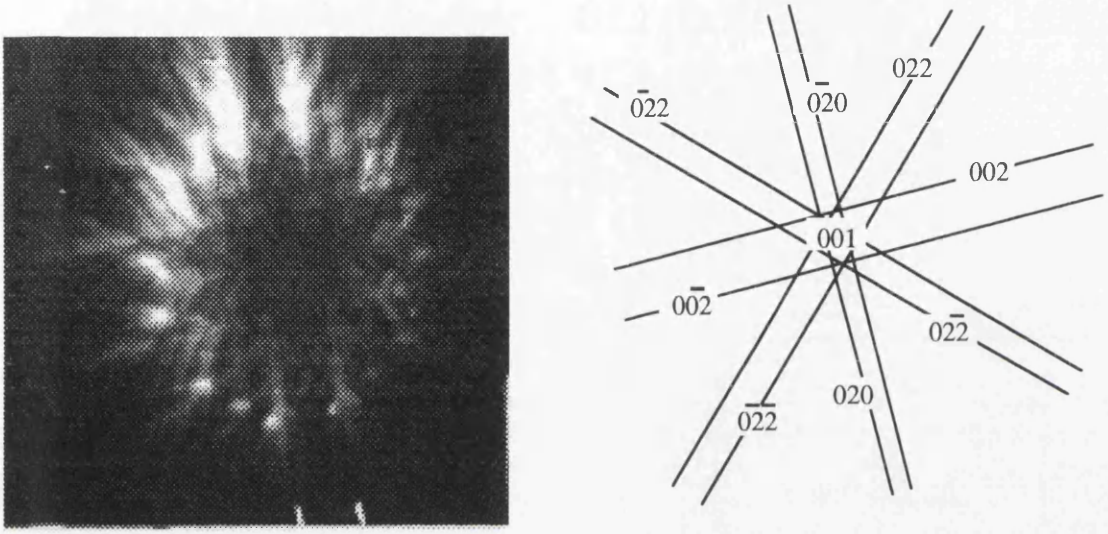

Figure 7.5: (a) Kikuchi bands from the GaAs specimen centred on [001] and (b) the orientation indexed to the bands.

7.4.2 As-grown material

The specimen from the as-grown material appears perfect under the microscope (Figure 7.4a). All GaAs and AlGaAs layers were well resolved, no damage was observed and well defined interfaces between GaAs and AlGaAs were clearly resolved for the as-grown material. The diffraction patterns showed the standard damage-free crystalline patterns of the GaAs/AlGaAs system with similar patterns to that given in Figure 7.3a.

7.4.3 Boron implanted, and implanted and annealed GaAs/AlGaAs

No damage or microstructure was observed throughout the implanted range in the boron as-implanted samples. Even the topmost layer appeared perfect under the microscope. Due to the low dose levels, no amorphous layer was observed. The diffraction patterns from this specimen were identical to the as-grown material indicating a single crystal structure. Point defects, especially vacancies and interstitials, are undoubtedly generated after ion implantation but were below the

[7]M.H. Loretto, R.E. Smallman, 'Defect analysis in electron microscopy', Chapman and Hall, London. (1975).

resolution limit for detection by this type of TEM study. Similar results have been observed by Magee *et al.*[8,9,10] with higher boron implantation doses in bulk GaAs.

Dislocation loops appeared after RTA at 925 °C for 30 s. The size of these dislocation loops varied from a few nm to a few tens of nm. It has been suggested that these defects are formed during annealing by accumulation of lattice damage, introduced by ion implantation[11,12]. These dislocation loops are shown in Figure 7.6 and Figure 7.7 under dark- and bright-field conditions respectively. Interface roughness can be clearly observed in the region 0.4 μm and deeper below the surface under the (004) condition (Fig. 7.6b.). Similar observations have been previously related to trapped impurities at the interfaces[13].

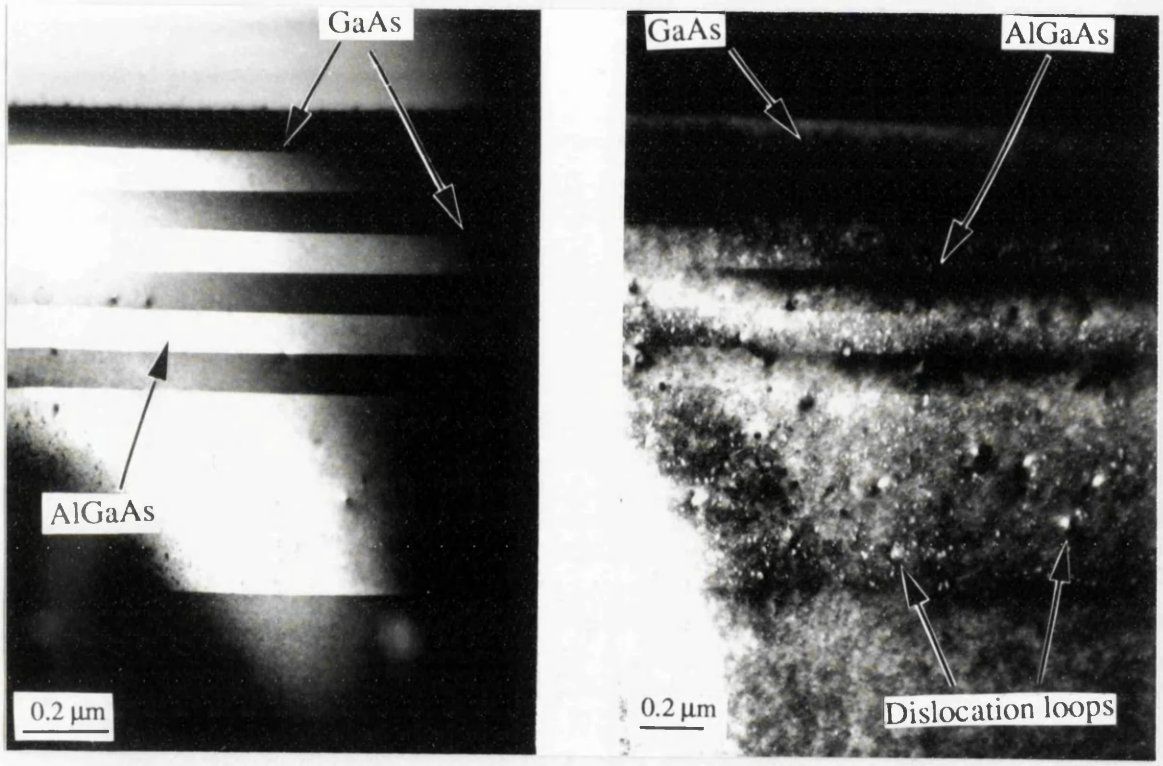

(a) (b)

Figure 7.6: Dark field images of B-implanted GaAs/AlGaAs sample rapid thermal annealed at 925 °C for 30 s in (a) the (002) orientation and (b) in the (004) orientation.

---

[8]T.J. Magee, K.S. Lee, R. Ormond, C.A. Evans,Jr., R.J. Blattner, and C. Hopkins, 'Low-temperature redistribution of Cr in boron-implanted GaAs in the absence of encapsulatant stress', Appl. Phys. Lett. **37**, 635 (1980).

[9]T.J. Magee, H. Kawayoshi, R.D. Ormond, L.A. Christel, J.F. Gibbsons, C.G. Hopkins, C.A. Evans,Jr., D.S. Day, 'Stoichiometric disturbances in ion implanted GaAs and redistribution of Cr during annealing', Appl. Phys. Lett. **39**, 906 (1981).

[10]T.J. Magee, K.S. Lee, R. Ormond, R.J. Blattner, and C.A. Evans,Jr., 'Annealing of damage and redistribution of Cr in boron-implanted Si_3N_4-capped GaAs', Appl. Phys. Lett. 37, 447 (1980).

[11]S. Chen, S.T. Lee, G. Braunstein, G. Rajeswaran, and P. Fellinger, 'Correlation between defect characteristics and layer intermixing in Si implanted GaAs/AlGaAs superlattices', Mat. Res. Soc. Proc. **147**, 279, 1989

[12]E. Morita, J. Kasahara and S. Kawado, 'Transmission electron microscopic observation of microdefects in Zn+ -implanted GaAs', Jpn. J. Appl. Phys. **24**, 1274 (1985).

[13]P.M. Petroff, R.C. Miller, A.C. Gossard, and W. Wiegmann, 'Impurity trapping, interface structure, and luminescence of GaAs quantum wells grown by molecular beam epitaxy', Appl. Phys. Lett. **44**, 217 (1984).

Two distinct regions were observed in the boron implanted and annealed specimen (Figure 7.7). The first region, within around 0.4 μm of the surface, was damage-free with the interfaces remaining sharp and well-defined. The second region, below a depth of 0.4 μm, contained a dense network of dislocation loops. During RTA, the point defects diffused in random directions in the material and became trapped, hence forming dislocation loops, within this region. Defects which diffused towards the topmost layer will have relaxed and have disappeared at the surface.

The composition in the region of the defects is not known but is expected to be boron rich. Most of the dislocation loops appeared in the GaAs layers and close to the GaAs/AlGaAs interfaces. Boron is believed to be responsible for pinning these dislocation loops. A similar type of damage has been observed by Magee *et al* [8,9] in boron implanted GaAs; they concluded that this type of defect is caused by the diffusion of Cr, introduced during the crystal growth, gathering in the implanted damage region but it appears from our studies that boron can fulfil this role by itself.

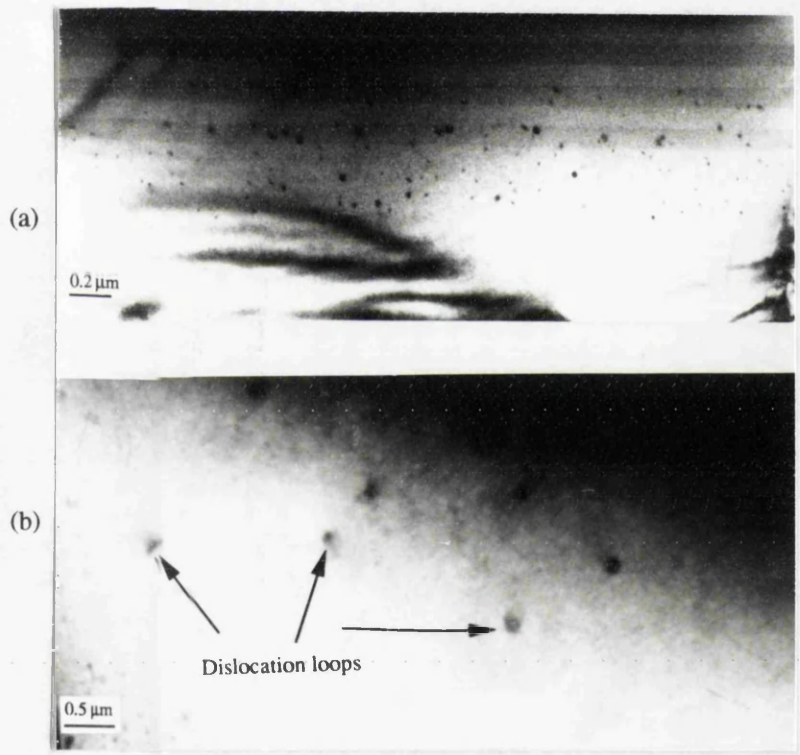

Figure 7.7: (a) Bright field image of B-implanted GaAs/AlGaAs sample. Note that the damage-free region extends to about 0.4 μm from the surface and a dense network of dislocation loops is found below this region. The GaAs layers appear to contain more dislocation loops than AlGaAs layers. (b) shows the dislocation loops which appeared in the thick AlGaAs layer under further magnification.

Comparing the 5th. layer to the 6th. layer (Figure 7.7), we noted that relatively more dislocation loops were found in the GaAs layer than in the AlGaAs layer. This may be due to the small misfit between the AlGaAs and GaAs which gives rise to tetragonal distortion[14] of the multilayer structure. This small misfit (with an order of $\Delta a/a \approx 4 \times 10^{-4}$ at room temperature, where a

[14] J.M. Brown, N. Holonyak Jr., R.W. Kaliski, M.J. Luodwise, W.T. Dietze, C.R. Lewis, 'Effect of layer size on lattice distortion in strained-layer superlattices', Appl. Phys. Lett. **44**, 1158 (1984).

is lattice constant)[13] favours the formation of point defect clusters and hence the formation of dislocation loops in the GaAs layers. Results from infrared reflection spectra have shown that the bond strength in AlGaAs is greater than that in GaAs[15]. This may also favour the formation of point defect clusters in the GaAs layers.

7.4.4 Fluorine implanted, and implanted and annealed GaAs/AlGaAs

As in the case of the boron as-implanted material, no damage could be resolved by TEM for the fluorine as-implanted material. After RTA, only a small number of dislocation loops appeared within a depth of 0.5 μm (Figure 7.8a). Figure 7.8b shows the damage which appeared for the (004) reflection in about the same region as Figure 7.8a (under (002) reflection). These defects were about the same size as in the boron implanted material and appeared in higher concentration at the GaAs/AlGaAs interfaces. Even though a few dislocations loops were formed, the interfaces between GaAs/AlGaAs in the damage region (Figure 7.8b) remained sharp and well-defined after RTA. This implies that the material quality is not degraded by fluorine and can be retained after annealing. On grounds of residual damage alone, fluorine therefore seems to be a better candidate than boron for IID since its use results in considerably less damage after RTA. This result also suggests the possibility of using fluorine for integrating active optoelectronic devices.

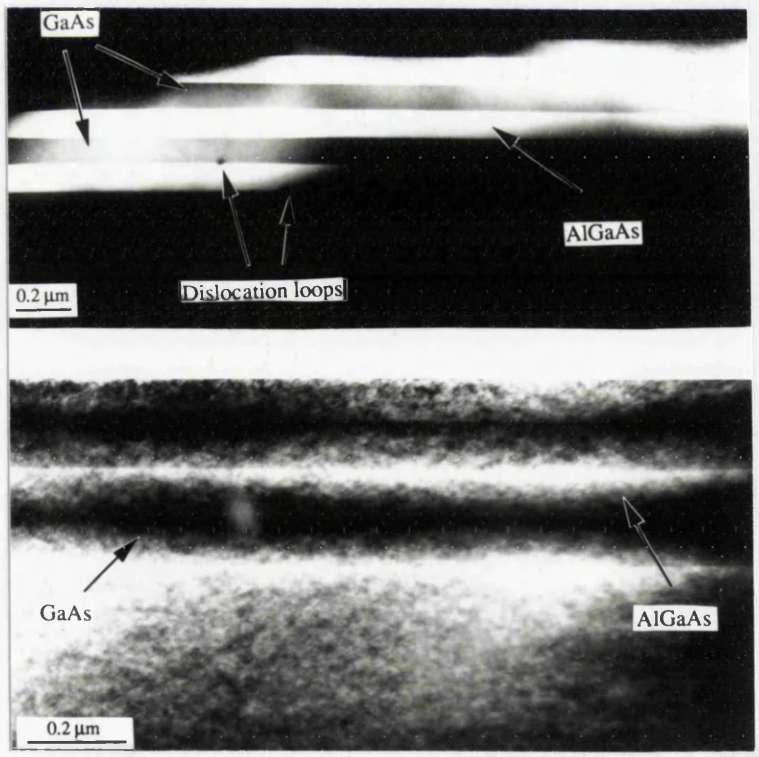

Figure 7.8: (a) Dark field (002) image of F-implanted GaAs/AlGaAs sample after RTA at 925 °C for 30 s. Only a small number of dislocation loops appeared in the region below 0.5 μm. (b) shows the dislocation loops in the dark field (004) orientation from the same sample.

---

[15] M. Ilegems and G.L. Pearson, 'Infrared reflection spectra of $Ga_{1-x}Al_xAs$ mixed crystals', Phys. Rev. B1, 1576 (1970).

The formation of dislocation loops caused by implantation damage or impurity diffusion has no direct relevance to layer intermixing in this experiment. No intermixing behaviour was observed, because the material structure used in this experiment contained neither QWs nor superlattices. However the above results suggest that, by optimising the implantation and RTA conditions, it is possible to produce damage-free devices using the fluorine implantation IID process. The above experiment shows clearly that fluorine is a better species in the IID technique for fabricating optoelectronic integrated circuits (OEIC's) and photonic integrated circuits (PIC's). A Large density of dislocation loops has been found to inhibit the intermixing effect[16], therefore the above observations also provide some of the explanation why samples implanted with boron shows lower degrees of intermixing than fluorine.

7.5 Summary and conclusion

Bright- and dark-field image formation in the TEM has been briefly introduced. The contrast difference between GaAs and AlGaAs under the (002) dark-field has also discussed in this Chapter.

In conclusion, no damage has been observed in either boron or fluorine as-implanted material. The implantation damage which undoubtedly exists, is not resolvable by the TEM technique reported here. After RTA, interstitial dislocation loops were observed in boron implanted material. These defects appeared in a region 0.4 μm or deeper from the top surface. The majority of defects were observed to cluster in GaAs layers and some were formed at the GaAs/AlGaAs interfaces. The boron atoms trapped at the interfaces are proposed to be responsible for these defects.

The fluorine implanted and annealed material showed relatively less damage compared to boron implanted and annealed material. By comparing the residual damage and the diffusion behaviour of these two species, it is clear that fluorine is a better candidate than boron in neutral IID applications. Fluorine has the potential to be utilised in the fabrication of damage-free IID optoelectronic devices if the implantation and RTA conditions are optimised.

---

[16]T. Venkatesan, S.A. Schwarz, D.M. Hwang, R. Bhat, M. Koza, H.W. Yoon, P. Mei, Y. Arakawa and A. Yariv, 'Dose-dependent mixing of AlAs-GaAs superlattices by Si ion implantation', Appl. Phys. Lett. **49**, 701 (1986).

Chapter 8 Loss measurements in fluorine IID rib waveguides

8.1 Outline

This Chapter presents the results of loss measurements performed on fluorine IID rib waveguides. The first part of this Chapter is concerned with the Fabry-Perot loss measurement technique. The fabrication process of the DQW rib waveguides is described and the measurement results are presented. Losses obtained from measurements and simulations are compared in the last Section of this Chapter.

8.2 Introduction

Semiconductor waveguides are the 'wires' used to route optical signals from component to component in OEICs and PICs. Therefore, low-loss waveguides are required to ensure high efficiency operation of the circuit and to allow the circuit to be operated at reasonable injected current levels.

In general, there are three important mechanisms responsible for losses in a rib waveguide. These mechanisms are absorption, scattering and leakage.

In the case of integrated optic devices, lasing action always occurs at a wavelength very close to the band edge, therefore unpumped passive waveguide sections will be highly absorbing. One of the solutions to this problem was to use QWI, because an intermixing process shifts the absorption edge to a higher energy, therefore a low-loss passive waveguide can be formed and operated at the lasing wavelength of the non-disordered active section. Apart from the band edge absorption, absorption can also arise from free carriers, dislocation loops, and even the absorption layer from dry etch damage[1].

Scattering losses in rib waveguides may arise from interface roughness and sidewall roughness. For an epitaxially grown III-V structure, the interface roughness can be reduced to an insignificant level. Losses as low as 0.1 dB cm^{-1} (at a wavelength of 830 nm) and 0.4 dB cm^{-1} (at a wavelength of 1.3 μm) have been measured in single mode waveguides fabricated in MOVPE and MBE grown double heterostructures[2,3]. However, sidewall roughness, due to both dry and wet etching processes, is still important. It has been suggested that the scattering loss due to sidewall roughness in single mode waveguides increases with the square of the roughness amplitude[4]. A rough etched surface also contributes to a certain degree of scattering loss[5].

---

[1]R.J. Deri, and E. Kapon, 'Low loss III-V semiconductor optical waveguides', IEEE J. Quantum Electron. **27**, 626 (1991), and references within.

[2]M.K. Hibbs-Brenner and C.T. Sullivan, 'Low loss AlGaAs optical rectangular waveguides at 830 nm', Appl. Phys. Lett. **56**, 1529 (1990).

[3]R.J. Deri, E. Kapon, J.P. Harbison, M. Seto, C.P. Yun, and L.T. Florez, 'Low-loss GaAs/AlGaAs waveguide phase modulator using a W-shaped index profile', Appl. Phys. Lett. **53**, 1803 (1988).

[4]P.K. Tien, 'Light waves in thin films and integrated optics', Appl. Opt. **10**, 2395 (1971).

[5]R.J. Deri, R.J. Hawkins, and E. Kapon, 'Rib profile effects on scattering in semiconductor optical waveguides', Appl. Phys. Lett. **53**, 1483 (1988).

When the waveguides are supported on a substrate or capped with a material which has refractive index equal to or greater than the waveguide index, leakage of guided light into the substrate or the cap occurs. This situation exists for the GaAs/AlGaAs material system, in which thick upper and lower AlGaAs cladding layers are required to minimise the leakage loss.

The propagation loss of fluorine IID rib waveguides, partially intermixed using different implantation concentrations and annealing conditions, is investigated in this Chapter. Propagation losses as a function of wavelength, measured using the Fabry-Perot technique are reported. Losses due to the free carrier absorption from the p- and n-doped cladding layers, and the leakage loss into the GaAs cap layer are quantified.

8.3 Fabry-Perot Loss measurements

The Fabry-Perot loss measurement technique was developed by Walker[6]. As its name suggests, this technique is based on the Fabry-Perot cavity resonance action of a semiconductor waveguide. This measurement technique is simple, non-destructive and is insensitive to input and output intensities, therefore, an accurate measurement is possible.

Assuming the wave transmitted through the device cavity is coherent and monochromatic, the resonant T_R and antiresonant T_A transmitted intensities, are given by:

$$T_R = I_o\left[\frac{\gamma}{(1-\gamma^2 R)}\right]^2 \tag{8.1}$$

and

$$T_A = I_o\left[\frac{\gamma}{(1+\gamma^2 R)}\right]^2, \tag{8.2}$$

where I_o is the input intensity (and includes terms due to input and output coupling efficiencies), R is the geometric mean of the two power reflection coefficients at the facets and γ is the single-pass amplitude reduction factor. Defining the ratio $k = \frac{T_R}{T_A}$, the propagation loss α can be written as:

$$\alpha = \left(-\frac{10}{L}\right)\log\left[\frac{(\sqrt{k}-1)}{R(\sqrt{k}-1)}\right] \text{ dB cm}^{-1} \tag{8.3}$$

where L is the device cavity length in cm.

---

[6]R.G. Walker, 'Simple and accurate loss measurement technique for semiconductor optical waveguides', Electron. Lett. **21**, 581 (1985).

It can be seen from Equation (8.3) that this loss measurement technique is independent of the input and output intensities, therefore accurate coupling of light into the waveguide is not crucial and a high accuracy of measurement can be achieved .

The experimental set-up of the Fabry-Perot measurement used is given in Figure 8.1.

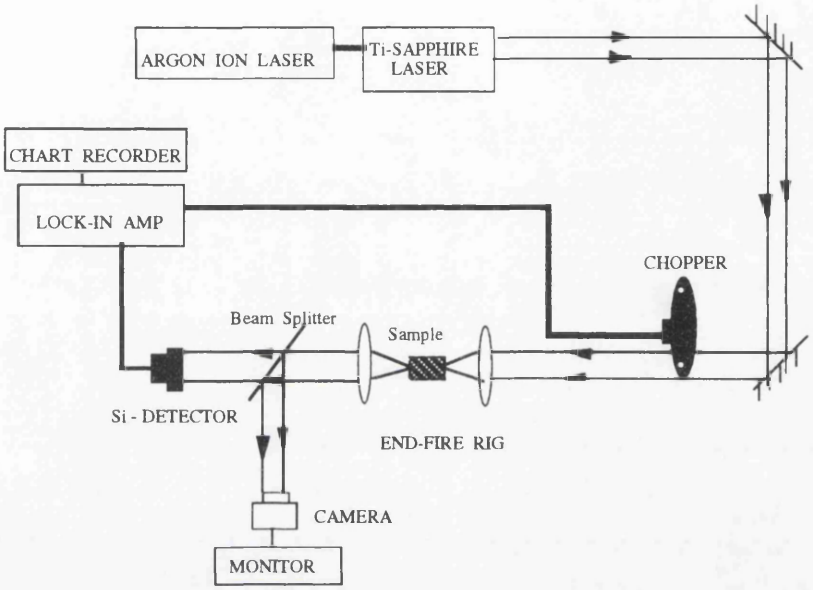

Figure 8.1: The set-up of the Fabry-Perot loss measurement technique used in this experiment.

In brief, an argon-ion laser is used to pump the Ti-sapphire laser which is tuneable over the wavelength range 700-1000 nm using a micrometer adjusted birefringent filter in conjunction with an interchangeable set of mirrors. An etalon is installed in the cavity of the Ti-Sapphire laser to ensure narrow linewidth operation (60 MHz). The laser light is aligned such that it passes through the centre of the objective lens in the end-fire rig. The camera and monitor are used to assist in the alignment of the output facet and to confirm maximum guiding in the waveguides. A reference signal from the chopper and the output signal from the Si-detector are input to the lock-in amplifier. The voltage induced by the light absorbed in the detector is measured by the lock-in amplifier and the results are then plotted by a chart recorder.

This loss measurement technique requires a heat source to warm the waveguides so changing the optical length of the cavity. The heating source used here was a 100 Ω resistor. Heat will change both the length and the refractive index of the waveguides and hence result in the cavity sweeping through its resonances. The value of k can therefore be determined from an average of five or six of the resonance/antiresonances cycles which are recorded on the chart recorder during the heating and cooling stages. Single mode guiding is important in this measurement since multimode guiding will provide resonance fringes which will not be in phase with each other, so resulting in measurement error. An example of such Fabry-Perot fringes obtained from a 6 mm long single mode waveguide are given in Figure 8.2.

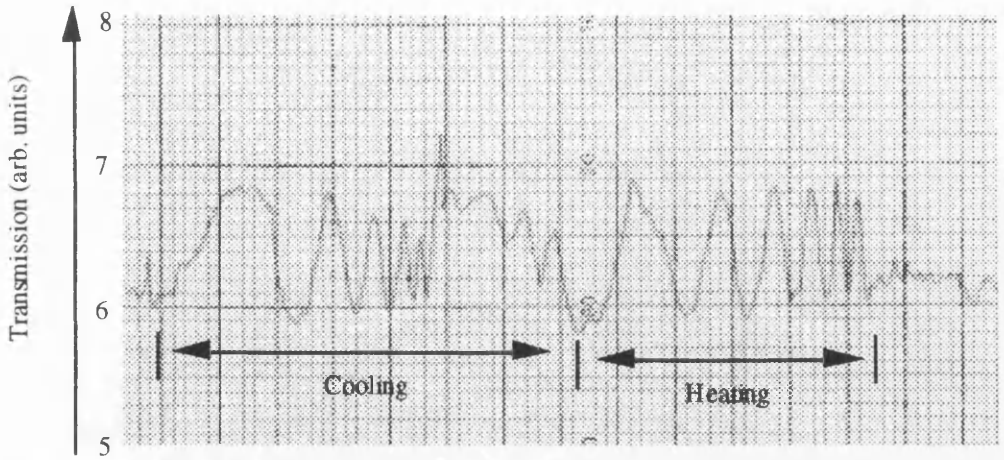

Figure 8.2: The Fabry-Perot fringes taken from a single mode 6 mm long waveguide at wavelength of 880 nm.

8.4 Experiment and waveguides fabrication

The DQW laser material used here was grown by MOVPE at Sheffield University. The DQW section was sandwiched between the 0.9 μm upper cladding and 1.5 μm lower cladding layers. The DQW guiding region consists of two 100 Å GaAs quantum wells separated by a 100 Å $Al_{0.2}Ga_{0.8}As$ barrier. The details of this material structure are given in Figure 8.3 and also documented in Appendix A5.

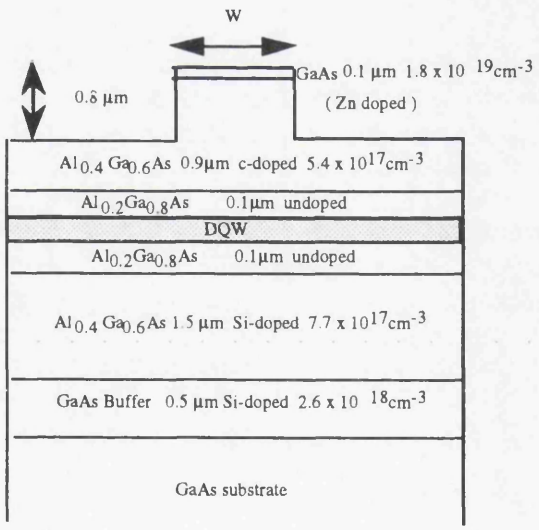

Figure 8.3: The DQW sample and the rib waveguide structure. W is the waveguide width, which varied from 2 to 4 μm in this study.

The fluorine implantation energies and doses were calculated by TRIM[7]. Three implantation energies and doses were used to make up a constant fluorine concentration throughout the DQW region. The implantation energies were 1.0, 1.1, and 1.3 MeV and concentrations of 1×10^{17}, 5×10^{17} and 1×10^{18} cm^{-3} were implanted into three different samples from the same wafer. The range of

[7]J.F. Ziegler, J.P. Biersack, and U. Littmark, *'The Stopping and Range of Ions in Solids'*, (Pergamon, New York, 1985).

implantation is directly proportional to the implantation energy. The sample used here has an upper cladding layer of only 0.9 μm in order to ensure that fluorine can be implanted to the QW position with a reasonable implantation energy without transforming the surface of the sample an amorphous layer. The implantation profiles as predicted by TRIM are given in Figure 8.4 and the implant doses are summarised in Table 8.1.

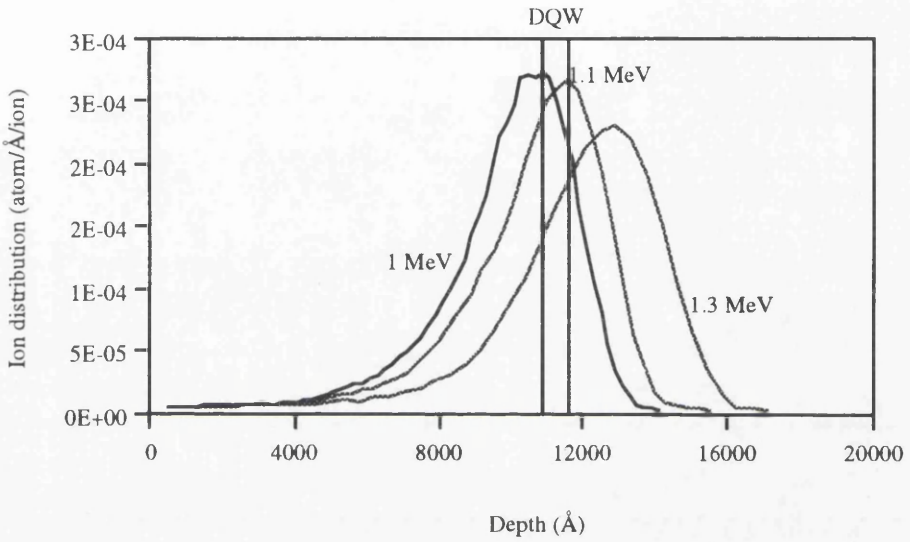

Figure 8.4: The fluorine implantation profiles as predicted by TRIM.

Sample	Concentration (cm^{-3})	Energy (MeV)	Dose (x 10^{13} cm^{-2})
S1	1 x 10^{17}	1	0.33
		1.1	0.36
		1.3	0.40
S2	5 x 10^{17}	1	1.67
		1.1	1.78
		1.3	2.00
S3	1 x 10^{18}	1	3.30
		1.1	3.57
		1.3	4.00

Table 8.1: The conditions of the fluorine implantation.

An RTA was used for the annealing step. The annealing caps used here were layers of SrF_2/SiO_2 (200 nm + 200 nm). For 77 K PL measurements, the annealing time was fixed at 30 s and the temperature was varied from 800 °C to 975 °C. The selected intermixing conditions were then applied to 6 x 8 mm^2 samples prior to rib waveguide fabrication.

The fabrication of the rib waveguides was carried out using standard photolithography and dry etching. A layer of 200 nm of SiO_2 was deposited after intermixing. Waveguides of widths 2, 3, and 4 μm with a spacing of 300 μm were transferred onto the SiO_2 surface using photolithography. After development, the unmasked SiO_2 layer was dry-etched using C_2F_6 plasma (100 W, -450 V, 20 sccm, 15 mTorr) to define the waveguide patterns. The samples were then subsequently etched using $SiCl_4$ plasma (100 W, -350 V, 9 sccm, 10 mTorr) to a depth of 0.8 μm using SiO_2 as an etching mask to form the rib waveguides (Figure 8.3). The SiO_2 layer was removed using buffered HF solution after $SiCl_4$ etching. The waveguides were then cleaved into lengths of 5 or 6 mm and were ready for measurement. For comparison, waveguides were also fabricated from the as-grown sample using similar processes. In this study, single mode waveguiding could be obtained easily from the 2 μm wide waveguide.

8.5 Results and discussion

8.5.1 PL measurements

The as-grown material gives exciton peaks of 806 nm at 77 K and 858 nm at room temperature. This implies that the absorption peak of the as-grown samples is also at 858 nm at room temperature. Figure 8.5 shows the bandgap shifts from samples with different implant concentrations as a function of RTA temperature. The annealing time was kept constant at 30 s.

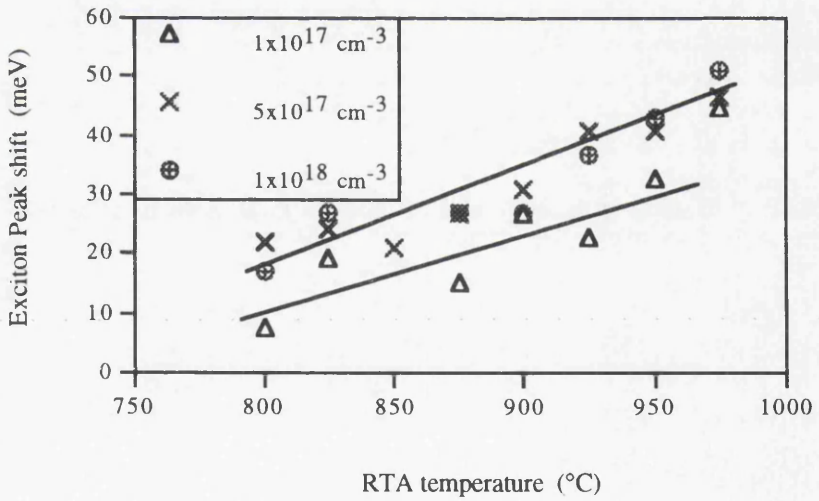

Figure 8.5: The bandgap shift as a function of RTA temperature from samples S1 to S3. The RTA time was fixed at 30 s. The lines from the curve fitting are intended to be a guide line for vision only.

It is noticed that samples implanted with 5 x 10^{17} and 1 x 10^{18} cm^{-3} showed very similar energy shifts. This indicates that the intermixing induced by fluorine may saturate at about a concentration of 5 x 10^{17} cm^{-3}. Sample S1, however, showed shifts half of those seen in S2 and S3.

8.5.2 *Loss measurements*

Fluorine impurities are not expected to contribute to free carrier absorption after IID, since fluorine is neutral in GaAs at room temperature. IID using fluorine will only change the bandgap energy of the QW and reduce the losses due to band edge absorption. Losses, as a function of wavelength in the range 860 to 950 nm, were measured using the Fabry-Perot method explained in Section 8.3.

In general, the plot of the waveguide losses as a function of wavelength can be divided into two regions. The first region showed a dramatic increase in loss towards short wavelengths, and the second region gave a gradually increasing loss towards the longer wavelength region. Taking the as-grown waveguides as an example, the loss increases dramatically below 915 nm in region I (Figure 8.6). The loss comes to a 'floor' of around 13 dB cm^{-1} at about 915 to 930 nm, and then shows a slow increase towards long wavelengths region. The fast increase in loss in region I, the short wavelength region, is dominated by band edge absorption since the guides at these wavelengths are near to the Urbach tail of the band edge. The gradual increase in loss in region II may be due to the combined effects of the free carrier absorption from the p- and n-doped cladding layers and the radiation leakage loss due to the high refractive index and the heavily p-doped GaAs cap of layer. The loss mechanisms in this region will be studied in more detail using simulation in a later section of this Chapter.

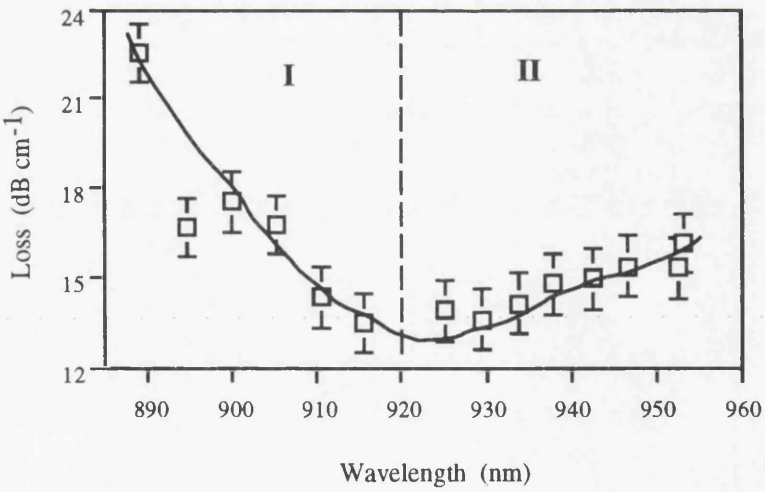

Figure 8.6: The plot of the propagation loss as a function of wavelength for the as-grown waveguides.

The disordered waveguides were to have their losses measured as close to their band edge as possible. All of these plots have a similar form to that observed from the as-grown sample (Figure 8.6). The losses measured in waveguides prepared from samples S1 to S3 are presented in Figure 8.7. For comparison, losses measured from the as-grown samples are also included in each figure.

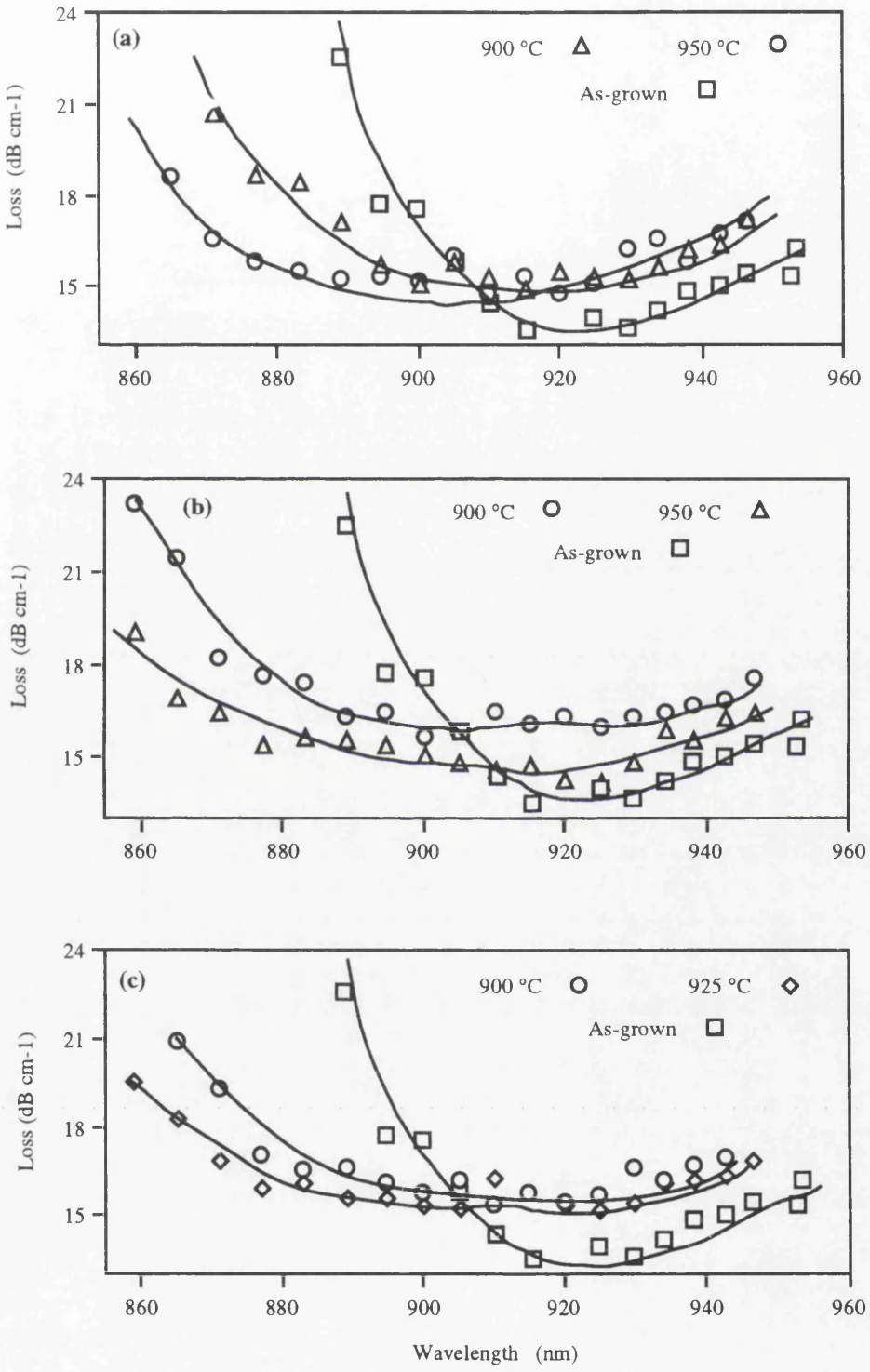

Figure 8.7: The propagation loss as a function of wavelength from waveguides fabricated from fluorine implant concentration of (a) 1 x 10^{17}, (b) 5 x 10^{17}, and (c) 1 x 10^{18} cm^{-3}. RTA temperatures for these waveguides are given inset and the annealing time was fixed at 30 s. For comparison, the waveguides loss curve for the as-grown sample was included in each figure. An error of about ± 0.5 dB cm^{-1} has to be considered in all of these results. The curve fitting is intended as a guide line for vision only.

Consider, first, the wavelength region from 910 nm towards shorter wavelengths. All of the disordered waveguides show a significant decrease in loss, allowing the measurement range to be extended to a wavelength as short as 860 nm for most cases. Since the band gaps have been shifted to higher energies (as given by the PL results in Figure 8.5), wavelengths which are highly absorbed in the as-grown material now have become transparent in the partially intermixed samples. Losses as low as 20 dB cm^{-1} have been observed in most of the partially intermixed waveguides at the undisordered lasing wavelength of 860 nm. In the region 910 nm and below, the losses are dependent on the degree of intermixing. The losses are not, however, seen to have any obvious correlation with the fluorine concentration.

Waveguides fabricated from the MOVPE samples are expected to have a minimal scattering loss due to interface roughness. Samples from fluorine IID with concentrations of 5 x 10^{17} cm^{-3} and below will have similar sharp interfaces (on the scale of the optical wavelength), and only relatively small concentrations of dislocation loops were observed in multilayer GaAs/AlGaAs samples implanted with fluorine (5 x 10^{17} cm^{-3}) and annealed (Chapter 7). This implies that, although QWI taken place, the separate confinement heterostructure (SCH) interfaces will be still smooth. The formation of dislocation loops may be favoured for a higher concentration implantation. However, the bandgap shift (Figure 8.5) and the loss characteristics (Figure 8.6(b) and (c)), of sample S3 show similar behaviour to that of sample S2, which implies that the scattering loss due to dislocation loops of S2 and S3 may also be of a similar degree for these waveguides. The losses contributed by the fabrication process are expected to be constant for all of the waveguides since they were all fabricated in the same manner.

At the long wavelength side of the plots, i.e. 910 nm and above, the as-grown and all implanted samples show a floor with losses of 15 ± 2 dB cm^{-1}. Similarly to the as-grown sample, losses increase gradually with increasing wavelength. The probable causes for this increase have been investigated using Fwave III[8], a program for solving electromagnetic wave propagation in a waveguide using the finite difference method, and the results are discussed in the next Section.

8.6 Simulation of waveguides losses using Fwave III

Fwave III, developed by Michael Taylor at Glasgow University, is a numerical finite difference program for solving the vector electromagnetic wave equations. This software can be used to calculate the effective refractive index, the guiding conditions of different rib heights and the 2D field distribution profiles for both TE and TM modes of a waveguide.

Fwave III is used here to simulate the 2D optical field distribution in a 2 μm wide, 0.8 μm high rib waveguide with the same layer structure as the as-grown samples. Possible absorption from

[8]M.R.S. Taylor, *Fwave-A vector E-M solver*, University of Glasgow, 1993.

the free carriers in the cladding layers and the absorption of the GaAs cap layer are investigated. An example for a 2 μm wide, and 0.8 μm high rib waveguide, as used in this experiment, is given in Figure 8.8.

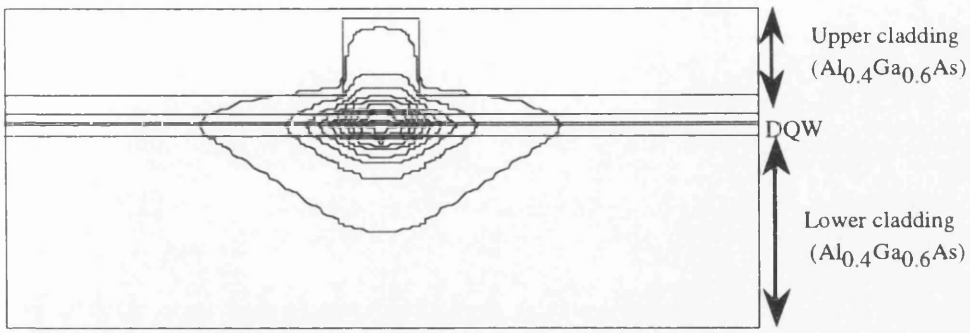

Figure 8.8: The 2D modal of intensity distribution in a 2 μm wide, 0.8 μm high rib waveguide simulated by Fwave III at wavelength of 900 nm. The contours represent 10% steps in the electrical field and the outmost wave is the 1% contour.

Simulations were carried out to study the field distribution in the as-grown sample in the wavelength range 850 to 950 nm. This program does not accept a GaAs cap layer since it has a higher refractive index than the waveguide core. Therefore, a 1.0 μm thick upper cladding layer was used in the simulation instead of 0.9 μm. The analysis of the electrical field interaction in the GaAs cap layer was then taken from the top 0.1 μm region of this layer. The values of the refractive indices of GaAs/AlGaAs at the particular wavelengths and aluminium fractions used in this simulation were taken from Adachi[9]. The program was stopped after about 100 iterations.

Data obtained from the simulation consists of the electrical field distribution in arbitrary units, which is directly proportional to the square root of the power, in both the x and y directions. Suppose that the field distributed in the x direction is E_x and in the y direction is E_y, the total field E_{total} distributed in a waveguide can be found from:

$$E_{total}^2 = E_x^2 + E_y^2 \qquad (8.4)$$

The total intensity I_{total} of the guided light is directly proportional to the integrated square of the field which can be expressed as:

$$\int_{-\infty}^{+\infty} E_{total}^2 dxdy \propto I_{total}. \qquad (8.5)$$

Similarly, the guided intensity in a particular layer can be written as:

[9]S. Adachi, 'GaAs, AlAs, and $Al_xGa_{1-x}As$: material parameters for use in research and device applications', J. Appl. Phys. **58**, R1 (1985).

$$\int_{layer(n)} E^2_{layer(n)} dxdy \propto I_{layer(n)}. \qquad (8.6)$$

The optical overlap with the cladding layers and the leakage loss into the GaAs cap layer are calculated from the interaction of light in the particular layer expressed as a fraction of the total intensity. The loss due to the free carrier absorption in the cladding regions will be:

$$\alpha_{UC} = C_{UC} \frac{I_{UC}}{I_{total}}, \qquad (8.7)$$

and

$$\alpha_{LC} = C_{LC} \frac{I_{LC}}{I_{total}} \qquad (8.8)$$

where α_{UC} and α_{LC} are the losses due to the absorption from the holes and electrons from the upper and lower cladding layers, C_{UC} and C_{LC} are the loss coefficients and I_{UC} and I_{LC} are the intensities overlapping with the upper and lower cladding layers respectively. Data from Fwave III show that the ratio $\frac{I_{UC}}{I_{total}}$ varies from 0.1246 to 0.1433, and $\frac{I_{LC}}{I_{total}}$ varies from 0.1380 to 0.1595 at wavelengths from 850 to 950 nm.

By using a Kramers-Kroenig analysis, Casey *et al* [10] show that free carrier absorption is linear with wavelength in the range between 860 nm and 950 nm. Absorption coefficients of about 15 cm^{-1} for a hole concentration of about 5 x 10^{17} cm^{-3} and less than 10 cm^{-1} for an electron concentration of 5 x 10^{17} cm^{-3} were given in this linear region. These data are, however, in contrast with the classical theory of an electron plasma[11] which predicts that $\alpha_{fc} \propto \lambda^2$, where α_{fc} is the loss due to the free carrier absorption and λ is the wavelength. However, the relation [12]:

$$\alpha_{fc} \approx 7 \times 10^{-18} \times P + 3 \times 10^{-18} \times N \qquad (8.9)$$

where P and N are the densities of holes and electrons respectively in cm^{-3}, was found to fit various experiment data, and is widely used.

In this analysis, we therefore take C_{UC} as 3.78 cm^{-1} and C_{LC} as 2.31 cm^{-1} for p- and n-doped with concentrations of 5.4 x 10^{17} cm^{-3} and 7.7 x 10^{17} cm^{-3} respectively using Equation (8.9), and assume that C_{UC} and C_{LC} are constant throughout the range of wavelength studied. Substituting these values into Equation 8.7 and 8.8 and without taking the band edge absorption into account, α_{UC} and α_{LC} will change from 0.47 to 0.54 cm^{-1} and 0.32 to 0.37 cm^{-1} at wavelengths between 850 and 950 nm. The increase of loss with increasing wavelength is rather small and the loss

[10] H.C. Casey, Jr., D.D Sell, and K.W. Wecht, 'Concentration dependence of the absorption coefficient for n- and p-type GaAs between 1.3 and 1.6 eV', J. Appl. Phys. **46**, 250 (1975).

[11] see for example, C. Kittel, *Interoduction to solid state physics*, 5th edn, Wiley, New York, 1976.

[12] H.C. Casey, Jr., and M.B. Panish, *Heterostructure Lasers, Part A*, Acadamic Press, New York, 1978.

can be considered to be constant within this range of wavelength. Summary results of $\alpha_{cladding}$, where $\alpha_{cladding} = \alpha_{UC} + \alpha_{LC}$, are given in Figure 8.9.

Similarly, the loss due to radiation leakage into the GaAs cap region can be expressed:

$$\alpha_{cap} = C_{GaAs(cap)} \frac{I_{GaAs(cap)}}{I_{total}} \qquad (8.10)$$

where $C_{GaAs(cap)}$ is the loss coefficient of this layer. This coefficient includes the absorption due to heavy hole doping (1.8×10^{19} cm^{-3}) and the radiation leakage resulting from the fact that the GaAs cap has a higher refractive index than that of the core guiding layer. From Equation 8.9, the losses contributed from the heavily p-doped layer are 126 cm^{-1}. The value of $C_{GaAs(cap)}$ will then be 226 cm^{-1} by assuming that the radiation leakage loss into this layer is 100 cm^{-1} (as predicted by Garmire[13]). The ratio of $\frac{I_{GaAs(cap)}}{I_{total}}$ obtained from Fwave III varies from 0.0134 to 0.0242, therefore the loss contributed by α_{cap} will sit in the range 12.73 dB cm^{-1} to 22.94 dB cm^{-1} in the wavelength range 850 nm to 950 nm.

The total losses due to the combined effects of $\alpha_{cladding}$ and α_{cap} in the wavelength range 850 to 950 nm are given in Figure 8.9.

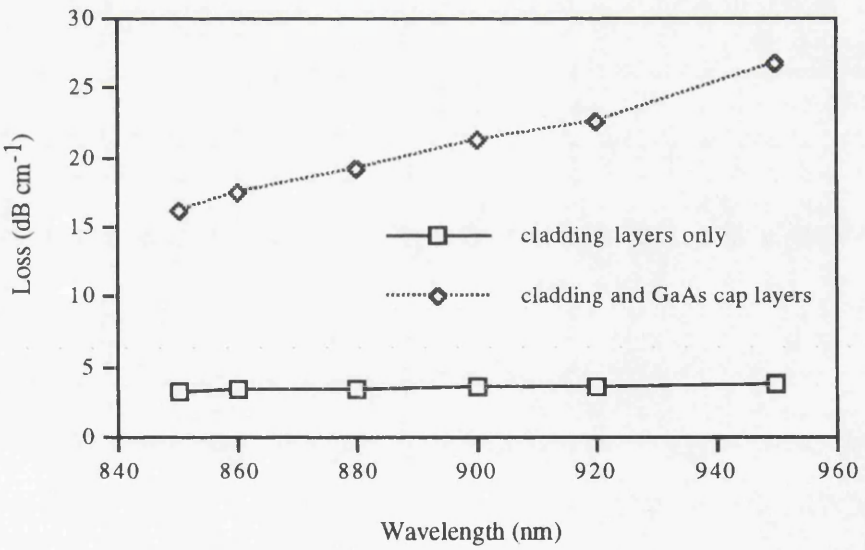

Figure 8.9: The absorption from the free carriers in the cladding layers and from the GaAs cap layer as a function of wavelength as predicted by Fwave III.

We see from Figure 8.9 that the optical field overlapping with the cladding layer and absorbed by free carriers from the p- and n-dopant layers shows only a very small increase with increasing

[13]E. Garmire, 'Optical waveguides in single layers of $Ga_{1-x}Al_xAs$ grown on GaAs substrates', Appl. Phys. Lett. **23**., 403 (1973).

wavelength. However, if the leakage of the light into the cap region is considered, the loss towards the long wavelength region will increase gradually, and has a similar form to the results obtained from the measurements.

8.7 Summary and conclusion

Rib waveguides were fabricated using DQW material treated with different fluorine IID concentration and annealing conditions. The propagation loss of these waveguides was measured using the Fabry-Perot technique. The resulting blue shifts in the band gap of around 30 to 40 meV have been shown to reduce losses at the lasing wavelength dramatically to as low as 20 dB cm^{-1}. At wavelengths near to the absorption edge, the losses were found to be dependent on the degree of intermixing. The optical field spreads and is radiated into the GaAs cap layer for wavelengths away from the absorption edge towards the long wavelength side. The propagation loss is only found to be dependent on the intermixing degree but not on the concentration of the fluorine impurity.

Chapter 9 Spatial control of quantum well intermixing using IFVD technique

9.1 Outline

This Chapter documents the study of spatial control of quantum well intermixing, or selective intermixing in selected areas (SISA), using the IFVD technique. A brief account of the background and the development of this technique are presented. Oxide stripe bandgap tuned lasers were fabricated using this technique and the results are discussed. The applications of this technique in fabricating other devices are presented in the last Section of this Chapter.

9.2 Introduction

A short introduction to the IFVD technique, using SiO_2 caps to induce the creation of group III vacancies and either SrF_2 or Si_3N_4 as an intermixing mask, has been presented in Chapter 6. This technique has been widely used to define area selective intermixing regions on QW material. In this Chapter the spatial control of the degree of intermixing, based on the IFVD technique, is studied.

The out-diffusion of Ga atoms during RTA from GaAs/AlGaAs material into SiO_xN_y has previously been found to increase with increasing oxygen content in the dielectric cap. This implies that the bandgap of a QW structure can be controlled by capping with layers of different chemical composition of SiO_xN_y[1]. The spatial control of the bandgap has also been studied by varying the thickness of the SiO_2 cap layer on the QW material.[2,3] These techniques, however, increase the number of processing steps of lithography and dielectric cap deposition, or increase the number of etching steps needed to control the thickness of SiO_2, which, therefore, makes sample preparation rather complicated. In addition, the reliability of these techniques are still in doubt, since control of the oxygen composition in SiO_xN_y layers is complex and the experimental results obtained using different thicknesses of SiO_2 are not reproducible.

Spatial control of the degree of intermixing has been demonstrated using small patterns of SrF_2 as a bandgap control mask[4]. This technique is known as selective intermixing in selected areas (SISA) in the Department. This technique is achieved by patterning the semiconductor with very small squares of SrF_2 , using electron beam lithography, followed by deposition of SiO_2 over the samples to act as an intermixing source. The degree of intermixing is then found to be dependent on the area of

---

[1] M. Kuzuhara, T. Nozaki, T. Kamejima, 'Characterisation of Ga out-diffusion from GaAs into SiO_xN_y films during thermal annealing', J. Appl. Phys. **66**, 5833 (1989).

[2] M. Ghisoni, R. Murray, A.W. Rivers, M. Pate, G. Hill, K. Woodbridge, G. Parry, 'An optical study of encapsulant thickness-controlled interdiffusion of asymmetric GaAs quantum well material', Semicon. Sci. and Technol. **8**, 1791 (1993).

[3] E.S. Koteles, B. Elman, P. Melman, J.Y. Chi, C.A. Armiento, 'Quantum well shape modification using vacancy generation and rapid thermal annealing', Optical and Quantum Electronics **23**, S779 (1991).

[4] S.G. Ayling, J. Beauvais, and J.H. Marsh, 'Spatial control of quantum well intermixing in GaAs/AlGaAs using a one-step process', Electron. Lett. **28**, 2240 (1992).

sample in direct contact with the SiO_2 layer. This technique is simple, a one-step process and more controllable.

The main objective of the study in this Chapter is to apply the SISA technique in device fabrication. Broad area bandgap tuned oxide stripe lasers have been fabricated on a single chip, using the SISA technique. Five distinguishable lasing wavelengths have been observed from lasers fabricated from five SISA intermixed regions on a single chip. The possible uses of this technique in fabricating other photonic devices are also introduced in the last Section of this Chapter.

9.3 Background

SiO_2 is known to induce out-diffusion of Ga and generate vacancies in the material during the annealing stage. The vacancies generated on the group III sub-lattice promote the diffusion of Al into the QWs and Ga into the barriers. This in turn shifts the bottom of the well upwards in the energy scale and also makes the effective width of the well narrow, although the top of the well is widened. Similar arguments can also be applied to the valence band. Both of these effects cause the energy levels in the well to shift to higher energies.

By patterning small features in a SrF_2 mask under the SiO_2 layer, it is possible to reduce the contact area of the SiO_2 layer with the surface of the material being intermixed, and thus control the amount of Ga out-diffusion into the SiO_2 capping layer. These mask patterns, however, have to be small enough to allow uniform intermixing at the quantum well depth by overlap of the diffusion regions (Figure 9.1). As a result, it is possible to achieve spatial control of the bandgap shift using a single RTA step. Through the use of this technique, it is thus possible to carry out selective intermixing in selected areas (SISA).

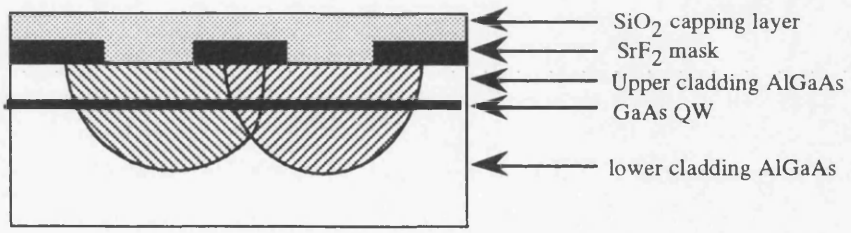

Figure 9.1: Schematic representation of vacancy diffusion in SrF_2 masked QW material. After Ayling *et al.*[4]

The SISA technique was first demonstrated by Ayling *et al*[4] using a SQW wafer in which the fraction of the surface area covered by the SrF_2 masking layer varied from 5 to 15%. The SQW material was grown by molecular beam epitaxy (MBE) and consisted of a 5 nm thick GaAs QW, sandwiched between two AlAs layers, 2 nm in thickness, to provide a high concentration of Al atoms in close proximity to the QW which increased the bandgap change during intermixing. The lower and upper barriers were $Al_{0.4}Ga_{0.6}As$ with the thickness of 20 nm and 1 μm respectively. The topmost layer consisted of a 5 nm GaAs capping layer to prevent oxidation of the material.

The pattern for the SrF_2 capping layer, consisting of an array of submicrometre rectangles, was prepared using electron beam lithography, followed by thermal evaporation of 65 nm of SrF_2 and then lift-off in acetone. A 200 nm SiO_2 capping layer was then sputtered on the surface of the material. The dimensions of the SrF_2 rectangles used for the patterning ranged from 0.49 x 0.28 μm^2 to 0.84 x 0.49 μm^2 . The spacing of these rectangles was the same for all patterns and was 2.1 x 1.3 μm^2. The surface area of the QW material covered by SrF_2 masking layer thus varied from 5 to 15%. Each of these patterns was written in a field of 250 x 350 μm^2 in size using 25 frames 50 x 70 μm^2. After SiO_2 dielectric capping, the samples were annealed in an RTA at 950 °C for 30 s with GaAs proximity caps on the front and back surfaces. PL measurements, at 77 K, were performed to assess the QW luminescence and the degree of intermixing. Homogeneous intermixing was obtained and the bandgap shift as a function of SrF_2 masked area coverage is given in Figure 9.2.

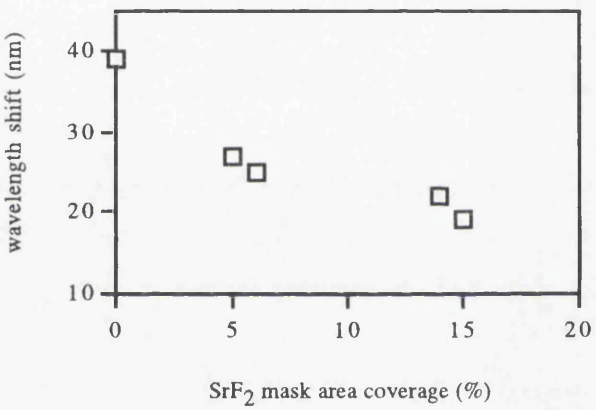

Figure 9.2: The uniform bandgap shift observed using SISA technique in SQW material. These results are after Ayling *et al.*

9.4 SISA technique on DQW material

Before applying this technique to fabricating devices, the reproducibility of the technique was checked using a double quantum well (DQW) sample. The material used here was of a similar structure to that given in Appendix A3 (with an upper cladding layer thickness of 0.9 μm). In this experiment, a wider SrF_2 coverage range was studied than in the experiments of Ayling *et al.* The percentage range was varied between 0 and 50%. Instead of using the rectangular patterns, an array of stripes was used to make the recognition and the organisation of the selected area easier.

9.4.1 Experimental procedures and results discussion

First of all, the sample was cleaved into dimensions 8 x 10 mm^2. Electron beam lithography was used in this experiment since the patterns to be created are only 1 μm wide, which is difficult to obtain using optical lithography. The positive electron beam resist used here was PMMA (poly methacryllate), which is a long polymer carbon chain and is sensitive to electron radiation. A bilayer of PMMA was used to create undercut and to ease the lift-off process. The first layer of PMMA was 8% BDH, from BDH Chemical Ltd, with 85000 molecular weight (mw), dissolved in xylene. The

sample was then baked at 180 °C for 1.5 hours before the second layer of PMMA was coated. The second layer of PMMA was of high mw known as 4% ELV ('Elvacite' from Dupont, with 350000 mw), also dissolved in xylene. A longer bake, more than 2 hours, is required for this layer of PMMA at the same temperature. Both of these layers were spun at 5000 rpm for 60 s. The sample was ready for e-beam exposure after this stage.

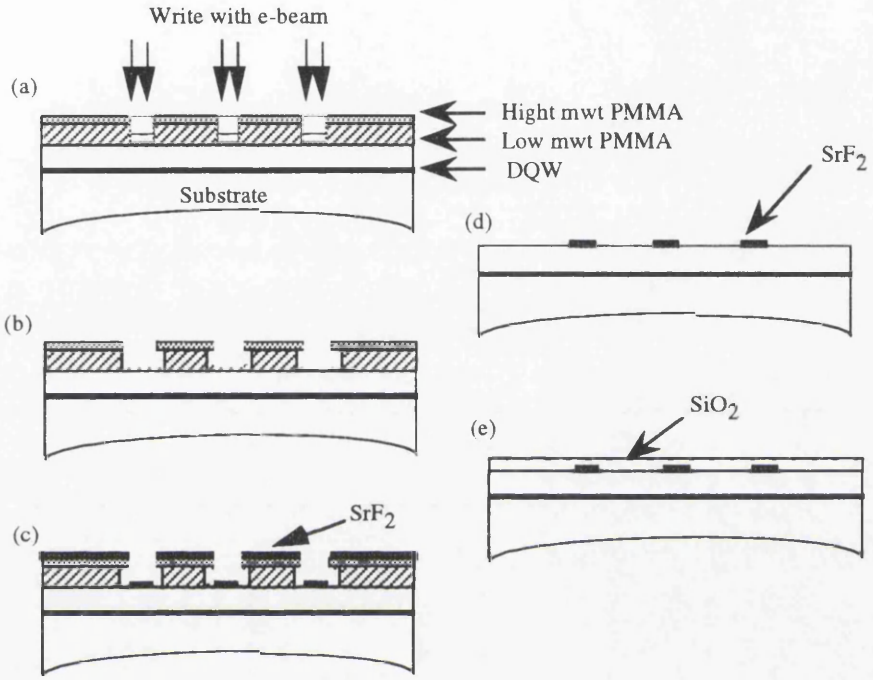

Figure 9.3: Diagrams representing the experimental procedures. (a), (b) Bilayer PMMA was used to create an undercut after development. The deposition of SrF_2 (c) was then performed using a evaporator and lift off in warm acetone (d) to define the stripe patterns. The final step was the deposition of a layer of SiO_2 using PECVD.

The e-beam exposure was performed using a modified Philips PSEM 500 scanning electron microscope. Six fields with a size of 2 x 2 mm^2 each containing 1 μm x 2 mm stripes were created. The coverage area studied here varied between 8 and 50% (8, 12, 38, 25 and 50%), which was achieved by varying the spacing between the 1 μm stripes. A 100% SrF_2 region was also prepared and the 0% reference was taken from the area outside the written fields. The electron beam energy used was 50 keV, exposure dose 380 μC cm^{-2}, resolution 0.1 μm and spot size 160 nm. These optimum conditions were obtained from an exposure test of similar patterns.

The sample was developed using MIBK:IPA (2.5:1) at 23 °C for 30 s, followed by rinse in IPA for 1 min, where MIBK is methylisobutylketone, and IPA is isopropyl alcohol. An evaporator was used for SrF_2 deposition. In order to obtain good lift-off, only about 120 nm of SrF_2 was deposited, since the total thickness of the bilayer resist was around 300 nm. The lift-off process was performed in acetone, in a beaker placed in an warm water bath (45 °C). This process took about 2 to 3 hours to complete. A layer of 200 nm SiO_2 was deposited using PECVD after lift-off. The procedure of sample preparation is schematically represented in Figure 9.3.

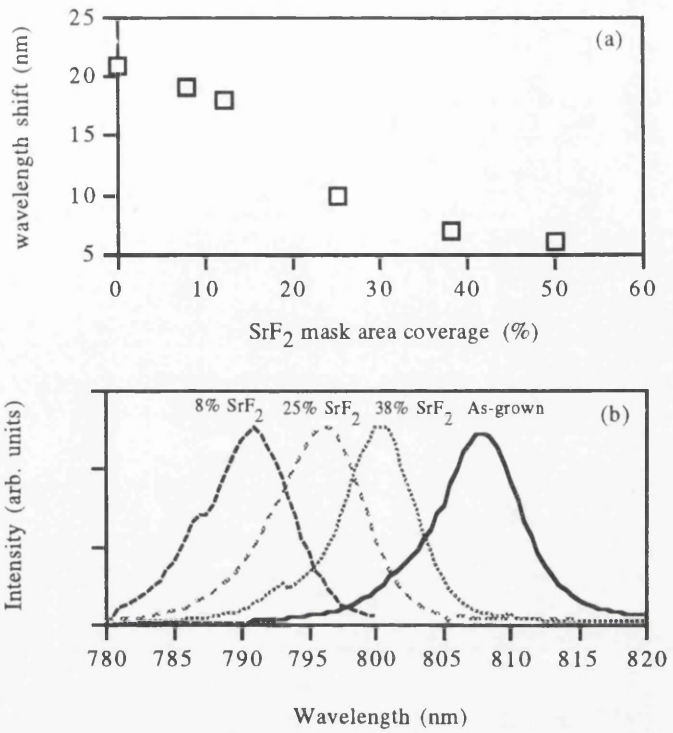

Figure 9.4: (a) Wavelength shift and (b) PL spectra observed from the DQW material disordered using the SISA technique. The PL measurements were performed at 77 K.

Annealing was performed using an RTA at 925 °C for 30 s. Samples were cleaved into pieces according to the size of their field for PL measurements performed at 77 K. The bandgap shifts observed from the peak exciton are given in Figure 9.4a. Intermixing was inhibited in the 100% SrF_2 region (not shown in Figure 9.4a) proving that SrF_2 is a good candidate for suppressing intermixing. Compared to the SQW material, the DQW seemed to exhibit smaller bandgap shifts, which is almost certainty due to the Al concentration in the barrier being higher in the SQW material. In addition, a lower annealing temperature was used in this study in order to obtain a good surface after RTA. Although the bandgap shift is not linear, it is however observed that the degree of bandgap shift was dependent on the area coverage of the SrF_2. The PL spectra of these measurements are given in Figure 9.4b. It is noticed that the PL signals do not exhibit any significant broadening of their FWHM and do not appear to be double peaked. This implies that the intermixing is even and homogeneous. The SISA technique is therefore proven to be a promising and reproducible technique.

9.5 Bandgap tuned lasers fabricated using SISA technique

The fabrication process of bandgap tuned oxide stripe lasers using the SISA technique is documented in this Section. Lasers expected to lase at 5 different wavelengths, intermixed to different degrees, were fabricated on a single chip. The performance of these lasers is also discussed in the last part of this Section.

9.5.1 Fabrication procedures

The material used in the fabrication of the oxide stripe lasers was that of a DQW structure with similar parameters to those documented in Appendix A4. The active region of this material was placed below an upper cladding AlGaAs layer 1.5 μm thick.

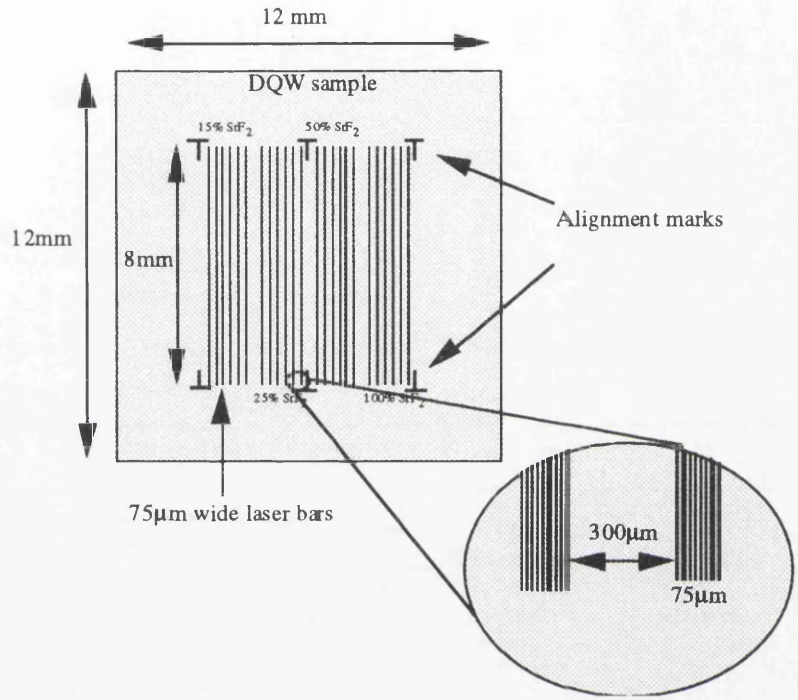

Figure 9.5: The schematic diagram represents the patterns generated by the e-beam lithography on the DQW material for fabricating SISA lasers.

A sample of dimensions 12 x 12 mm^2 was cleaved. A bilayer of PMMA was coated as described in Section 9.4. The 'T' shaped alignment-marks (Figure 9.5) were defined using e-beam lithography and lift-off of 50 nm NiCr. These 'T' shaped alignment marks were formed by 75 μm wide, 100 μm vertical and horizontal bars, which were to be used during the optical lithography process for aligning lasers to the intermixed regions.

The second stage of the electron-beam lithography involved the creation of the 1 μm x 8 mm stripe patterns within the 75 μm wide laser regions. Five different SrF_2 coverage fractions, 0, 15, 25, 50 and 100%, were studied here. Again, these percentages of SrF_2 coverage were achieved by varying the spacing between stripes within the 75 μm x 8 mm bars. The 0% SrF_2 coverage region was taken from the control region outside the stripe patterns. These regions were to be used to fabricate lasers after intermixing. The rest of the intermixing procedures were the same as illustrated in Figure 9.3. After intermixing, the SiO_2 layer was removed using HF solution and the removal of the SrF_2 was performed using concentrated HCl, with the assistance of a cotton bud. PL measurements were performed, at 77 K, randomly over the intermixed regions, and the spectrum is given in Figure 9.6.

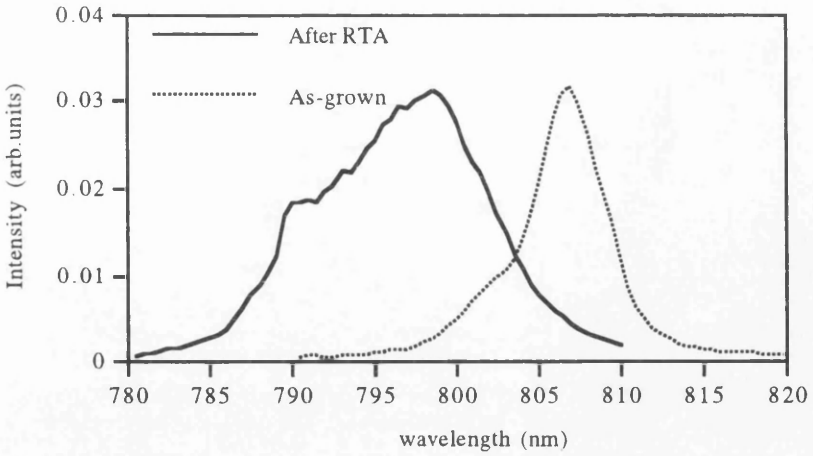

Figure 9.6: Spectrum taken randomly on the intermixed region. A spectrum with broad FWHM was obtained indicating that these regions have been intermixed with different degrees of intermixing.

It can be seen from Figure 9.6 that the spectrum has been broadened and at least two peaks can clearly be identified. The signal peak appearing at the wavelength of 787 nm is believed to be contributed from the SiO_2 region and the 799 nm peak may come from the 50% SrF_2 coverage area. At least three spectra are expected to be superimposed in the intermixed spectrum after comparing the FWHM with the as-grown spectrum. The spectrum taken did not cover the whole SISA region, since the fibre tip for the PL measurement set-up is less than 0.5 mm in diameter.

After the removal of the SrF_2/SiO_2 layers, a new layer of 200 nm SiO_2 was deposited. Oxide stripe bandgap tuned lasers were then fabricated on the sample using the fabrication procedures given in Chapter 5. Lasers were also fabricated from the 100% SiO_2 coverage region on the same sample. For comparison, 75 μm wide oxide stripe lasers were also fabricated on as-grown material. The lasers were then cleaved into different lengths from 300 μm to 900 μm and were ready for measurement.

9.5.2 Results and discussion

The lasers were tested under pulsed current mode at room temperature at around 20 °C. The current pulse width was 400 ns and the repetition rate was 1 kHz (duty cycle 1:2500). The *L–I* curves were measured and the lasing spectra were recorded using a spectrum analyser. An average of about 8 lasers was measured for each of 4 different cavity lengths from 6 sets of lasers intermixed under different coverage percentages of SrF_2.

Lasers with cavity lengths of 500 μm operated at just above threshold were used to assess the lasing wavelength. The summary of the results is tabulated in Table 9.1. Five different lasing wavelengths were observed, as desired, from the five sets of SISA intermixed lasers. The largest shift was observed from lasers fabricated from the 100% SiO_2 region, the rest of the lasing wavelengths depending on the area coverage by the SrF_2. These lasing wavelengths agree with the PL spectrum given in Figure 9.6, since, apart from the sample S2, the lasing wavelengths observed from these lasers

were within the range predicted by the 77 K PL signal. As indicated from the PL signal, the largest bandgap shift of around 20 nm is from the SiO_2 region and the exciton peak appeared at 799 nm is probably from the 50% SrF_2 coverage area. Therefore, the SISA technique was proven to be successfully applied in fabricating devices.

Sample	SrF_2 coverage (%)	Lasing wavelength (nm)	Wavelength shifted (nm)
S1	(As-grown)	863	—
S2	0	840	23
S3	15	844	19
S4	25	848	15
S5	50	855	8
S6	100	861	2

Table 9.1: The summary of the lasing wavelength taken from 500 μm operated at just above threshold. The degree of lasing wavelength shift was found to depend on the area of sample in direct contact with the SiO_2 layer.

The lasing spectra of the lasers are given in Figure 9.7. It can be seen that the lasing spectra are well spread using the coverage percentages of SrF_2 chosen for this study. The lasing spectrum of laser from S6 is not given since it is too close to the lasing spectrum from the as-grown laser. However, the lasing wavelength shift of about 2 nm is negligible and the use of the SrF_2 layer as an intermixing mask was again proven to be effective. Multimoded spectra are observed from these lasers since they are 75 μm wide, are gain-guided and are simple Fabry Perot devices.

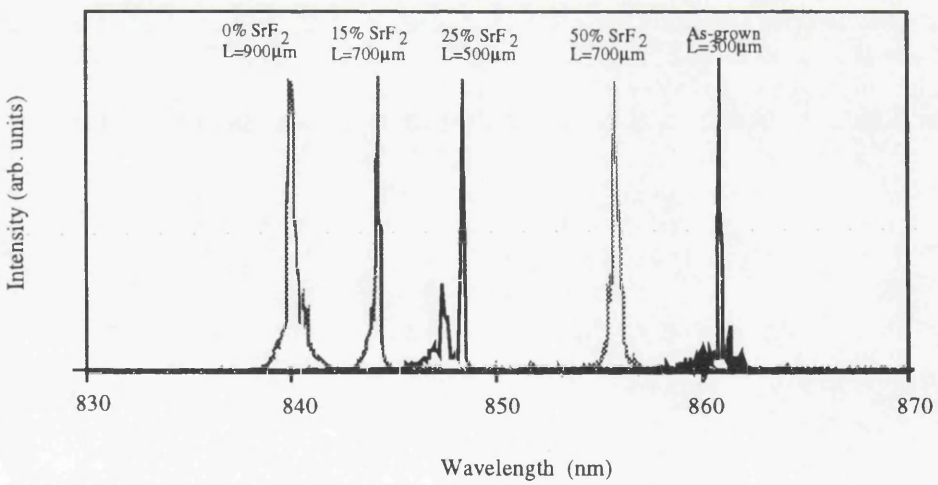

Figure 9.7: The lasing spectra from lasers bandgap-shifted using the SISA technique. L is the cavity length of the lasers.

The *L–I* characteristics were measured and the data were analysed using the method described in Chapter 5 Section 5.3.1. The plot of the natural log of threshold current density versus the inverse of cavity length is given in Figure 9.8.

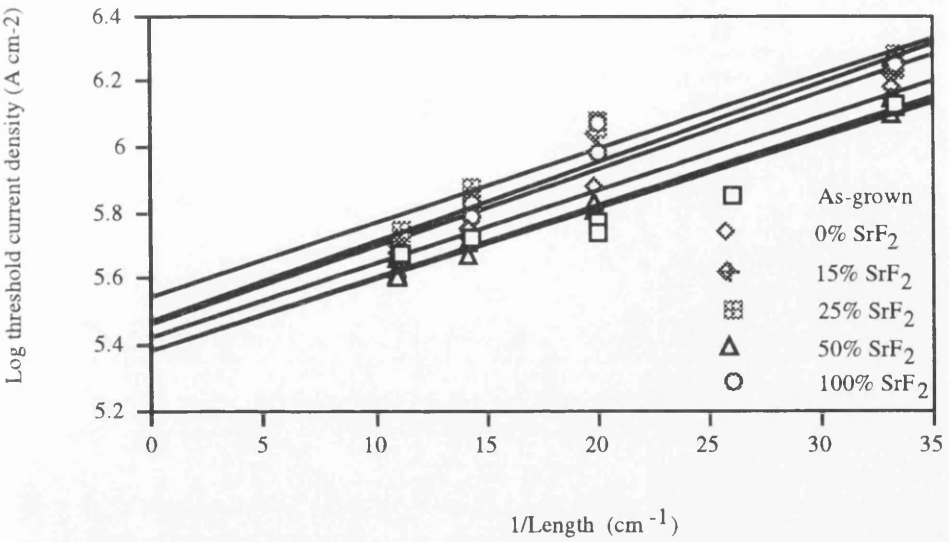

Figure 9.8: The plot of the natural log of the best threshold current devices versus the inverse of the laser cavity length.

The results recorded in Figure 9.8 were taken from those devices which had the best threshold current for a particular cavity length. Straight lines have been fitted to the six sets of data points by the method of least squares. It is noted from Figure 9.8 that, although the threshold current density changes depending on the SrF_2 coverage, the slopes of the fitted lines show only a negligible change, which suggests that the internal gain of these lasers exhibited only a small change.

A summary of the threshold current density for laser of infinite length (J_o), transparency current density (J_t), internal quantum efficiencies (η_i) and the internal propagation loss (α) from sample S1 to S6 is tabulated in Table 9.2. The definitions of the above parameters are given in Chapter 5 Section 5.3. These lasers show only relatively small changes in their J_o and no correlation can be found between the degree of intermixing and J_o. An increment of only 4% was observed from the sample S2. This increment is about 4 times smaller than that observed in lasers intermixed to a similar degree using the plasma intermixing process (Chapter 5). The transparency currents are almost identical for samples intermixed by different degrees, apart from sample S4, which may be due to bad facet quality or measurement error. The above results suggest that the QW gain was still dominated by 2D rather than 3D effects after intermixing as suggested by Li *et al* [5]. The internal quantum efficiencies of the intermixed material are a few percent lower than the as-grown material. However, these changes are small and not significant. We, therefore, conclude that a bandgap shift of around 20 nm is not significant enough to convert the 2D effect of QW to 3D, and the quality of the material remains good after being intermixed using the SISA technique.

[5]E.H. Li, K.S. Chan, 'Laser gain and current density in a disordered AlGaAs/GaAs quantum well', Electron. Lett. **29**, 1233 (1993).

Sample	SrF_2 coverage (%)	J_o (A cm^{-2})	J_t (A cm^{-2})	η_i (%)	α (cm^{-1})
S1	(as-grown)	218	62	71	14.7
S2	0	227	62	68	14.5
S3	15	235	64	68	14.5
S4	25	251	68	66	14.0
S5	50	217	60	64	12.1
S6	100	237	63	65	12.0

Table 9.2: Summary of the threshold current density for laser of infinite length (J_o), transparency current (J_t), internal quantum efficiency (η_i) and the internal propagation loss (α) from samples S1 to S6.

9.6 Possible applications of SISA

One of the straightforward applications of this technique is to fabricate a wavelength division multiplexer (WDM), in which a number of independent wavelengths can be transmitted simultaneously via a single optical fibre. Even though two-wavelength demultiplexers have already been demonstrated using the IFVD technique[6,7] the use of the SISA technique can extend the number of channels that can be demultiplexed to a higher level. The SISA technique can also be used to produced photonic integrated circuits with a number of lasers each operating at different wavelengths, as sources for WDM, since the lasers produced by SISA presented above showed no significant differences in their lasing parameters.

9.7 Summary and conclusion

The SISA technique was demonstrated to be reproducible in DQW material using stripe patterns 1 μm wide. Oxide stripe bandgap tuned lasers have been successfully fabricated on a single chip using this technique. The tuning of the lasing wavelengths was achieved by varying the coverage area of SrF_2 on the surface of the material. These lasers shown no significant change in transparency currents, internal quantum efficiencies and losses of the material, which indicate that the material quality has not been changed after intermixing using the SISA technique.

[6] T. Miyazawa, T. Kagawa, H. Iwamura, O. Mikami and M. Naganuma, 'Two-wavelength demultiplexing p-i-n GaAs/AlGaAs photodetector using partially disordered multiple quantum well structures', Appl. Phys. Lett. **55**, 828 (1989).

[7] A.N.M. Masum Choudhury, P. Melman, A. Silletti, E.S. Koteles, B. Foley and B. Elman, 'Metal-semiconductor-metal demultiplexing waveguide photodetectors in InGaAs/GaAs quantum well structures by selective bandgap tuning', IEEE Photon. Technol. Lett. **3** , 817 (1991).

Chapter 10 Conclusions and future work

10.1 Results summary and conclusion

10.1.1 Reactive ion etching (RIE)

The surface quality of GaAs/AlGaAs samples after overetching of SiO_2 using C_2F_6, and subsequent etching of GaAs/AlGaAs using $SiCl_4$ plasmas was investigated. An understanding of this effect is important since these processes are used in fabricating devices in this project and elsewhere. C_2F_6 was found to etch GaAs layers with a relatively high etch rate (20 nm min^{-1}) at 100 W. This high etch rate is undesired but was found to reduce with reducing rf power. A contamination layer, probably C-F contaminants, was found to deposit on the GaAs surface after C_2F_6 overetch. The thickness of this layer increased with decreasing C_2F_6 rf power. Although these deposits protect the AlGaAs surface from subsequent oxidation, they did increase the induction time of AlGaAs layers during the subsequent etch of these layers using $SiCl_4$. These contaminant layers were also found to result in surface roughness after subsequent etching using $SiCl_4$.

A new RIE damage detection technique using a quantum well intermixing probe was developed. By using this technique, both the RIE damage profile and the propagation depth of the point defects generated by ion bombardment could be probed and profiled. This technique has been applied to some commonly used RIE processes in the Department such as the C_2F_6 and $SiCl_4$ processes. Damage depths of around 650 Å and point defect propagation depths of 4000 Å have been found for the C_2F_6 process, and damage depths of about 100 Å with similar point defect propagation depths were found for the $SiCl_4$ process. A model of RIE damage was developed to explain the behaviour of both high and low etch rate processes based on the experimental results obtained.

A new quantum well intermixing process, called plasma damage induced layer intermixing (PDILI), was developed. An H_2 plasma, created using a high energy ($\approx$ 1 keV) glow discharge system, has been used to create point defects on the surface of semiconductor samples, followed by annealing, using an RTA at 850 °C for 30 s, to diffuse the point defects down into the QW region. Repeated cycles of plasma exposure and annealing were used here to drive-in diffuse the point defects to the 1.3 μm deep QW region, and hence disorder the QWs. A significant degree of intermixing ($\approx$ 30 meV) has been obtained after about 6 cycles of the process.

Oxide stripe bandgap shifted lasers have been fabricated from the material intermixed to different degrees using this technique. *L-I* characteristics have been measured from these lasers and the threshold currents and the slope efficiencies have been analysed. No significant changes in the threshold current density and in the internal quantum efficiency were observed. These results indicate that the materials are still of high quality after intermixing using this technique.

Oxide stripe extended cavity lasers have been fabricated to demonstrate the use of this intermixing technique in a photonic integrated circuit application. The results showed that selective quantum well intermixing helped to reduce the threshold current by a factor of 5. Losses as low as 18 dB cm^{-1} have been measured in a laser with a 500 μm long extended cavity section intermixed using the plasma damage induced layer intermixing process.

10.1.2 Neutral impurity induced disordering

Neutral IID using boron and fluorine is rather well developed in the Department. In this project studies have been extended to understanding the mechanisms of intermixing and the residual damage to the material after intermixing using these two species.

Boron was found to show significant diffusion in p-doped AlGaAs material. In contrast, only a very small amount of diffusion was observed in the n-doped material after annealing. It was, however, found that the degree of intermixing is larger in n-type than in p-type samples. Boron sits on both the Ga and As sites to form isoelectric B_{Ga} and the deep acceptor B_{As} in both n- and p-type materials. The concentration of B_i, a rapid diffusing species, is proposed to be higher in p-type than in n-type material. The presence of B_i is also proposed to suppress the concentration of Ga_i and therefore reduces the interdiffusion rate of Al-Ga in p-type material.

Extremely fast fluorine diffusion rates and a relatively high degree of intermixing have been observed in both p- and n-type AlGaAs material. Due to the fast diffusion behaviour, fluorine in GaAs/AlGaAs was proposed to be diffused through interstitial related mechanisms. Fluorine is postulated to be ionised and charged negative at the annealing temperature, and therefore promotes intermixing by increasing the total electron concentration. A greater intermixing rate has been observed from the n-type than p-type material since the total electron concentration is very much higher in n-type than in p-type material following the ionisation of fluorine at the annealing temperature.

TEM investigations of GaAs/AlGaAs multilayer structures implanted with both fluorine and boron at a concentration of 5 x 10^{17} cm^{-3} have been carried out. Observations made before annealing have shown no visible damage for either implant species. After annealing, dislocation loops were observed at a depth of between 0.4 μm and 0.8 μm in the boron implanted material. The dislocation loop concentration was orders of magnitude lower in the fluorine implanted material.

By comparing the residual damage and the diffusion behaviour of these two species, it is concluded that fluorine is a better candidate than boron in neutral IID applications.

Rib waveguides spatially intermixed using fluorine IID (F-IID) have been fabricated and it was found to be possible to reduce the propagation loss to as low as ≈ 20 dB cm^{-1} at the lasing wavelength.

10.1.3 Impurity free vacancy disordering (IFVD)

A new technique, using the IFVD process, has been developed to control the degree of quantum well intermixing spatially across a wafer. This technique is called selective intermixing in selected areas (SISA). The SISA process is realised by patterning an array of narrow stripes of SrF_2 which act as a bandgap control mask. The degree of intermixing is found to be dependent on the fraction of the area of the sample in direct contact with the SiO_2 so, by varying the spacing between the stripes, the degree of intermixing can be controlled.

The SISA technique was applied to the fabrication of bandgap tuned lasers on a single chip. Five different SrF_2 coverage fractions, 0, 15, 25, 50, and 100%, were realised by varying the spacing between 1 μm stripes within 75 μm x 8 mm bars, which were to form the laser gain regions. These lasers fabricated on a single chip were observed to operate at five well separated wavelengths (861 nm, 855 nm, 848 nm, 844 nm and 840 nm) and the quality of the material was found to be maintained after being intermixed using this technique.

10.2 Comparison of QWI processes

Each of the intermixing techniques studied here has its own advantages and shortcomings, which have to be considered in order to fabricate reliable devices.

F-IID is rather well developed and understood. The optimum conditions of this process have been found and integrated photonic devices such as extended cavity lasers have been demonstrated. F-IID is also proven to be more reliable, more reproducible, to give lower loss, and to cause less residual damage than boron IID. Therefore the use of boron IID can be eliminated.

Potential applications of disordering have resolution requirements which span several orders of magnitude: eg. low-loss passive sections have a resolution requirement ≈ 10 μm, buried heterostructures ≈ 1 μm, gratings ≈ 100 nm; and quantum well wires (QWWs) ≈ 10 nm. Therefore, the spatial resolutions of PDILI, F-IID and IFVD are important for the fabrication of devices containing the above features. From the diffusion profiles studied using SIMS analysis, it is predicted that a spatial resolution of about a few micrometers can be obtained from F-IID. Since diffusion of point defects is involved in these processes, the spatial resolution of IFVD and PDILI processes are expected to be similar or somewhat lower than F-IID. Therefore the fabrication of devices such as low-loss passive waveguides is not a problem for these processes. More detail experiments can be carried out using a TEM to investigate the spatial resolution of these processes.

The high quality of the material after being intermixed with these processes has been shown to be maintained. Active devices, such as band gap tuned lasers, have been fabricated using the IFVD and PDILI processes, and only a very small number of dislocation loops has been observed from the fluorine implanted and annealed samples. F-IID, PDILI and IFVD all have similar losses in DQW

material (19±8.4 dB cm^{-1}, 18.1 dB cm^{-1} and 17 dB cm^{-1} for F-IID, PDILI and IFVD respectively)[1]. It is learned from Chapter 8 that losses contributed by the free carrier absorption can be significant. A lower doping concentration has to be used to ensure a lower free carrier absorption to the material.

The material used in PDILI and F-IID has to be a shallow well sample, in order to enable the point defects or the impurity to reach the QW, and hence disorder the QW. This material structure has been a major draw back for these processes, since a shallow well material will have high radiation leakage loss to the GaAs cap layer (Chapter 8). In the case of IFVD process, however, material with the wells as deep as 1.5 μm was still found useful.

Both IFVD and PDILI are 'in-house' processes, ie the whole process can be carried out within the Department. In contrast, fluorine implantation has to be performed at Surrey University, therefore adding time to the whole process.

The main advantage of PDILI is that it can be carried out at a relatively low annealing temperature, ie 850 °C or potentially lower using an RTA , which is around 100 °C lower than IFVD and F-IID. High temperature annealing destroys the SrF_2 mask and makes the removal of the SrF_2 layer difficult. Therefore, intermixing in the masked areas will be more controllable if a low RTA temperature is used.

In short, the IFVD process still seems to have more advantages than F-IID and PDILI, in terms of low-loss, it can be applied to thick upper cladding material so reducing the leakage loss, it is impurity free and is able to provide spatial control. The PDILI process has yet to be optimised, however, to make it to be more competitive with F-IID.

10.3 Future work

10.3.1 Plasma damage induced layer intermixing (PDILI)

The optimum process conditions for IFVD and F-IID are rather well developed in the Department. However, the optimum conditions for PDILI are still to be found. At present, the main problems encountered are the relatively high etch rate of the GaAs layer and long processes cycles needed to achieve significant degrees of intermixing. Parameters of the plasma exposure process such as the plasma exposure time, H_2 flow rate, pressure and dc bias have to be optimised to ensure a low etch rate of the GaAs layer.

The intermixing degree of PDILI was found to saturate after about 20 nm of wavelength shifts. In addition, this process was found to be QW depth dependent. This implies that a material structure with a relatively thin upper cladding layer, and high Al composition is required. The number

[1] J.H. Marsh, A.C. Bryce, and R.M. De La Rue, 'Recent progress in quantum well intermixing and application to waveguide devices', to be published in Material Scien. Engin. 1994.

of process cycles needed to achieve significant degree of intermixing is expected to be reduced if a shallow well sample is used, and the degrees of intermixing is expected to increase with increasing Al composition.

This technique is ready to be used for the fabrication of devices such as integrated lasers, low-loss passive waveguides and modulators. The spatial resolution of this technique has to be found in order to fabricate more advance devices such as distributed Bragg reflection lasers, and to form gratings for distributed feedback lasers before overgrowth. The study of the spatial resolution can be performed using a TEM.

Mechanisms for both the drive-in diffusion and the intermixing seem to be complex for the PDILI process. These mechanisms need to be fully understood in order to make the process more controllable and reproducible. The use of PDILI in other material systems is promising and should be investigated.

10.3.2 Neutral IID

The study of fluorine IID will be almost completed if the spatial resolution of this process is known.

Among the intermixing processes studied here, only IID using the implantation technique has the potential to provide spatial resolution on a nanometer scale. However, fluorine has a relatively low atomic mass, which will result in large lateral straggle during ion implantation, hence a steep lateral intermixing profile is difficult to obtain. Therefore, other neutral IID species need to be found for the fabrication of low dimensional devices such as buried quantum well wires (QWWs) and quantum dots. One of the potential species is As, since it is neutral, has a relatively high atomic mass, and therefore a low straggle range is expected during ion implantation.

10.3.3 Selective intermixing in selected areas (SISA)

The SISA technique has reached the stage where it can be used in fabricating other more powerful photonic integrated circuits such as wavelength division multiplexers or demultiplexers. A similar technique also has the potential to be applied to InP-based semiconductors for long wavelength devices.

10.4 Summary

This thesis has addressed QWI processes using PDILI, F-IID and IFVD in the GaAs/AlGaAs system. These QWI processes have been shown to effectively shift the QW band gap to a higher energy level. Devices such as low-loss waveguides, bandgap tuned lasers and extended cavity lasers have been demonstrated. These QWI processes look promising for future fabrication of potentially low-cost integrated photonic devices.

References

Chapter 1

[1]S.E. Miller, Bell Syst. Tech. J. **48**, 2059 (1969).

[2]D.G. Deppe and N. Holonyak, Jr., 'Atom diffusion and impurity-induced layer disordering in quantum well III-V semiconductor heterostructures', J. Appl. Phys. **64**, R93 (1988).

[3]see for example, J.H. Marsh, 'Quantum well intermixing', Semicond. Sci. Technol.. **8**, 1136 (1993).

[4]J.H. Marsh, S.R. Andrew, S.G. Ayling, J. Beauvais, S.A. Bradshaw, A.C. Bryce, S.I. Hansen, R.M. De La Rue and R.W. Glew, 'Neutral impurity disordering of III-V quantum well structures for optoelectronic integration', Mat. Res. Soc. Symp.Proc. **240**, 679 (1992).

[5]J.H. Marsh, S.I. Hansen, A.C. Bryce, R.M. De La Rue, 'Applications of neutral impurity disordering in fabricating low-loss optical waveguides and integrated waveguide devices', Optical and Quantum Electronics **23** , S941 (1991).

[6]M.W. Austine, 'GaAs/GaAlAs curved rib waveguides', J. of Quantum Electronics QE**18**, 795 (1982).

[7]S.J. Pearton, M.J. Valise, K.S. Jones, K.T. Short, E. Lane, T.R. Fullowan, A.E. Von Neida, N.M. Hagel, 'Reaction ion etching of GaAs with CCl_2F_2:O_2: Etch rates, surface chemistry, and residual damage ', J. Appl. Phys. **65**, 1281 (1989).

[8]K.L. Seaward, N.J. Moll, D.J. Coulma, and W.F. Stickle, 'An analytical study of etch and etch-stop reactions for GaAs on AlGaAs in CCl_2F_2 plasma', J. Appl. Phys. **61**, 2358 (1987).

Chapter 2

[1]B. Chapman, 'Glow discharge process', (Wiley, New York, 1980).

[2]S.M. Sze, 'VLSI Technology', 2nd. edit., (Mcgraw–Hill, New York,1988).

[3]S.K. Muraad, PhD thesis, University of Glasgow, 1994.

[4]CRC Handbook of Chemistry and Physics (Chemical Rubber, Cleveland, Ohio, 1970).

[5]S.C. McNevin, 'Chemical etching of GaAs and InP by chorine: The thermodynamic predicted dependence on Cl_2 pressure and temperature', J.Vac.Sci. Technol. B **4**,1216 (1986).

[6]H.F. Winters, J.W. Coburn, and E. Kay, 'Plasma etching – A pseado-black box approach', J. Appl. Phys. **48**, 4973 (1977).

[7]see for example, S. Salimian, C.Yuen, C. Shih, C. Smith and C.B. Cooper, 'Damage studies of dry etched GaAs recessed gates for field effect transistors', J.Vac. Sci. Technol. B **9**, 114 (1991).

[8]T. Hara, H. Suzuki, and A. Suga, 'Radiation damage of GaAs induced by reactive ion etching', J. Appl. Phys. **62**, 4109 (1987).

[9]R.Cheung, Y.H. Lee, K.Y. Lee, T.P. Smith, and D.P. Kern, S.P. Beaumont and C.D.W. Wilkinson, 'Comparison of damage in the dry etching of GaAs by conventional reactive ion etching and by reactive ion etching with an electron cyclotron resonance generated plasma', J. Vac. Sci. Technol. B **7**, 1462 (1989).

[10]K. Gamo, H. Miyake, Y. Yuba, and S. Nambe, 'Defect study in GaAs bombarded by low-energy focused ion beams', J. Vac. Sci. Technol. B **6**, 2124 (1988).

[11]H.F. Wong, D.L. Green, T.Y. Liu, D.G. Lishan, M. Bellis, E.L. Hu, M. Petroff, P.O. Holtz, and J.L. Merz, 'Investigation of reactive ion etching induced damage in GaAs/AlGaAs quantum well structures', J. Vac. Sci. Technol. B **6**, 19 (1988).

[12]S.W. Pang, G.A. Lincoln, P.W. McClelland, P.D. DeGraff, M. Geiss, and W.J. Piacontini, 'Effects of dry etching on GaAs', J. Vac. Sci. Technol. B **1**, 1334 (1983).

[13]S. Thoms, S.P. Beaumont, C.D.W. Wilkinson, J. Frost, and C.R. Stanley, in Microcircuit Engineering (1986), edited by H. W. Lehman and Ch. Bleicker (North Holland, Amsterdam, 1986), p.249.

[14] S.K. Murad, C.D.W. Wilkinson, P.D. Wang, W. Parkes, C.M. Sotomayar-Torres, and N. Cameron, 'Very low damage etching of GaAs', J. VAc. Sci. Technol. B **11**, 2237 (1993).

[15]R. Cheung, S. Thoms, M. Watt, M.A. Ford, C.M. Sotomayor-Torres, C.D.W. Wilkinson, U.J. Cox, R.A. Cowley, C. Dunscombe, and R.H. Williams, 'Reactive ion etching induced damage in GaAs and $Al_{0.3}Ga_{0.7}As$ using $SiCl_4$', Semicon. Sci. Technol. **7**, 1189 (1992).

[16]M. Rahman, N.P. Jhonson, M.A. Ford, A.R. Long, M.C. Holland and C.D.W. Wilkinson, 'Model for conductance in dry-etching damaged n-GaAs structures', Appl. Phys. Lett. **61**, 2335 (1992).

[17]S.W. Pang, W.D. Goodhue, T.M. Lyszczarz, D.J. Ehrlich, R.B. Goodman, and G.D. Johnson, 'Dry etching induced damage on vertical sidewalls of GaAs channels', J. Vac. Sci. Technol. B **6**, 1916 (1988).

[18]A.C. Papadopoulo, C. Dubon-Chevallier, J.F. Bresse, A.M. Duchenois, and F.Heliot, 'Etching procedures of GaAs : Cathodoluminescence study of the induced damages and of the recovering techniques', J. Vac. Sci. Technol. B **8**, 407 (1990).

[19]see for example, P. Collot, T. Diallo and J. Canteloup, 'Dry-etch monitoring of III-V heterostructures using laser reflectometry and optical emmision spectroscopy ', J. Vac. Sci. Technol. B **9**, 2497 (1991).

[20]see for example, S.E. Hicks, W. Parkes, J.A.H. Wilkinson and C.D.W. Wilkinson, 'Reflectance modelling for In-situ dry etch monitoring of bulk SiO_2 and III-V miltilayer structures', to be appeared in Nov. 1994 issue of J. Vac. Sci. Technol. B.

[21]see for example, T.R. Hayers, P.A. Heimann, V.M. Donnelly, and K.E. Strege, 'Maskless laser interferometric monitoring of InP/InGaAsP heterostructure reactive ion etching', Appl. Phys. Lett. **57**, 2817 (1990).

[22]see for example, R. Muller, '*In-situ* etching depth monitoring for reactive ion etching of InGaAs(P)/InP heterostructure by ellipsometry', Appl. Phys. Lett. **57**, 1020 (1990).

[23]B.S. Ooi, S.E. Hichs, A.C. Bryce, C.D.W. Wilkinson, and J.H. Marsh, 'Study of C_2F_6 overetch induced damage and the effects of overetch on subsequent $SiCl_4$ etch of GaAs/AlGaAs', summited to J. Appl. Phys.

[24]S. Adachi, 'GaAs, AlAs, and $Al_xGa_{1-x}As$: material parameters for use in research and device applications', J. Appl. Phys. **58**, R1 (1985).

[25]see for example, J.H. Marsh, 'Quantum well intermixing', Semicond. Sci. Technol. 8, 1136 (1993).

[26]J.C. Mikkelsen, Jr. and I-W. Wu, 'Severe loss of dopant activity due to CHF_3+CO_2 reactive ion etch damage', Appl. Phys. Lett. **49**, 103 (1986).

[27]S.J. Pearton, U.K. Chakrabarti, and W.S. Hobson, 'Reactive ion etching induced damage in GaAS and AlGaAs using $C2H_6/H_2/Ar$ or CCl_2F_2/O_2 gas mixtures', J. Appl. Phys. **66**, 2061 (1989).

[28]see for example, B.S. Ooi, A.C. Bryce, J.H.Marsh, and J.Martin, 'Transmission electron microscope study of fluorine and boron implanted and annealed GaAs/AlGaAs', Appl. Phys. Lett. **65**, 85 (1994).

[29]see for example, S. Chen, S.T. Lee, G. Rajeswaran and P. Fellinger, 'Correlation between defetc characteristics and layer intermixing in Si implanted GaAs/AlGaAs superlattices', Mat. Res. Soc. Symp. Proc. **147**, 279 (1989).

[30]see for example, P.M. Petroff, 'Role of electron microscopy in semiconductor electronic defects analysis', Mat. Res. Soc. Symp. Proc. **46**, 433 (1985).

[31]see for example, H.L. Tsai, Y.C. Kao, 'Generation and propagation of threading dislocation in GaAs grown on Si', J. Appl. Phys. **67**, 2862 (1990).

[32]P.M. Petroff., ' Transmission electron microscopy of interfaces in III–V compound semiconductors', J. Vac. Sci. Technol. **14**, 973 (1977).

[33]M.A. Ford, Ph D thesis, University of Glasgow, (1992).

[34]S.Pang, paper presented at EPIB, to be appeared in J. Vac. Sci. Technol. B , Nov. 1994.

[35]Y. Hirayama, Y. Suzuki, and H. Okamoto, 'Ion-species dependedce of interdiffusion in ion-implantated GaAs–AlAs superlattices', Jpn. J. Appl. Phys. **24**, 1498 (1985).

[36]C. Kittel, 'Introduction to solid state physics', 6th. edit., (Wiley, New York, 1991).

[37]F. Stern and W.E. Howard, Phys. Rev. **163**, 816 (1967).

Chapter 3

[1]S.J. Pearton, M.J. Valise, K.S. Jones, K.T. Short, E. Lane, T.R. Fullowan, A.E. Von Neida, N.M. Hagel, 'Reactive ion etching of GaAs with CCl_2F_2:O_2: Etch rates, surface chemistry, and residual damage', J. Appl. Phys. **65**, 1281 (1989).

[2]K.L. Seaward, N.J. Moll, D.J. Coulma, and W.F. Stickle, 'An analytical study of etch and etch-stop reactions for GaAs on AlGaAs in CCl2F2 plasma', J. Appl. Phys. **61**, 2358 (1987).

[3]S. Salimian and C.B. Cooper, III, 'Selective dry etching of GaAs over AlGaAs in $SF_6/SiCl_4$ mixtures' J. Vac. Sci. Technol. B **6**, 1641 (1988).

[4]W.F. Stickle and K.D. Bomben, Thin Solid Film **154**, 301 (1987).

[5]S.J. Pearton, U.K. Chakrebarti, W.S. Hobson, and A.P. Kinsella, 'Reactive ion etching of GaAs, AlGaAs, and GaSb in Cl_2 and $SiCl_4$', J. Vac. Sci. Technol. B **8**, 607 (1990).

[6]J.W. Coburn and H.F. Winters, 'Plasma etching — A discussion of mechanisms', J. Vac. Sci. Technol. **16**, 391 (1979).

Chapter 4

[1]H.F. Wong, D.L. Green, T.Y. Liu, D.G. Lishan, M. Bellis, E.L. Hu, P.M. Petroff, P.O. Holtz, and J.L. Merz, 'Investigation of reactive ion etching induced damage in GaAs–AlGaAs quantum well structures', J. Vac. Sci. Technol. B **6**, 1906 (1988).

[2]J.M. Moison, K. Elcess, F. Houzay, J.Y. Marzin, J.M. Gerard, F. Bathe, and M. Bensoussan, 'Near-surface $GaAs/Ga_{0.7}Al_{0.3}As$ quantum wells: Interaction with the surface states', Phys. Rev. B **41**, 12945 (1990).

[3]D.L. Green, J.A. Skidmore, D.G. Lishan, E.L. Hu, and P.M. Petroff, 'Calibration of the multiple quantum well probe technique for dry-etching-induced damage analysis', Appl. Phys. Lett. **62**, 1253 (1993).

[4]R. Germann, A. Forchel, and M. Bresch, and H.P. Meier, 'Energy dependence and depth distribution of dry etching-induced damage in III-V semiconductor heterostructures', J. Vac. Sci. Technol. B **7**, 1475 (1989).

[5]M. Joseph, F.E.G. Guimaraes, J. Kraus, and F.J. Tegude, 'Characterisation of reactive ion etched AlGaAs/GaAs heterostructures by photoluminescence and low temperature Hall measurements', J. Vac. Sci. Technol. B **9**, 1456 (1991).

[6]E.M. Clausen,Jr., J.G. Craighead, J.P. Harbision, A.Scherer, L.M. Schiavone, B. Van der Gaag, and L.T. Florez, J. Vac. Sci. Technol. B **7**, 2011 (1989).

[7]Y. Idle, N. Takado, and K. Asakawa, 'Optical characterisation of reactive ion beam etching induced damage using GaAs/AlGaAs quantum well structures', Inst. Phys. Conf. Ser. No 106: Chapter 7, paper presented at Int. Symp. GaAs and Related Counpound, Japan, 495 (1989).

[8]D. Lootens, P. Van Daele, P. Demeester and P. Clauws, 'Study of electrical damage in GaAs induced by $SiCl_4$ reactive ion etching', J. Appl. Phys. **70**, 221 (1991).

[9]D.G.Deppe and N.Holonyak, Jr., 'Atom diffusion and impurity-induced layer disordering in quantum well III-V semiconductor heterostructures', J. Appl. Phys. **64**, R93 (1988).

[10]J. Chevallier, W.C. Dautremont-Smith, C.W. Tau, and S..J. Pearton, Appl. Phys. Lett. **47**, 108 (1985).

[11]M. Rahman, M.A. Foad, S. Hichs, M.C. Holland and C.D.W. Wilkinson, 'Defects penetration during the plasma etching of semiconductors', Mat. Res. Soc. Proc. **279**, 775 (1993) (and references within)

[12]S.K. Murad, C.D.W. Wilkinson and S.P. Beaumont, 'Selective and Nonselective RIE of GaAs and $Al_xGa_{1-x}As$ in $SiCl_4$ plasma', Microelectronic Eng. **23**, 357 (1994).

[13]J. Beauvais, J.H. Marsh, A.H. Kean, A.C. Bryce, and C. Button, 'Suppression of bandgap shifts in GaAs/AlGaAs quantum wells using strontium fluoride caps', Electron. Lett. **28**, 1670 (1992).

[14]J.F. Ziegler, J.p. Biersack, and U. Littmark, *The Stopping and Range of Ions in Solids,* (Pergamon, New York, 1985).

[15]S.W. Pang, G.A. Lincoln, R.W. McClelland, P.D. DeGraff, M.W. Geis, and W.J. Piacentini, 'Effects of dry etching on GaAs', J. Vac. .Sci. Technol. B **4**, 1334 (1983).

[16]M.E. Harper, J.J. Cuomo, and H.R. Kaufman, 'Technology and applications of broad-beam ion sources used in sputtering. Part II. Applications', J. Vac. Sci. Technol. **21**, 737 (1982).

[17]J.C. Bean, G.E. Becker, P.M. Petroff, and T.E. Seider, J. Appl. Phys. **48**, 907 (1977).

[18]A.C. Papadopoulo, C. Dubon-Chevallier, J.F. Bresse, A.M. Duchenois, and F. Heliot, 'Etching procedures of GaAs: Cathodoluminescence study of the induced damages and of the recovering techniques', J. Vac. Sci. Technol. B8, 407 (1990).

Chapter 5

[1]D. Lootens, P. Van Daele, P. Demeester and P. Clauws, 'Study of electrical damage in GaAs induced by $SiCl_4$ reactive ion etching', J. Appl. Phys. **70**, 221 (1991).

[2]S.J. Pearton, U.K. Chakrabarti, and W.S. Hobson, 'Reactive ion etching induced damage in GaAs and AlGaAs using C_2H_6/H_2/Ar or CCl_2F/O_2 gas mixtures', J. Appl. Phys. **66**, 2061 (1989).

[3]S.W. Pang, 'Surface damage induced on GaAs by reactive ion etching and sputter etching', J. Electrochem. Soc. **133**, 784 (1986).

[4]see for example, R. Cheung, S. Thoms, S.P. Beaumont, G. Doughty, V. Law, C.D.W. Wilkinson, 'Reactive ion etching of GaAs using a mixture of methane and hydrogen', Electron. Lett. **23**, 857 (1987).

[5]see for example, J. Werking, J. Schramm, C. Nguyen, E.L. Hu, and H. Kroemer, 'Methane/hydrogen-based reactive ion etching of InAs, InP, GaAs, and GaSb', Appl. Phys. Lett. **58**, 2003 (1991).

[6]R.A. Gottscho, B.L. Preppernau, S.J. Pearton, A.B. Emerson, and K.P. Giapis, 'Real-time monitoring of low-temperature hydrogen plasma passivation of GaAs', J. Appl. Phys. **68**, 440 (1990) and references within.

[7]R.P.H. Chang, C.C. Chang, and S. Darack, 'Hydrogen plasma etching of semiconductors and their oxides', J. Vac. Sci. Technol.. **20**, 45 (1982).

[8]J.F. Ziegler, J.P. Biersack, and U. Littmark, *The stopping and Range of Ions in Solids*, (Pergamon, New York, 1985).

[9]T. Venkatesan, S.A. Schwarz, D.M. Hwang, R.Bhat, M. Koza, H.W. Yoon, P. Mei, Y. Arakawa, and A. Yariv, 'Dose-dependent mixing of AlAs-GaAs superlattices by Si ion implantation', Appl. Phys. Lett. **49**, 701 (1986).

[10]I. Gontijo, T. Krauss, R.M. De La Rue, J.S. Roberts and J.H. Marsh, 'Very low loss extended cavity GaAs/AlGaAS lasers made by impurity-free vacancy diffusion', Electron. Lett. **30**, 145 (1994).

[11]S.R. Andrew, J.H. Marsh, M.C. Holland, and A.H. Kean, 'Quantum well laser with integrated passive waveguide fabricated by neutral impurity disordering', IEEE Photonics Technol. Lett. **4**, 426 (1990).

[12]J. Werner, T.P. Lee, E. Kapon, E. Colas, N.G. Stoffel, S.A. Schwarz, L.C. Schwartz, and N.C. Andreadakis, 'Single and double quantum well lasers with a monolithically integrated passive section', Appl. Phys. Lett. **57**, 810 (1990).

[13]R.L. Thornton, J.E. Epler, and T.L. Poili, 'Monolithic integration of a transparent dielectric waveguide into an active laser cavity by impurity–induced disordering', Appl. Phys. Lett. **51**, 1983 (1987).

[14]S. Tarucha and H. Okamoto, 'Monolithic integration of a laser diode and an optical waveguide modulator having a GaAs/AlGaAs quantum well double heterostructure', Appl. Phys. Lett. **48**, 1 (1986).

Chapter 6

[1]D.G.Deppe and N.Holonyak,Jr., 'Atom diffusion and impurity-indueced layer disordering in quantum well III-V semiconductor heterostructures', J. Appl. Phys. **64** , R93 (1988).

[2]W.D. Laidig, N. Holonyak,Jr., M.D. Camras, K. Hess, J.J. Coleman, P.D. Dapkus, and J. Bardeen, 'Disorder of AlAs-GaAs superlattice by impurity diffusion', Appl. Phys. Lett. **38**, 776 (1981).

[3]J.H. Marsh, S.I. Hansen, A.C. Bryce, R.M. De La Rue, 'Applications of neutral impurity disording in fabricating low-loss optical waveguides and integrated waveguide devices', Optical and Quantum Electronics **23** , S941 (1991).

[4]C.J. McLean, J.H. Marsh, R.M. De La Rue, A.C. Bryce, B. Garrett, R.W. Glew, 'Layer selective disordering by photoabsorption induced thermal diffusion in InGaAs/InP based multiplequantum well structures', Electron.Lett. **28**, 1117 (1992).

[5]C.J. McLean, A. McKee, J.H. Marsh, R.M. De La Rue, 'Lateral control of the bandgap in GaInAs/GaInAsP MQW structures using photoabsorption induced disordering', Electron.Lett. **29**, 1657 (1993).

[6]J. Ralston, A.L. Moretti, R.K. Jain, F.A. Chambers, 'Intermixing of $Al_xGa_{1-x}As$/Gaas superlattices by pulsed laser irradiation', Appl. Phys. Lett. **50**, 1817 (1987).

[7]J.E. Epler, R.D. Burnham, R.L. Thornton, T.L. Paoli, and M.C. Bashaw, 'Laser induced disordering of GaAs-AlGaAs superlattice and incorporation of Si impurity', Appl. Phys. Lett. **49**, 1447 (1986).

[8]J.H. Marsh, S.R. Andrew, S.G. Ayling, J. Beauvais, S.A. Bradshaw, A.C. Bryce, S.I. Hansen, R.M. De La Rue and R.G. Glew, 'Neutral impuity disordering of III-V quantum well structure for optoelectronic integration', Mat. Res. Soc. Symp.Proc. **240**, 679 91992).

[9]J.H. Marsh, 'Quantum well intermixing', Semicond. Sci. Technol. **8**, 1136 (1993)

[10]M. O'Neil, J.H. Marsh, R.M. De La Rue, J.S. Roberts, C. Jeynes, 'Multiple quantum well optical waveguides with large absorption edge blue shift produced by boron and fluorine impurity-induced disordering', Appl. Phys. Lett. **55**, 1373 (1989).

[11]M. O'Neil, J.H. Marsh, R.M. De La Rue, J.R. Roberts, and R. Gwilliam, 'Reduction of the propagation losses n imprity disordered quantum well waveguides', Electron. Lett. **26**. 1613 (1990).

[12]S.R. Andrew, J.H. Marsh, M.C. Holland and A.H. Kean, 'Quantum well laser with integrated passive waveguide fabricated by neutral impurity disordering', Photonics Tech. Lett. **4**, 426 (1992).

[13]J.H. Marsh, S.A. Bradshaw, A.C. Bryce, R. Gwilliam and R.W. Glew, J. Electron Mater. **20**, 973 (1991).

[14]A.C. Bryce, J.H. Marsh, R. Gwilliam and R.W. Glew, 'Impurity induced disordering in InGaas/InGaAsP quantum wells using implanted fluorine and boron', IEE Proc. Pt. J: optoelectronics **138**, 87 (1991).

[15]L. Guido, N. Holonyak, Jr., K.C. Hsieh, R.W. Kaliski, W.E. Plano, R.D. Burnham, R.C. Thornton, J.E. Epler, and T.L. Paoli, 'Effects of dielectric encapsulation and As overpressure on Al-Ga interdiffusion in $Al_xGa_{1-x}As$-GaAs quantum well heterostructure', J. Appl. Phys. **61**, 1372 (1987).

[16]A. Furuya, O. Wada, A. Takamori, and H. Hashimoto, 'Arsenic pressure dependence of interdiffusion of AlGaAs/GaAs interface of quantum well', Jpn. Appl. Phys. **26**, L926 (1987).

[17]C.R. Abernathy, S.J. Pearton, R. Canuso, F. Ren, and J. Kovalchik, 'Ultrahigh doping of GaAs by carbon during metalorganic molecular beam epitaxy', Appl. Phys Lett. **55**, 1750 (1990).

[18]B.T. Cunningham, L.J. Guido, J.E. Baker, J.S. Major,Jr., N. Holonyak,Jr., and G.E. Stilman, 'Carbon diffusion in undoped, n-type, and p-type GaAs', Appl. Phys. Lett. **50**, 687 (1987).

[19]T.J. Magee, K.S. Lee, R. Ormond, R.J. Blattner, and C.A. Evans,Jr., 'Annealing of damage and redistribution of Cr in boron-implanted Si_3N_4-capped GaAs', Appl. Phys. Lett. **37**, 447 (1980).

[20]C.G. Hopkins, V.R. Deline, R.J. Blatnner, C.A. Evans,Jr., and T.J. Magee, 'Incorporation of boron during the growth of GaAs single crystals', Appl. Phys. Lett. **36**, 989 (1980).

[21]J. Woodhead, R.C. Newman, I. Grant, D. Rumsby, and R.M. Ware, 'Boron impurity anti-site defects in p-type gallium-rich gallium arsenide', J. Phys. C. **16**, 5523 (1983).

[22]D.W. Fischer, P.W. Yu, 'Infrared absorption and photoluminescence of defect level in the 204 to 255 meV range in p-type GaAs', J. Appl. Phys. **59**, 1952 (1986).

[23]E.V.K. Rao, N. Duhamel, P.N. Favennec, and H. L'Haridon, 'Investigation of compensation in implanted n-GaAs', J. Appl. Phys. **49**, 3898 (1978).

[24]B.S. Ooi, A.C. Bryce, J.H. Marsh, J. Martin, 'Transmission electron microscopy study of fluorine and boron implanted and annealed GaAs/AlGaAs', Appl. Phys. Lett. **65**, 58 (1994).

[25]T. Venkatesan, S.A. Schwarz, D.M. Hwang, R. Bhat, M. Koza, H.W. Yoon, P. Mei, Y. Arakawa, and A. Yariv, 'Dose-dependent mixing of AlAs-GaAs superlattices by Si ion implantation', Appl. Phys. Lett. **49**, 701 (1986).

[26]M.L. Gray, J.M. Parsey, Jr., R.E. Ahrens, S.J. Oearton, K.T. Short, L. Sargent, and J.S. Blakemore, 'Characterisation of n-type regions in GaAs formed by silicon fluride molecular ion implantation', J. Appl. Phys. **66**, 4176 (1989).

Chapter 7

[1]L.J. Guido, N. Holonyak,Jr., K.C. Hsieh, R.W. Kaliski, and W.E. Plano, R.D. Burnham, R.L. Thornton, J.E. Epler, and T.L. Paoli, 'Effects of dielectric encapsulation and As overpressure on Al-Ga interdiffusion in $Al_xGa_{1-x}As$-GaAs quantum-well heterostructures', J. Appl. Phys. **61**, 1372 (1987).

[2]L.J. Guido, J.S. Major,Jr., J.E. Baker, W.E. Plano, N. Holonyak,Jr., K.C. Hsieh, R.D. Burnham, 'Column III vacancy- and impurity-induced layer disordering of $Al_xGa_{1-x}As$-GaAs heterostructures with SiO_2 or Si_3N_4 diffusion source', J. Appl. Phys. **67**, 6813 (1990).

[3]see for example, B.C. De Cooman, S.H. Chen, C.B. Carter, J. Ralston and G.D. Wicks, 'The structure of ion implanted $Al_xGa_{1-x}As$/GaAs seperlattices', Microsc. Semiconductor. Mater. **76**, 301 (1985).

[4]see for example, C. Kittel, 'Introduction to Solid State Physics', Wiley (1986).

[5]P.M. Petroff, 'Transmission electron microscopy of interfaces in III-V compound semiconductors', J. Vac. Sci. Technol. **14**, 973 (1977).

[6]P.M. Petroff, 'Role of electron microscope in semiconductor electronic defects analysis', Mat. Rec. Soc. Symp. Proc. **46**, 433 (1985).

[7]M.H. Loretto, R.E. Smallman, 'Defect analysis in electron microscopy', Chapman and Hall, London. (1975).

[8]T.J. Magee, K.S. Lee, R. Ormond, C.A. Evans,Jr., R.J. Blattner, and C. Hopkins, 'Low-temperature redistribution of Cr in boron-implanted GaAs in the absence of encapsulatant stress', Appl. Phys. Lett. **37**, 635 (1980).

[9]T.J. Magee, H. Kawayoshi, R.D. Ormond, L.A. Christel, J.F. Gibbsons, C.G. Hopkins, C.A. Evans,Jr., D.S. Day, 'Stoichiometric disturbances in ion implanted GaAs and redistribution of Cr during annealing', Appl. Phys. Lett. **39**, 906 (1981).

[10]T.J. Magee, K.S. Lee, R. Ormond, R.J. Blattner, and C.A. Evans,Jr., 'Annealing of damage and redistribution of Cr in boron-implanted Si_3N_4-capped GaAs', Appl. Phys. Lett. 37, 447 (1980).

[11]S. Chen, S.T. Lee, G. Braunstein, G. Rajeswaran, and P. Fellinger, 'Correlation between defect characteristics and layer intermixing in Si implanted GaAs/AlGaAs superlattices', Mat. Res. Soc. Proc. **147**, 279, 1989

[12]E. Morita, J. Kasahara and S. Kawado, 'Transmission electron microscopic observation of microdefects in Zn+ -implanted GaAs', Jpn. J. Appl. Phys. **24**, 1274 (1985).

[13]P.M. Petroff, R.C. Miller, A.C. Gossard, and W. Wiegmann, 'Impurity trapping, interface structure, and luminescence of GaAs quantum wells grown by molecular beam epitaxy', Appl. Phys. Lett. **44**, 217 (1984).

[14]J.M. Brown, N. Holonyak Jr., R.W. Kaliski, M.J. Luodwise, W.T. Dietze, C.R. Lewis, 'Effect of layer size on lattice distortion in strained-layer superlattices', Appl. Phys. Lett. **44**, 1158 (1984).

[15]M. Ilegems and G.L. Pearson, 'Infrared reflection spectra of $Ga_{1-x}Al_xAs$ mixed crystals', Phys. Rev. **B1**, 1576 (1970).

[16]T. Venkatesan, S.A. Schwarz, D.M. Hwang, R. Bhat, M. Koza, H.W. Yoon, P. Mei, Y. Arakawa and A. Yariv, 'Dose-dependent mixing of AlAs-GaAs superlattices by Si ion implantation', Appl. Phys. Lett. **49**, 701 (1986).

Chapter 8

[1]R.J. Deri, and E. Kapon, 'Low loss III-V semiconductor optical waveguides', IEEE J. Quantum Electron. **27**, 626 (1991), and references within.

[2]M.K. Hibbs-Brenner and C.T. Sullivan, 'Low loss AlGaAs optical rectangular waveguides at 830 nm', Appl. Phys. Lett. **56**, 1529 (1990).

[3]R.J. Deri, E. Kapon, J.P. Harbison, M. Seto, C.P. Yun, and L.T. Florez, 'Low-loss GaAs/AlGaAs waveguide phase modulator using a W-shaped index profile', Appl. Phys. Lett. **53**, 1803 (1988).

[4]P.K. Tien, 'Light waves in thin films and integrated optics', Appl. Opt. **10**, 2395 (1971).

[5]R.J. Deri, R.J. Hawkins, and E. Kapon, 'Rib profile effects on scattering in semiconductor optical waveguides', Appl. Phys. Lett. **53**, 1483 (1988).

[6]R.G. Walker, 'Simple and accurate loss measurement technique for semiconductor optical waveguides', Electron. Lett. **21**, 581 (1985).

[7]J.F. Ziegler, J.P. Biersack, and U. Littmark, *'The Stopping and Range of Ions in Solids'*, (Pergamon, New York, 1985).

[8]M.R.S. Taylor, *Fwave-A vector E-M solver*, University of Glasgow, 1989-93.

[9]S. Adachi, 'GaAs, AlAs, and $Al_xGa_{1-x}As$: material parameters for use in research and device applications', J. Appl. Phys. **58**, R1 (1985).

[10]H.C. Casey, Jr., D.D Sell, and K.W. Wecht, 'Concentration dependence of the absorption coefficient for n- and p-type GaAs between 1.3 and 1.6 eV', J. Appl. Phys. **46**, 250 (1975).

[11]see for example, C. Kittel, *Interoduction to solid state physics*, 5th edn, Wiley, New York, 1976.

[12]H.C. Casey, Jr., and M.B. Panish, *Heterostructure Lasers, Part A,* Acadamic Press, New York, 1978.

[13]E. Garmire, 'Optical waveguides in single layers of Gal-xAlxAs grown on GaAs substrates', Appl. Phys. Lett. **23**., 403 (1973).

Chapter 9

[1]M. Kuzuhara, T. Nozaki, T. Kamejima, 'Characterisation of Ga out-diffusion from GaAs into SiO_xN_y films during thermal annealing', J. Appl. Phys. **66**, 5833 (1989).

[2]M. Ghisoni, R. Murray, A.W. Rivers, M. Pate, G. Hill, K. Woodbridge, G. Parry, 'An optical study of encapsulant thickness-controlled interdiffusion of asymmetric GaAs quantum well material', Semicon. Sci. and Technol. **8**, 1791 (1993).

[3]E.S. Koteles, B. Elman, P. Melman, J.Y. Chi, C.A. Armiento, 'Quantum well shape modification using vacancy generation and rapid thermal annealing', Optical and Quantum Electronics **23**, S779 (1991).

[4]S.G. Ayling, J. Beauvais, and J.H. Marsh, 'Spatial control of quantum well intermixing in GaAs/AlGaAs using a one-step process', Electron. Lett. **28**, 2240 (1992).

[5]E.H. Li, K.S. Chan, 'Laser gain and current density in a disordered AlGaAs/GaAs quantum well', Electron. Lett. **29**, 1233 (1993).

[6]T. Miyazawa, T. Kagawa, H. Iwamura, O. Mikami and M. Naganuma, 'Two-wavelength demultiplexing p-i-n GaAs/AlGaAs photodetector using partially disordered multiple quantum well structures', Appl. Phys. Lett. **55**, 828 (1989).

[7]A.N.M, Masum Choudhury, P. Melman, A. Silletti, E.S. Koteles, B. Foley and B. Elman, 'Metal-semiconductor-metal demultiplexing waveguide photodetectors in InGaAs/GaAs quantum well structures by selective bandgap tuning', IEEE Photon. Technol. Lett. **3** , 817 (1991).

Chapter 10

[1]J.H. Marsh, A.C. Bryce, and R.M. De La Rue, 'Recent progress in quantum well intermixing and application to waveguide devices', to be published in Material Scien. Engin. 1994.

List of publications

1. B.S. Ooi, A.C. Bryce, C.D.W. Wilkinson, and J.H. Marsh, 'Study of reactive ion etching-induced damage in GaAs/AlGaAs structures using a quantum well intermixing probe', Applied Physics Letter, Vol. **64**, pp598-600, 1994.

2. B.S. Ooi, A.C. Bryce, J.H. Marsh, and J. Martin, 'Transmission electron microscope study of fluorine and boron implanted and annealed GaAs/AlGaAs', Applied Physics Letter, Vol. **65**, pp85-87, 1994.

3. B.S. Ooi, S. E. Hicks, A.C. Bryce, C.D.W. Wilkinson and J.H. Marsh, 'Study of C_2F_6 overetch induced damage and the effects of overetch on subsequent $SiCl_4$ etch of GaAs/AlGaAs', accepted by Journal of Applied Physics.

4. B.S. Ooi, S.G. Ayling, A.C. Bryce, J.H. Marsh, 'Multiple wavelength laser chip fabricated using spatially controlled quantum well intermixing', submitted to Conference on Laser and Electro-Optics (CLEO), Maryland U.S.A., May 1995.

5. B.S. Ooi, A.C. Bryce, J.H. Marsh, 'Plasma-based integration process for photonic integrated circuits', submitted to Conference on Laser and Electro-Optics (CLEO), Maryland U.S.A., May 1995.

6. B.S. Ooi, S.G. Ayling, A.C. Bryce, J.H. Marsh, 'Fabrication of multiple wavelength lasers in GaAs/AlGaAs structures using a spatially controlled quantum well intermixing technique', submitted to IEEE Photonics Technology Letter.

7. B.S. Ooi, A.C. Bryce, J.H. Marsh, 'A novel integration process for photonic integrated circuits using plasma damage induced layer intermixing', submitted to Electronic Letter.

References

Chapter 1

[1]S.E. Miller, Bell Syst. Tech. J. **48**, 2059 (1969).

[2]D.G. Deppe and N. Holonyak, Jr., 'Atom diffusion and impurity-induced layer disordering in quantum well III-V semiconductor heterostructures', J. Appl. Phys. **64**, R93 (1988).

[3]see for example, J.H. Marsh, 'Quantum well intermixing', Semicond. Sci. Technol.. **8**, 1136 (1993).

[4]J.H. Marsh, S.R. Andrew, S.G. Ayling, J. Beauvais, S.A. Bradshaw, A.C. Bryce, S.I. Hansen, R.M. De La Rue and R.W. Glew, 'Neutral impurity disordering of III-V quantum well structures for optoelectronic integration', Mat. Res. Soc. Symp.Proc. **240**, 679 (1992).

[5]J.H. Marsh, S.I. Hansen, A.C. Bryce, R.M. De La Rue, 'Applications of neutral impurity disordering in fabricating low-loss optical waveguides and integrated waveguide devices', Optical and Quantum Electronics **23** , S941 (1991).

[6]M.W. Austine, 'GaAs/GaAlAs curved rib waveguides', J. of Quantum Electronics QE**18**, 795 (1982).

[7]S.J. Pearton, M.J. Valise, K.S. Jones, K.T. Short, E. Lane, T.R. Fullowan, A.E. Von Neida, N.M. Hagel, 'Reaction ion etching of GaAs with CCl_2F_2:O_2: Etch rates, surface chemistry, and residual damage ', J. Appl. Phys. **65**, 1281 (1989).

[8]K.L. Seaward, N.J. Moll, D.J. Coulma, and W.F. Stickle, 'An analytical study of etch and etch-stop reactions for GaAs on AlGaAs in CCl_2F_2 plasma', J. Appl. Phys. **61**, 2358 (1987).

Chapter 2

[1]B. Chapman, 'Glow discharge process', (Wiley, New York, 1980).

[2]S.M. Sze, 'VLSI Technology', 2nd. edit., (Mcgraw–Hill, New York,1988).

[3]S.K. Murad, PhD thesis, University of Glasgow, 1994.

[4]CRC Handbook of Chemistry and Physics (Chemical Rubber, Cleveland, Ohio, 1970).

[5]S.C. McNevin, 'Chemical etching of GaAs and InP by chorine: The thermodynamic predicted dependence on Cl_2 pressure and temperature', J.Vac.Sci. Technol. B **4**,1216 (1986).

[6]H.F. Winters, J.W. Coburn, and E. Kay, 'Plasma etching – A pseado-black box approach', J. Appl. Phys. **48**, 4973 (1977).

[7]see for example, S. Salimian, C.Yuen, C. Shih, C. Smith and C.B. Cooper, 'Damage studies of dry etched GaAs recessed gates for field effect transistors', J.Vac. Sci. Technol. B **9**, 114 (1991).

[8]T. Hara, H. Suzuki, and A. Suga, 'Radiation damage of GaAs induced by reactive ion etching', J. Appl. Phys. **62**, 4109 (1987).

[9]R.Cheung, Y.H. Lee, K.Y. Lee, T.P. Smith, and D.P. Kern, S.P. Beaumont and C.D.W. Wilkinson, 'Comparison of damage in the dry etching of GaAs by conventional reactive ion etching and by reactive ion etching with an electron cyclotron resonance generated plasma', J. Vac. Sci. Technol. B **7**, 1462 (1989).

[10]K. Gamo, H. Miyake, Y. Yuba, and S. Nambe, 'Defect study in GaAs bombarded by low-energy focused ion beams', J. Vac. Sci. Technol. B **6**, 2124 (1988).

[11]H.F. Wong, D.L. Green, T.Y. Liu, D.G. Lishan, M. Bellis, E.L. Hu, M. Petroff, P.O. Holtz, and J.L. Merz, 'Investigation of reactive ion etching induced damage in GaAs/AlGaAs quantum well structures', J. Vac. Sci. Technol. B **6**, 19 (1988).

[12]S.W. Pang, G.A. Lincoln, P.W. McClelland, P.D. DeGraff, M. Geiss, and W.J. Piacontini, 'Effects of dry etching on GaAs', J. Vac. Sci. Technol. B **1**, 1334 (1983).

[13]S. Thoms, S.P. Beaumont, C.D.W. Wilkinson, J. Frost, and C.R. Stanley, in Microcircuit Engineering (1986), edited by H. W. Lehman and Ch. Bleicker (North Holland, Amsterdam, 1986), p.249.

[14] S.K. Murad, C.D.W. Wilkinson, P.D. Wang, W. Parkes, C.M. Sotomayar-Torres, and N. Cameron, 'Very low damage etching of GaAs', J. VAc. Sci. Technol. B **11**, 2237 (1993).

[15]R. Cheung, S. Thoms, M. Watt, M.A. Ford, C.M. Sotomayor-Torres, C.D.W. Wilkinson, U.J. Cox, R.A. Cowley, C. Dunscombe, and R.H. Williams, 'Reactive ion etching induced damage in GaAs and $Al_{0.3}Ga_{0.7}As$ using $SiCl_4$', Semicon. Sci. Technol. **7**, 1189 (1992).

[16]M. Rahman, N.P. Jhonson, M.A. Ford, A.R. Long, M.C. Holland and C.D.W. Wilkinson, 'Model for conductance in dry-etching damaged n-GaAs structures', Appl. Phys. Lett. **61**, 2335 (1992).

[17]S.W. Pang, W.D. Goodhue, T.M. Lyszczarz, D.J. Ehrlich, R.B. Goodman, and G.D. Johnson, 'Dry etching induced damage on vertical sidewalls of GaAs channels', J. Vac. Sci. Technol. B **6**, 1916 (1988).

[18]A.C. Papadopoulo, C. Dubon-Chevallier, J.F. Bresse, A.M. Duchenois, and F.Heliot, 'Etching procedures of GaAs : Cathodoluminescence study of the induced damages and of the recovering techniques', J. Vac. Sci. Technol. B **8**, 407 (1990).

[19]see for example, P. Collot, T. Diallo and J. Canteloup, 'Dry-etch monitoring of III-V heterostructures using laser reflectometry and optical emmision spectroscopy ', J. Vac. Sci. Technol. B **9**, 2497 (1991).

[20]see for example, S.E. Hicks, W. Parkes, J.A.H. Wilkinson and C.D.W. Wilkinson, 'Reflectance modelling for In-situ dry etch monitoring of bulk SiO_2 and III-V miltilayer structures', to be appeared in Nov. 1994 issue of J. Vac. Sci. Technol. B.

[21]see for example, T.R. Hayers, P.A. Heimann, V.M. Donnelly, and K.E. Strege, 'Maskless laser interferometric monitoring of InP/InGaAsP heterostructure reactive ion etching', Appl. Phys. Lett. **57**, 2817 (1990).

[22]see for example, R. Muller, '*In-situ* etching depth monitoring for reactive ion etching of InGaAs(P)/InP heterostructure by ellipsometry', Appl. Phys. Lett. **57**, 1020 (1990).

[23]B.S. Ooi, S.E. Hichs, A.C. Bryce, C.D.W. Wilkinson, and J.H. Marsh, 'Study of C_2F_6 overetch induced damage and the effects of overetch on subsequent $SiCl_4$ etch of GaAs/AlGaAs', summited to J. Appl. Phys.

[24]S. Adachi, 'GaAs, AlAs, and $Al_xGa_{1-x}As$: material parameters for use in research and device applications', J. Appl. Phys. **58**, R1 (1985).

[25]see for example, J.H. Marsh, 'Quantum well intermixing', Semicond. Sci. Technol. 8, 1136 (1993).

[26]J.C. Mikkelsen, Jr. and I-W. Wu, 'Severe loss of dopant activity due to CHF_3+CO_2 reactive ion etch damage', Appl. Phys. Lett. **49**, 103 (1986).

[27]S.J. Pearton, U.K. Chakrabarti, and W.S. Hobson, 'Reactive ion etching induced damage in GaAS and AlGaAs using $C2H_6/H_2/Ar$ or CCl_2F_2/O_2 gas mixtures', J. Appl. Phys. **66**, 2061 (1989).

[28]see for example, B.S. Ooi, A.C. Bryce, J.H.Marsh, and J.Martin, 'Transmission electron microscope study of fluorine and boron implanted and annealed GaAs/AlGaAs', Appl. Phys. Lett. **65**, 85 (1994).

[29]see for example, S. Chen, S.T. Lee, G. Rajeswaran and P. Fellinger, 'Correlation between defetc characteristics and layer intermixing in Si implanted GaAs/AlGaAs superlattices', Mat. Res. Soc. Symp. Proc. **147**, 279 (1989).

[30]see for example, P.M. Petroff, 'Role of electron microscopy in semiconductor electronic defects analysis', Mat. Res. Soc. Symp. Proc. **46**, 433 (1985).

[31]see for example, H.L. Tsai, Y.C. Kao, 'Generation and propagation of threading dislocation in GaAs grown on Si', J. Appl. Phys. **67**, 2862 (1990).

[32]P.M. Petroff., ' Transmission electron microscopy of interfaces in III–V compound semiconductors', J. Vac. Sci. Technol. **14**, 973 (1977).

[33]M.A. Ford, Ph D thesis, University of Glasgow, (1992).

[34]S.Pang, paper presented at EPIB, to be appeared in J. Vac. Sci. Technol. B , Nov. 1994.

[35]Y. Hirayama, Y. Suzuki, and H. Okamoto, 'Ion-species dependedce of interdiffusion in ion-implantated GaAs–AlAs superlattices', Jpn. J. Appl. Phys. **24**, 1498 (1985).

[36]C. Kittel, 'Introduction to solid state physics', 6th. edit., (Wiley, New York, 1991).

[37]F. Stern and W.E. Howard, Phys. Rev. **163**, 816 (1967).

Chapter 3

[1]S.J. Pearton, M.J. Valise, K.S. Jones, K.T. Short, E. Lane, T.R. Fullowan, A.E. Von Neida, N.M. Hagel, 'Reactive ion etching of GaAs with CCl_2F_2:O_2: Etch rates, surface chemistry, and residual damage', J. Appl. Phys. **65**, 1281 (1989).

[2]K.L. Seaward, N.J. Moll, D.J. Coulma, and W.F. Stickle, 'An analytical study of etch and etch-stop reactions for GaAs on AlGaAs in CCl2F2 plasma', J. Appl. Phys. **61**, 2358 (1987).

[3]S. Salimian and C.B. Cooper, III, 'Selective dry etching of GaAs over AlGaAs in $SF_6/SiCl_4$ mixtures' J. Vac. Sci. Technol. B **6**, 1641 (1988).

[4]W.F. Stickle and K.D. Bomben, Thin Solid Film **154**, 301 (1987).

[5]S.J. Pearton, U.K. Chakrebarti, W.S. Hobson, and A.P. Kinsella, 'Reactive ion etching of GaAs, AlGaAs, and GaSb in Cl_2 and $SiCl_4$', J. Vac. Sci. Technol. B **8**, 607 (1990).

[6]J.W. Coburn and H.F. Winters, 'Plasma etching — A discussion of mechanisms', J. Vac. Sci. Technol. **16**, 391 (1979).

Chapter 4

[1]H.F. Wong, D.L. Green, T.Y. Liu, D.G. Lishan, M. Bellis, E.L. Hu, P.M. Petroff, P.O. Holtz, and J.L. Merz, 'Investigation of reactive ion etching induced damage in GaAs–AlGaAs quantum well structures', J. Vac. Sci. Technol. B **6**, 1906 (1988).

[2]J.M. Moison, K. Elcess, F. Houzay, J.Y. Marzin, J.M. Gerard, F. Bathe, and M. Bensoussan, 'Near-surface GaAs/$Ga_{0.7}Al_{0.3}$As quantum wells: Interaction with the surface states', Phys. Rev. B **41**, 12945 (1990).

[3]D.L. Green, J.A. Skidmore, D.G. Lishan, E.L. Hu, and P.M Petroff, 'Calibration of the multiple quantum well probe technique for dry-etching-induced damage analysis', Appl. Phys. Lett. **62**, 1253 (1993).

[4]R. Germann, A. Forchel, and M. Bresch, and H.P. Meier, 'Energy dependence and depth distribution of dry etching-induced damage in III-V semiconductor heterostructures', J. Vac. Sci. Technol. B **7**, 1475 (1989).

[5]M. Joseph, F.E.G. Guimaraes, J. Kraus, and F.J. Tegude, 'Characterisation of reactive ion etched AlGaAs/GaAs heterostructures by photoluminescence and low temperature Hall measurements', J. Vac. Sci. Technol. B **9**, 1456 (1991).

[6]E.M. Clausen,Jr., J.G. Craighead, J.P. Harbision, A.Scherer, L.M. Schiavone, B. Van der Gaag, and L.T. Florez, J. Vac. Sci. Technol. B **7**, 2011 (1989).

[7]Y. Idle, N. Takado, and K. Asakawa, 'Optical characterisation of reactive ion beam etching induced damage using GaAs/AlGaAs quantum well structures', Inst. Phys. Conf. Ser. No 106: Chapter 7, paper presented at Int. Symp. GaAs and Related Counpound, Japan, 495 (1989).

[8]D. Lootens, P. Van Daele, P. Demeester and P. Clauws, 'Study of electrical damage in GaAs induced by $SiCl_4$ reactive ion etching', J. Appl. Phys. **70**, 221 (1991).

[9]D.G.Deppe and N.Holonyak, Jr., 'Atom diffusion and impurity-induced layer disordering in quantum well III-V semiconductor heterostructures', J. Appl. Phys. **64**, R93 (1988).

[10]J. Chevallier, W.C. Dautremont-Smith, C.W. Tau, and S..J. Pearton, Appl. Phys. Lett. **47**, 108 (1985).

[11]M. Rahman, M.A. Foad, S. Hichs, M.C. Holland and C.D.W. Wilkinson, 'Defects penetration during the plasma etching of semiconductors', Mat. Res. Soc. Proc. **279**, 775 (1993) (and references within)

[12]S.K. Murad, C.D.W. Wilkinson and S.P. Beaumont, 'Selective and Nonselective RIE of GaAs and $Al_xGa_{1-x}As$ in $SiCl_4$ plasma', Microelectronic Eng. **23**, 357 (1994).

[13]J. Beauvais, J.H. Marsh, A.H. Kean, A.C. Bryce, and C. Button, 'Suppression of bandgap shifts in GaAs/AlGaAs quantum wells using strontium fluoride caps', Electron. Lett. **28**, 1670 (1992).

[14]J.F. Ziegler, J.p. Biersack, and U. Littmark, *The Stopping and Range of Ions in Solids*, (Pergamon, New York, 1985).

[15]S.W. Pang, G.A. Lincoln, R.W. McClelland, P.D. DeGraff, M.W. Geis, and W.J. Piacentini, 'Effects of dry etching on GaAs', J. Vac. .Sci. Technol. B **4**, 1334 (1983).

[16]M.E. Harper, J.J. Cuomo, and H.R. Kaufman, 'Technology and applications of broad-beam ion sources used in sputtering. Part II. Applications', J. Vac. Sci. Technol. **21**, 737 (1982).

[17]J.C. Bean, G.E. Becker, P.M. Petroff, and T.E. Seider, J. Appl. Phys. **48**, 907 (1977).

[18]A.C. Papadopoulo, C. Dubon-Chevallier, J.F. Bresse, A.M. Duchenois, and F. Heliot, 'Etching procedures of GaAs: Cathodoluminescence study of the induced damages and of the recovering techniques', J. Vac. Sci. Technol. B8, 407 (1990).

Chapter 5

[1]D. Lootens, P. Van Daele, P. Demeester and P. Clauws, 'Study of electrical damage in GaAs induced by $SiCl_4$ reactive ion etching', J. Appl. Phys. **70**, 221 (1991).

[2]S.J. Pearton, U.K. Chakrabarti, and W.S. Hobson, 'Reactive ion etching induced damage in GaAs and AlGaAs using C_2H_6/H_2/Ar or CCl_2F/O_2 gas mixtures', J. Appl. Phys. **66**, 2061 (1989).

[3]S.W. Pang, 'Surface damage induced on GaAs by reactive ion etching and sputter etching', J. Electrochem. Soc. **133**, 784 (1986).

[4]see for example, R. Cheung, S. Thoms, S.P. Beaumont, G. Doughty, V. Law, C.D.W. Wilkinson, 'Reactive ion etching of GaAs using a mixture of methane and hydrogen', Electron. Lett. **23**, 857 (1987).

[5]see for example, J. Werking, J. Schramm, C. Nguyen, E.L. Hu, and H. Kroemer, 'Methane/hydrogen-based reactive ion etching of InAs, InP, GaAs, and GaSb', Appl. Phys. Lett. **58**, 2003 (1991).

[6]R.A. Gottscho, B.L. Preppernau, S.J. Pearton, A.B. Emerson, and K.P. Giapis, 'Real-time monitoring of low-temperature hydrogen plasma passivation of GaAs', J. Appl. Phys. **68**, 440 (1990) and references within.

[7]R.P.H. Chang, C.C. Chang, and S. Darack, 'Hydrogen plasma etching of semiconductors and their oxides', J. Vac. Sci. Technol.. **20**, 45 (1982).

[8]J.F. Ziegler, J.P. Biersack, and U. Littmark, *The stopping and Range of Ions in Solids*, (Pergamon, New York, 1985).

[9]T. Venkatesan, S.A. Schwarz, D.M. Hwang, R.Bhat, M. Koza, H.W. Yoon, P. Mei, Y. Arakawa, and A. Yariv, 'Dose-dependent mixing of AlAs-GaAs superlattices by Si ion implantation', Appl. Phys. Lett. **49**, 701 (1986).

[10]I. Gontijo, T. Krauss, R.M. De La Rue, J.S. Roberts and J.H. Marsh, 'Very low loss extended cavity GaAs/AlGaAS lasers made by impurity-free vacancy diffusion', Electron. Lett. **30**, 145 (1994).

[11]S.R. Andrew, J.H. Marsh, M.C. Holland, and A.H. Kean, 'Quantum well laser with integrated passive waveguide fabricated by neutral impurity disordering', IEEE Photonics Technol. Lett. **4**, 426 (1990).

[12]J. Werner, T.P. Lee, E. Kapon, E. Colas, N.G. Stoffel, S.A. Schwarz, L.C. Schwartz, and N.C. Andreadakis, 'Single and double quantum well lasers with a monolithically integrated passive section', Appl. Phys. Lett. **57**, 810 (1990).

[13]R.L. Thornton, J.E. Epler, and T.L. Poili, 'Monolithic integration of a transparent dielectric waveguide into an active laser cavity by impurity–induced disordering', Appl. Phys. Lett. **51**, 1983 (1987).

[14]S. Tarucha and H. Okamoto, 'Monolithic integration of a laser diode and an optical waveguide modulator having a GaAs/AlGaAs quantum well double heterostructure', Appl. Phys. Lett. **48**, 1 (1986).

Chapter 6

[1]D.G.Deppe and N.Holonyak,Jr., 'Atom diffusion and impurity-indueced layer disordering in quantum well III-V semiconductor heterostructures', J. Appl. Phys. **64** , R93 (1988).

[2]W.D. Laidig, N. Holonyak,Jr., M.D. Camras, K. Hess, J.J. Coleman, P.D. Dapkus, and J. Bardeen, 'Disorder of AlAs-GaAs superlattice by impurity diffusion', Appl. Phys. Lett. **38**, 776 (1981).

[3]J.H. Marsh, S.I. Hansen, A.C. Bryce, R.M. De La Rue, 'Applications of neutral impurity disording in fabricating low-loss optical waveguides and integrated waveguide devices', Optical and Quantum Electronics **23** , S941 (1991).

[4]C.J. McLean, J.H. Marsh, R.M. De La Rue, A.C. Bryce, B. Garrett, R.W. Glew, 'Layer selective disordering by photoabsorption induced thermal diffusion in InGaAs/InP based multiplequantum well structures', Electron.Lett. **28**, 1117 (1992).

[5]C.J. McLean, A. McKee, J.H. Marsh, R.M. De La Rue, 'Lateral control of the bandgap in GaInAs/GaInAsP MQW structures using photoabsorption induced disordering', Electron.Lett. **29**, 1657 (1993).

[6]J. Ralston, A.L. Moretti, R.K. Jain, F.A. Chambers, 'Intermixing of $Al_xGa_{1-x}As$/Gaas superlattices by pulsed laser irradiation', Appl. Phys. Lett. **50**, 1817 (1987).

[7]J.E. Epler, R.D. Burnham, R.L. Thornton, T.L. Paoli, and M.C. Bashaw, 'Laser induced disordering of GaAs-AlGaAs superlattice and incorporation of Si impurity', Appl. Phys. Lett. **49**, 1447 (1986).

[8]J.H. Marsh, S.R. Andrew, S.G. Ayling, J. Beauvais, S.A. Bradshaw, A.C. Bryce, S.I. Hansen, R.M. De La Rue and R.G. Glew, 'Neutral impuity disordering of III-V quantum well structure for optoelectronic integration', Mat. Res. Soc. Symp.Proc. **240**, 679 91992).

[9]J.H. Marsh, 'Quantum well intermixing', Semicond. Sci. Technol. **8**, 1136 (1993)

[10]M. O'Neil, J.H. Marsh, R.M. De La Rue, J.S. Roberts, C. Jeynes, 'Multiple quantum well optical waveguides with large absorption edge blue shift produced by boron and fluorine impurity-induced disordering', Appl. Phys. Lett. **55**, 1373 (1989).

[11]M. O'Neil, J.H. Marsh, R.M. De La Rue, J.R. Roberts, and R. Gwilliam, 'Reduction of the propagation losses n imprity disordered quantum well waveguides', Electron. Lett. **26**. 1613 (1990).

[12]S.R. Andrew, J.H. Marsh, M.C. Holland and A.H. Kean, 'Quantum well laser with integrated passive waveguide fabricated by neutral impurity disordering', Photonics Tech. Lett. **4**, 426 (1992).

[13]J.H. Marsh, S.A. Bradshaw, A.C. Bryce, R. Gwilliam and R.W. Glew, J. Electron Mater. **20**, 973 (1991).

[14]A.C. Bryce, J.H. Marsh, R. Gwilliam and R.W. Glew, 'Impurity induced disordering in InGaas/InGaAsP quantum wells using implanted fluorine and boron', IEE Proc. Pt. J: optoelectronics **138**, 87 (1991).

[15]L. Guido, N. Holonyak, Jr., K.C. Hsieh, R.W. Kaliski, W.E. Plano, R.D. Burnham, R.C. Thornton, J.E. Epler, and T.L. Paoli, 'Effects of dielectric encapsulation and As overpressure on Al-Ga interdiffusion in $Al_xGa_{1-x}As$-GaAs quantum well heterostructure', J. Appl. Phys. **61**, 1372 (1987).

[16]A. Furuya, O. Wada, A. Takamori, and H. Hashimoto, 'Arsenic pressure dependence of interdiffusion of AlGaAs/GaAs interface of quantum well', Jpn. Appl. Phys. **26**, L926 (1987).

[17]C.R. Abernathy, S.J. Pearton, R. Canuso, F. Ren, and J. Kovalchik, 'Ultrahigh doping of GaAs by carbon during metalorganic molecular beam epitaxy', Appl. Phys Lett. **55**, 1750 (1990).

[18]B.T. Cunningham, L.J. Guido, J.E. Baker, J.S. Major,Jr., N. Holonyak,Jr., and G.E. Stilman, 'Carbon diffusion in undoped, n-type, and p-type GaAs', Appl. Phys. Lett. **50**, 687 (1987).

[19]T.J. Magee, K.S. Lee, R. Ormond, R.J. Blattner, and C.A. Evans,Jr., 'Annealing of damage and redistribution of Cr in boron-implanted Si_3N_4-capped GaAs', Appl. Phys. Lett. **37**, 447 (1980).

[20]C.G. Hopkins, V.R. Deline, R.J. Blatnner, C.A. Evans,Jr., and T.J. Magee, 'Incorporation of boron during the growth of GaAs single crystals', Appl. Phys. Lett. **36**, 989 (1980).

[21]J. Woodhead, R.C. Newman, I. Grant, D. Rumsby, and R.M. Ware, 'Boron impurity anti-site defects in p-type gallium-rich gallium arsenide', J. Phys. C. **16**, 5523 (1983).

[22]D.W. Fischer, P.W. Yu, 'Infrared absorption and photoluminescence of defect level in the 204 to 255 meV range in p-type GaAs', J. Appl. Phys. **59**, 1952 (1986).

[23]E.V.K. Rao, N. Duhamel, P.N. Favennec, and H. L'Haridon, 'Investigation of compensation in implanted n-GaAs', J. Appl. Phys. **49**, 3898 (1978).

[24]B.S. Ooi, A.C. Bryce, J.H. Marsh, J. Martin, 'Transmission electron microscopy study of fluorine and boron implanted and annealed GaAs/AlGaAs', Appl. Phys. Lett. **65**, 58 (1994).

[25]T. Venkatesan, S.A. Schwarz, D.M. Hwang, R. Bhat, M. Koza, H.W. Yoon, P. Mei, Y. Arakawa, and A. Yariv, 'Dose-dependent mixing of AlAs-GaAs superlattices by Si ion implantation', Appl. Phys. Lett. **49**, 701 (1986).

[26]M.L. Gray, J.M. Parsey, Jr., R.E. Ahrens, S.J. Oearton, K.T. Short, L. Sargent, and J.S. Blakemore, 'Characterisation of n-type regions in GaAs formed by silicon fluride molecular ion implantation', J. Appl. Phys. **66**, 4176 (1989).

Chapter 7

[1]L.J. Guido, N. Holonyak,Jr., K.C. Hsieh, R.W. Kaliski, and W.E. Plano, R.D. Burnham, R.L. Thornton, J.E. Epler, and T.L. Paoli, 'Effects of dielectric encapsulation and As overpressure on Al-Ga interdiffusion in $Al_xGa_{1-x}As$-GaAs quantum-well heterostructures', J. Appl. Phys. **61**, 1372 (1987).

[2]L.J. Guido, J.S. Major,Jr., J.E. Baker, W.E. Plano, N. Holonyak,Jr., K.C. Hsieh, R.D. Burnham, 'Column III vacancy- and impurity-induced layer disordering of $Al_xGa_{1-x}As$-GaAs heterostructures with SiO_2 or Si_3N_4 diffusion source', J. Appl. Phys. **67**, 6813 (1990).

[3]see for example, B.C. De Cooman, S.H. Chen, C.B. Carter, J. Ralston and G.D. Wicks, 'The structure of ion implanted $Al_xGa_{1-x}As$/GaAs seperlattices', Microsc. Semiconductor. Mater. **76**, 301 (1985).

[4]see for example, C. Kittel, 'Introduction to Solid State Physics', Wiley (1986).

[5]P.M. Petroff, 'Transmission electron microscopy of interfaces in III-V compound semiconductors', J. Vac. Sci. Technol. **14**, 973 (1977).

[6]P.M. Petroff, 'Role of electron microscope in semiconductor electronic defects analysis', Mat. Rec. Soc. Symp. Proc. **46**, 433 (1985).

[7]M.H. Loretto, R.E. Smallman, 'Defect analysis in electron microscopy', Chapman and Hall, London. (1975).

[8]T.J. Magee, K.S. Lee, R. Ormond, C.A. Evans,Jr., R.J. Blattner, and C. Hopkins, 'Low-temperature redistribution of Cr in boron-implanted GaAs in the absence of encapsulatant stress', Appl. Phys. Lett. **37**, 635 (1980).

[9]T.J. Magee, H. Kawayoshi, R.D. Ormond, L.A. Christel, J.F. Gibbsons, C.G. Hopkins, C.A. Evans,Jr., D.S. Day, 'Stoichiometric disturbances in ion implanted GaAs and redistribution of Cr during annealing', Appl. Phys. Lett. **39**, 906 (1981).

[10]T.J. Magee, K.S. Lee, R. Ormond, R.J. Blattner, and C.A. Evans,Jr., 'Annealing of damage and redistribution of Cr in boron-implanted Si_3N_4-capped GaAs', Appl. Phys. Lett. 37, 447 (1980).

[11]S. Chen, S.T. Lee, G. Braunstein, G. Rajeswaran, and P. Fellinger, 'Correlation between defect characteristics and layer intermixing in Si implanted GaAs/AlGaAs superlattices', Mat. Res. Soc. Proc. **147**, 279, 1989

[12]E. Morita, J. Kasahara and S. Kawado, 'Transmission electron microscopic observation of microdefects in Zn+ -implanted GaAs', Jpn. J. Appl. Phys. **24**, 1274 (1985).

[13]P.M. Petroff, R.C. Miller, A.C. Gossard, and W. Wiegmann, 'Impurity trapping, interface structure, and luminescence of GaAs quantum wells grown by molecular beam epitaxy', Appl. Phys. Lett. **44**, 217 (1984).

[14]J.M. Brown, N. Holonyak Jr., R.W. Kaliski, M.J. Luodwise, W.T. Dietze, C.R. Lewis, 'Effect of layer size on lattice distortion in strained-layer superlattices', Appl. Phys. Lett. **44**, 1158 (1984).

[15]M. Ilegems and G.L. Pearson, 'Infrared reflection spectra of $Ga_{1-x}Al_xAs$ mixed crystals', Phys. Rev. B**1**, 1576 (1970).

[16]T. Venkatesan, S.A. Schwarz, D.M. Hwang, R. Bhat, M. Koza, H.W. Yoon, P. Mei, Y. Arakawa and A. Yariv, 'Dose-dependent mixing of AlAs-GaAs superlattices by Si ion implantation', Appl. Phys. Lett. **49**, 701 (1986).

Chapter 8

[1]R.J. Deri, and E. Kapon, 'Low loss III-V semiconductor optical waveguides', IEEE J. Quantum Electron. **27**, 626 (1991), and references within.

[2]M.K. Hibbs-Brenner and C.T. Sullivan, 'Low loss AlGaAs optical rectangular waveguides at 830 nm', Appl. Phys. Lett. **56**, 1529 (1990).

[3]R.J. Deri, E. Kapon, J.P. Harbison, M. Seto, C.P. Yun, and L.T. Florez, 'Low-loss GaAs/AlGaAs waveguide phase modulator using a W-shaped index profile', Appl. Phys. Lett. **53**, 1803 (1988).

[4]P.K. Tien, 'Light waves in thin films and integrated optics', Appl. Opt. **10**, 2395 (1971).

[5]R.J. Deri, R.J. Hawkins, and E. Kapon, 'Rib profile effects on scattering in semiconductor optical waveguides', Appl. Phys. Lett. **53**, 1483 (1988).

[6]R.G. Walker, 'Simple and accurate loss measurement technique for semiconductor optical waveguides', Electron. Lett. **21**, 581 (1985).

[7]J.F. Ziegler, J.P. Biersack, and U. Littmark, *'The Stopping and Range of Ions in Solids'*, (Pergamon, New York, 1985).

[8]M.R.S. Taylor, *Fwave-A vector E-M solver*, University of Glasgow, 1989-93.

[9]S. Adachi, 'GaAs, AlAs, and $Al_xGa_{1-x}As$: material parameters for use in research and device applications', J. Appl. Phys. **58**, R1 (1985).

[10]H.C. Casey, Jr., D.D Sell, and K.W. Wecht, 'Concentration dependence of the absorption coefficient for n- and p-type GaAs between 1.3 and 1.6 eV', J. Appl. Phys. **46**, 250 (1975).

[11]see for example, C. Kittel, *Interoduction to solid state physics*, 5th edn, Wiley, New York, 1976.

[12]H.C. Casey, Jr., and M.B. Panish, *Heterostructure Lasers, Part A,* Acadamic Press, New York, 1978.

[13]E. Garmire, 'Optical waveguides in single layers of Ga1-xAlxAs grown on GaAs substrates', Appl. Phys. Lett. **23**., 403 (1973).

Chapter 9

[1]M. Kuzuhara, T. Nozaki, T. Kamejima, 'Characterisation of Ga out-diffusion from GaAs into SiO_xN_y films during thermal annealing', J. Appl. Phys. **66**, 5833 (1989).

[2]M. Ghisoni, R. Murray, A.W. Rivers, M. Pate, G. Hill, K. Woodbridge, G. Parry, 'An optical study of encapsulant thickness-controlled interdiffusion of asymmetric GaAs quantum well material', Semicon. Sci. and Technol. **8**, 1791 (1993).

[3]E.S. Koteles, B. Elman, P. Melman, J.Y. Chi, C.A. Armiento, 'Quantum well shape modification using vacancy generation and rapid thermal annealing', Optical and Quantum Electronics **23**, S779 (1991).

[4]S.G. Ayling, J. Beauvais, and J.H. Marsh, 'Spatial control of quantum well intermixing in GaAs/AlGaAs using a one-step process', Electron. Lett. **28**, 2240 (1992).

[5]E.H. Li, K.S. Chan, 'Laser gain and current density in a disordered AlGaAs/GaAs quantum well', Electron. Lett. **29**, 1233 (1993).

[6]T. Miyazawa, T. Kagawa, H. Iwamura, O. Mikami and M. Naganuma, 'Two-wavelength demultiplexing p-i-n GaAs/AlGaAs photodetector using partially disordered multiple quantum well structures', Appl. Phys. Lett. **55**, 828 (1989).

[7]A.N.M, Masum Choudhury, P. Melman, A. Silletti, E.S. Koteles, B. Foley and B. Elman, 'Metal-semiconductor-metal demultiplexing waveguide photodetectors in InGaAs/GaAs quantum well structures by selective bandgap tuning', IEEE Photon. Technol. Lett. **3** , 817 (1991).

Chapter 10

[1]J.H. Marsh, A.C. Bryce, and R.M. De La Rue, 'Recent progress in quantum well intermixing and application to waveguide devices', to be published in Material Scien. Engin. 1994.

List of publications

1. B.S. Ooi, A.C. Bryce, C.D.W. Wilkinson, and J.H. Marsh, 'Study of reactive ion etching-induced damage in GaAs/AlGaAs structures using a quantum well intermixing probe', Applied Physics Letter, Vol. **64**, pp598-600, 1994.

2. B.S. Ooi, A.C. Bryce, J.H. Marsh, and J. Martin, 'Transmission electron microscope study of fluorine and boron implanted and annealed GaAs/AlGaAs', Applied Physics Letter, Vol. **65**, pp85-87, 1994.

3. B.S. Ooi, S. E. Hicks, A.C. Bryce, C.D.W. Wilkinson and J.H. Marsh, 'Study of C_2F_6 overetch induced damage and the effects of overetch on subsequent $SiCl_4$ etch of GaAs/AlGaAs', accepted by Journal of Applied Physics.

4. B.S. Ooi, S.G. Ayling, A.C. Bryce, J.H. Marsh, 'Multiple wavelength laser chip fabricated using spatially controlled quantum well intermixing', submitted to Conference on Laser and Electro-Optics (CLEO), Maryland U.S.A., May 1995.

5. B.S. Ooi, A.C. Bryce, J.H. Marsh, 'Plasma-based integration process for photonic integrated circuits', submitted to Conference on Laser and Electro-Optics (CLEO), Maryland U.S.A., May 1995.

6. B.S. Ooi, S.G. Ayling, A.C. Bryce, J.H. Marsh, 'Fabrication of multiple wavelength lasers in GaAs/AlGaAs structures using a spatially controlled quantum well intermixing technique', submitted to IEEE Photonics Technology Letter.

7. B.S. Ooi, A.C. Bryce, J.H. Marsh, 'A novel integration process for photonic integrated circuits using plasma damage induced layer intermixing', submitted to Electronic Letter.

Appendix A Wafer structures

This appendix documents the layer structures used in this project.

A1: DQW laser material (1.3 μm upper cladding)

Method of growth: MOVPE

Layer	Thickness (μm)	Material	Dopant (cm^{-3})	Purpose of layer
1	0.5	GaAs	n-type, Si, 5 x 10^{18}	n-contact layer
2	1.5	$Al_{0.4}Ga_{0.6}As$	n-type, Si, 5 x 10^{17}	lower cladding
3	0.1	$Al_{0.2}Ga_{0.8}As$	Undoped	graded barrier
4	0.01	GaAs	Undoped	QW
5	0.01	$Al_{0.2}Ga_{0.8}As$	Undoped	barrier
6	0.01	GaAs	Undoped	QW
7	0.1	$Al_{0.2}Ga_{0.8}As$	Undoped	graded barrier
8	1.3	$Al_{0.4}Ga_{0.6}As$	p-type, C, 5 x 10^{17}	upper cladding
9	0.1	GaAs	p-type, Zn, 5 x 10^{18}	contact layer

A2. Multiple QWI probe

Method of growth: MOVPE **Doping of layers**: Undoped

Layer	Thickness (μm)	Material	Purpose of layer	77 K PL λ (nm)
1	0.2	GaAs	buffer layer	—
2	0.02	$Al_{0.4}Ga_{0.6}As$	barrier	—
3	0.0095	GaAs	reference QW	710
4	0.3	$Al_{0.4}Ga_{0.6}As$	barrier	—
5	0.007	GaAs	5th QW	741
6	0.02	$Al_{0.4}Ga_{0.6}As$	barrier	—
7	0.006	GaAs	4th QW	760
8	0.02	$Al_{0.4}Ga_{0.6}As$	barrier	—
9	0.0043	GaAs	3rd QW	778
10	0.02	$Al_{0.4}Ga_{0.6}As$	barrier	—
11	0.0036	GaAs	2nd QW	786
12	0.02	$Al_{0.4}Ga_{0.6}As$	barrier	—
13	0.0025	GaAs	1st QW	800
14	0.025	$Al_{0.4}Ga_{0.6}As$	barrier	—
15	0.005	GaAs	cap layer	—

A3: DQW laser material (0.9μm upper cladding)

Method of growth: MOVPE

Layer	Thickness (μm)	Material	Dopant (cm^{-3})	Purpose of layer
1	0.5	GaAs	n-type, Si, 2.6 x 10^{18}	n-contact layer
2	1.5	$Al_{0.4}Ga_{0.6}As$	n-type, Si, 7.7 x 10^{17}	lower cladding
3	0.1	$Al_{0.2}Ga_{0.8}As$	Undoped	graded barrier
4	0.01	GaAs	Undoped	QW
5	0.01	$Al_{0.2}Ga_{0.8}As$	Undoped	barrier
6	0.01	GaAs	Undoped	QW
7	0.1	$Al_{0.2}Ga_{0.8}As$	Undoped	graded barrier
8	0.9	$Al_{0.4}Ga_{0.6}As$	p-type, C, 5.4 x 10^{17}	upper cladding
9	0.1	GaAs	p-type, Zn, 1.8 x 10^{19}	contact layer

A4: DQW laser material (1.5 μm upper cladding)

Method of growth: MOVPE

Layer	Thickness (μm)	Material	Dopant (cm^{-3})	Purpose of layer
1	0.5	GaAs	n-type, Si, 5 x 10^{18}	n-contact layer
2	1.5	$Al_{0.4}Ga_{0.6}As$	n-type, Si, 5 x 10^{17}	lower cladding
3	0.1	$Al_{0.2}Ga_{0.8}As$	Undoped	graded barrier
4	0.01	GaAs	Undoped	QW
5	0.01	$Al_{0.2}Ga_{0.8}As$	Undoped	barrier
6	0.01	GaAs	Undoped	QW
7	0.1	$Al_{0.2}Ga_{0.8}As$	Undoped	graded barrier
8	1.5	$Al_{0.4}Ga_{0.6}As$	p-type, C, 5 x 10^{17}	upper cladding
9	0.1	GaAs	p-type, Zn, 5 x 10^{18}	contact layer

A5. p-type AlGaAs material for the study of F and B diffusion (QT592)

Method of growth: MOVPE

Layer	Thickness (μm)	Material	Dopant (cm^{-3})	Purpose of layer
1	1.0	GaAs	Undoped	buffer layer
2	1.0	$Al_{0.37}Ga_{0.63}As$	p-type, C, 1.4x 10^{17}	lower barrier
3	0.02	GaAs	Undoped	QW and SIMS marker
4	0.1	$Al_{0.37}Ga_{0.63}As$	p-type, C, 1.4x 10^{17}	upper barrier
5	0.9	$Al_{0.37}Ga_{0.63}As$	p-type, C, 4.8x 10^{17}	p-doped upper barrier
6	0.01	GaAs	Undoped	cap layer

A6. n-type AlGaAs material for the study of F and B diffusion (QT595R)

Method of growth: MOVPE

Layer	Thickness (μm)	Material	Dopant (cm^{-3})	Purpose of layer
1	1.0	GaAs	Undoped	buffer layer
2	1.0	$Al_{0.37}Ga_{0.63}As$	Undoped	lower barrier
3	0.02	GaAs	Undoped	QW and SIMS marker
4	0.1	$Al_{0.37}Ga_{0.63}As$	Undoped	upper barrier
5	0.9	$Al_{0.37}Ga_{0.63}As$	n-type, Si, 5.6x 10^{17}	n-doped upper barrier
6	0.01	GaAs	Undoped	cap layer

A7. Multi-GaAs/AlGaAs layer

Method of growth: MBE **Doping of layers**: Undoped

Layer	Thickness (μm)	Material
1	0.5	GaAs
2	0.5	$Al_{0.26}Ga_{0.74}As$
3	0.1	GaAs
4	0.1	$Al_{0.26}Ga_{0.74}As$
5	0.1	GaAs
6	0.1	$Al_{0.26}Ga_{0.74}As$
7	0.1	GaAs
8	0.1	$Al_{0.26}Ga_{0.74}As$
9	0.1	GaAs

Appendix B TEM cross-section specimen preparation for GaAs/AlGaAs QWs structures

B.1 Introduction

This Appendix documents the method used to produce cross-section TEM specimens from GaAs/AlGaAs QW structures. It is a modified form the methods developed by Helmersson *et al.*[1] and Scott[2]. Several difficulties have been overcome in converting these techniques to the GaAs/AlGaAs QW structures. The preparation technique described below has the advantages of producing more specimens in a relatively short time, and reducing the artefacts introduced by ion-milling to a minimum.

B.2 Cross-Section Preparation

Samples are scribed or cleaved from the wafer along [110] direction into bars of dimensions about 1.6 x 15 mm^2. These bars are used to form the cross-section samples. The bars have next to be reduced in thickness from about 500 μm to 200 μm, i.e. half of the width of the slot described in the next Section. The method used is to stick the cross-sections face down using wax onto a steel sample polishing stage, which is used in laser thinning, and hand grind to the required thickness using a "figure of eight" motion on a flat glass plate with 9 μm alumina powder. After thinning, the cross-sections must be cleaned of wax in a soxhlet type reflux condenser for about 1 hour using trichoroethene. Final cleaning is carried out in an ultrasonic bath using acetone then methanol for 5 min each.

B.3 Encapsulation

In order to withstand the subsequent thinning process the cross-sections must be mounted in a mechanically stable structure. A brass tube and slotted molybdenum insert (Fig. B.1) are used for this purpose. The brass tube is machined with an outer diameter of 3 mm (standard TEM specimen diameter) and an inner diameter of 2 mm. The hollow section extends for ~ 20 mm ending in a larger diameter cylinder used for clamping the rod during diamond sawing. The dimensions of the cylinder are not important, except that the end flat must be perpendicular to the axis of the tube, so that it can be used as a reference.

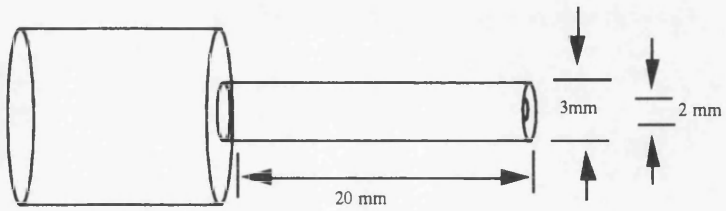

Figure B.1: The brass holder used to hold the molybdenum (Mo) insert.

The Mo insert is supplied in rod form in lengths of 1 m with a diameter of 2 mm from Goodfellow. Inserts of length 2 cm are sawn from the Mo rod. A slot of length ~15 mm is then cut in each insert using a

---

[1] U.Helmersson, and J.E.Sundgren , 'Cross Section Preparation for TEM of Film-Substrate Combination With A Large Difference in Sputtering Yields', J.Elec.Micr.Tech. **4** , 361 (1986).

[2] C.Scott, Private Communication

diamond saw. Since the GaAs/AlGaAs cross section is very fragile when thinned below 200 μm, the slot should be at least 400 μm wide. This can be achieved by sawing the Mo slot using a 0.0015" (375 μm) thick diamond blade. Accurate knowledge of the width of this slot is important as it determines the final thickness of the cross section sample described in the previous section. It is crucial that the two dimensions closely match. The completed rod and insert are then degreased for ~30 mins using the same method as for the cross sections. The cross sections are bonded together face to face using a thin layer of Devcon " 5 Minute Epoxy", and immediately glued into the Mo insert (Figure 2). This, in turn, is glued into the brass tube and the whole assembly left to cure overnight.

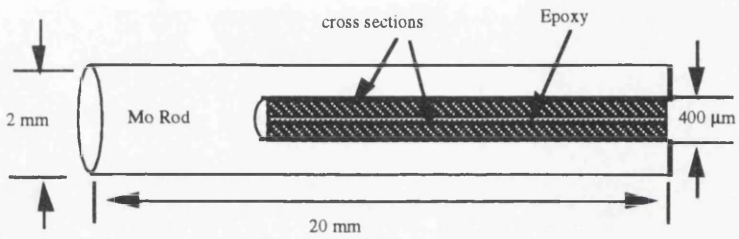

Figure B.2: The schematic diagram represent two thinned strips after inserted and glued in the Mo slot.

B.4 Cutting and Polishing

Once the glue in the rod is sufficiently hardened, individual disks can be diamond sawn. For efficiency a thinner diamond saw (300 μm) is used, each cut being made on a 600 μm pitch giving specimens ~ 300 μm in thickness. The flat end of the brass rod is used as a reference to ensure that the disks are cut square. Normally at least 12 disks can be cut from each pair of cross-sections. To cause less damage to the specimen, the plane of the cross section is oriented to be nearly tangential to the blade. A number of these disks (usually 6) are then hand thinned to ~140 μm. This is done in the same way as for the cross sections, except both sides are ground. After each side has been ground, it is polished to mirror brightness using 3 μm diamond paste on a flat lapping cloth rotating at 500 rpm. Figure 3 is a plan diagram of the resulting specimen.

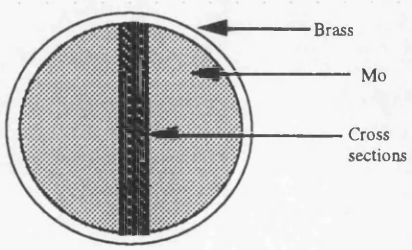

Figure B.3 : The plan diagram of the resulting specimen after sawing, thinning, and 2-side polishing.

B. 5 Dimple Grinding

A Gatan model 656 dimple grinder is used to thin the specimens mechanically to the thickness required for ion-milling. This grinder is equipped with an accurate micrometer with digital display. Before that, an optical microscope is used to select the best polished specimen for grinding. The best disk is

mounted on a glass stub using beeswax, and dimple ground to ~90 μm using a standard 15 mm diameter phosphor bronze spherical section wheel with 3 μm diamond paste. The optimum settings are grinder weight of 25 grams and the rotation speed of approximately 500 rpm. At regular intervals the specimen should be monitored for crack formation. Cracks which penetrate the whole thickness of the substrate near the centre of the disk are terminal and the specimen should be abandoned. Peripheral cracks are usually acceptable and cracks which are not through the whole thickness can be polished out. Having reached the required thickness, a felt wheel is substituted and a final polish with 0.25 μm diamond paste is done. The grinding weight should be increased to the maximum of 25 grams. at this stage, which usually takes ~ 10 mins. At the end of this time the specimen should be mirror smooth with no scratches visible on the substrate.

Removal and cleaning of the specimens is carried out in the soxhlet extractor. The specimen is ready to be ion milled at the end of this stage.

B.6 Ion Milling

The final stage in the preparation procedure is to ion mill the dimpled disk to electron transparency. The ion miller used was a Gatan 600 series 'Duomill'. Each sample is cooled during milling using the Gatan's liquid nitrogen cooled stage, to reduce radiation damage. The optimum milling conditions were found to be an ion incidence angle of 11 degrees, ion current of 0.5 mA per gun, and 5 kV accelerating voltage. The rotation of the specimen stage was set at 2 rpm. Best results are obtained if the milling is stopped as soon after breakthrough as possible- in general the smaller the hole formed the better the sample. At this stage the specimen should be removed and examined in the electron microscope. If further thinning is deemed necessary, it can be carried out at a lower angle of incidence (6 degrees) using the special chemically assisted ion beam etching (CAIBE) stage supplied with the ion miller.